SLAC-R-976

Measurement of CP Violation in B Anti-B Mixing on the Recoil of Partially Reconstructed Anti-B0 to D* L- Anti-Nu/L Using Kaon Tags

By Alessandro Gaz

SLAC National Accelerator Laboratory, Stanford University, Stanford CA 94309
Work funded in part by DOE Contract DE-AC02-76SF00515

UNIVERSITÀ DEGLI STUDI DI PADOVA

Sede Amministrativa: Università degli Studi di Padova
Dipartimento di Fisica Galileo Galilei

DOTTORATO DI RICERCA IN: FISICA
XX CICLO

Measurement of CP Violation in $B\overline{B}$ Mixing on the Recoil of partially reconstructed $\overline{B}^0 \rightarrow D^{*+}\ell^-\bar{\nu}_\ell$ using Kaon Tags

Coordinatore: *Prof. Attilio Stella*

Supervisore: *Prof. Franco Simonetto*

Co-Supervisore: *Dott. Martino Margoni*

Dottorando: *Alessandro Gaz*

Contents

Introduzione

Dopo la sua formulazione negli anni '60, il Modello Standard delle Interazioni Fondamentali è passato attraverso un'impressionante serie di successi, iniziata con la scoperta delle correnti deboli neutre [1] e l'osservazione sperimentale dei portatori massivi delle interazioni deboli, i bosoni $W^{\pm}$ e Z^0 [2], [3]. Misure di alta precisione effettuate a LEP e SLAC verificano la validità della teoria ad un livello di accuratezza senza precedenti e non mostrano alcuna deviazione significativa dalle previsioni del Modello Standard.

Una delle caratteristiche più attraenti del Modello Standard è la descrizione dei fenomeni che violano la simmetria tra materia ed antimateria (simmetria CP), e questa violazione dipende unicamente (nel settore dei quark) da una fase debole nella matrice che descrive gli accoppiamenti tra quark di diverso sapore.

La violazione di CP fu scoperta nel 1964 come un piccolo effetto nel mescolamento del sistema $K^0 - \bar{K}^0$ [12] ma, dopo alcuni decenni di studi della fisica dei mesoni K, non si è potuta ottenere una forte conferma del Modello Standard sul meccanismo che genera la violazione di CP.

D'altro canto la fisica dei mesoni B si presta ad un numero piuttosto elevato di misure che possono confermare o smentire questo aspetto della teoria.

L'obiettivo principale del programma di fisica degli esperimenti *BABAR* e Belle è la verifica della descrizione della violazione di CP e della fisica dei sapori principalmente dallo studio dei decadimenti dei mesoni B_u e B_d. Poco dopo l'inizio della presa dati nel 1999, è stata scoperta la violazione di CP nell'interferenza tra decadimento e mescolamento nel *canale d'oro* $B^0 \to J/\psi K^0$ [17] [18], mentre nel 2004 una cospicua asimmetria di carica è stata osservata nel canale $B^0 \to K^+\pi^-$ [16].

Esiste un terzo tipo di violazione di CP che può essere esibito dal sistema $B_d - \bar{B}_d$, la cosiddetta violazione di CP nel mescolamento. Il Modello Standard prevede che questa asimmetria sia molto piccola, potenzialmente fuori dalla portata degli esperimenti attuali, tuttavia numerosi modelli di Nuova Fisica contengono nuove particelle ed accoppiamenti che possono innalzarla fino a valori misurabili.

In questa tesi cercheremo di misurare effetti di violazione di CP nel mescolamento $B_d - \bar{B}_d$ all'esperimento *BABAR*. Uno dei due mesoni B prodotti al collisore elettromagnetico PEP-II viene ricostruito utilizzando la tecnica della ricostruzione parziale, mentre il sapore dell'altro è dedotto dalla carica di un kaone identificato tra i suoi prodotti di decadimento.

Data l'esiguità dell'effetto che vogliamo misurare, un aspetto cruciale di quest'analisi riguarda il controllo delle asimmetrie di carica fittizie che sorgono dall'interazione delle particelle con il materiale del rivelatore. Questo è ottenuto utilizzando un campione di controllo di kaoni carichi sugli stessi dati che impieghiamo per l'analisi della violazione di CP.

Dopo una breve introduzione sul formalismo teorico e sulla fenomenologia dei decadimenti dei mesoni B ad una B-factory (capitoli 1 e 2), passeremo in rassegna nel capitolo 3 gli attuali risultati sperimentali in questo campo.

Descriveremo quindi le caratteristiche del collisore e dell'apparato sperimentale (capitolo 4) usati per effettuare la nostra misura. Il campione di dati disponibile e le tecniche di pre-selezione degli eventi sono trattate nel capitolo 5, mentre il metodo di analisi è discusso in dettaglio nel capitolo seguente.

Nei capitoli 7 e 8 diamo le definizioni delle *funzioni densità di probabilità* usate per descrivere ciascuna componente del nostro campione e queste vengono validate utilizzando eventi simulati. Campioni di Monte Carlo Toy e Monte Carlo ripesato sono usati nel capitolo 9 per verificare la sensibilità della nostra procedura di fit ai parametri fisici collegati alla violazione di CP; il capitolo 10 discute la possibilità di modellizzare alcune delle componenti del nostro campione direttamente sui dati.

Infine il fit sui dati reali è descritto nel capitolo 11 e la trattazione delle incertezze sistematiche è svolta nel capitolo 12, mentre il risultato finale è presentato nel capitolo 13.

Introduction

After its formulation in 1960's the Standard Model of Fundamental Interactions has gone through an impressive series of successes, begun with the discovery of neutral weak currents [1] and the experimental observations of the massive carriers of weak interactions, the $W^{\pm}$ and Z^0 bosons [2], [3]. High precision measurements performed at LEP and SLAC test the validity of the theory to an unprecedented level of accuracy and do not show any significant deviations with respect to the Standard Model predictions.

One of the attractive features of the Standard Model is the description of the phenomena which violate the matter-antimatter symmetry (CP), and this violation uniquely depends (in the quark sector) on a weak phase in the matrix describing the couplings among different quark flavors.

CP-violation was discovered in 1964 as a tiny effect in the mixing of the $K^0 - \bar{K}^0$ system [12] but, after a few decades of study of the physics of K mesons, no strong confirmation of the Standard Model can be obtained on the mechanism which generates CP-violation.

On the other hand the physics of B mesons is suitable for a pretty large number of measurements which can confirm or disprove this aspect of the theory.

The main goal of the BABAR and Belle experiments physics program is to test the description of CP-violation and flavor physics mainly from the decays of B_u and B_d mesons. Soon after the beginning of data-taking in 1999, CP-violation was discovered in the interference between mixing and decay in the golden channel $B^0 \rightarrow J/\psi K^0$ [17] [18], while in 2004 a large direct charge asymmetry was observed in the $B^0 \rightarrow K^+\pi^-$ channel [16].

There is a third kind of CP-violation which can be exhibited by the $B_d - \bar{B}_d$ system, the so called CP-violation in mixing. The Standard Model predicts this asymmetry to be small, possibly out of reach of current experiments, but several New Physics models contain new particles and couplings which can enhance it up to detectable levels.

In this thesis we search for CP-violation in $B_d - \bar{B}_d$ mixing at the BABAR experiment. We reconstruct one of the two B mesons produced at the PEP-II electromagnetic collider using the partial reconstruction technique, while the flavor of the other B is inferred by the charge of a kaon identified among its decay products.

Given the smallness of the physical asymmetry we want to measure, a crucial aspect of this analysis is the control of spurious charge asymmetries arising from the interaction of particles with the detector material. We accomplish this by using a control sample of charged kaons on the same data we use in our analysis.

After a brief introduction of the theoretical framework and the phenomenology of the decays of B mesons at a B-factory (chapters 1 and 2), we will review in chapter 3 the current experimental results on this topic.

We will then describe the characteristics of the collider and the experimental apparatus (chapter 4) used to perform our measurement. The available dataset and the event pre-selection techniques are treated in chapter 5, while the analysis method is discussed in detail in the following one.

In chapters 7 and 8 the definitions of the *probability density functions* used to model each component of our sample are given and then they are tested in samples of simulated data. Toy and reweighted Monte Carlo data are used in chapter 9 to test the sensitivity of our fitting procedure to the physical parameters related to CP violation; chapter 10 discusses the possibility of modeling some of the components of our sample directly on the data.

Finally the fit on the real data sample is described in chapter 11 and the treatment of systematic uncertainties is done in chapter 12, while the final result is given in chapter 13.

Chapter 1

Theoretical Framework

In this chapter, a brief introduction of the Standard Model of fundamental interaction will be given, with particular emphasis on the mechanism which gives rise to phenomena where the symmetry between matter and anti-matter is broken. We will then review the phenomenology of mixing and decay of a coherent state $B^0\overline{B}^0$.

The different kinds of CP-violation in the $B\overline{B}$ system will then be discussed and finally we will focus on the theoretical predictions of CP-violation in $B^0\overline{B}^0$ mixing and their potential implications in the search for New Physics beyond the Standard Model.

1.1 The Standard Model of Fundamental Interactions

The Standard Model (SM) is a global theory that unifies strong, weak and electromagnetic interactions in a gauge theory formalism. In the Standard Model, the elementary particles, or *fields*, are divided in two groups: half-integer spin particles (*fermions*), that represent the constituents of matter, and integer-spin particles (*bosons*), mediating the interactions. Bosons are divided into *vector* and *scalar* bosons, according to the value of their spin being 1 or 0 respectively.

Fermions are organized in two categories (*quarks* and *leptons*), each of which is divided into three generations.

- Lepton doublets:
$$\begin{pmatrix} \nu_e \\ e^- \end{pmatrix} \begin{pmatrix} \nu_\mu \\ \mu^- \end{pmatrix} \begin{pmatrix} \nu_\tau \\ \tau^- \end{pmatrix},$$
  where the elements in the upper line have 0 electric charge and the elements in the lower one have charge equal to -1.
- Quark doublets:
$$\begin{pmatrix} u \\ d \end{pmatrix} \begin{pmatrix} c \\ s \end{pmatrix} \begin{pmatrix} t \\ b \end{pmatrix},$$
  where the elements in the upper line have electric charge equal to +2/3 (electron charges) and the elements in the lower one have charge equal to -1/3.

with their relative anti-particles.

The gauge (vector) bosons are:

- the photon, mediator of the electromagnetic interaction;
- the $W^\pm$ and the Z^0, gauge bosons of weak interactions;
- 8 gluons, mediators of the strong interactions.

The Higgs boson, a scalar field whose coupling with the other fields generates their masses while preserving the gauge-invariance of the theory, has not been experimentally observed yet.

In the Standard Model [5], interactions are generated by a Lagrangian density that is invariant under transformations of the group $SU(3)_C \otimes SU(2)_L \otimes U(1)_Y$, which is made up by the strong interaction symmetry group (or *color* symmetry) $SU(3)_C$ and the electro-weak interaction group $SU(2)_L \otimes U(1)_Y$, product of the *weak isospin* and *hypercharge* symmetries. This Lagrangian density can be expressed as a sum of four contributions:

$$\mathcal{L}_{SM} = \mathcal{L}_{fermions} + \mathcal{L}_{Yang-Mills} + \mathcal{L}_{Higgs} + \mathcal{L}_{Yukawa} \,, \tag{1.1}$$

describing respectively:

- the dynamics of fermions in terms of their kinetic energy and their couplings to the gauge bosons ($\mathcal{L}_{fermions}$);
- the dynamics of gauge bosons in terms of their kinetic energy and their self-couplings, associated to local (non-Abelian) symmetry groups ($\mathcal{L}_{Yang-Mills}$);
- the spontaneous symmetry breaking term, derived from the Higgs mechanism, by which bosons acquire a finite mass ($\mathcal{L}_{Higgs}$);
- the fermion mass terms, derived from the same symmetry breaking mechanism and the Yukawa couplings of the fermions with the Higgs scalar ($\mathcal{L}_{Yukawa}$).

The last two terms, that would not appear in a massless particle theory, stem from the spontaneous breaking of the invariance of the SM Lagrangian in the group $SU(3)_C \otimes U(1)_Q$, where $U(1)_Q$ is the symmetry associated to electric charge conservation. This is due to the introduction of a scalar Higgs field with a non-zero vacuum expectation value. The Lagrangian 1.1 not only accounts for massive fermions and gauge bosons, but also allows the violation of the fundamental symmetry (CP *symmetry*) that is given by the composition of two discrete symmetries, namely the parity inversion and the charge conjugation.

1.1.1 Violation of the CP symmetry in the Standard Model

For a given field theory, symmetry operators can be defined to describe peculiar invariances of the Lagrangian density. We will refer to *discrete* symmetries when the corresponding operators have a finite number of eigenvalues. Three among the most important discrete symmetry operators are:

- the Parity operator (P), whose action generates an inversion of the spatial field coordinates $(t,\, \overline{x}) \mapsto (t,\, -\overline{x})$. This is equivalent to a reversal of the momentum direction and the helicity sign of a particle;
- the Time reversal operator (T), that corresponds to an inversion of the time coordinate $(t,\, \overline{x}) \mapsto (-t,\, \overline{x})$;
- the Charge conjugation operator (C), that changes the field associated to a particle into that of its anti-particle, i. e. reverses its charge and all its intrinsic quantum numbers.

The composition of all these symmetries (CPT) is particularly meaningful since, according to the CPT theorem [6], all Lorentz-invariant relativistic field theories must be strictly invariant under the product of C, P and T. CP symmetry becomes therefore a very important property of the theory because its violation implies also a violation of T. No violation of either C, P or T has ever been observed experimentally in processes involving only the strong and electromagnetic interactions. In weak interactions, conversely, C and P are largely violated as separate symmetries [7], while the product CP (and so the T symmetry) is, to a very good approximation,

Table 1.1: Transformation under CP of the fermionic bilinear forms (top lines). Transformation under CP of scalar (H), pseudoscalar (A) and vector ($W^{\pm.\mu}$) bosons and of the derivative operator (bottom lines). $\eta = 1$ for $\mu = 0$ and $\eta = -1$ for $\mu = 1, 2, 3$.

Term	$\overline{\Psi}_j\Psi^k$	$i\overline{\Psi}_j\gamma^5\Psi^k$	$\overline{\Psi}_j\gamma^\mu\Psi^k$	$\overline{\Psi}_j\gamma^\mu\gamma^5\Psi^k$
CP transformed	$\overline{\Psi}_k\Psi^j$	$-i\overline{\Psi}_k\gamma^5\Psi^j$	$-\eta\overline{\Psi}_k\gamma^\mu\Psi^j$	$-\eta\overline{\Psi}_k\gamma^\mu\gamma^5\Psi^j$
Term	H	A	$W^{\pm,\mu}$	∂^μ
CP transformed	H	$-A$	$-\eta W^{\pm,\mu}$	$\eta\partial^\mu$

conserved. Nevertheless, CP-violation has been detected in some rare weak processes involving decays of neutral K and B mesons.

It is interesting to apply the CP transformation to the SM Lagrangian to check under which assumption CP-violation can be theoretically allowed. Since eq. 1.1 must be covariant under Lorentz transformations, the generic fermion fields (Ψ) can enter the Lagrangian only in particular combinations known as *bilinear* and their first derivatives, while there are no restrictions for boson fields. In table 1.1 all fermionic bilinear terms that are present in the SM Lagrangian, the boson fields and the derivative operator are listed together with their corresponding transformed term under CP. The Lagrangian must be a linear combination of these terms with coefficients (e. g. masses, coupling constants, etc.) that can be real or complex. When imposing the hermiticity of the Lagrangian, hermitian conjugate terms also appear in its expression, therefore CP is not necessarily preserved in presence of complex coefficients.

More precisely, a physically meaningful complex coefficient is one that cannot be transformed into a real quantity by a mere global phase rotation. When, in a given field theory, coefficients whose phases are not convention-dependent are present, CP-violation can occur. In the SM case, the complex phase appears in the term that determines the coupling of quarks to the $W^\pm$ bosons (contained in the $\mathcal{L}_{fermions}$ part of eq. 1.1). This kind of coupling can be effectively described by means of a complex quark mixing matrix, as we will now see in detail.

1.2 The CKM Matrix

The terms in the SM Lagrangian which describe the coupling between quarks and the $W^\pm$ bosons are of the (maximally parity violating) form:

$$\mathcal{L}_{fermions} = -\frac{g}{\sqrt{2}}(\mathcal{J}^\mu W^+_\mu + \mathcal{J}^{\mu\dagger}W^-_\mu)\,, \tag{1.2}$$

where the W^+_μ operator annihilates a W^+ or creates a W^- (vice-versa for the W^-_μ) and the *current operator* $\mathcal{J}^\mu$ can be explicitly written as:

$$\mathcal{J}^\mu = \sum_i \bar{u}_i\gamma^\mu\frac{1}{2}(1-\gamma^5)V_{ij}d_i\,, \tag{1.3}$$

for quarks. The field operators $\bar{u}_i$ annihilate u, c and t or create their antiparticles, while the d_i operators annihilate d, s and b or create their antiparticles.

In the quark case, transitions between different generations are determined by the quantities V_{ij}, (with the indices i, j running through the three quark generations) that are the elements of a 3 × 3 unitary matrix, the Cabibbo-Kobayashi-Maskawa (CKM) matrix [15].

From a physical point of view, the CKM matrix can be regarded as a rotation matrix between the mass eigenstates basis (d, s, b) and a set of new states (d', s', b') with diagonal couplings to (u, c, t). Feynman amplitudes of processes where a W^- is emitted ($d_j \to W^-u_i$, $\bar{u}_i \to W^-\bar{d}_j$)

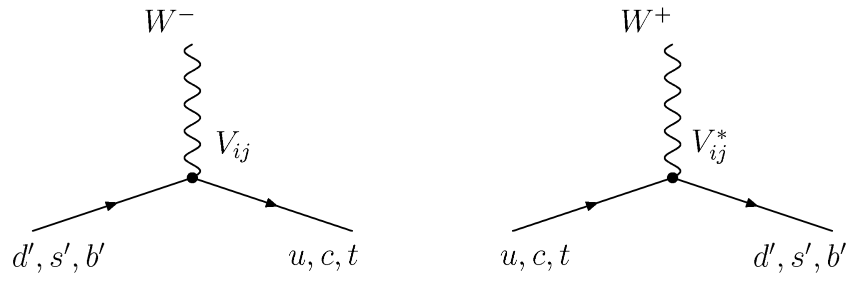

Figure 1.1: Feynman box diagrams for charged-current weak interaction vertices.

are then proportional to V_{ij}, while when a W^+ is emitted ($u_i \to W^+ d_j$, $\bar{d}_j \to W^+ \bar{u}_i$) they are proportional to V_{ij}^*, as depicted in figure 1.1.

The standard notation for the CKM matrix [8] is:

$$\begin{pmatrix} d' \\ s' \\ b' \end{pmatrix} = \begin{pmatrix} V_{ud} & V_{us} & V_{ub} \\ V_{cd} & V_{cs} & V_{cb} \\ V_{td} & V_{ts} & V_{tb} \end{pmatrix} \begin{pmatrix} d \\ s \\ b \end{pmatrix} . \tag{1.4}$$

The dominant terms in the CKM matrix are the diagonal ones, thus transitions between two different quark generations are suppressed with respect to $u \to d$, $c \to s$ and $t \to b$ transitions. The key feature of the CKM matrix is that its elements can be non-trivially complex, allowing for CP-violation phenomena in charged-current transitions.

Like fermion masses, the CKM elements are free parameters in the Standard Model and their values are not predicted by the theory.

1.2.1 Parametrization of the CKM matrix - the Unitarity Triangle

Several representations of the CKM elements exist, according to particular choices of the parametrization.

First we have to notice that the number of free parameters is smaller than the number of independent coefficients of a generic 3×3 complex matrix, due to the physical constraints the CKM matrix needs to satisfy. A general $n \times n$ complex matrix is specified by $2n^2$ real parameters; the request of unitarity ($V^\dagger V = V V^\dagger = \mathbb{1}$) removes n^2 free parameters. Moreover, with n quark generations, we are free to arbitrarily re-define $2n - 1$ quark field phases. So the physically meaningful parameters are $2n^2 - n^2 - (2n - 1) = (n - 1)^2$ thus, with 3 generations, the physics of the CKM matrix is determined by 4 real parameters. This is a remarkable result because, since a real unitary matrix is specified by just 3 rotation angles, we are left with one complex phase that cannot be removed by a re-definition of the quark fields.

One common parametrization for the CKM matrix is, in fact, expressed in terms of three rotation angles, θ_{12}, θ_{23} and θ_{13} and a complex phase, δ_{13} [4]:

$$V = \begin{pmatrix} c_{12}c_{13} & s_{12}s_{13} & s_{13}e^{-i\delta_{13}} \\ -s_{12}c_{23} - c_{12}s_{23}s_{13}e^{i\delta_{13}} & c_{12}c_{23} - s_{12}s_{23}s_{13}e^{i\delta_{13}} & s_{23}c_{13} \\ s_{12}s_{23} - c_{12}c_{23}s_{13}e^{-i\delta_{13}} & -c_{12}s_{23} - s_{12}c_{23}s_{13}e^{i\delta_{13}} & c_{23}c_{13} \end{pmatrix} l, \tag{1.5}$$

where $c_{jk} = \cos\theta_{jk}$ and $s_{jk} = \sin\theta_{jk}$.

A more useful representation, as far as the hierarchy in the magnitude of its elements is concerned, is the Wolfenstein representation [9], where the four real parameters are: A, ρ, η and $\lambda = \sin\theta_C \simeq 0.2272 \pm 0.0010$ [4], θ_C being the Cabibbo mixing angle. In this parametrization, the matrix elements can be expanded in powers of λ, yielding:

$$V = \begin{pmatrix} 1-\frac{1}{2}\lambda^2 & \lambda & A\lambda^3(\rho - i\eta) \\ -\lambda & 1-\frac{1}{2}\lambda^2 & A\lambda^2 \\ A\lambda^3(1-\rho-i\eta) & -A\lambda^2 & 1 \end{pmatrix} + \mathcal{O}(\lambda^4)\,. \tag{1.6}$$

The parameters of the two representations are connected by the relations:

$$s_{12} \equiv \lambda, \quad s_{23} \equiv A\lambda^2, \quad s_{13}e^{-i\delta_{13}} \equiv A\lambda^3(\rho - i\eta). \tag{1.7}$$

A very useful pictorial representation of the CKM parameters is offered by the *Unitarity Triangle* formalism. Explicitly, the unitarity conditions of V are stated as:

$$\sum_{j=u,c,t} V_{ji}V^*_{jk} = \delta_{ik}\,, \tag{1.8}$$

Let us consider eq. 1.8 in the case $i \neq k$. The sum of three complex numbers being equal to zero corresponds to a triangle of vectors in the complex plane; we can in this way define 6 *unitarity triangles* made up by products of CKM parameters as sides. All triangles are connected to one another by having the same area, proportional to the Jarlskog invariant [10]:

$$\text{Area} = \frac{J}{2} \propto \text{Im}\,[V_{ud}V_{cs}V^*_{us}V^*_{cd}] \tag{1.9}$$

This quantity is non-vanishing under the assumptions that the quark masses are not degenerate, the mixing angles are different from 0 and $\pi/2$ and there is a non-zero complex phase.

Even though the areas are equal, the shapes of the triangles can be very different, since the size of the sides depends on the powers of λ appearing in their definitions. Considering the particular case $i = d$ and $k = b$ in eq. 1.8, we have:

$$V_{ud}V^*_{ub} + V_{cd}V^*_{cb} + V_{td}V^*_{tb} = 0\,, \tag{1.10}$$

and considering the Wolfenstein parametrization, all sides are found to be of order λ^3. We will take this particular triangle as the Unitarity Triangle. Figure 1.2 shows a common representation of it; usually its sides are rescaled and rotated so that one of its sides lies on the real axis and its vertices have coordinates $(0,0)$ and $(1,0)$. This choice is particularly useful, since the amount of CP-violation generated by the CKM matrix is determined by the coordinates of the upper vertex.

The position of the apex of the Unitarity Triangle can be determined (and even over-constrained) by measurements performed at the B-factories, while additional information is provided by CP-violation in the $K^0 - \overline{K}^0$ system and by the mixing of $B_s - \bar{B}_s$.

The upper vertex is usually represented using the coordinates $(\bar\rho, \bar\eta)$ in the complex plane, related to (ρ, η) by:

$$\bar\rho = \rho\left(1 - \frac{\lambda^2}{2}\right)\,, \quad \bar\eta = \eta\left(1 - \frac{\lambda^2}{2}\right)\,. \tag{1.11}$$

Since CP-violation is related to the displacement of the apex of the Unitarity Triangle from the real axis, the measurement of its angles being non trivial (0 or π) would be a proof of CP-violation. The angles of the Unitarity Triangle are related to the elements of the CKM matrix through the relations:

$$\phi_2 \equiv \alpha \equiv \arg\left[-\frac{V_{td}V^*_{tb}}{V_{ud}V^*_{ub}}\right]\,, \quad \phi_1 \equiv \beta \equiv \arg\left[-\frac{V_{cd}V^*_{cb}}{V_{td}V^*_{tb}}\right]\,, \quad \phi_3 \equiv \gamma \equiv \arg\left[-\frac{V_{ud}V^*_{ub}}{V_{cd}V^*_{cb}}\right]\,. \tag{1.12}$$

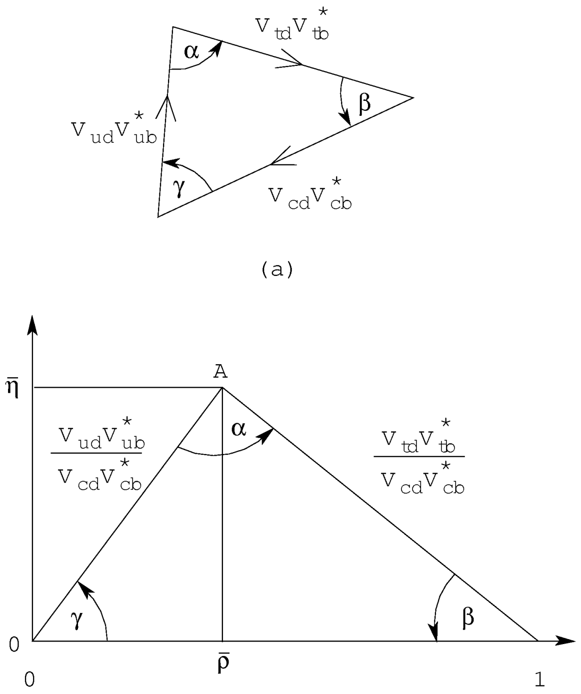

(a)

(b)

Figure 1.2: The Unitarity Triangle, before (a) and after (b) the rotation of $V_{cd}V^*_{cb}$ and the normalization of its sides by the factor $1/|V_{cd}V^*cb|$.

1.2.2 Experimental tests of the CKM mechanism

As we have seen, the presence of a non-trivial complex phase in the CKM mechanism can lead to processes where the CP symmetry is violated. A crucial question is then whether this is the only source of CP-violation in the Standard Model or its extensions.

In the last decade, the CKM mechanism has undergone a vast campaign of experimental tests which has confirmed its substantial correctness. Potential deviations from its predictions are now constrained to be small, carrying to the implication that either New Physics occurs at energy scales much higher than the one accessible by present experiments or there are not new sources of CP-violation other than the CKM phase.

Figures 1.3 and 1.4 depict the allowed regions in the $(\bar{\rho}, \bar{\eta})$ plane for the apex of the Unitarity Triangle derived from several measurements performed at the B-factories and by other experiments.

We are not going to discuss in detail each measurement, but we limit ourselves to stress the overall consistency of the CKM picture and the very good agreement of the pretty large sample of experimental observables employed in this analysis. The results of the global fit [11] are:

$$\begin{aligned} \bar{\rho} &= 0.147 \pm 0.029\,, \\ \bar{\eta} &= 0.342 \pm 0.016\,. \end{aligned}$$

1.3 B^0 Mixing and Decay

In this section we will focus on the phenomenology of B_d mixing and decay. The same formalism can be applied to the mixing and decay of K^0, D^0 and B_s mesons.

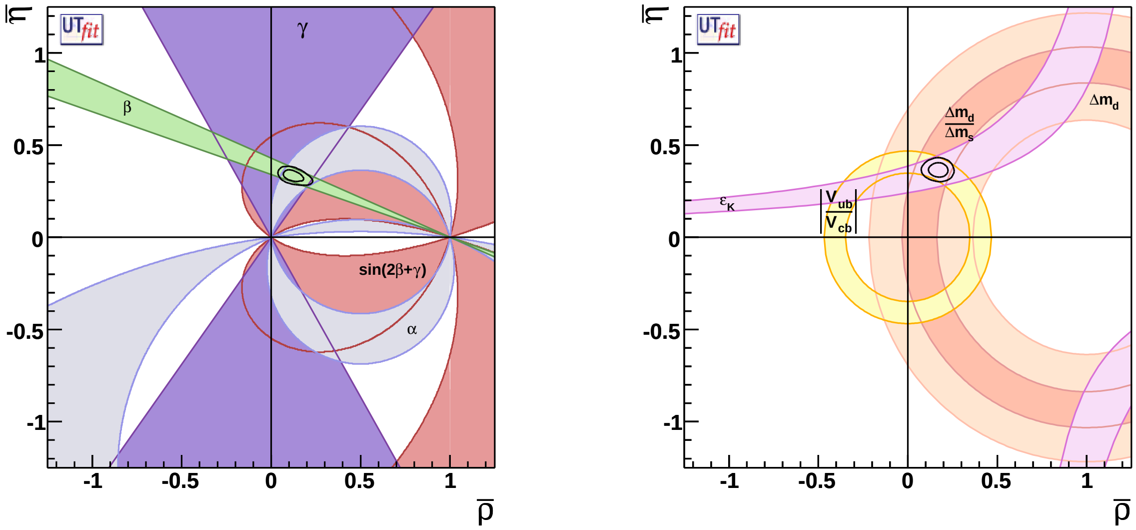

Figure 1.3: Constraints on the position of the apex of the Unitarity Triangle on the $(\bar{\rho}, \bar{\eta})$ complex plane. On the left plot the constraints from measurements of the angles α, β, γ and $2\beta + \gamma$ are shown. On the right one, all the other constraints, coming from measurements of the $B_d - \bar{B}_d$ and $B_s - \bar{B}_s$ mass differences, the ratio $|V_{ub}/V_{cb}|$ and the ε_K parameter driving CP-violation in the $K^0 - \bar{K}^0$ system. The two independent set of measurements constrain the apex to lie in two regions very well consistent with one another.

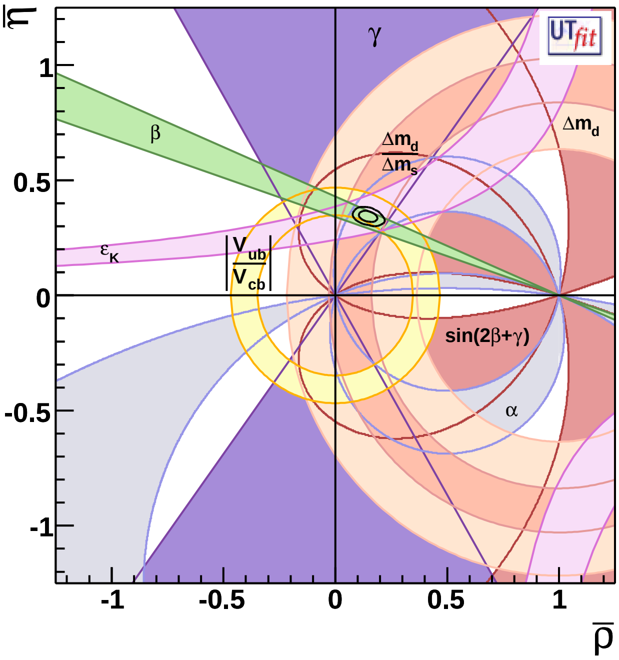

Figure 1.4: Constraint on the position of the apex of the Unitarity Triangle obtained by combining all the observables separately used in figure 1.3.

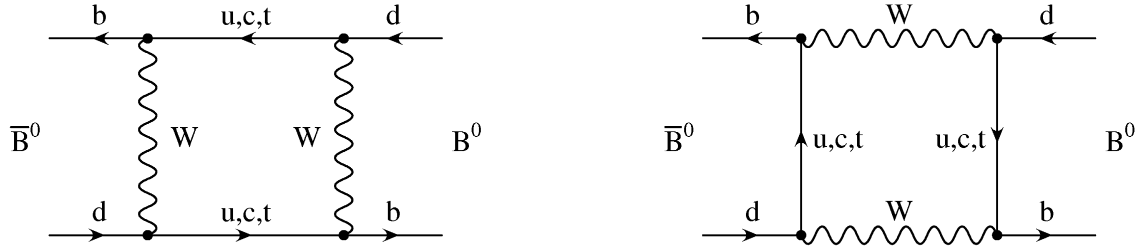

Figure 1.5: Feynman box diagrams entering the $B^0\overline{B}^0$ mixing.

We will call $|B^0\rangle$ and $|\bar{B}^0\rangle$ the antiquark-quark $(\bar{b}d)$ and $(\bar{d}b)$ bound states. These are the *flavor* (or *interaction*) eigenstates of the $B\overline{B}$ system.

A $|B^0\rangle$ ($|\bar{B}^0\rangle$) can oscillate into a $|\bar{B}^0\rangle$ ($|B^0\rangle$) through one of the amplitudes depicted by the Feynman diagrams of figure 1.5.

The effective Hamiltonian which drives the mixing and decay of B_d mesons can be written as:

$$H = \left(M - i\frac{\Gamma}{2} \right), \tag{1.13}$$

where M and Γ are 2×2 Hermitian matrices. If CPT is preserved (as we will assume throughout this thesis), we have $M_{11} = M_{22}$ and $\Gamma_{11} = \Gamma_{22}$.

The time evolution of the neutral B mesons doublet follows the Schroedinger equation:

$$i\frac{d}{dt}\begin{pmatrix} B^0 \\ \bar{B}^0 \end{pmatrix} = \begin{pmatrix} M_{11} - \frac{i}{2}\Gamma_{11} & M_{21}^{*} - \frac{i}{2}\Gamma_{21}^{*} \\ M_{21}^{2} - \frac{i}{2}\Gamma_{21} & M_{22} - \frac{i}{2}\Gamma_{22} \end{pmatrix}\begin{pmatrix} B^0 \\ \bar{B}^0 \end{pmatrix}. \tag{1.14}$$

The Hamiltonian (*mass*) eigenstates, having masses m_L and m_H and decay widths Γ_L and Γ_H respectively, can be written as:

$$|B_L\rangle = \frac{1}{\sqrt{1+(q/p)^2}}\left(p|B^0\rangle + q|\bar{B}^0\rangle\right) \tag{1.15}$$

$$|B_H\rangle = \frac{1}{\sqrt{1+(q/p)^2}}\left(p|B^0\rangle - q|\bar{B}^0\rangle\right), \tag{1.16}$$

where p and q are complex parameters[1]. If $|p| = |q|$, $|B_L\rangle$ and $|B_H\rangle$ are also CP-eigenstates.

An initial state, produced as B^0 or $\overline{B}^0$ at $t = 0$ evolves respectively as [30]:

$$|B^0_{phys}(t)\rangle = g_+(t)|B^0\rangle - \frac{q}{p}g_-(t)|\bar{B}^0\rangle \tag{1.17}$$

$$|\bar{B}^0_{phys}(t)\rangle = g_+(t)|\bar{B}^0\rangle - \frac{p}{q}g_-(t)|B^0\rangle, \tag{1.18}$$

where:

$$g_\pm(t) = \frac{1}{2}(e^{-i\omega_H t} \pm e^{-i\omega_L t}), \tag{1.19}$$

and

$$\omega_{H,L} = m_{H,L} - \frac{i}{2}\Gamma_{H,L}\,. \tag{1.20}$$

The experimental observables in B^0 mixing are the mixing frequency $\Delta m = m_H - m_L$, the decay width difference $\Delta\Gamma = \Gamma_L - \Gamma_H$ and $|q/p|$, which drives CP-violation in mixing, as will be shown in the following. In terms of M_{21} and Γ_{21}, those observables can be expressed as:

---

[1] Throughout the rest of this thesis the ratio q/p will always be referred to the B_d system, whereas for the B_s, we will use $(q/p)_s$.

$$(\Delta m)^2 - \frac{1}{4}(\Delta\Gamma)^2 = 4|M_{21}|^2 - |\Gamma_{21}|^2 \tag{1.21}$$

$$\Delta m \Delta\Gamma = -4\mathrm{Re}(M_{21}^* \Gamma_{21}) \tag{1.22}$$

$$|q/p| = \left|\sqrt{\frac{2M_{21} - i\Gamma_{21}}{2M_{21}^* - i\Gamma_{21}^*}}\right|. \tag{1.23}$$

In the $B^0\overline{B}^0$ system, the ratio Γ_{21}/M_{21} is $\mathcal{O}(m_b^2/m_t^2) \simeq 10^{-3}$, thus neglecting terms $\mathcal{O}(m_b^4/m_t^4)$ we can write:

$$\Delta m = 2|M_{21}| \tag{1.24}$$

$$\Delta\Gamma = -2|M_{21}|\mathrm{Re}\left(\frac{\Gamma_{21}}{M_{21}}\right) \tag{1.25}$$

$$|q/p| = 1 + \frac{1}{2}\mathrm{Im}\left(\frac{\Gamma_{21}}{M_{21}}\right). \tag{1.26}$$

The Matrix Elements M_{21} and Γ_{21} have been computed at different perturbative orders in the Standard Model and in several extensions. We will summarize the predictions on CP-violation in $B^0\overline{B}^0$ mixing in section 1.5.

1.4 CP violation in neutral and charged B mesons

CP-violation could manifest itself in the $B\overline{B}$ system in different ways. We will call A_f ($\bar{A}_f$) the amplitude of a B^0 ($\overline{B}^0$) decaying to the final state f.

We can have **Direct CP-violation** (either in charged or in neutral B mesons) when we have:

$$|A_f| = |\langle f|H|B\rangle| \neq |\langle \bar{f}|H|\bar{B}\rangle| = |\bar{A}_{\bar{f}}| \tag{1.27}$$

This kind of violation arises in decay channels where two or more amplitudes A_j of comparable magnitude are characterized by different strong (δ_j, CP-even) and weak (ϕ_j, CP-odd) phases:

$$A_f = \sum_j A_j e^{i\delta_j} e^{i\phi_j} \tag{1.28}$$

$$\bar{A}_{\bar{f}} = \sum_j A_j e^{i\delta_j} e^{-i\phi_j}. \tag{1.29}$$

The different behavior under the CP transformation of δ_j and ϕ_j determines the asymmetry.

This kind of CP violation has been first observed in the $B^0 \to K^+\pi^-$ decay channel [16] and is yet to be observed in charged B mesons.

The **Indirect CP-violation** or **CP-violation in Mixing**, which is the subject of this thesis, arises from $|q/p|$ being different from 1.

In this case, the probability of a B^0 to oscillate into a $\overline{B}^0$ is different from the probability of the conjugate process. As we will see in the following, the Standard Model predicts $|q/p|$ to be very close to 1 and no hint of CP-violation in mixing has been detected by recent and current experiments.

The third case is the **CP-violation in the interference between mixing and decay**. It is given by processes where B^0's and $\overline{B}^0$'s decay to a common final state f. Even if $|A_f| = |\bar{A}_f|$

and $|q/p| = 1$, we can have CP-violation if:

$$\mathrm{Im}(\lambda) = \mathrm{Im}\left(\frac{q}{p}\frac{\bar{A}_f}{A_f}\right) \neq 0 \tag{1.30}$$

The Standard Model prediction of large values of $\mathrm{Im}(\lambda)$ for decay channels such as $B \to J/\psi K^0$ motivated the construction of the B-factories which led, in 2001, to the discovery of CP-violation in the $B\overline{B}$ system [17], [18].

1.5 Theoretical predictions

Given that the mass of the b quark (m_b) is much larger than Λ_{QCD}, an Operator Product Expansion (OPE) can be used to compute the B meson decay width Γ [19].

As for the $\Delta\Gamma$ and $|q/p|$ parameters, which we are interested in, the leading term in the expansion is given by the so-called *spectator effect* contributions. This involves the computation of the matrix elements M_{21} and Γ_{21}, which are related to the dispersive and absorptive parts of the $\Delta B = 2$ transitions respectively.

A computation of M_{12} at the Next to Leading Order (NLO) in QCD has been carried out in [20] and leads to:

$$M_{12} = \frac{G_F^2 M_W^2 \eta_B}{(4\pi)^2(2M_{B^0})}(V_{tb}^* V_{td})^2 S_0(x_t) \langle \bar{B}|(\bar{b}_i\gamma_\mu(1-\gamma_5)d_i)(\bar{b}_j\gamma_\mu(1-\gamma_5)d_j)|B\rangle \ , \tag{1.31}$$

where $x_t = \bar{m}_t^2/m_W^2$, η_B is the QCD correction factor and S_0 is the Inami-Lim function. The sum over the color indices i and j is implied.

The calculation of Γ_{21} differs from the one on M_{21} because of the presence of two expansion parameters: $\bar{\Lambda}/m_b$ and $\alpha_s(m_b)$, where m_b is the mass of the b quark and $\bar{\Lambda} \sim (M_{B^0} - m_b)$ is the relevant hadronic scale of the problem.

A calculation of Γ_{21} with NLO QCD corrections can be found in [21]. The effects of a non-zero charm quark mass m_c cannot be neglected in computing the amount of CP-violation in mixing: in the limit of a vanishing m_c, $|q/p|$ is exactly equal to 1.

Up to the order of $1/m_b$, Γ_{21} can be written as

$$\Gamma_{21} = -\frac{G_F^2 m_b^2}{24\pi M_{B^0}}\left[c_1(\mu_2)\langle\bar{B}|\mathcal{O}_1(\mu_2)|B\rangle + c_2(\mu_2)\langle\bar{B}|\mathcal{O}_2(\mu_2)|B\rangle + \delta_{1/m}\right] \tag{1.32}$$

where

$$\begin{aligned} \mathcal{O}_1 &= \bar{b}_i\gamma_\mu(1-\gamma_5)d_i\,\bar{b}_j\gamma_\mu(1-\gamma_5)d_j && (1.33)\\ \mathcal{O}_2 &= \bar{b}_i(1-\gamma_5)d_i\,\bar{b}_j(1-\gamma_5)d_j \ , && (1.34)\end{aligned}$$

μ_2 is the scale of the $\Delta B = 2$ operators, c_i are the Wilson coefficients and $\delta_{1/m}$ corresponds to the $1/m_b$ sub-leading corrections. They can be written as

$$\begin{aligned} c_i &= (V_{tb}^*V_{td})^2 D_i^{uu} + 2V_{cb}^*V_{cd}V_{tb}^*V_{td}(D_i^{uu} - D_i^{cu})\\ &+ (V_{cb}^*V_{cd})^2(D_i^{cc} + D_i^{uu} - 2D_i^{cu}) && (1.35)\\ \delta_{1/m} &= (V_{tb}^*V_{td})^2\delta_{1/m}^{uu} + 2V_{cb}^*V_{cd}V_{tb}^*V_{td}(\delta_{1/m}^{uu} - \delta_{1/m}^{cu})\\ &+ (V_{cb}^*V_{cd})^2(\delta_{1/m}^{cc} + \delta_{1/m}^{uu} - 2\delta_{1/m}^{cu}) \ . && (1.36)\end{aligned}$$

The labels cc, cu and uu denote the intermediate quark pair contributing to Γ_{21}, as depicted in figure 1.6.

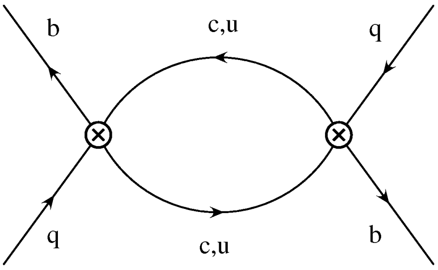

Figure 1.6: Feynman diagram contributing to Γ_{21} at the Leading Order (LO) in QCD. q refers to the light quark in the B meson, the d quark in our case.

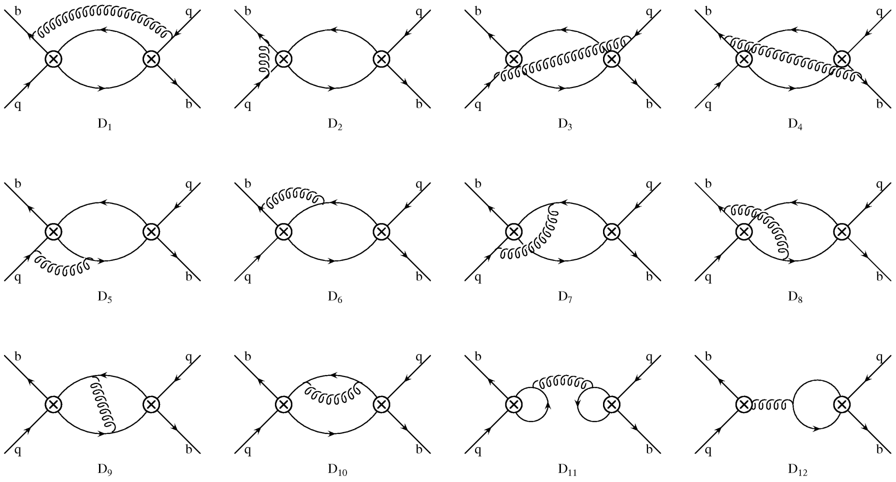

Figure 1.7: Feynman diagram contributing at the NLO to the $\Delta B = 2$ transitions

.

The computation of NLO corrections to Γ_{21} involves the calculation of the Feynman diagrams shown in figure 1.7 and the ones containing one-loop self-energy corrections to the external fields.

The final results show that NLO corrections on the evaluation of $|q/p|$ are numerically important, as can be seen from figures 1.8 and 1.9.

The first shows the theoretical distributions for $|q/p|$ - 1 before and after applying the NLO corrections, the second shows the (pretty strong) dependence of it on the CKM angle β.

The numerical result reported by [21] is:

$$\left|\frac{q}{p}\right| - 1 = (2.96 \pm 0.67) \times 10^{-4} \; . \tag{1.37}$$

The amount of CP violation predicted by the Standard Model is therefore one order of magnitude smaller than the current experimental limits (see chapter 3). For completeness, we give also the result for the B_s system, where CP-violation in mixing is further suppressed by a factor $\sin\beta_s \sim \lambda^2$, where λ is the sine of the Cabibbo angle:

$$\left|\frac{q}{p}\right|_s - 1 = (1.28 \pm 0.27) \times 10^{-5} \; . \tag{1.38}$$

The uncertainties on the B_d and B_s mixing parameters are dominated by the ones on m_c/m_b and the CKM parameters. The dependence on the B-parameters, derived from Lattice QCD (see e.g. [22]), is very weak, thus these predictions are basically free from hadronic uncertainties.

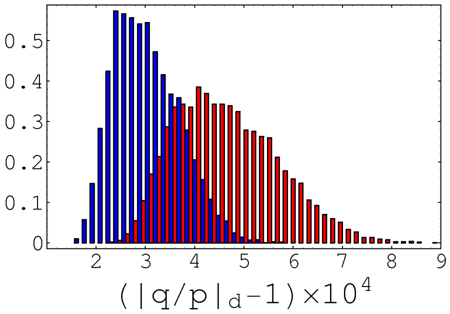

Figure 1.8: Theoretical distributions for $|q/p|$ - 1 at the LO (red histogram) and at the NLO (blue).

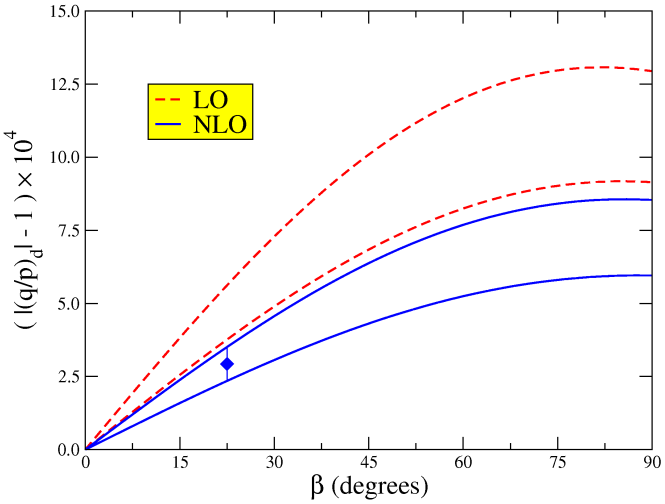

Figure 1.9: Dependence of $|q/p|$ - 1 as a function of the CKM angle β, again shown at the LO (dashed red line) and at the NLO (solid blue).

1.6 Theoretical interest in $|q/p|_d$

There is a strong interest in the community of theorists on the experimental measurements (or limits) of $|q/p|$. We have seen in the previous section that the theoretical prediction on CP-violation in mixing is pretty strong and precise in the Standard Model, thus any significant deviation from it would be a hint of new particles or interactions entering the box diagrams of figure 1.5.

Moreover, an extensive experimental campaign on the properties of the $B_s - \bar{B}_s$ system has begun or is about to begin at the hadronic colliders. It has been pointed out ([21], [23]) that the measurement of ratios of observables of the $B_d - \bar{B}_d$ and $B_s - \bar{B}_s$ systems could be basically free of hadronic uncertainties and would therefore be a strong test of the theory in sight of a high precision era made possible by a *Super B-factory* [25].

The quantity which is often measured to refer to CP-violation in B^0 $\overline{B}^0$ mixing is $\mathcal{A}_{SL}$ (see also eq. 2.9):

$$\mathcal{A}_{SL} = \frac{1-|q/p|^4}{1+|q/p|^4} \simeq 2\left(1 - \left|\frac{q}{p}\right|\right) . \tag{1.39}$$

It has been already pointed out by [24] that, within a Superweak theory of CP-violation, $\mathcal{A}_{SL}$ could be enhanced up to the percent level. Despite the loss of interest for this framework, more recently the effects of New Physics in a scenarios where the CKM matrix is real have been taken into account in [26]. While preserving the consistency with other CP-observables like $\mathcal{A}_{B^0\to\psi K^0}$ or $\mathcal{A}_{B^0\to\pi^+\pi^-}$, it is shown that $\mathcal{A}_{SL}$ could reach the current experimental limit.

It is generally believed (simply assuming the unitarity of the CKM matrix and that tree level processes are dominated by the exchange of SM gauge bosons) that New Physics, contributing to an enhancement of A_{SL} would enter the dispersive part of the Hamiltonian M_{21}, leaving Γ_{21} basically unchanged.

Under the above (weak) assumptions, we can parametrize the NP effects introducing the amplitude C_{B_d} and the phase φ_{B_d}:

$$M_{21}^{NP} = C_{B_d}^2 e^{2i\varphi_{B_d}} M_{21}^{SM} . \tag{1.40}$$

The semileptonic asymmetry can then be written as (see [27]):

$$A_{SL} = \mathrm{Im}\left(\frac{\Gamma_{21}}{M_{21}}\right)^{SM} \frac{\cos 2\varphi_{B_d}}{C_{B_d}} - \mathrm{Re}\left(\frac{\Gamma_{21}}{M_{21}}\right)^{SM} \frac{\sin 2\varphi_{B_d}}{C_{B_d}} . \tag{1.41}$$

Given the size of $\mathrm{Im}(\Gamma_{21}/M_{21})$, even a small φ_{B_d} can enhance induce a significant enhancement of A_{SL}. Depending on the value of φ_{B_d}, the sign of the asymmetry could also be opposite to the one predicted by the Standard Model.

Several New Physics models are taken into account in the literature. Some Supersymmetric (SUSY) scenarios are treated in [28]. An enhancement by up to one order of magnitude on the SM prediction can be achieved in some particular scenario through the contributions of soft scalar masses at a scale of few hundreds of GeV. It is also stressed that, if SUSY is responsible of a significant contribution to CP-violation in mixing, A_{SL} can be used to distinguish among different soft supersymmetry-breaking models.

The effects of New Physics in Littlest Higgs models are treated in [27]. In these models, new flavor interactions are introduced, besides the ones coming from the CKM matrix. These new contributions affect several CP-observables and the correlations between them are studied. In particular, the correlation between $A_{B^0\to\psi K^0}$ and A_{SL} is shown in figure 1.10, showing that there is still room for significant deviations from the Standard Model predictions.

Precision measurements of the mixing parameters of the $B_d - \bar{B}_d$ systems are also required for the reduction of theory uncertainties which will be possible once new measurements on $B_s - \bar{B}_s$ will be available from the Tevatron or the Large Hadron Collider. A measurement of the possible

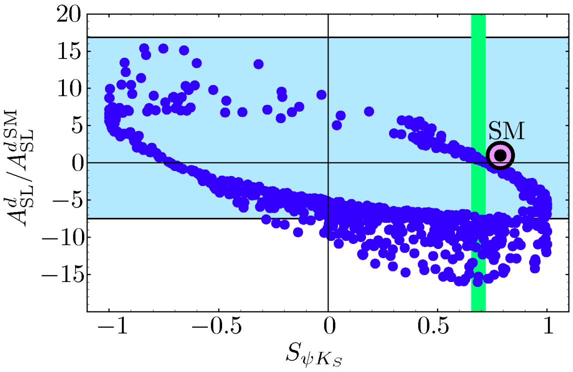

Figure 1.10: The ratio A_{SL}/A^{SM}_{SL} is plotted versus the CP-asymmetry measured on $B^0 \to \psi K^0$ (data points). The shaded areas represent the regions allowed by current experimental data.

New Physics contribution ϕ_s^{Δ} to the mixing phase of the $B_s - \bar{B}_s$ system recently performed by the $D\emptyset$ Collaboration ([29]) in an angular analysis of $B_s \to J/\psi\phi$ decays, combined with other experimental information (see [23]), yields the result:

$$sin(\phi_s^{\Delta} - 2\beta_s) = -0.77 \pm 0.04 \pm 0.34\,, \tag{1.42}$$

(the first quoted error comes from theoretical uncertainties, the second from the experiments), which is compared to the Standard Model prediction $sin(-2\beta_s) = -0.04 \pm 0.01 \pm 0.34$. A discrepancy of about 2 standard deviations is certainly not sufficient to claim for New Physics, but nevertheless points to something which needs to be carefully inspected in the near future.

Chapter 2

Phenomenology of B decays at a B-factory

In this section, we will treat the phenomenology of a coherently produced pair of $B^0\overline{B}^0$ mesons, which is the case of a B-factory. Different methods of determining the flavor of a B meson will be briefly presented and the difference between *lepton tags* and *kaon tags*, due to the presence of Doubly Cabibbo Suppressed decays, will be discussed. Finally, in section 2.5, we will treat the experimental attractiveness of $\overline{B}^0 \to D^{*+}\ell^-\bar{\nu}_\ell$ decays, which will be used in our analysis.

2.1 Time evolution of a coherent $B^0\overline{B}^0$ pair

In the B-factory environment, B^0 mesons are produced through the decay of the vector meson $\Upsilon(4S)$, created by the collision of an e^+e^- pair with an energy, in the center of mass frame, corresponding to the mass of the $\Upsilon(4S)$.

The $\Upsilon(4S)$, which carries the quantum numbers $J^{PC} = 1^{--}$, decays mostly, and with approximately the same probability, to a pair of B^+B^- or $B^0\overline{B}^0$ mesons. The decay of the $\Upsilon(4S)$ is driven by the strong interaction, thus the quantum number relative to charge conjugation is preserved.

As long as both the B mesons have not decayed, they are forced to carry opposite flavor; in the neutral case, once one of the mesons decays, the other is free to oscillate to the opposite flavor, with frequency given by Δm.

If one of the B mesons decays to the final state f_1 and the other to the final state f_2, we will call $A_{1,2}$ and $\bar{A}_{1,2}$ the amplitudes of respectively a B^0 or $\overline{B}^0$ decay to the final states $f_{1,2}$ [30]. The overall amplitude of the coherent state is given by:

$$\mathcal{A} = a_+ g_+(t) + a_- g_-(t)\ , \tag{2.1}$$

where

$$\begin{aligned} a_+ &= -A_1\bar{A}_2 + \bar{A}_1 A_2 && (2.2)\\ a_- &= \frac{p}{q}A_1 A_2 - \frac{q}{p}\bar{A}_1\bar{A}_2\ . && (2.3)\end{aligned}$$

We can now write the differential decay rate,

$$\begin{aligned}\frac{dN}{dt} = &\propto\ e^{-\Gamma|\Delta t|}\Big[\frac{1}{2}(|a_+|^2 + |a_-|^2)\cosh(\Delta\Gamma\Delta t/2) + \frac{1}{2}(|a_+|^2 - |a_-|^2)\cos(\Delta m\Delta t) -\\ &-\ \mathrm{Re}(a_+^* a_-)\sinh(\Delta\Gamma\Delta t/2) + \mathrm{Im}(a_+^* a_-)\sin(\Delta m\Delta t)\Big] \qquad (2.4)\end{aligned}$$

where Δt is the difference between the decay times of the two B mesons. Given the current experimental limits on $\Delta\Gamma$ [30], we will neglect, from now on, the term $\mathrm{Re}(a_+^* a_-)\sinh(\Delta\Gamma\Delta t/2)$.

2.2 Probability Density Functions - lepton tag

Besides fully reconstructing a B meson to final states accessible only by a specific flavor (the so called *flavor eigenstates*, B_{flav}), which has a very low efficiency (only a few permille), several techniques are used to measure the flavor of a B meson. A tagging technique is characterized by its efficiency ε (i. e. the fraction of B mesons which are selected by the algorithm) and by the probability ω of assigning the wrong flavor to the B meson under study. Having defined the *dilution* as $D = 2(1-\omega)$, the statistical power (*tagging efficiency*) of a tagging technique is given by:

$$Q = \varepsilon D^2 \,. \tag{2.5}$$

The highest purity is achieved by the *lepton tag* methods, which exploits the identification of semileptonic B decays. Those decays are dominated by *tree level* amplitudes, where the b quark decays to a c (or a u) through the emission of a virtual W^- boson, which decays to a charged lepton (either ℓ^- or μ^-) and its relative anti-neutrino[1]. Given that the semileptonic decays are dominated by a single tree level amplitude, we do not expect to have direct CP-violation at observable levels in these decays.

A positively charged primary lepton tags a B^0 while a negative one tags a $\overline{B}^0$. Wrong flavor attributions (*mistags*) arise from hadrons incorrectly identified as leptons of from secondary leptons originating from semileptonic decays of charmed mesons among the decay products of the original B, which have opposite charge with respect to the primary ones. This source of mistags can be effectively reduced by applying a cut on the lepton momentum.

The typical performance for this method of B-flavor tagging shows an efficiency of ~ 8.5 %, with a mistag probability of ~ 3 % [31].

Due to the existence of $B^0\overline{B}^0$ mixing, the two B's can be tagged as B^0-$\overline{B}^0$, $\overline{B}^0$-B^0 (*Unmixed Events*) or as B^0-B^0, $\overline{B}^0$-$\overline{B}^0$ (*Mixed Events*).

Neglecting mistags, the *Probability Density Function* (PDF) normalized to unity for having an Unmixed Event is:

$$\mathcal{F}(\Delta t) = \frac{\Gamma}{2} e^{-\Gamma|\Delta t|}\Big[\cosh(\Delta\Gamma\Delta t/2) + \cos(\Delta m\Delta t)\Big] \,. \tag{2.6}$$

In the case of Mixed Events, we need to distinguish between B^0-B^0 events (Mixed Positive) and $\overline{B}^0$-$\overline{B}^0$ (Mixed Negative). The PDF's for these two categories are, respectively:

$$\begin{aligned} \mathcal{F}(\Delta t) &= \frac{\Gamma}{2} e^{-\Gamma|\Delta t|}\left|\frac{p}{q}\right|^2 \Big[\cosh(\Delta\Gamma\Delta t/2) - \cos(\Delta m\Delta t)\Big] && (2.7)\\ \mathcal{F}(\Delta t) &= \frac{\Gamma}{2} e^{-\Gamma|\Delta t|}\left|\frac{q}{p}\right|^2 \Big[\cosh(\Delta\Gamma\Delta t/2) - \cos(\Delta m\Delta t)\Big] \,. && (2.8)\end{aligned}$$

The effect of $|q/p|$ being different from 1, while preserving the PDF's shapes of the CP-conserving case, affects the relative normalization of Mixed Positive and Negative events. CP-violation in mixing can be measured through the *Semileptonic Asymmetry* $\mathcal{A}_{SL}$, computed from the number of Positive and Negative Mixed events:

$$\mathcal{A}_{SL} = \frac{N(B^0B^0) - N(\overline{B}^0\overline{B}^0)}{N(B^0B^0) + N(\overline{B}^0\overline{B}^0)} = \frac{N(\ell^+\ell^+) - N(\ell^-\ell^-)}{N(\ell^+\ell^+) + N(\ell^-\ell^-)} = \frac{1-|q/p|^4}{1+|q/p|^4} \simeq 2\left(1 - \left|\frac{q}{p}\right|\right) \,, \tag{2.9}$$

where the last equality holds for $|q/p|$ close to 1, which is our case.

---

[1] The same applies to the conjugate process.

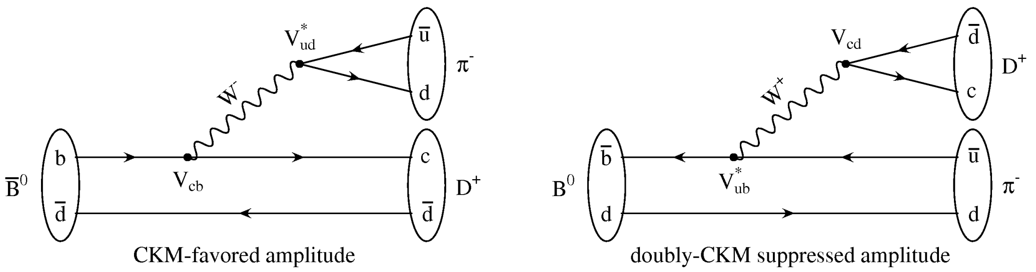

Figure 2.1: Cabibbo favored (left) and Doubly Cabibbo suppressed (right) amplitudes for the final state $D^+\pi^-$. The interference between the CKM-favored amplitude (left diagram) and the doubly CKM-suppressed (right) gives rise to distortions in the theoretical pdf's which need to be taken into account.

Current experimental limits on $|q/p|$ obtained with lepton tags will be presented in chapter 3.

2.3 Effects of Doubly Cabibbo Suppressed Decays

The statistical power of the lepton tag technique can be superseded by identifying charged kaons among the decay products of a B meson. As in the lepton case, the charge of the K is correlated to the flavor of the mother B, even though in this case the mistag rate is significantly higher. A positive kaon is likely to originate from a B^0 while a negative one is likely to come from a $\overline{B}^0$.

The typical efficiency of kaon tagging is in the range $11 - 17$ %, with mistag probability $4.5 - 15$ %, depending on the requirements applied in the selection of the $K^\pm$ track [31].

The lower purity is not the only feature distinguishing lepton tags from kaon tags. It has been pointed out in [32] that the existence of Doubly Cabibbo Suppressed decays could lead to observable effects in the measurements of CP-violating processes in the $B^0\overline{B}^0$ system.

Let us consider a decay channel of interest for flavor tagging: $B \to D^+\pi^-$ (the D^+ decays with a probability of $\sim 30\%$ to a K^-). As shown in figure 2.1, this final state can be accessed by a $\overline{B}^0$ through the Cabibbo favored (CF) process $b \to c\bar{u}d$ or by a B^0 through the Doubly Cabibbo suppressed (DCS) $\bar{b} \to \bar{u}c\bar{d}$.

The magnitude of the DCS amplitude $\mathcal{A}_{DCS}$ is expected to be, with respect to the CF one $\mathcal{A}_{CF}$:

$$\frac{\mathcal{A}_{DCS}}{\mathcal{A}_{CF}} \approx \left|\frac{V_{ub}^* V_{cd}}{V_{cb} V_{ud}^*}\right| \approx 0.02 \;, \tag{2.10}$$

and the relative weak phase between the two is the CKM angle γ.

For B-flavor tagging purposes we are going to consider the tagging category T, which is given by all the final states with a charged kaon which passes our selection. Considering a final state f, belonging to the tagging category T, and accessible to a B^0 through a CF amplitude $\mathcal{A}_{CF,f}$ and to a $\overline{B}^0$ through a DCS amplitude $\overline{\mathcal{A}}_{DCS,f}$, we have the usual parameter:

$$\lambda_f = \frac{q}{p}\frac{\overline{\mathcal{A}}_{DCS,f}}{\mathcal{A}_{CF,f}} = r_f e^{i(2\beta+\gamma)} e^{i\delta_f} \;, \tag{2.11}$$

where r_f is a real number of order 0.02, δ_f is the strong phase difference between the two amplitudes and 2β is the weak phase of the $B^0\overline{B}^0$ mixing:

$$\frac{q}{p} = \left|\frac{q}{p}\right| e^{-2i\beta} . \tag{2.12}$$

Now considering all the final states in the tagging category T, and neglecting quadratic terms in r_f as it is reasonable to do, we get:

$$r' e^{i\delta'} = \frac{\sum_{f\in T} \varepsilon_f |\mathcal{A}_f|^2 r_f e^{i\delta_f}}{\sum_{f\in T} \varepsilon_f |\mathcal{A}_f|^2} , \tag{2.13}$$

where ε_f is the relative tagging efficiency for the state f.

From the inequality:

$$|r'| \leq \frac{\sum_{f\in T} \varepsilon_f |\mathcal{A}_f|^2 |r_f|}{\sum_{f\in T} \varepsilon_f |\mathcal{A}_f|^2} , \tag{2.14}$$

we notice that, unless all the final states have roughly the same strong phases, the different contributions tend to cancel out.

In section 2.4, we will discuss how the presence of Doubly Cabibbo suppressed decays affect our analysis of CP-violation in mixing.

2.4 Probability Density Functions - Kaon tag

In this analysis, we will identify one of the B mesons through partial reconstruction (see 2.5) of the decay $\overline{B}^0 \to D^{*+}\ell^-\bar{\nu}_\ell$ (the charge of the lepton tags its flavor). We will refer to it as the B_{rec}, or the B in the *decay side.* We will assume throughout the rest of this thesis that there is no CP-violation in the decay side.

Of the other B, which will be called B_{tag} or B in the *tag side*, we will select only a charged kaon among its decay products. Doubly Cabibbo suppressed decays will affect only the tag side.

In the computation of the overall PDF, we re-write equations 2.2, 2.3 as:

$$a_+ = -A_{tag}\bar{A}_{rec} + \bar{A}_{tag}A_{rec} \tag{2.15}$$

$$a_- = \frac{p}{q}A_{tag}A_{rec} - \frac{q}{p}\bar{A}_{tag}\bar{A}_{rec} . \tag{2.16}$$

Considering Doubly Cabibbo suppressed decays affecting $\mathcal{A}_{tag}$ and $\overline{\mathcal{A}}_{tag}$, and defining the two effective parameters:

$$b = 2r' \sin(2\beta+\gamma)\cos(\delta') \tag{2.17}$$

$$c = -2r' \cos(2\beta+\gamma)\sin(\delta') , \tag{2.18}$$

we are now able to write the global PDF's for Unmixed ($B^0\overline{B}^0$) and Mixed (B^0B^0 or $\overline{B}^0\overline{B}^0$) events. Unlike the lepton tag case, we will need to separate the Unmixed events $B_{tag} = B^0$ (which we will call Positive from the most likely charge of the tag side kaon) from the Negative ones $B_{tag} = \overline{B}^0$.

In order to separate the four categories of events, we introduce the indices s_t and s_m. s_t is 1 (-1) for the B_{tag} being a B^0 ($\overline{B}^0$), s_m is 1 (-1) for an Unmixed (Mixed) event, as it is summarized in table 2.1.

The four PDF's are then written as:

$$s_t = 1,\ s_m = -1 :$$

$$\mathcal{F}(\Delta t) = \frac{\Gamma}{2(1+r'^2)} e^{-\Gamma|\Delta t|} \left|\frac{p}{q}\right|^2 \left[\left(1 + \left|\frac{q}{p}\right|^2 r'^2\right) \cosh(\Delta\Gamma\Delta t/2) - \right. \tag{2.19}$$

Table 2.1: Value of s_t and s_m indexes for the four possible signal final states.

B_{rec} is a	B_{tag} is a	s_t	s_m
B^0	B^0	1	-1
$\overline{B}^0$	B^0	1	1
B^0	$\overline{B}^0$	-1	1
$\overline{B}^0$	$\overline{B}^0$	-1	-1

$$- \left(1 - \left|\frac{q}{p}\right|^2 r'^2\right) \cos(\Delta m \Delta t) + \left|\frac{q}{p}\right| (b+c) \sin(\Delta m \Delta t)\Big]$$

$$\begin{aligned} &s_t = 1,\ s_m = 1 : \\ &\mathcal{F}(\Delta t) = \frac{\Gamma}{2(1+r'^2)} e^{-\Gamma|\Delta t|} \Big[\left(1 + \left|\frac{q}{p}\right|^2 r'^2\right) \cosh(\Delta\Gamma\Delta t/2) + \\ &+ \left(1 - \left|\frac{q}{p}\right|^2 r'^2\right) \cos(\Delta m \Delta t) - \left|\frac{q}{p}\right| (b+c) \sin(\Delta m \Delta t)\Big] \end{aligned} \tag{2.20}$$

$$\begin{aligned} &s_t = -1,\ s_m = 1 : \\ &\mathcal{F}(\Delta t) = \frac{\Gamma}{2(1+r'^2)} e^{-\Gamma|\Delta t|} \Big[\left(1 + \left|\frac{p}{q}\right|^2 r'^2\right) \cosh(\Delta\Gamma\Delta t/2) + \\ &+ \left(1 - \left|\frac{p}{q}\right|^2 r'^2\right) \cos(\Delta m \Delta t) + \left|\frac{p}{q}\right| (b-c) \sin(\Delta m \Delta t)\Big] \end{aligned} \tag{2.21}$$

$$\begin{aligned} &s_t = -1,\ s_m = -1 : \\ &\mathcal{F}(\Delta t) = \frac{\Gamma}{2(1+r'^2)} e^{-\Gamma|\Delta t|} \left|\frac{q}{p}\right|^2 \Big[\left(1 + \left|\frac{p}{q}\right|^2 r'^2\right) \cosh(\Delta\Gamma\Delta t/2) - \\ &- \left(1 - \left|\frac{p}{q}\right|^2 r'^2\right) \cos(\Delta m \Delta t) - \left|\frac{p}{q}\right| (b-c) \sin(\Delta m \Delta t)\Big] \end{aligned} \tag{2.22}$$

The above PDF's with arbitrary (and unrealistically large) values of the CP-violating parameters are drawn in figures 2.2, 2.3.

It can be seen that the only effect of $|q/p|$ being different from 1 is to cause a difference in the normalization of Mixed Positive and Mixed Negative events, with no effect on PDF's shapes and on the normalization of Unmixed Events.

On the other side, DCS decays, adding terms proportional to $\sin(\Delta m \Delta t)$, do not affect the overall normalization of the PDF's, but cause distortions on their shapes, which are more evident in the Mixed samples.

2.5 The $\overline{B}^0 \to D^{*+}\ell^-\bar{\nu}_\ell$ decay

The $\overline{B}^0 \to D^{*+}\ell^-\bar{\nu}_\ell$ semileptonic decay is characterized by a clear experimental signature and a large branching fraction: $(5.29 \pm 0.19) \times 10^{-2}$ [4]. These properties allow the selection of big samples of events with favorable signal/background ratio.

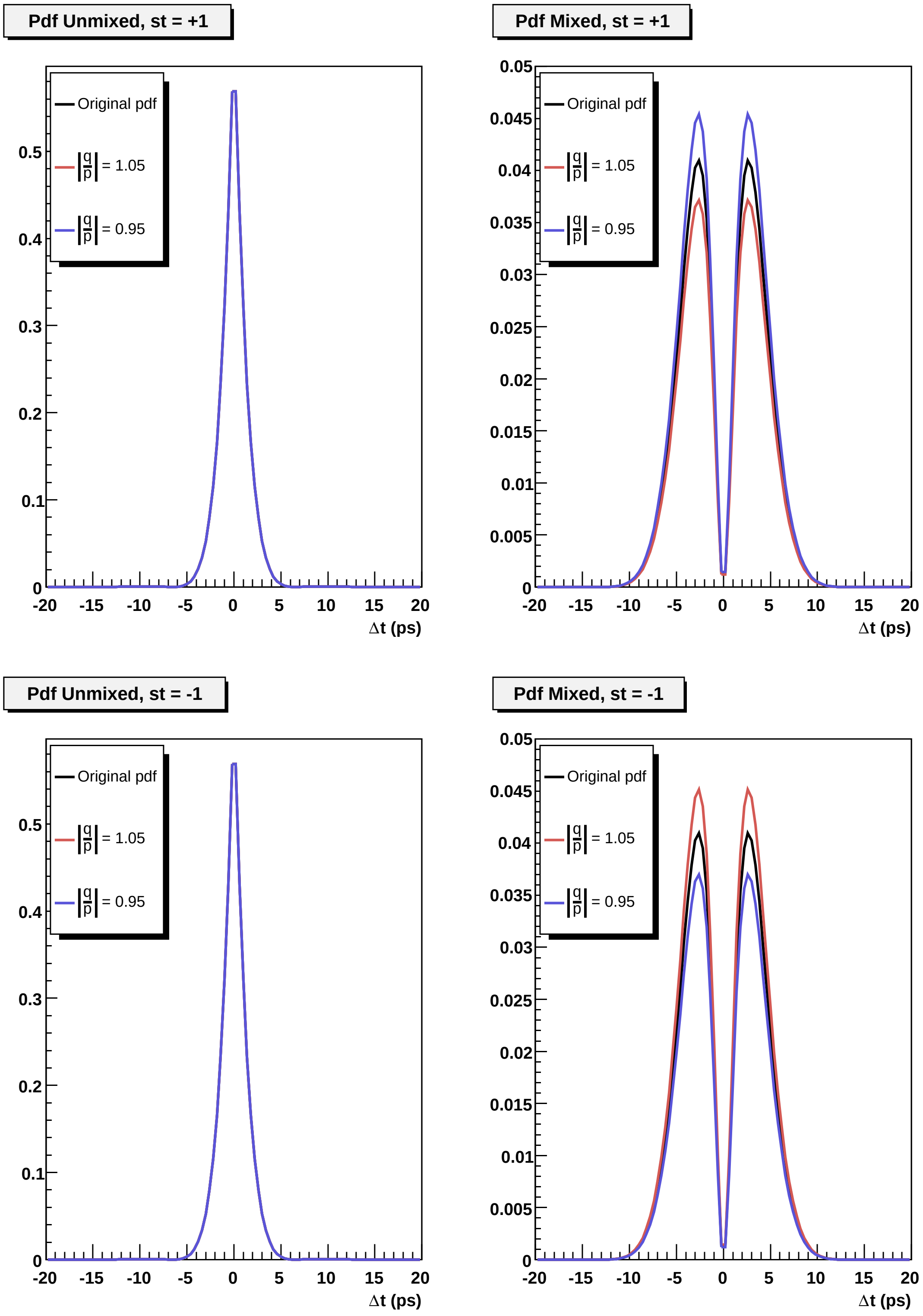

Figure 2.2: PDF's for Unmixed Positive (top left plot), Mixed Positive (top right), Unmixed Negative (bottom left) and Mixed Negative (bottom right) in the case where $|q/p|$ is the only CP violating parameter. To enhance the effect, an unrealistically large value has been chosen: the black curve represents the CP-conserving case, the red one has been generated with $|q/p| = 1.05$ and the blue curve has $|q/p| = 0.95$.

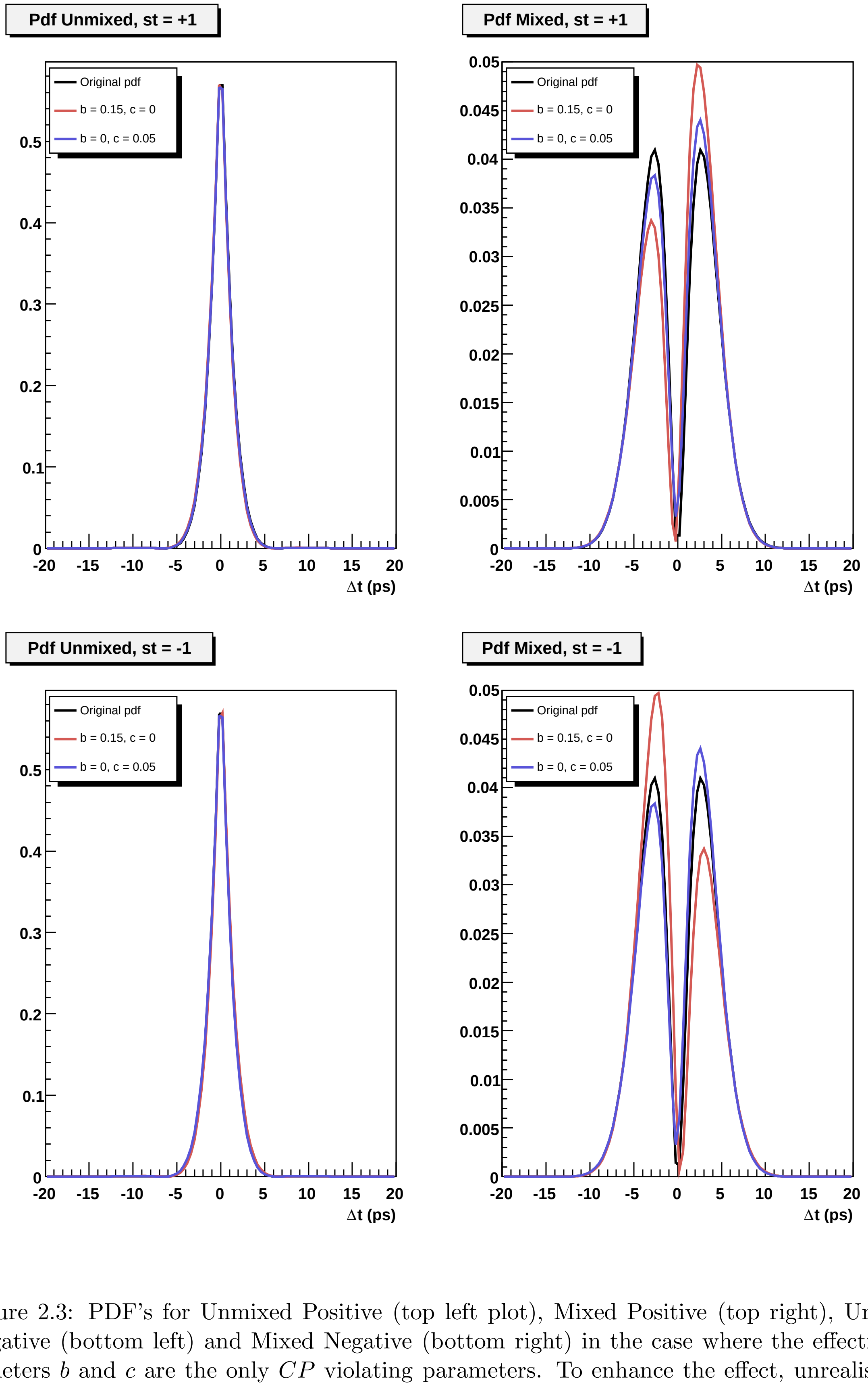
Pdf Unmixed, st = +1

Pdf Mixed, st = +1

Pdf Unmixed, st = -1

Pdf Mixed, st = -1

Figure 2.3: PDF's for Unmixed Positive (top left plot), Mixed Positive (top right), Unmixed Negative (bottom left) and Mixed Negative (bottom right) in the case where the effective parameters b and c are the only CP violating parameters. To enhance the effect, unrealistically large values have been chosen: the black curve represents the CP-conserving case, the red one has been generated with $(b, c) = (0.15, 0.)$ and the blue curve has $(b, c) = (0., 0.05)$.

For this reason this process has been widely used in the past to determine several properties of the B^0 mesons, such as the lifetime τ_{B^0} and the mixing frequency Δm [33], [34]. In those measurements, the D^{*+} is reconstructed through its decay $D^{*+} \to D^0\pi^+$ and the D^0 is identified by means of few final states which provide high selection efficiency and high background rejection. We will refer to this method as *exclusive reconstruction*.

Due to the restricted phase-space of the $D^{*+} \to D^0\pi^+$ transition, it is however possible to tag this process by identifying only the charged pion, without reconstructing the D^0. This *inclusive* approach allows the selection of a sample of events about ten times larger than the one used by the exclusive analysis.

This method has been extensively used by the ARGUS and CLEO collaborations (taking data at the $\Upsilon(4S)$) to determine several B^0 and D^0 properties [35] and by DELPHI and OPAL to measure V_{cb}, τ_{B^0} and Δm [36], [37].

More recently, the *BABAR* collaboration performed several measurements using the inclusive (or *partially reconstructed*, since only the charged pion is used among the D^{*+} decay products) sample. These include the measurement of τ_{B^0} [38], of Δm [39], of the Branching Fraction $\Upsilon(4S) \to B^0\overline{B}^0$ (with double tagging) [40] and the measurement of the Branching Fraction $D^0 \to K^-\pi^+$ [41].

The basic kinematical property that allows the partial reconstruction of $\overline{B}^0 \to D^{*+}\ell^-\bar{\nu}_\ell$ is the fact that the charged pion is emitted with a very low momentum (roughly 40 MeV/c) in the D^{*+} rest frame. Hereafter it will be referred to as the *soft pion* (π_{soft}). In a $\overline{B}^0 \to D^{*+}\ell^-\bar{\nu}_\ell$ decay, the π_{soft} flight direction lies in a cone of ~ 1 rad aperture, with axis coincident with the flight direction of the mother D^{*+}. The magnitude of the D^{*+} momentum can be estimated through a polynomial function of the magnitude of the soft pion momentum.

The $\overline{B}^0 \to D^{*+}\ell^-\bar{\nu}_\ell$ decay can thus be detected with high efficiency by selecting an oppositely charged (ℓ, π_{soft}) pair, where ℓ (as we will intend throughout the rest of this thesis) is either an electron or a muon.

Assuming (as it is reasonable to do, due to the low momentum of the $\overline{B}^0$ meson, $p_B \simeq 340$ MeV/c in the $\Upsilon(4S)$ rest frame, as compared to its energy, $E_B \simeq m_B = 5.27$ GeV) that the $\overline{B}^0$ is produced at rest in the c.m. frame, we can compute the quantity:

$$m_\nu^2 = (\mathcal{P}_{B^0} - \mathcal{P}_{D^*} - \mathcal{P}_\ell)^2, \tag{2.23}$$

where $\mathcal{P}_x$ indicates the four-momentum of particle x. m_ν^2 is an efficient discriminating variable. For a true $\overline{B}^0 \to D^{*+}\ell^-\bar{\nu}_\ell$ decay it coincides with the quadratic invariant mass of the neutrino, which is the only undetected particle in the event.

Figure 2.4 shows the m_ν^2 distributions for the *BABAR* data sample which will be used in this analysis and the properly normalized Monte Carlo events. It can be seen that signal events distribute over a peak centered at zero whose width is dominated by the approximations taken in the computation of m_ν^2, while background events, besides a small peaking component, populate a wider region which extends towards negative values of m_ν^2.

Figure 2.4 clearly shows the large number of $B^0\overline{B}^0$ events which can be selected by using the partial reconstruction technique, with the favorable signal/background ratio. The detailed discussion of the composition of our data sample will be treated in section 5.5.

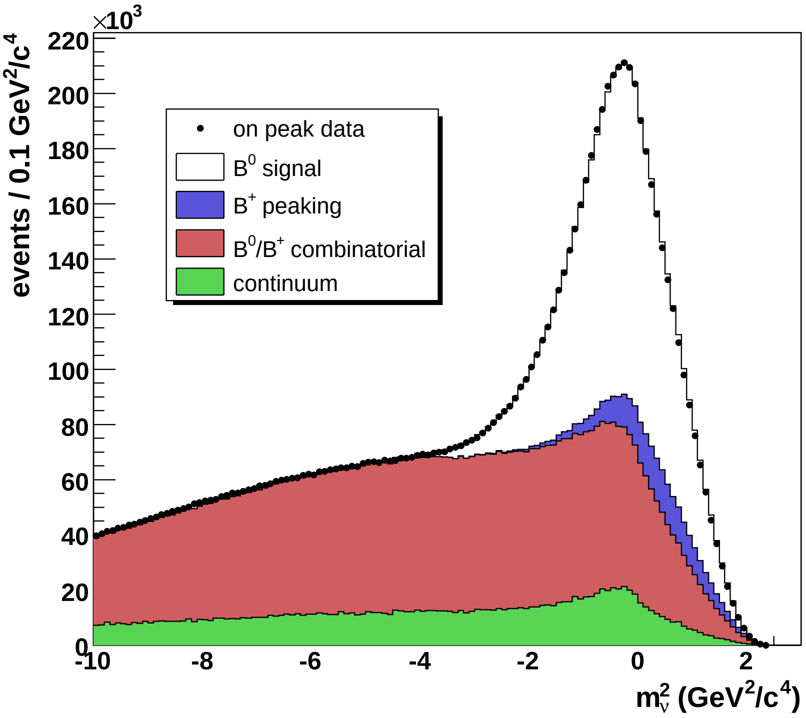

Figure 2.4: m_ν^2 distribution for data (points) and the various components of Monte Carlo (histograms) in events with at least one charged kaon candidate. The white histogram represents signal events, while the other colors are referred to the different kind of backgrounds which will be thoroughly discussed in section 5.5. Monte Carlo has been normalized to match the difference between on-peak data and properly renormalized off-peak data, which we use to model the continuum background.

Chapter 3

Experimental Results

In this chapter, we will review the recent experimental activity carried on by BABAR and other High Energy Physics experiments in this field and summarize the current experimental limits on $|q/p|$.

3.1 $|q/p|$ from dileptons at the B-factories

As we have seen in chapter 2, the measurement of the asymmetry $\mathcal{A}_{SL}$ allows the measurement of $|q/p|$, through the relation expressed by equation 2.9.

The large statistics of B mesons collected by the B-factories, their clean environment and the high resolution in decay vertices reconstruction permit to perform very precise measurements which would not be possible at a hadronic collider.

The Belle Collaboration presented a measurement of $\mathcal{A}_{SL}$, based on a data sample of 78 fb^{-1} of $\Upsilon(4S)$ decays, which corresponds to roughly 84 millions of $B\overline{B}$ events [42].

The B mesons are flavor-tagged by selecting two leptons (either electrons or muons) with momentum (in the $\Upsilon(4S)$ rest frame) in the range $1.2 < p_\ell < 2.3$ GeV/c. The lower cut is imposed in order to exclude leptons originating from semileptonic decays of charmed mesons (which carry opposite charge with respect to the *primary* leptons from semileptonic B decays) while the higher cut is used to suppress *continuum* events (for the definition of *continuum background* see section 4.1.3). Several other requests are applied to reject events with photon conversions ($\gamma \to e^+e^-$) in the detector material, events with a J/ψ candidate and misidentified hadrons coming from continuum jet-like events.

For the measurement of $\mathcal{A}_{SL}$, the leptons are requested to carry the same electric charge. Although not strictly necessary for the overall determination of $\mathcal{A}_{SL}$, a binned Maximum Likelihood fit on the distance Δz between the projections onto the beam axis (z) of the two decay vertices is performed. The PDF used has the form:

$$P^{\pm\pm} = N^{\pm\pm} e^{-|\Delta z|/\tau_{B^0}} (1 - \cos(\Delta m \Delta z)) , \tag{3.1}$$

where $N^{\pm\pm}$ are the normalization factors for Mixed Positive and Negative events (from which $\mathcal{A}_{SL}$ is computed).

Charge asymmetries in the detector response are studied by means of the following control samples: $e^+e^- \to e^+e^-(e^+e^-)$ (for electrons) and simulated muon tracks added to data hadronic events for muons. The probability of selecting a hadron as a lepton (mostly a muon) is studied with samples of $K^0_S \to \pi^+\pi^-$, $\phi \to K^+K^-$ and $\Lambda \to p\pi^-$ ($\bar{\Lambda} \to \bar{p}\pi^+$).

The largest contribution to the systematic uncertainty comes from the subtraction of continuum background (taken from 9 fb^{-1} of data collected using a collision energy slightly below the mass of the $\Upsilon(4S)$).

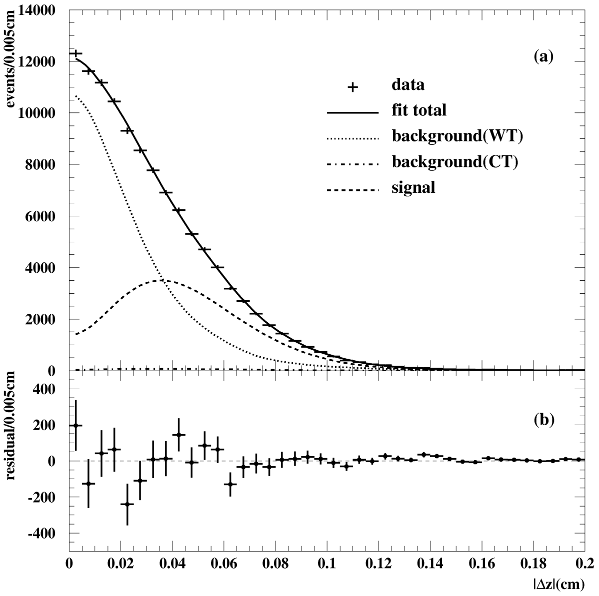

Figure 3.1: The top plot shows the results of the binned fit on $|\Delta z|$. Points with error bars represent the data, the dotted line is the background caused by wrong tags (WT), the dot-dashed line is the background with correct tags (CT), the dashed line is the signal component and the sum of all the components is given by the solid line. The bottom plot shows the residuals of the $|\Delta z|$ fit.

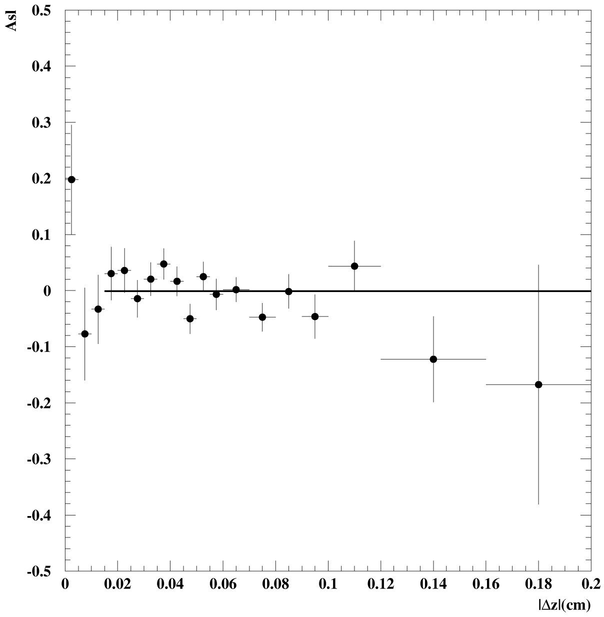

Figure 3.2: $\mathcal{A}_{SL}$ as a function of $|\Delta z|$.

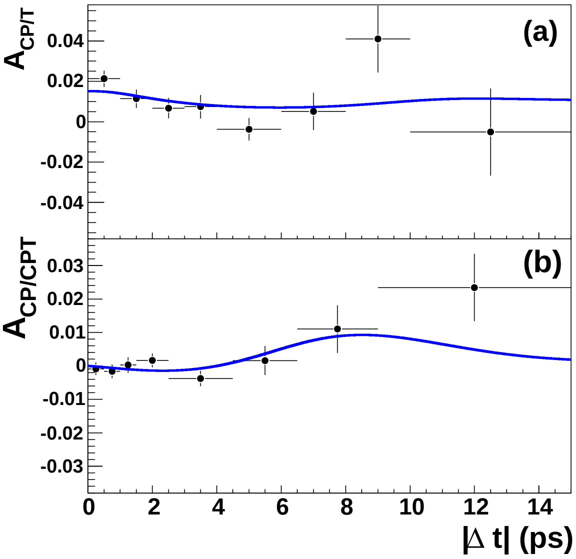

Figure 3.3: Results of the Maximum Likelihood fit of the BABAR dilepton analysis. In the top plot the asymmetry between equally charged leptons is shown (this is equivalent to $\mathcal{A}_{SL}$), while in the bottom plot the asymmetry $\mathcal{A}_{CP/CPT}$ is represented. Both results are consistent with zero.

Figures 3.1 and 3.2 show the results of the fit and the dependence of the measured $\mathcal{A}_{SL}$ as a function of $|\Delta z|$.

The final result is:

$$\mathcal{A}_{SL} = (-1.1 \pm 7.9 \pm 7.0) \times 10^{-3} \ , \tag{3.2}$$

which corresponds to:

$$|q/p| - 1 = (0.5 \pm 4.0 \pm 3.5) \times 10^{-3} \ , \tag{3.3}$$

where the first quoted error is the statistical one, while the second is the systematic.

The dilepton sample is also exploited by the BABAR Collaboration, in an analysis on a data sample of about 232 million of $B\overline{B}$ pairs [43].

With respect to Belle's one, this analysis is more sophisticated and allows a test also on CPT violation, by taking into account also oppositely charged leptons. The asymmetry measured, in this case is:

$$\mathcal{A}_{CP/CPT} = \frac{N^{+-}(\Delta t > 0) - N^{+-}(\Delta t < 0)}{N^{+-}(\Delta t > 0) + N^{+-}(\Delta t < 0)} \ . \tag{3.4}$$

The momentum range used in the preselection of lepton candidates is $0.8 < p_\ell < 2.3$ GeV/c; the dilution originating from semileptonic decays of charmed mesons is restored by means of a neural network which discriminates between primary and secondary leptons using a set of kinematic variables. Also, the effects of a non-zero $\Delta\Gamma$ are taken into account.

As in the previous case, detector related charge asymmetries need to be taken care of by means of suitable control samples: radiative Bhabha events for electrons and $e^+e^- \to \mu^+\mu^-\gamma$ for muons. The probability of mis-identifying a hadron is estimated on the control samples: $D^0 \to K^-\pi^+$, $\bar{\Lambda} \to p\pi^-$ (and charge conjugates), $K^0_S \to \pi^+\pi^-$, and one-prong and three-prong τ decays.

Figure 3.3 shows the results of the nominal fit, which takes into account both the CP-violation in mixing due to $|q/p|$ being different from 1 and other potential CPT-violating effects. The quoted result, which is currently the leading measurement, for CP-violation in mixing is:

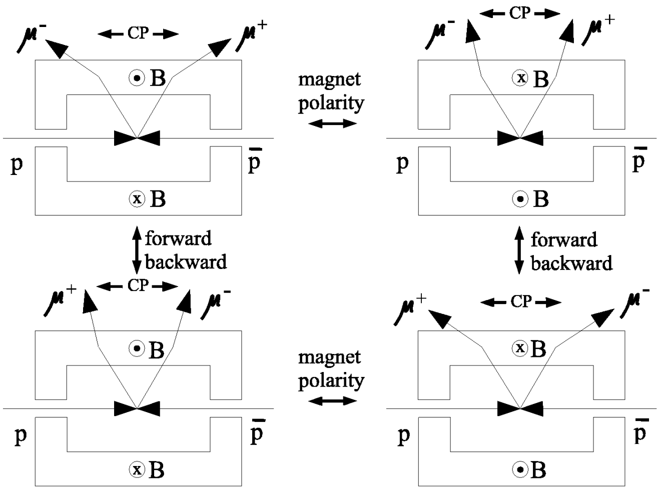

Figure 3.4: The four different configurations of the magnetic field in the *D∅* detector used in the data-taking.

$$|q/p| - 1 = (-0.8 \pm 2.7 \pm 1.9) \times 10^{-3} , \tag{3.5}$$

where again the first error is statistical and the second systematic.

3.2 $|q/p|$ from dimuons at the Tevatron

The parameter $|q/p|$ can be measured also in the very different environment of a hadronic collider, such as the Tevatron at FNAL, where protons and anti-protons collide head-on with an energy (the laboratory frame coincides with the center of mass frame) of 1.96 TeV.

The *D∅* Collaboration recently presented a measurement of $\mathcal{A}_{SL}$, based on an integrated luminosity of 1.0 fb^{-1}, from dimuon events [44]. Given that B_d and B_s are produced in roughly the same amount and that the two states are not distinguishable in this kind of analysis, this is a measurement of an average between $|q/p|_d$ and $|q/p|_s$ and it is therefore complementary to the other measurements presented in this chapter.

The measurement of tracks momenta is performed by the *D∅* detector taking advantage of the magnetic field produced by a central solenoid, surrounded by external toroids. The polarity of both the solenoid and the toroids can be inverted, giving the possibility of taking data with four different configurations of the magnetic field (see figure 3.4).

This feature is particularly useful for controlling the charge asymmetries which could arise from mechanical imperfections on the detector, displacements of the *beam spot* and so on. By swapping the polarity of either the solenoid or the toroids, a track that has been called positive in the first configuration, will be called negative in the second; by taking the same amount of data in the four possible configurations, all the asymmetries due to geometrical imperfections are canceled out, at the first order.

The events preselection consists of a series of quality cuts on the two candidate tracks in order to suppress the hadronic and cosmic backgrounds and to ensure that the two muon candidates originate from the *beam spot*. A positive charge asymmetry is measured in the tracking efficiency of the central tracker, due to the presence of charged particles originating from interactions of primary tracks with the detector material.

The asymmetry $\mathcal{A}_{SL}$ is computed from the number of $\mu^+\mu^+$ and $\mu^-\mu^-$ events, once all detector related effects have been corrected and a correction factor f, which takes into account the other physical processes which could give a dimuon event and dilute the asymmetry, is calculated.

The final result is:

$$\mathcal{A}_{SL} = (-9 \pm 4 \pm 3) \times 10^{-3} \, , \tag{3.6}$$

the dominant systematic uncertainty comes from the presence of prompt muons and the decays of $K^\pm$.

3.3 $|q/p|$ from Partially Reconstructed $\overline{B}^0 \to D^{*+}\ell^-\bar{\nu}_\ell$ events - lepton tag

The limiting factor of *BABAR* dileptons analysis is the need to rely on dedicated control samples in order to manage the detector related charge asymmetries. This can be superseded by performing an analysis in which the reconstruction and flavor-tagging are carried out using different techniques for the two B mesons.

The *BABAR* Collaboration recently presented a preliminary measurement of CP-violation in $B^0\overline{B}^0$ mixing, using a data sample roughly equivalent to the one used in [43]. In this work one of the two B mesons is partially reconstructed (for details about the partial reconstruction technique, see section 2.5) through the decay chain $\overline{B}^0 \to D^{*+}\ell^-\bar{\nu}_\ell$, $D^{*+} \to D^0\pi^+$; its flavor is tagged by the electric charge of the lepton. As for the other B, its flavor is determined by identifying a high momentum lepton ($1.0 < p_\ell < 2.35$ GeV/c for electrons, $1.1 < p_\ell < 2.35$ GeV/c for muons) among its decay products.

The loss in statistics due to the tighter selection criteria is compensated by the gain in sensitivity due to the strong reduction of the B^+B^- component and the time-dependent fit to both mixed and unmixed events, which allows one to separate and fit to the data the charge asymmetries from the two sides.

Figure 3.5 shows the results of the time-dependent fit to the four possible combinations of flavors for the two B mesons in the partially reconstructed and tag side.

While using a data sample an order of magnitude smaller than the one used by the dileptons analysis, the sensitivity of this analysis is not substantially worse. The preliminary result quoted reads:

$$|q/p| - 1 = (6.5 \pm 3.4 \pm 2.0) \times 10^{-3} \, , \tag{3.7}$$

where the first error is statistical and the second systematic. The most important contributions to the systematic error come from the determination of the charge asymmetries on the combinatorial and continuum background and from the determination of the data sample composition, which is performed prior to the time-dependent fit.

In this thesis, we will adopt the same strategy used by the partially reconstructed $\overline{B}^0 \to D^{*+}\ell^-\bar{\nu}_\ell$ analysis, but we will use charged kaons instead of leptons to tag the flavor of the unreconstructed B. Despite the higher probability of wrong assignments given by this approach, the tagging efficiency of kaon tagging is slightly better than the lepton one and, due to the presence of Doubly Cabibbo Suppressed decays (see 2.3), can allow a first estimate of the related effective parameters b and c. Finally, being completely independent of the lepton tag, the two results can be combined in an almost straight-forward way.

Table 3.1 summarizes the most recent results on the determination of CP-violation in $B^0\overline{B}^0$ mixing.

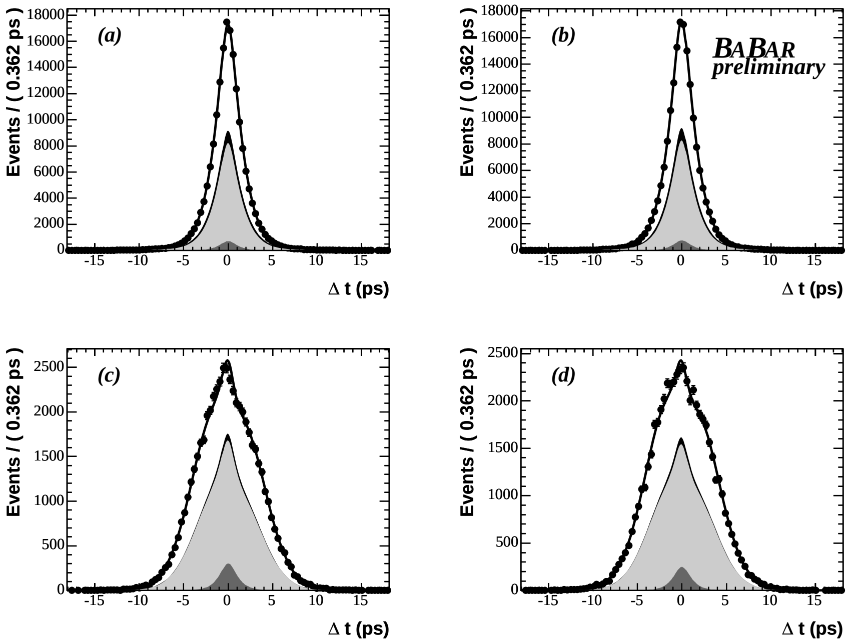

Figure 3.5: Results of the time-dependent fit of the partially reconstructed $\overline{B}^0 \rightarrow D^{*+}\ell^-\bar{\nu}_\ell$ analysis with lepton tags. Data (points) are superimposed to the sum of continuum background (dark gray), combinatorial (light Gray), peaking background (black) and signal (white) components for unmixed (top plots) and mixed events. Left (right) plots show events in which the non-reconstructed B has been tagged as a B^0 ($\overline{B}^0$).

Table 3.1: Recent results on $|q/p|$ or $\mathcal{A}_{SL}$. The first quoted error is the statistical one, while the second is the systematic.

Analysis	Luminosity	Result
Belle dileptons	78 fb^{-1}	$\mathcal{A}_{SL} = (-1.1 \pm 7.9 \pm 9.5) \times 10^{-3}$
BABAR dileptons	210 fb^{-1}	$\lvert q/p\rvert - 1 = (-0.8 \pm 2.7 \pm 1.9) \times 10^{-3}$
D∅ ($\mu\mu$)	1.0 fb^{-1}	$\mathcal{A}_{SL} = (-9 \pm 4 \pm 3) \times 10^{-3}$
BABAR PR $D^*\ell\nu$ leptonic tag	200 fb^{-1}	$\lvert q/p\rvert - 1 = (6.5 \pm 3.4 \pm 2.0) \times 10^{-3}$

Chapter 4

The PEP-II B-factory and the *BABAR* detector

In this chapter we will briefly describe the outline of the B-factory PEP-II, located at the Stanford Linear Accelerator Center, and the *BABAR* detector, along with their performance for the years relevant for this thesis. Some emphasis will be used in the aspects particularly important for the analysis of CP-violation in $B^0\overline{B}^0$ Mixing.

4.1 The B-factory PEP-II

The clean experimental environment of an e^+e^- collider can be used to study the properties of B mesons by producing a large number of $\Upsilon(4S)$ mesons. The $\Upsilon(4S)$ whose mass is 10.58 GeV/c^2, is the lightest bottomonium vector state which can decay to pairs of *open beauty* mesons: $B_u^+B_u^-$ and $B_d^0\bar{B}_d^0$ in roughly the same amount. Table 4.1 summarizes the cross sections for the various processes accessible by colliding two e^+e^- beams at the energy corresponding to the mass of the $\Upsilon(4S)$ in the center of mass (c.m.) reference frame [46].

Table 4.1: Cross sections for the different processes taking place at an e^+e^- collider with c.m. energy corresponding to the mass of the $\Upsilon(4S)$.

$e^+e^- \rightarrow$	Cross section (nb)
$b\bar{b}$	1.05
$c\bar{c}$	1.30
$s\bar{s}$	0.35
$u\bar{u}$	1.39
$d\bar{d}$	0.35
$\tau^+\tau^-$	0.94
$\mu^+\mu^-$	1.16
e^+e^-	$\sim$ 40

Given that the mass of the $\Upsilon(4S)$ is slightly larger than twice the mass of a B meson, the $B\overline{B}$ pair is emitted with a momentum of $\sim$ 335 MeV/c in the c.m. frame, and considering the lifetime of the B mesons being $\sim$ 1.5 ps, the average distance of the two decay vertices would be roughly 60 μm. With the state of the art vertex detectors, this value is too small to allow time-dependent analyses of the $B^0\overline{B}^0$ system in a traditional symmetric e^+e^- collider.

This motivated the proposal [47] for the construction of an asymmetric e^+e^- collider, where the B mesons are boosted in the laboratory frame, so that the average separation between the two B decay vertices is inflated to measurable values.

The Conceptual Design Report for the construction of the PEP-II B-factory at the Stanford Linear Accelerator Center was submitted in 1993 [48] as a proposal of an upgrade of the existing PEP facility and first colliding beams were stored in 1999.

4.1.1 Design and machine parameters

At the PEP-II B-factory a 9.0 GeV electron beam collides head-on against a 3.1 GeV positron beam, resulting in a $\beta\gamma = 0.56$ boost of the c.m. frame with respect to the laboratory. The beams are stored in two different rings: the High Energy Rings (HER) for the electrons, while the Low Energy Ring (LER) for the positrons. The interaction region, placed inside the magnetic field of the *BABAR* solenoid, comprises a series of samarium-cobalt permanent magnets which separate the bunches along the horizontal plane outside the luminous region.

The main machine parameters are collected in table 4.2; the design values are compared to the record running values reached in 2006 and to the ultimate goals that the PEP-II team plans to reach during the last year of data-taking [49].

Table 4.2: Main machine parameters of the PEP-II collider. The design values are compared to the ones reached during the summer 2006 and to the ultimate parameters which should be reached at the end of the data-taking.

Parameter	Design	Current (2006)	Ultimate (2008)
Energy LER/HER (GeV)	3.1/8.9918	3.1/8.9918	3.1/8.9918
Current LER/HER (A)	2.15/0.75	3.0/1.9	4.0/2.2
Number of bunches	1658	1730	1730
Bunch length (mm)	15	11	9
Luminosity (10^{33} cm^{-2}s^{-1})	3.0	12.0	20.0
Daily integrated luminosity (pb^{-1}d^{-1})	135	910	1500

The design luminosity has been reached pretty quickly at the end of the first year of data-taking and in the following few years the record values have superseded the design ones by a factor of four in terms of instantaneous luminosity and a factor of seven for the integrated one.

The instantaneous luminosity is monitored by the PEP-II operators by measuring the Bhabha scattering rates, while a more precise value is computed offline, by studying other QED processes (primarily e^+e^- and $\mu^+\mu^-$ production). The r.m.s. energy spreads for the LER and HER beams are 2.3 MeV and 5.5 MeV, while the systematic uncertainty in the absolute beam energies is of the order of 5-10 MeV.

The beam directions, the position and size of the luminous region (which are critical in time-dependent analyses) are continuously monitored on a run by run basis (a *run* is a data-taking period typically lasting one hour). These parameters are measured by using well reconstructed two-tracks events, like $e^+e^- \to e^+e^-$, $\mu^+\mu^-$. The uncertainties in the average beam position are of the order of a few μm in the transverse plane, and $\sim 100\mu$m in the longitudinal direction. Variations of these parameters over two consecutive runs are typically of the same order of magnitude of their uncertainties.

4.1.2 Machine backgrounds

Several components contribute to the machine-related background [50]:

- Synchrotron Radiation in the proximity of the interaction region, caused by the bending of the beams in the proximity of the permanent magnets. Careful design of the interaction region has been studied in order to limit the effects of this source of background.

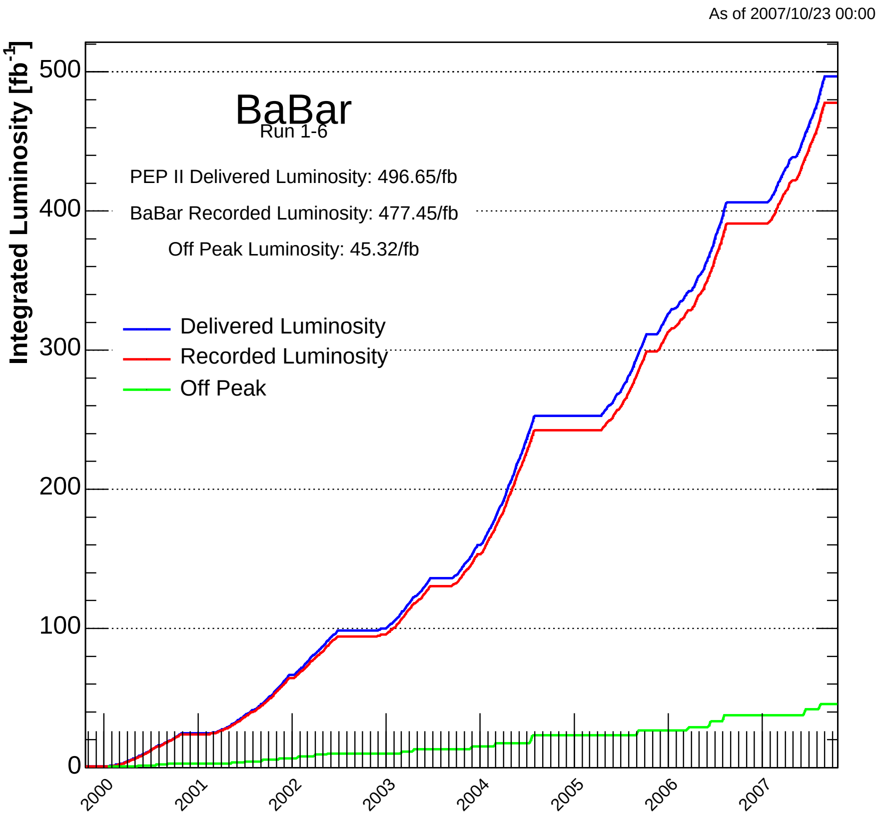

Figure 4.1: The data-taking progression since the beginning of operations is shown here. The blue line represents the luminosity delivered by PEP-II, while the red one corresponds to the luminosity actually recorded by the *BABAR* detector. The light green line shows the amount of data recorded in *off-resonance* mode.

- Beam-Gas Scattering, caused by the interaction of the beams with residual gas in the beam pipe. Even though the quality of vacuum has superseded the expectations, this is the most severe source of radiation damage to the SVT and the dominant source of background for all the sub-systems, except the DIRC.

- Luminosity Background, caused by energy-degraded electrons produced in radiative Bhabha events which enter the *BABAR* detector causing electromagnetic showers. This source of background is directly proportional to the luminosity and is already the largest source of background for the DIRC.

Other sources of background include beam losses during injection, intense bursts of radiation caused by tiny dust particles which become trapped in the beams and non-Gaussian tails from beam-beam interactions. The last background sources are a concern especially for the radiation protection of the SVT.

4.1.3 Delivered luminosity

The data-taking operations begun in 1999 and are currently underway.

Figure 4.1 shows the progression of delivered luminosity; the data-taking has been subdivided into the following periods:

- **Run1**, which corresponds to data taken in the period: May 1999 through October 2000;
- **Run2** January 2001 through July 2002;
- **Run3** November 2002 through July 2003;
- **Run4** September 2003 through July 2004;
- **Run5** April 2005 through August 2006;
- **Run6** January 2007 through September 2007;

The last period of operations (Run7) is scheduled to begin by middle-December 2007 and last till September 2008.

During the first years of PEP-II running, data-taking was held only with the beams in *coasting* mode, that is without injecting new bunches of electrons/positrons to compensate for the beam dispersions. Data-taking runs were interleaved by short periods during which the beam currents were restored to the desired values.

Since the beginning of Run4, thanks to the improvements in the accelerator stability and the reduction in the injection backgrounds, data-taking can be conducted in *trickle injection* mode, that is injecting (with a frequency of a few Hz) fresh bunches to both the LER and the HER in order to keep the beam currents to a constant level. A system has been developed in order to skip the collisions (which are affected by a higher background level) of a bunch during its first orbits.

Most of data are collected setting the c.m. collision energy to the mass of the $\Upsilon(4S)$ (we call them *on-resonance* data). In order to study the events which do not originate from the decay of a $\Upsilon(4S)$, the so called *continuum* events, about 10% of the data are collected lowering by 40 MeV the energy of the collisions, which is enough to avoid the production of the $\Upsilon(4S)$ (whose width is ~ 20 MeV).

It is particularly important to get a reliable estimate of the number of B mesons produced during a particular data-taking period. The procedure (called *B counting*), which computes this number compares the ratio of the number hadronic events over the number of $e^+e^- \to \mu^+\mu^-$ events produced in on-resonance and off-resonance data samples, assuming that the excess seen in the on-resonance is entirely due to $\Upsilon(4S)$ decays. The number of events passing the kinematical selection N_Υ is given by:

$$N_\Upsilon = N_{MH} - N_{\mu\mu} \cdot R_{off} \cdot \kappa \tag{4.1}$$

where N_{MH} is the number of events passing the selection in the on-resonance sample, $N_{\mu\mu}$ is the number of $\mu^+\mu^-$ events in the on-resonance sample, $R_{off} = N_{MH}^{off}/N_{\mu\mu}^{off}$ is the ratio of hadronic events to muon pairs in the off-resonance sample and κ is a numerical factor close to 1, which accounts for the energy dependence of the $e^+e^- \to \mu^+\mu^-$ cross section and variations in the selection efficiencies.

Monte Carlo simulations carefully validated on data are used to compute the selection efficiencies; the overall systematic error on the B counting procedure is estimated to be $\sim 1\%$.

4.2 The *BABAR* detector

The *BABAR* detector is described in detail in [51]. Its design has been optimized for the measurement of time-dependent CP-violation of the B mesons, but it is also suitable for rare decays of the B and D mesons, τ physics, searches of new hadronic states and Initial State Radiation. It should also be mentioned the recent discovery of the $D^0\bar{D}^0$ oscillations achieved by the *BABAR* and Belle collaborations [52], [53].

The required characteristics of *BABAR* are:

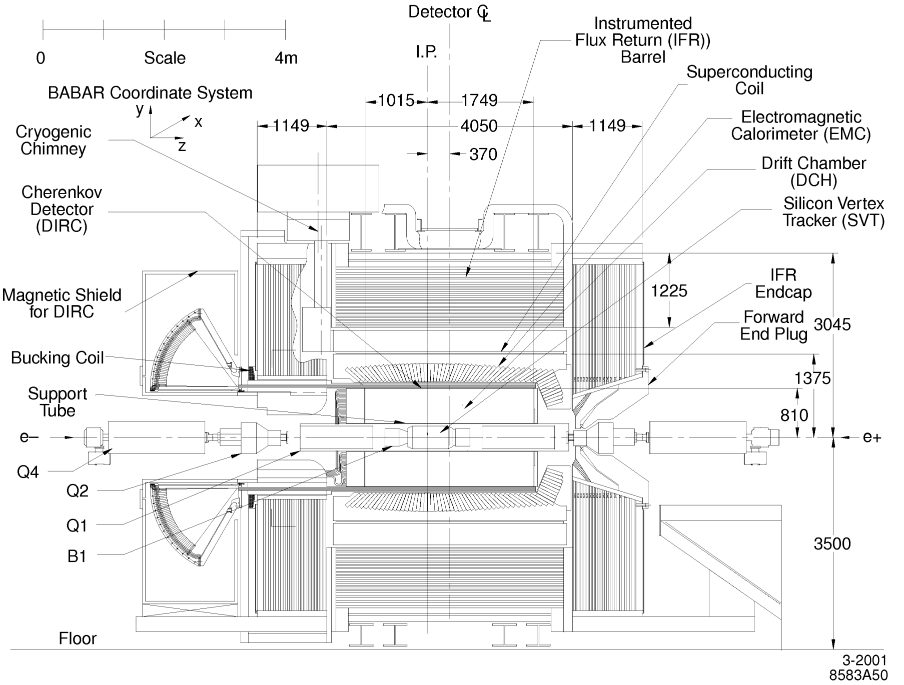

Figure 4.2: Longitudinal view of the *BABAR* detector.

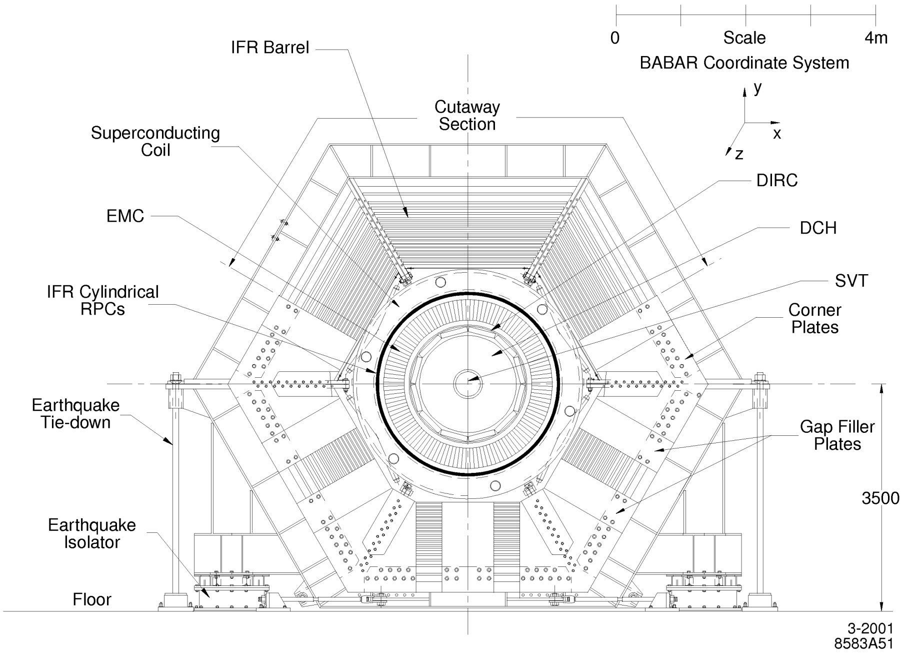

Figure 4.3: Front view of the *BABAR* detector.

- a large and uniform acceptance down to small polar angles relative to the boost direction;
- excellent reconstruction efficiency for charged particles down to 60 MeV/c and for photons to 20 MeV;
- very good momentum resolution to separate small signals from background;
- excellent energy and angular resolution for the detection of photons from π^0 and η^0 decays, and from radiative decays in the range from 20 MeV to 4 GeV;
- very good vertex resolution, both transverse and parallel to the beam direction;
- efficient electron and muon identification, with low misidentification probabilities for hadrons;
- efficient and accurate identification of hadrons over a wide range of momenta for B flavor-tagging. This feature is crucial for this analysis;
- a flexible, redundant and selective trigger system;
- detailed monitoring and automated calibration;
- detector components that can tolerate significant radiation doses and operate reliably under high-background conditions.

Figures 4.2 and 4.3 show respectively the longitudinal and front views of the detector. It is installed around the interaction region; in order to maximize the acceptance, due to the asymmetry of the beam energies, its center is displaced by 37 cm with respect to the luminous region towards the lowest energy beam direction. The detector axis is off-set by about 20 mrad with respect to the collision axis in order to minimize the perturbations to the beams induced by its magnetic field. The asymmetric energy collisions naturally define a *forward* and a *backward* side of the detector: most particles (and radiation) produced in the luminous region fly in the hemisphere (the forward one) of the outgoing HER beam. For this reason the radiation-sensitive electronics have been placed in the backward side of the detector, when possible.

A standard cartesian reference frame is defined, with the z axis parallel to the longitudinal axis of the detector and pointing in the direction of the HER, the y axis oriented vertically and upward and the x axis, which lays on the horizontal plane pointing in the opposite direction of the center of PEP-II rings.

The detector is constituted by a superconducting solenoid which provides a magnetic field of 1.5 T, surrounded by a steel return yoke. The five sub-detectors used in physics measurements are, from the center of the detector to the outside: a silicon vertex tracker (**SVT**) and a drift chamber (**DCH**) devoted to tracking and decay vertices identification. A Čerenkov ring imaging detector (**DIRC**) provides information to discriminate among different particles species (mostly to the $K\,/\,\pi$ separation) and a CsI crystals calorimeter (**EMC**) is used to detect electromagnetic showers produced by photons and electrons. All these detectors are locate inside the solenoid; the fifth sub-detector (**IFR**), is placed in the return yoke and is devoted to the identification of neutral hadrons and the tracking of muons.

A full simulation of the *BABAR* detector has been implemented, based on GEANT4 [54]. Particles production and decays are simulated by an event generator interfaced to the LUND/JETSET [55] packages and the description of radiation from charged particles is provided by the PHOTOS [56] program.

Each sub-detector and its performance will be briefly described in the next sections.

4.2.1 SVT: Silicon Vertex Tracker

The Silicon Vertex Tracker is the innermost sub-detector and, together with the DCH, performs the tracking of charged particles. Its crucial (mostly for time-dependent analyses) task is to provide precise and accurate determination of the secondary decay vertices with a resolution considerably better than the average separation of the two B decay vertices ($\sim$ 250 μm in the PEP-II environment). Due to the more precise track-hit position determination, the SVT is more important than the DCH in the measurement of high momentum tracks. On the other side, due to the bending caused by the solenoidal field, the SVT is often the only device which can detect very low momentum (less than 120 MeV/c) particles, a feature that will be crucial for the analysis described in this thesis. Finally, the SVT provides some information for *particle identification* (PID), through the measurement of energy loss (dE/dx) inside the detector material.

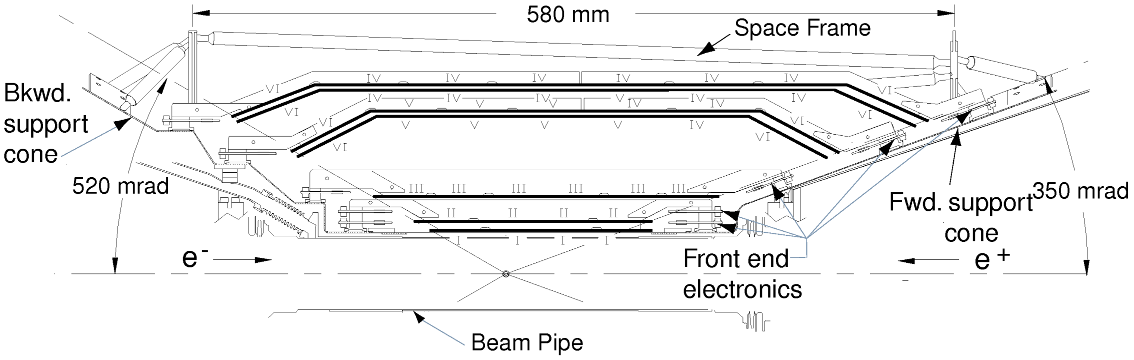

Figure 4.4: Longitudinal view of the Silicon Vertex Tracker.

Figures 4.4 and 4.5 show a schematical representation (on a longitudinal and transverse view, respectively) of the SVT. Due to the presence of the permanent magnets close to the interaction region, the acceptance is limited to polar angles larger than 20° in the forward direction, while in the backward tracks can be detected down to 30° from the beam line. The proximity to the *beam spot* causes an intense exposure to ionizing radiation; the SVT has been designed to withstand an integrated dose of 2 MRad. The heat generated by the electronics is removed by a cooling system.

The SVT is made up of five layers of double-sided silicon strips sensors, organized in 6, 6, 6, 16 and 18 modules respectively, as can be seen from figure 4.5. The sensors are 300 μm thick double-sided silicon strip devices, built on high-resistivity n-type substrates with p^+ and n^+ on the two opposite sides. These strips are oriented orthogonally to each other: the ϕ measuring strips (*ϕ strips*) run parallel to the beam and the z measuring strips (*z strips*) are oriented transversely to the beam axis. The modules of the inner three layers are straight, while the modules of layers 4 and 5 are *arch*-shaped (see figure 4.4). This arch design has been chosen to minimize the amount of silicon required to cover the solid angle, while increasing the crossing angle for particles near the edges of acceptance.

To satisfy the different geometrical requirements of the five SVT layers, five different sensor shapes are required to assemble the planar sections of the layers. The smallest detectors are 42 $\times$ 42 mm^2 ($z \times \phi$) and the largest are 68 $\times$ 53 mm^2. Two identical trapezoidal sensors are added (one each at the forward and backward ends) to form the arch modules. The half-modules are given mechanical stiffness by means of two carbon fiber/kevlar ribs. The ϕ strips sensors in the same half-module are electrically connected with wire bonds to form a single readout strip. This results in a total strip length up to 140 mm (240 mm) in the inner (outer) layers. The total number of readout channels is approximately 150,000; some ambiguity arising from connecting together 2 z strips in layer 4 and 5 is resolved by means of pattern recognition algorithms.

The inner modules are tilted in ϕ by 5°, allowing an overlap region between adjacent modules,

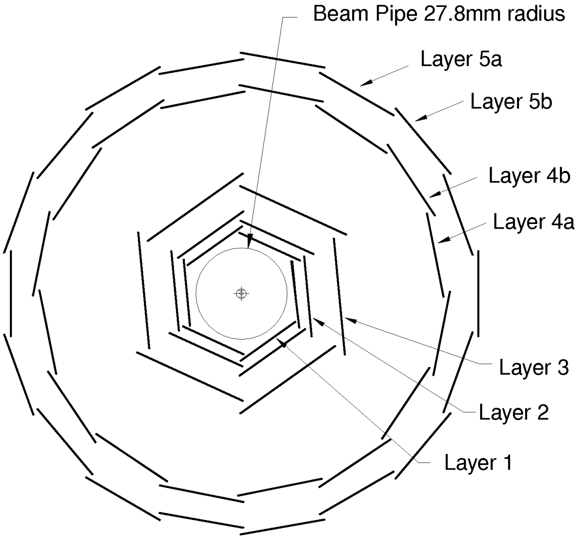

Figure 4.5: Front view of the Silicon Vertex Tracker.

Table 4.3: Geometrical parameters of the different SVT layers.

Layer/ view	Radius (mm)	R-O pitch (μm)	Strip length (mm)
1 z	32	100	40
1 ϕ	32	50-100	82
2 z	40	100	48
2 ϕ	40	55-100	88
3 z	54	100	70
3 ϕ	54	110	128
4 z	91-127	210	104
4 ϕ	91-127	100	224
5 z	114-144	210	104
5 ϕ	114-144	100	265

a feature that provides full azimuthal coverage and is advantageous for alignment, The outer modules cannot be tilted, because of the arch geometry. To avoid gaps and to have a suitable overlap in the ϕ coordinate, layers 4 and 5 are divided into two sub-layers and placed at slightly different radii. The relevant geometrical parameters of each layer are summarized in table 4.3.

In order to minimize the material in the acceptance region, the readout electronics are mounted entirely outside the active detector volume. An optical survey of the SVT in its assembly jig indicated that the global error in placement of the sensors with respect to design was $\sim 200\,\mu$m. The total active silicon area is 0.96 m^2 and the material traversed by particles is $\sim$ 4% of a radiation length. The geometrical acceptance of the SVT is 90% of the solid angle in the c.m. frame, typically 86% is used in charged particle tracking.

The SVT is mounted inside the 4.5 m long *support tube*, which can move independently of the rest of *BABAR* along the longitudinal axis, thus the need of measuring and monitoring its position on a run-by-run basis.

The challenges set by the requirements of the SVT front-end electronics led to the development of the ATOM (*A Time-Over-Threshold Machine*, [57]) dedicated circuit, which ensures reliable data transmission within the limited amount of acceptable information.

4.2.2 DCH: Drift CHamber

The Drift Chamber is devoted to the reconstruction of charged particles tracks, the measurement of their momenta and energy loss (dE/dx). It is a cylindrical crown shaped tank 3 m long, whose inner radius is 24 cm (surrounding the support tube) and the outer one is 84 cm.

It contains a 80:20 mixture of helium:isobutane gas kept 4 mbar above the atmospheric pressure; this composition has been chosen in order to minimize the effects of Coulomb scattering of a particle traversing the chamber volume. The DCH is made up of 7104 hexagonal cells 17.0 to 19.2 mm wide (see figure 4.6), each containing six grounded 120 μm aluminum field wires, surrounding a 20 μm tungsten-rhenium sense wire, which is kept at a voltage which varies between 1900 and 1960 V, depending on the data-taking periods. Guard and clearing wires, held at positive voltage, are added to improve the electrostatic performance of the cell and to collect charges created through proton conversions in the material of the walls. The typical gas gain factor is 5×10^4 for an operating voltage of 1960 V.

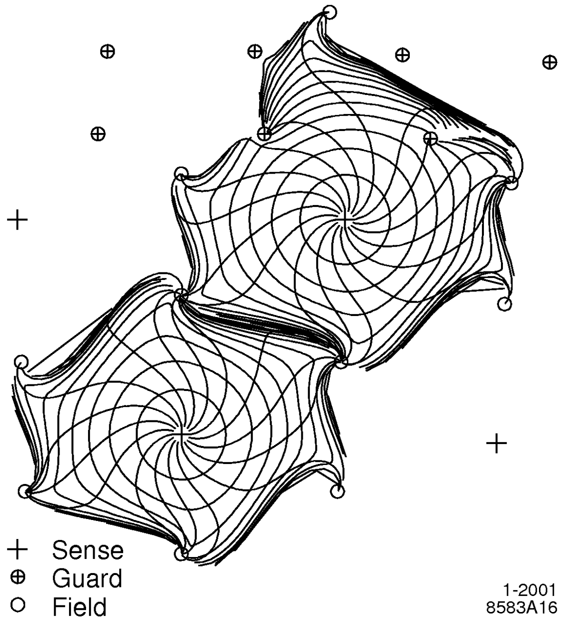

Figure 4.6: Two DCH drift cells are depicted. Besides the sense, field and guard wires, also the electric field and isochrones are shown. The latter are the contours of equal drift times of ions inside those cells and are spaced by 100 ns in this plot.

The cells are grouped into 40 layers, which are in turn grouped into 10 superlayers, with the wires is each superlayer oriented either in *axial* (that is, parallel to the longitudinal axis of the detector) or in *stereo* (at a small angle with respect to the detector axis): in this configuration, it is possible to get some information on the z coordinate. Figure 4.7 shows the configuration of the four innermost superlayers of the DCH.

The two end plates are made from 24 mm thick aluminum plates; in the forward side, the thickness is reduced to 12 mm outside a radius of 46.9 cm, in order to minimize the amount of material in front of the electromagnetic calorimeter. The inner cylindrical wall is made up by different sections of beryllium and aluminum tubes, while the outer wall is built from carbon fiber skins laminated to a 6 mm thick honeycomb core. The total thickness of the DCH at normal incidence is 1.08% X_0, of which the gas and the wires contribute with 0.2% X_0 and the inner wall with 0.28% X_0.

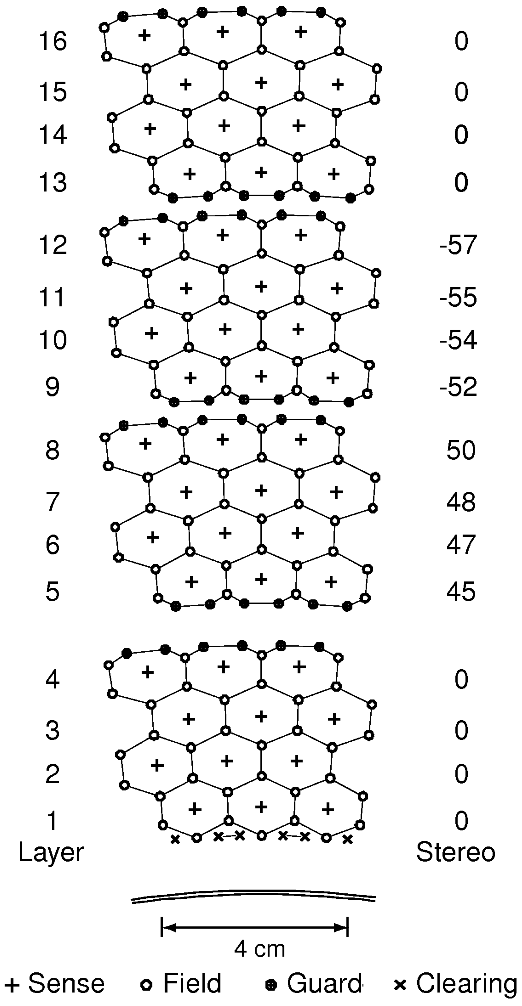

Figure 4.7: Schematic view of the four innermost layers of the DCH. Lines across field and guard wires have been drawn to help visualize the cell boundaries. The numbers on the right side give the stereo angles (in mrad) of sense wires in each layer.

The time-to-distance relation is performed offline using samples of $e^+e^- \to e^+e^-$, $\mu^+\mu^-$ events, where the drift distance is computed as the distance of closest approach between the track and the wire. To avoid biases, the fit on the track discards the hit of the wire under investigation.

The measurement of the electric charge deposited in each cell allows the determination of the specific energy loss (dE/dx). A resolution on this quantity of roughly 7% (see figure 4.8) permits a clean K/π separation up to 700 MeV/c, where the DIRC performance is not effective.

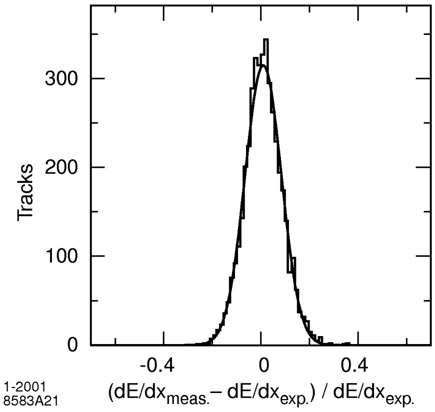

Figure 4.8: dE/dx resolution of the DCH during typical running conditions. The curve represents the result of a Gaussian fit to the data with a resolution of 7.5%.

Due to severe constraints of space, radiation and the need to minimize the material in front of the electromagnetic calorimeter, the Front End Electronics has been arranged with a compact and highly modular design. Calibrations to determine channel-by-channel corrections are performed on a daily basis by an automated procedure.

4.2.3 DIRC: Detector of Internally reflected Čerenkov light

The need of a high efficiency in B flavor-tagging using charged kaons and the study of CP-asymmetries in the channels $B^0 \to \pi^+\pi^-$, $K^+\pi^-$ motivated the development of a high performance device, capable of performing clean K/π separation in the momentum range 0.7-4.2 GeV/c.

The choice of the BABAR collaboration has been a newly developed ring-imaging Čerenkov detector, called the DIRC [58]. This device should be thin and uniform in order not to degrade the performance of the electromagnetic calorimeter and not to inflate its cost.

Particle identification of a charged particle is achieved by combining the measurement of its Čerenkov angle θ_C performed by the DIRC with its momentum. Čerenkov photons are produced by the passage of the particle through 17 mm thick, 35 mm wide and 4.9 m long fused synthetic silica bars, which have an index of refraction $n = 1.473$.

The principle exploited by the DIRC is the fact that the magnitude of the angles of Čerenkov light are preserved during multiple reflections from flat surfaces. The quartz bars serve both as radiators and as light pipes to convey the photons into the *standoff box*, a water filled tank instrumented with 10752 photomultipliers, where the light is collected. The 144 bars are arranged in 12 sections, each one made up of a hermetically sealed *bar box* containing 12 quartz bars each. The non-instrumented (forward) end of the bars is terminated with a mirror, while the interface between quartz bars and water is provided by a fused silica *wedge*.

The total radial thickness of DIRC radiators is 80 mm, corresponding to 17% X_0 at normal incidence; the solid angle subtended by the radiation bars corresponds to 94% of the azimuthal

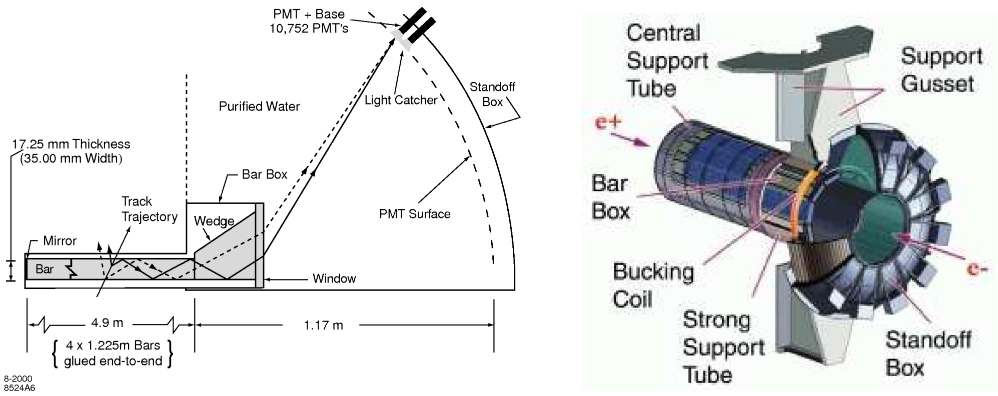

Figure 4.9: Scheme of a radiator bar (left picture) and exploded view of the DIRC (right).

angle and 83% of the c.m. polar angle cosine. Given the geometrical and optical properties of the system, the overall angular resolution on a single photon corresponds to 10 mrad.

The choice of the material for the radiator bars is due to the excellent properties of fused silica in terms of resistance to ionizing radiation, index of refraction, attenuation length, low chromatic dispersion and the possibility to get very accurate optical finish of surfaces (which is crucial to preserve the original information on θ_C). Figure 4.9 shows a schematic picture of the DIRC and its principle.

The Čerenkov light pattern expected at the standoff box is a conic section; besides the position of the associated hits, also the timing is measured in order to get rid of potential ambiguities and reduce the background, as can be seen from figure 4.10.

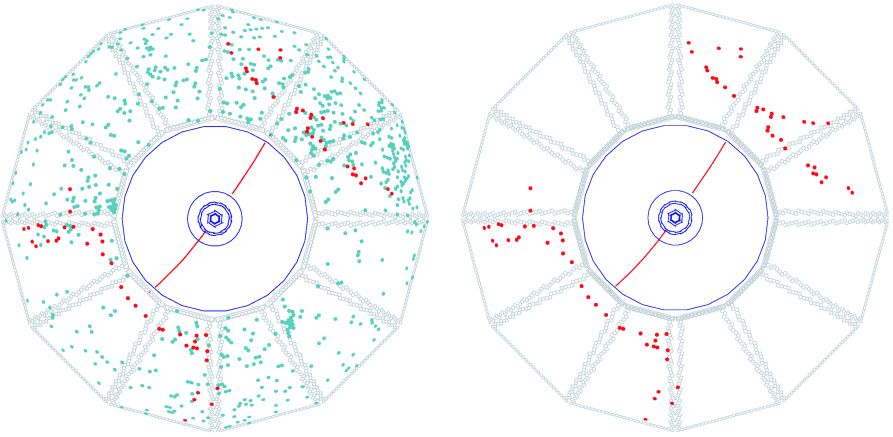

Figure 4.10: DIRC light pattern from a typical two-tracks event. On the left plot, all hits within the ±300 ns trigger window are shown, while on the right only the signals within 8 ns of the expected photon arrival time are shown. The background reduction factor is of the order of 40.

Background originate mostly from low energy photons coming from the PEP-II rings hitting the standoff box and is also reduced by lead shielding around the beam line.

The calibration procedure involves two steps. The first one is performed online by means of a light pulser system which generates 1 ns duration light pulses to determine the mean time delay of each photomultiplier. The global time delay is determined at the second step, where real data tracks are used to fit Δt_γ, that is the difference between the uncalibrated time minus the expected arrival time of a Čerenkov photon.

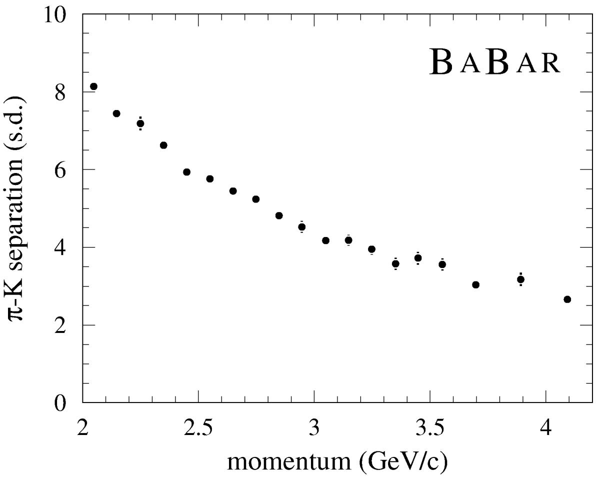

Figure 4.11: Number of standard deviations achievable in K/π separation with the DIRC as a function of the particle momentum.

Figure 4.11 shows the K/π which is achievable using the DIRC alone. More on its performance will be shown in section 4.2.8.

4.2.4 EMC: ElectroMagnetic Calorimeter

The electromagnetic calorimeter (EMC) is designed to measure electromagnetic showers with excellent efficiency and energy and angular resolutions over the energy range from 20 MeV to 9 GeV.

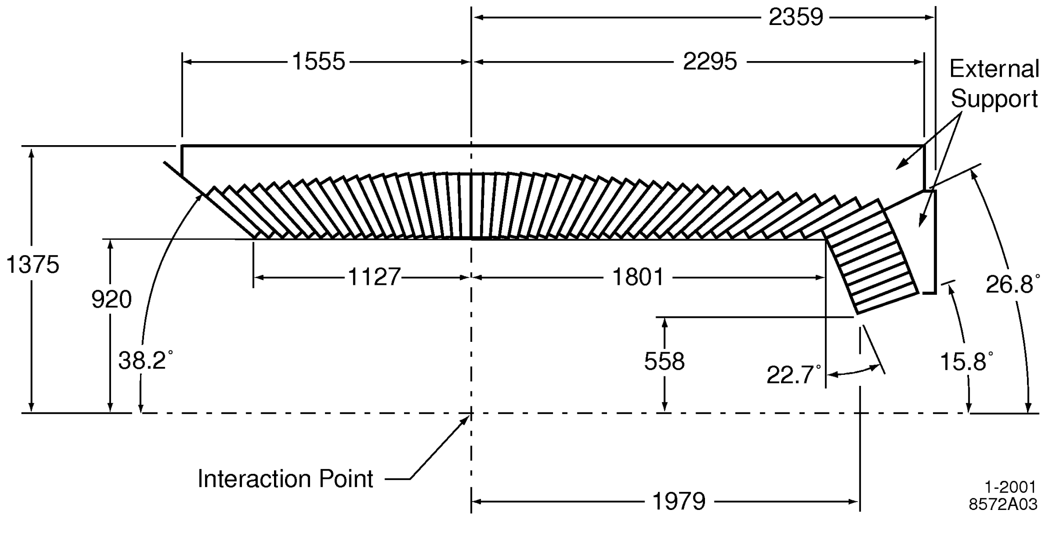

Figure 4.12: Longitudinal cross section of the EMC, showing the 56 crystal rings. The detector is axially symmetric around the z axis. All dimensions are expressed in mm.

Figure 4.12 shows the layout of the EMC. It is constituted by two sections: a cylindrical barrel, containing 5760 crystals disposed in 48 rings, and a conical endcap, carrying 820 crystals, arranged in 8 rings. The material chosen for the crystals is the tallium-doped CsI, whose properties match the desired energy and angular resolution. Depending on the position, the crystal are 29.6 cm to 32.4 cm long and they have trapezoidal shape, with the front face having an area of 4.7 × 4.7 cm^2 and the back face 6.1 × 6.0 cm^2.

The material in front of the calorimeter is 0.3-0.6 X_0 thick, for the barrel and the five outer rings of the endcap, while for the innermost rings of the endcap it reaches 3 X_0, mainly due to the SVT support structure and electronics and the permanent magnets.

Each crystal is read by a 2 × 1 cm^2 silicon PIN diode glued on the back face, connected to a low-noise preamplifier. Light pulses used for calibration issues are brought to each crystal through two optical fibers attached to the back face. Due to calibration stability and the need to avoid mechanical stress on the PIN diodes joints, it is crucial that the crystals be maintained at an accurately monitored constant temperature. This is achieved by two separated cooling systems for the barrel and the endcap sections of the calorimeter.

The energy resolution, measured in a wide energy range through different physical processes (Bhabha scattering, $\chi_{c1} \to J/\psi\gamma$, photons from π^0 and η decays) is determined to be (see figure 4.13):

$$\frac{\sigma_E}{E} = \frac{(2.32 \pm 0.30)\ \%}{\sqrt[4]{E(\mathrm{GeV})}} \oplus (1.85 \pm 0.12)\ \%\ , \tag{4.2}$$

while the angular resolution, determined using π^0 and η decays to pairs of photons with roughly equal energies, is:

$$\sigma_\theta = \sigma_\phi = \left(\frac{3.87 \pm 0.07}{\sqrt{E}\mathrm{GeV}} \pm 0.04\right)\ \mathrm{mrad}\ . \tag{4.3}$$

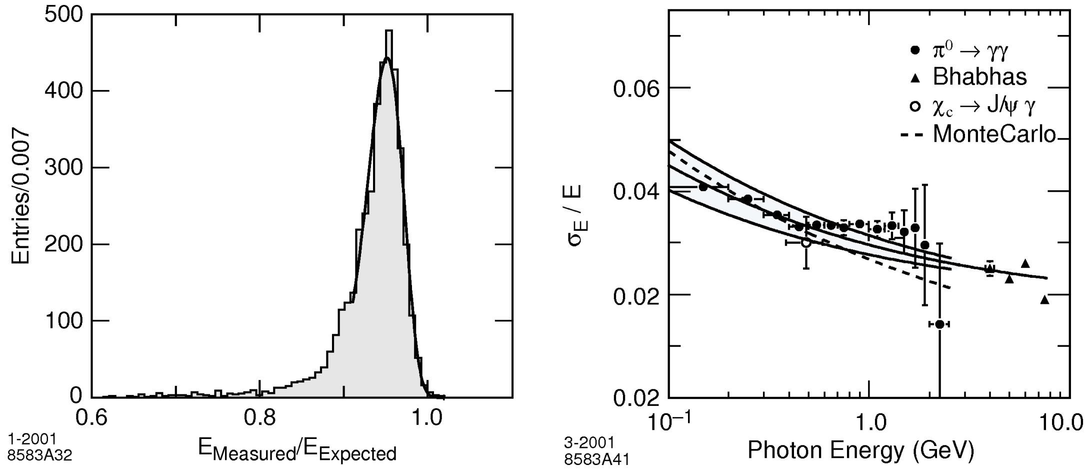

Figure 4.13: Performance of the EMC. Left: ratio of the measured energy to the expected one for Bhabha electrons of 7.5 GeV/c. Right: the energy resolution for the EMC for electrons and photons from various physical processes. The solid line represents the fit result of equation 4.2, while the shaded area displays the rms error associated to the fit.

Concerning the energy calibration of the EMC, it happens in two steps. First, the measured pulse height on each crystal has to be translated to the actual energy deposited. Second, the energy deposited in a shower spreading over several adjacent crystals has to be related to the energy of the incident particle by correcting for energy losses.

The calibration of the single crystals is performed at two energies at the opposite ends of the spectrum. The calibration at low energy uses a 6.13 MeV radioactive photon source provided by a low-energy neutron generator activating the cooling liquid which circulates on through the EMC. At high energies, Bhabha scattering events are used to constrain the deposited energy to the value predicted by a GEANT-based simulation of the detector. These two types of calibration are performed monthly.

As for the cluster energy correction, it is computed as a function of the incident energy and polar angle. At low energy it is performed by using π^0 decays in a mass constrained fit, while at higher energies, radiative Bhabha scattering events are utilized.

4.2.5 IFR: Instrumented Flux Return

The Instrumented Flux Return (IFR) is devoted to high efficiency muon tracking and the identification of neutral hadrons (K^0_L, neutrons) which traverse the inner part of the detector. Since the beginning of the data-taking the IFR has undergone several problems which led to an almost complete substitution of the original detectors; in this subsection we will briefly recall the original design, the major problems the IFR went through and the solutions which have been implemented.

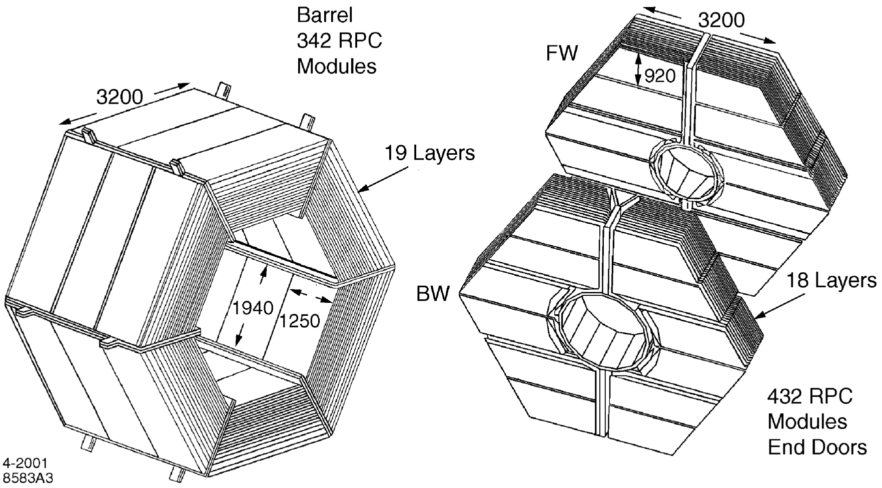

Figure 4.14: IFR layout: the barrel sector and the forward (FW) and backward (BW) end doors are displayed.

Original design

The return flux is finely segmented (see figure 4.14) into 18 steel plates, of thickness increasing from 2 cm for the inner nine plates to 10 cm of the outermost one. In the gaps between adjacent steel plates have been instrumented with 19 layers of *Resistive Plate Chambers* (RPC) in the barrel and 18 layers in the endcaps. Moreover, 2 layers of RPC's have been installed inside the superconducting solenoid (*cylindrical RPC's*).

The RPC concept ([59]) allows the easy and cheap instrumentation of a large volume with odd shapes with basically no dead regions. Figure 4.15 shows the cross section of a planar RPC, which consists of two bakelite sheets, 2 mm thick, separated by a 2 mm gap. The two external surfaces are coated with graphite and are connected to high voltage and ground. Streamers produced inside the gap by ionizing particles are readout by capacitive aluminum strips, glued outside a layer on insulating foam. Strips on opposite faces of a chamber are disposed orthogonally to each other, so it is possible to measure both the horizontal and the vertical coordinate of a streamer.

The chambers operate in limited streamer mode. The gas mixture has this typical composition: 57.7% Argon, 38.8% Freon 134 a and 4.5% isobutane. This mixture is non-flammable and the typical flow rate corresponds to four gas exchanges per day.

Several problems showed up during the early months of data-taking: due to production defects and operating temperatures way higher than expected (the cooling system was installed

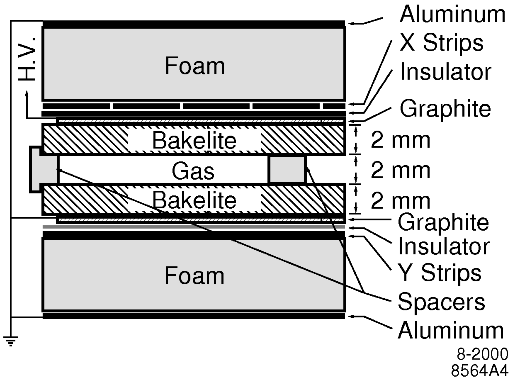

Figure 4.15: Cross section of a planar RPC.

after the first year of data taking), a large fraction of chambers exhibited a steadily decreasing rate in the detection efficiency and a significant increase of the dark current.

IFR upgrade

Even though the IFR is a highly redundant detector, the large decrease in efficiencies (and eventually the death) of a significant number of chambers severely impacted the muon identification efficiency, with consequent decrease in the B flavor-tagging and J/ψ reconstruction efficiencies.

This situation motivated the replacement of the chambers in the forward endcap (which collects almost 50% of the muons produced at the interaction point, due to the boost of the c.m. frame) with a new generation of RPC's during the pause between Run2 and Run3. The accurate quality control on the new production and the close monitoring of the running conditions allowed the new generation of detectors to survive till present days with an overall good efficiency ($\sim$ 90%) and smooth data-taking.

During Run5 and Run6, the operating mode of the inner middle chambers of the forward endcap has been switched from streamer to avalanche mode. This change was motivated by the fact that those chambers are heavily subject to beam-induced backgrounds, which causes higher rates, lower efficiencies and faster aging of the detectors. The gas mixture for avalanche running is typically: 22% Argon, 73% Freon and 5% isobutane and the high voltage is set to $\sim$ 9500 V, compared to $\sim$ 6700 V for the new generation RPC's in streamer mode.

The first experience of avalanche running showed a significant decrease of the charge produced by ionizing particles (thus a slower aging) and a recovery of the efficiency in the regions close to the beam line. For these reasons the forward endcap middle chambers of the seven innermost layers will continue running in avalanche mode till the end of data-taking.

On the other side, the original cylindrical chambers have been switched off at the beginning of Run6, since their efficiencies dropped to insufficient values; it is not planned to replace them.

A different strategy has been undertaken for recovering the efficiency in the barrel, adopting a different kind of detectors to replace the RPC's: the *Limited Streamer Tubes* (LST) [60]. Figure 4.16 shows a picture of a LST actually installed in *BaBar*.

LST's are made from PVC extrusion having either 7 or 8 17×17 mm^2 cells and covering the length of the barrel along the z axis. PVC surfaces are treated with a graphite paint, with a resistivity in the range 0.2 to 1.0 MΩ/cm^2. A 100 μm diameter silver wire is strung along the z axis at the center of each cell and is sustained at intervals of 50 cm by plastic holders. The wires are kept at $\sim$ 5600 V, where the plateau conditions are met with the gas mixture being used: 89% CO_2, 8% isobutane and 3% Argon.

Signals are read directly on the wires for the ϕ coordinate, while the z coordinate is read through cathode strips glued outside the modules. The detection efficiency is close to the limit

Figure 4.16: Picture of a LST installed in the barrel of *BABAR*.

of 95% set by the presence of dead material on each layer of LST's. The capability of separating muons from charged hadrons has been improved by adding 4 brass layers.

The first two sextants of LST's have been installed during the shutdown between Run4 e Run5, and the remaining four between Run5 and Run6. The first experience of running of the LST's showed a completely restored efficiency of the barrel and no hints of degradations of its performance have been manifested so far.

4.2.6 Trigger

The basic requirement for the trigger system is the selection of events of interest with a high, stable and well-understood efficiency while rejecting background events and keeping the total event rate to manageable levels.

The total trigger efficiency was required to exceed 99% for all $B\overline{B}$ events and at least 95% for continuum $q\bar{q}$ events. Less stringent requirements apply to other type of events, e.g. $\tau^+\tau^-$ events should have a 90-95% trigger efficiency, depending on the specific $\tau^\pm$ decay channel.

The trigger is implemented as a two-level hierarchy, the Level 1 (L1) in hardware followed by the Level 3 (L3) in software (a Level 2 trigger could have been developed in case L1 and L3 alone had not matched the requirements).

During normal operation at current luminosities, the L1 is configured to have an output rate of typically 1 kHz. Triggers are produced within a fixed latency window of 11-12 μs after the e^+e^- collision and delivered to the Fast Control and Timing System (FCTS). Data used to form the trigger decision are preserved with each event for efficiency studies. The L3 receives the output from L1, performs a second stage rate reduction for the main physics sources, and identifies and flags the special categories of events needed for luminosity determination, diagnostic and calibration purposes. The typical L3 output rate is 250 Hz.

The L1 trigger decision is based on charged tracks in the DCH above a preset transverse momentum, showers in the EMC, and tracks detected in the IFR. Trigger data are processed by three specialized hardware processors. The drift chamber trigger (DCT) and electromagnetic calorimeter trigger (EMT) both satisfy all trigger requirements independently with high efficiency, and thereby provide a high degree of redundancy, which enables the measurement of trigger efficiency. The instrumented flux return trigger (IFT) is used for triggering $\mu^+\mu^-$ and cosmic rays, mostly for diagnostic purposes. Some concerns on the L1 trigger are present for the last periods of data-taking when due to the high luminosity and potentially high backgrounds the L1 rate could hit the 5 kHz hardware limit. The overall structure of the L1 trigger is illustrated in figure 4.17.

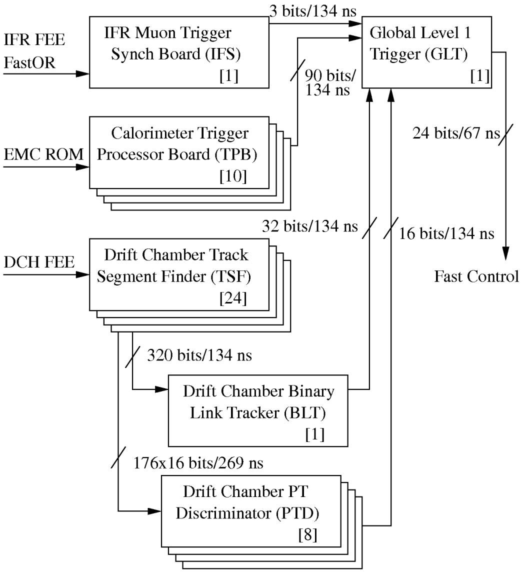

Figure 4.17: Simplified L1 trigger schematic. Indicated on the figure are the number of components (in square brackets) and the transmission rates between components in terms of total signal bits.

The L3 trigger software comprises event reconstruction and classifications, a set of event selection filters, and monitoring. This software runs on the online computer farms within the Online Event Processing (OPE) framework. Many events which pass L1 but must be rejected by L3 are beam-induced charged particle background that are produced in material close to the IP. The Level 3 trigger combines DCT tracks and EMT clusters with the full DCH and EMC information. The L3 DCH algorithm performs fast pattern recognition and fits L1 tracks to helices and is able to determine the z coordinate of closest approach of tracks, which is important for rejecting the above mentioned background. The L3 EMC based trigger identifies energy clusters with a higher sensitivity than L1 and filters events with either high energy deposits of high cluster multiplicity. The output of both the DCH and EMC L3 filters is dominated by Bhabha events which are mostly rejected, but also prescaled in L3 for calibration and luminosity online monitoring and offline measurements.

4.2.7 Tracking

Track reconstruction uses information from the SVT, the DCH and the L3 trigger. A track is defined by the following parameters:

- d_0, the distance in the $x-y$ plane of the *point of closest approach* of the helix to the beam spot;
- ϕ_0, the azimuthal angle corresponding to the track direction in the $x-y$ plane;
- ω, the signed geometrical curvature;
- z_0, the distance along the z-axis of the point of closest approach;
- $s = \tan\lambda$, the tangent of the dip angle, $\lambda = \pi/2 - \theta$, where θ is the polar angle in the lab frame.

The absolute event timing information (the event start time t_0) is determined iteratively by the track finding algorithms along with the five helix parameters.

The track finding and the fitting procedures make use of a Kalman filter algorithm that takes into account the detailed distribution of material in the detector and the full map of the magnetic field.

The track pattern recognition begins in the DCH, starting from tracks segments identified by the L1 trigger. Helix fits are performed on the hits used by the L3 track finding algorithm and then additional hits that may belong to the track under consideration are added. The re-fitted track is then extrapolated into the SVT and track segments are added, provided they are consistent with the errors in the extrapolation through the detector material and the inhomogeneous magnetic field.

Any remaining SVT hits are passed to the SVT standalone tracking algorithms. These are particularly important for the detection of D^* decays, where a charged slow pion is produced. Figure 4.18 shows the mass difference $\Delta M = M(K^-\pi^+\pi^+) - M(K^-\pi^+)$ for the total sample and the subsample in which the slow pion track has been detected by both the SVT and the DCH. The difference in these two distributions demonstrates the contribution from SVT standalone tracking, both in terms of the gain of signal events and of resolution.

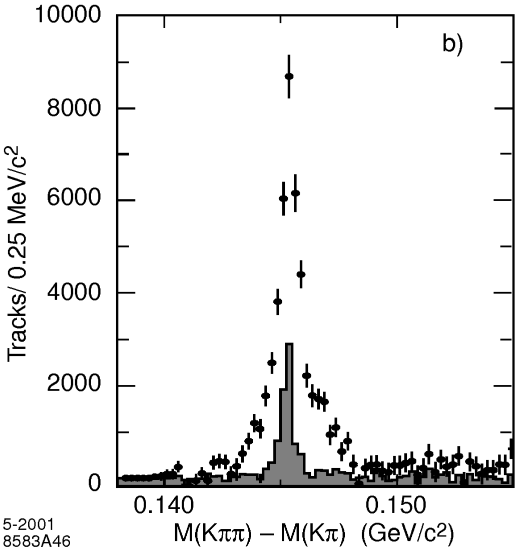

Figure 4.18: Reconstruction of low momentum pions originating from $D^{*+} \rightarrow D^0\pi^+$, $D^0 \rightarrow K^-\pi^+$. The mass difference $\Delta M = M(K^-\pi^+\pi^+) - M(K^-\pi^+)$ both for all detected events (data points) and for events in which the low momentum pion is reconstructed both in the SVT and DCH (histogram). Background from combinatorics and fake tracks, as well as non-resonant data have been subtracted.

The resolution in the five track parameters is monitored using e^+e^- and $\mu^+\mu^-$ events. It is further investigated offline in multi-hadron events and cosmic ray muons.

Cosmic rays that are recorded during normal data-taking offer a simple way of studying the track parameter resolution. The upper and lower halves of the cosmic ray tracks traversing the DCH and the SVT are fitted as two separate tracks, and the resolution is derived from the difference of the measured parameters for the two track halves. Based on the full width at half maximum of the distributions of those differences, the resolutions for single tracks can be stated as:

$$\sigma_{d_0} = 23\mu\text{m} \qquad \sigma_{\phi_0} = 0.43\,\text{mrad}$$
$$\sigma_{d_0} = 29\mu\text{m} \qquad \sigma_{\tan\lambda} = 0.53 \cdot 10^{-3}\ .$$

Figure 4.19 shows the resolution in the parameters d_0 and z_0 for tracks in multi-hadron events, as a function of the transverse momentum. The resolution is determined from the width of the distribution of the difference between the measured parameters, d_0 and z_0, and the coordinates of the vertex reconstructed from the remaining tracks in the event. These distributions peak at zero, but have a tail for positive values due to the effect of particle decays. Consequently, only the negative part of the distributions reflects the measurement error and is used to extract the resolution. The d_0 and z_0 resolutions so measured are about 25 μm and 40 μm respectively at a transverse momentum $p_t = 3$ GeV/c. These values agree well with expectations, and are also in reasonable agreement with the results obtained from cosmic rays.

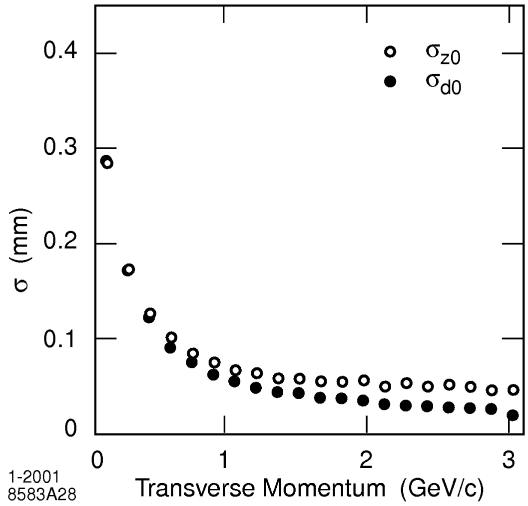

Figure 4.19: Resolution in the parameters d_0 and z_0 for tracks in multi-hadron events as a function of the transverse momentum. The data are corrected for the effects of particle decays and vertexing errors.

While the position and angle measurements near the interaction region are dominated by the SVT, the DCH contributes primarily to the p_t measurement. The resolution in the transverse momentum is:

$$\frac{\sigma_{p_t}}{p_t} = (0.13 \pm 0.01)\% \cdot p_t + (0.45 \pm 0.03)\% \,, \tag{4.4}$$

where p_t is measured in GeV/c. These values for the resolution parameters are very close to the initial estimates and can be well reproduced by Monte Carlo simulations.

The performance of the different selectors are checked by using some high purity data control samples.

4.2.8 Particle Identification

Each of the five sub-detectors of *BABAR* can contribute to the determination of the particle specie of a given track. In this section we will not treat extensively the general topic of *Particle Identification* (PID), rather we will focus on the information used by the *PID selectors* relevant for our analysis.

Electrons

The PID selector used in our analysis for the selection of electrons, named `PIDLHElectrons`, uses the information from DCH (dE/dx), DIRC (number of detected photons and Čerenkov angle) and EMC (deposited energy, lateral and longitudinal shower shape).

For each discriminating variable, probability density functions are constructed and, under the assumption of independent measurements from the individual subdetectors, they are combined to compute the likelihood $L(\xi)$ for each particle hypothesis $\xi \in \{e;\ \pi;\ K;\ p\}$:

$$L(\xi) = P(x_{EMC}, x_{DCH}, x_{DIRC}; \xi) = P(x_{EMC}; \xi)P(x_{DCH}; \xi)P(x_{DIRC}; \xi) \ , \tag{4.5}$$

where x_{EMC}, x_{DCH} and x_{DIRC} represent vectors of discriminating variables from each subsystem. Weighting the individual likelihoods with *a priori* probabilities p_ξ, the likelihood fraction f_L is computed:

$$f_L = \frac{p_e L(e)}{p_e L(e) + p_\pi L(\pi) + p_K L(K) + p_p L(p)} \ . \tag{4.6}$$

Using $p_e : p_\pi : p_K : p_p = 1 : 5 : 1 : 0.1$, a track is selected as electron if it passes some preselection cuts and a given cut on f_L, which may vary between 0 and 1.

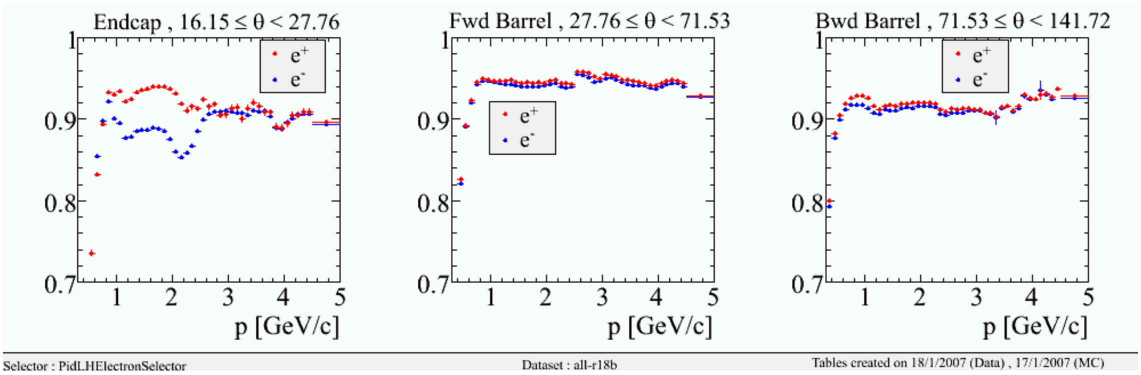

Figure 4.20: Performance of the `PIDLHElectrons` selector. The selection efficiency, as a function of momentum, in three different bins of the polar angle, is shown separately for e^- (blue dots) and e^+ (red).

Figure 4.20 shows the typical performance of the `PILHElectrons` selector. The selection efficiency is typically above 90% and there are no large charge asymmetries, excluding the forward region, severely affected by backgrounds.

Muons

The identification of muons relies mostly on the performance of the IFR. A set of simple *cut based* selectors has been developed for the selection of muon tracks at the beginning of the experiment. However, due to the non-optimal quantity of iron affecting the original design of the IFR and the fast degradation of the performance of RPCs, the development of more sophisticated algorithms proved to be necessary.

In our analysis, muons are selected by using the `NNLooseMuonSelection` selector, which is based on the use of the Neural Network (NN) technique. The variables used in the selection are (in the order as they appear on the input layer of the NN):

- $\Delta\lambda = \lambda_{exp} - \lambda_{meas}$: the difference between the expected and the measured number of interaction length traversed by the track in the muon hypothesis;
- $\chi^2_{mat} = \chi^2/d.o.f$ of the IFR hit strips in the cluster with respect to the track extrapolation;
- σ_m: the standard deviation of the average multiplicity of hit strips per layer;
- T_C: the continuity of the track in the IFR;

- E_{cal}: the energy deposited in the EMC;
- λ_{meas}: the number of interaction length traversed by the track;
- $\chi^2_{fit} = \chi^2/d.o.f$ of the IFR hit strips with respect to a third order polynomial fit of the cluster;
- $\bar{m}$: the average multiplicity of hit strips per layer.

The NN implemented uses one input layer accepting the 8 variables listed above, one hidden layer with 16 nodes and one output layer with one node. Due to the different performance of the chambers in the different sections of the IFR (old and new RPC's, LST's) and the decrease with time of RPC's' performance, the training sample for the Neural Network has been split into several subsamples.

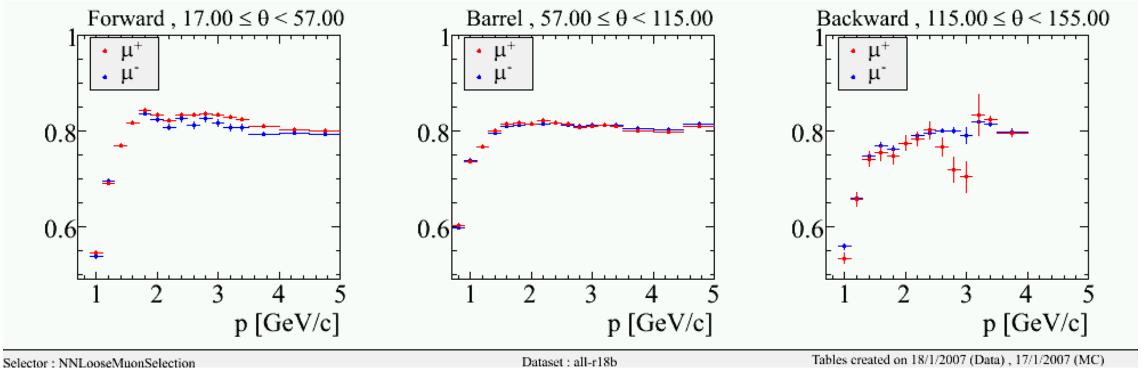

Figure 4.21: Performance of the `NNLooseMuonSelection`: the selection efficiency for separately μ^+ and μ^- as a function of momentum is shown in three different ranges of the polar angle.

Figures 4.21 and 4.22 show the efficiency and the pion mis-identification rate for the selector we use in our analysis, averaged over Run1-Run5 data-taking periods.

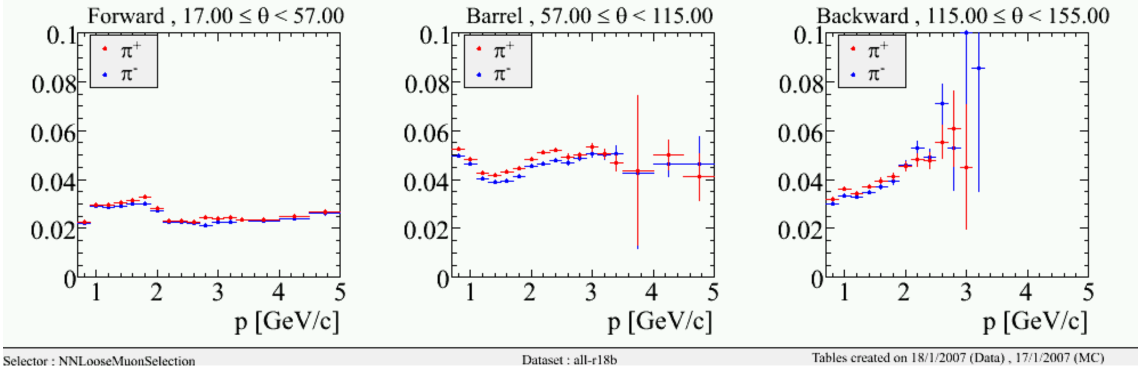

Figure 4.22: Performance of the `NNLooseMuonSelection`: the probability of π^+ and π^- to pass the selection as a function of momentum is shown in three different ranges of the polar angle.

Kaons

The selection of charged kaon tracks is one of the key issues of our analysis. Their signature in different detectors is complicated because they can decay or interact with the material of the detector. Furthermore, the hadronic interactions have different rates for the two charged modes.

About 20% of the kaons decay before they reach the DIRC, and they mostly decay to a final state where there is only one charged track, which may be not distinguishable from the original one.

We use the `LooseKaonMicroSelection` selector, which combines the dE/dx measurements from SVT and DCH and the information from the DIRC. Concerning the latter, every single hit is considered to compute a *global likelihood*, without fitting a single Čerenkov ring on a given pattern, as most selectors do.

The output for each sub-detector, expressed as a likelihood $L_x = L_{kaon;x}/(L_{kaon;x} + L_{pion;x})$ (only pions are considered as background and x = SVT, DCH or DIRC), and the track momentum are taken as inputs of a Neural Network using one 10-node hidden layer.

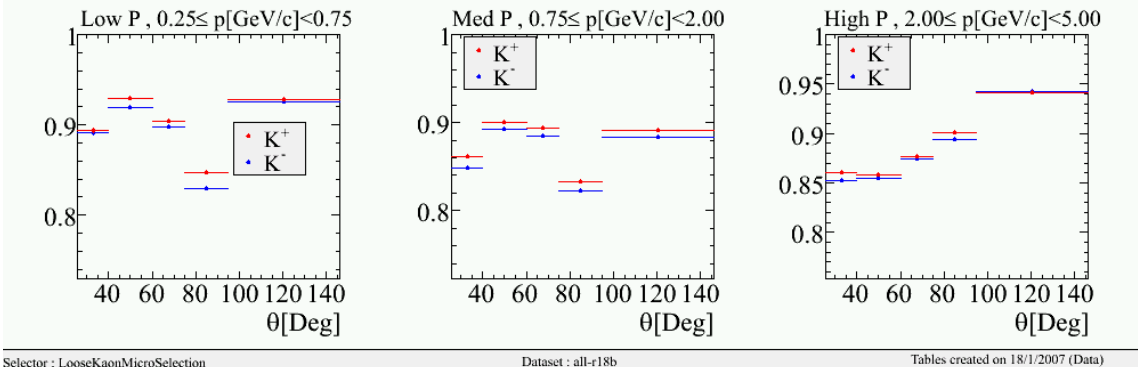

Figure 4.23: Performance of the `LooseKaonMicroSelection`: the selection efficiency for separately K^+ and K^- as a function of the polar angle is shown in three different ranges of momentum. Charge asymmetries can be clearly seen.

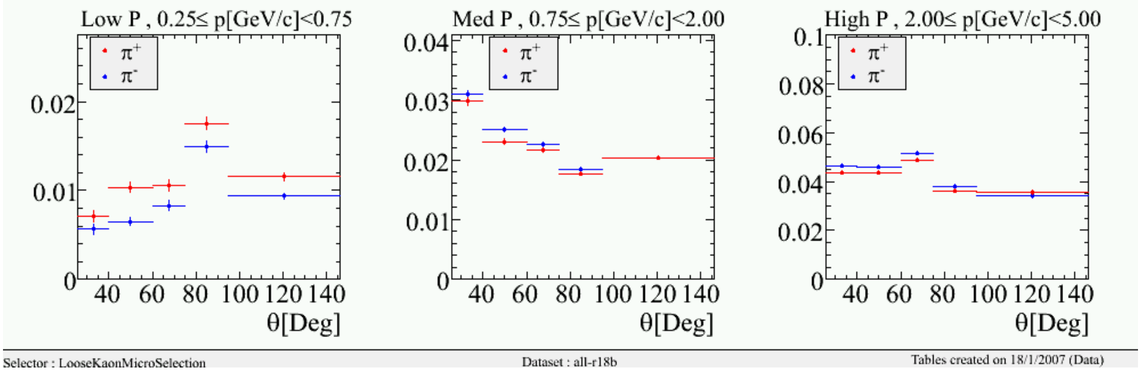

Figure 4.24: Performance of the `LooseKaonMicroSelection`: the probability of π^+ and π^- to pass the selection as a function of the polar angle is shown in three different ranges of momentum. Charge asymmetries can be clearly seen.

Figures 4.23 and 4.24 show respectively the selection efficiency and pion mis-identification probability for different ranges of the polar angle and momentum. It can be clearly seen that a pretty large charge asymmetry exists in both the efficiency and the pion-fake rate, arising mainly from the different cross sections for K^+ hadronic interactions in the detector material with respect to K^-.

Given that CP-violation in $B^0\overline{B}^0$ mixing is a tiny effect influencing the relative number of B^0B^0 and $\overline{B}^0\overline{B}^0$ events we need to control and reliably measure on data the detector related charge asymmetries.

4.2.9 Data taking performance

Besides the major problems on the IFR, the *BABAR* detector performed as expected, with data-taking efficiency close to 100%. After eight years of running, with PEP-II having reached a peak luminosity four times higher than design, only minor effects of degradation have shown up so far.

As two examples, we cite the SVT reconstruction efficiency for low momentum pions, which has decreased by a few percent due to the radiation damage on the sensors lying around the horizontal plane and the slight drop in the gain of DIRC photomultipliers due to some aging affecting the cathodes. The capability of the detector to achieve its physics goals remains basically unchanged for the last data-taking period, scheduled for 2008, when the total integrated luminosity should reach 750 fb^{-1}.

Some concerns arise from potential high background conditions which could be encountered when the accelerator reaches its ultimate configuration. This could cause the L1 trigger to reach the 5 kHz hardware limit; strategies are being developed in order to reduce the redundancy of the trigger design, causing negligible loss in the physics reach.

Chapter 5

Data sample and events preselection

5.1 Data processing in *BABAR*

The quality of data collected by the *BABAR* detector is checked online by the shifter on duty who discards the samples affected by sub-detectors bad performance or unacceptably high backgrounds.

The raw data undergo then the *Prompt Calibration* and *Event Reconstruction* stages. In the former all calibration parameters and alignments which can vary over the time are updated; this phase is done by SLAC's computing resources within a few hours from the data taking. In the latter, charged tracks and neutral particles are reconstructed from the single hits and energy deposits in each subdetector: this is performed at the dedicated processing farm in Padova, within the following 48 hours.

After the final validation, the data are subdivided into smaller samples (*skims*) which satisfy the needs of the main branches of physical analysis and are distributed over the computing facilities dedicated to data analysis.

Most of the work presented in this thesis has been done using the *Gridka* analysis farm, located in Karlsruhe, Germany.

5.2 Data and Monte Carlo samples

The current analysis is based on the data collected by *BABAR* during the data-taking periods Run1-Run5 (see 4.1.3 for details). Root-tuples have been produced over the `InclSemiLept` skim, which pre-selects events with at least one partially reconstructed $\overline{B}^0 \to D^{*+}\ell^-\bar{\nu}_\ell$ candidate. The full integrated luminosity of on-peak data used is equal to 348.1 fb^{-1}, equivalent to about 383 million $B\overline{B}$ pairs. Details on data samples are summarized in Table 5.1.

Table 5.1: Integrated luminosities of data samples

Data set	off-peak (fb^{-1})	on-peak (fb^{-1})	$N_{B\overline{B}}$ (10^6)
Run1	2.5	20.3	22.0
Run2	6.9	60.7	67.0
Run3	2.5	32.3	35.7
Run4	9.9	100.9	110.5
Run5	14.1	134.0	147.5
Total	35.9	348.1	382.7

This analysis has been set up using the generic $B\overline{B}$ Monte Carlo (MC) simulation available to the Collaboration. Again, simulated events are requested to pass the `InclSemiLept` skim criteria; the number of $B\overline{B}$ events is about 3 times larger than the data. Details can be found in Table 5.2.

No requests of special MC samples have been submitted for our analysis; control samples have been produced either by generating special *Toy Monte Carlo* samples or by reweighting the generic sample.

Table 5.2: Number of Generic Monte Carlo generated events

Data set	$B^0\overline{B}^0$ (10^6)	B^+B^-(10^6)
Run1	35.8	35.6
Run2	103.5	102.9
Run3	50.6	46.1
Run4	167.1	168.3
Run5	166.4	168.8
Total	523.4	521.7

5.3 Selection of partially reconstructed $\overline{B}^0 \to D^{*-}\ell^+\nu_\ell$ events

We reconstruct the $\overline{B}^0 \to D^{*+}\ell^-\nu_\ell$ (charge conjugation is always implied in this section) decay using only the information coming from the ℓ^- and the charged pion originating from the $D^{*+} \to D^0\pi^+$ decay (we will refer to the charged pion as the π_{soft}). We recall that the $\overline{B}^0$ which is partially reconstructed will be called B_{rec} in the following.

The momenta of the two particles are requested to satisfy the following cuts: $0.06 < |\vec{p}_{\pi_{soft}}| < 0.20$ GeV/c and $1.40 < |\vec{p}_\ell| < 2.30$ GeV/c. We veto, based on dE/dx measured in the SVT, electron tracks which could fake a π_{soft}, while for the two species of leptons we require them to pass the `PIDLHElectrons` and `muNNLoose` selectors, which have been briefly discussed in section 4.2.8.

The vertex of the (ℓ, π_{soft}) pair is computed constraining the x-y coordinates to the *beamspot* position (the width of the *beamspot* is enlarged to 50 μm in the vertical (y) direction, to account for the B-motion in the transverse plane). The momenta of the two particles and their probability to originate from a common vertex are combined into a Likelihood Ratio variable χ, which can vary from 0 (background like) and 1 (signal like), see figure 5.1. Events with $\chi < 0.3$ are rejected. Figure 5.2 shows the plot of the difference between the measured and the true z coordinate for B_{rec} mesons and the relative pull distribution at the end of our selection.

The size and purity of our $B^0\overline{B}^0$ enriched sample can be seen by using the m_ν^2 discriminating variable (figure 2.4), as anticipated in section 2.5.

5.4 Selection of charged kaons

The sign of a charged kaon identified as a decay product of the other B meson (the B_{tag}) is used to determine the flavor of the B_{tag} itself. The z coordinate of the B_{tag} decay vertex is computed by extrapolating the K track to the x, y coordinates of the *beamspot*. The extrapolation is performed assuming that the particle which gave that track has the pion mass; this causes a dependence of some of the parameters entering the resolution model on the kaon momentum, as discussed in chapter 7. In figure 5.3 we show the dependence of the width of the narrow component in the resolution function for B_{tag} signal events for genuine $K^\pm$ and pions faking kaons.

Figure 5.4 shows the distribution of the difference of the measured z coordinate and the true one along with its pull for B_{tag} kaons. The RMS of the latter deviates significantly from

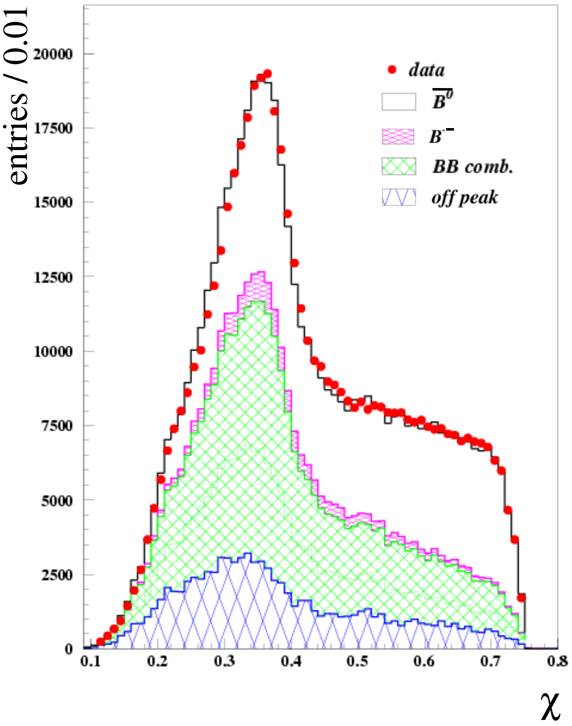

Figure 5.1: Likelihood Ratio variable χ for data (red dots), signal $B^0\overline{B}^0$ Monte Carlo (white histogram), peaking B^+B^- background (purple hatched histogram), $B\overline{B}$ combinatorial (green hatched histogram) and rescaled off-peak data (blue hatched histogram).

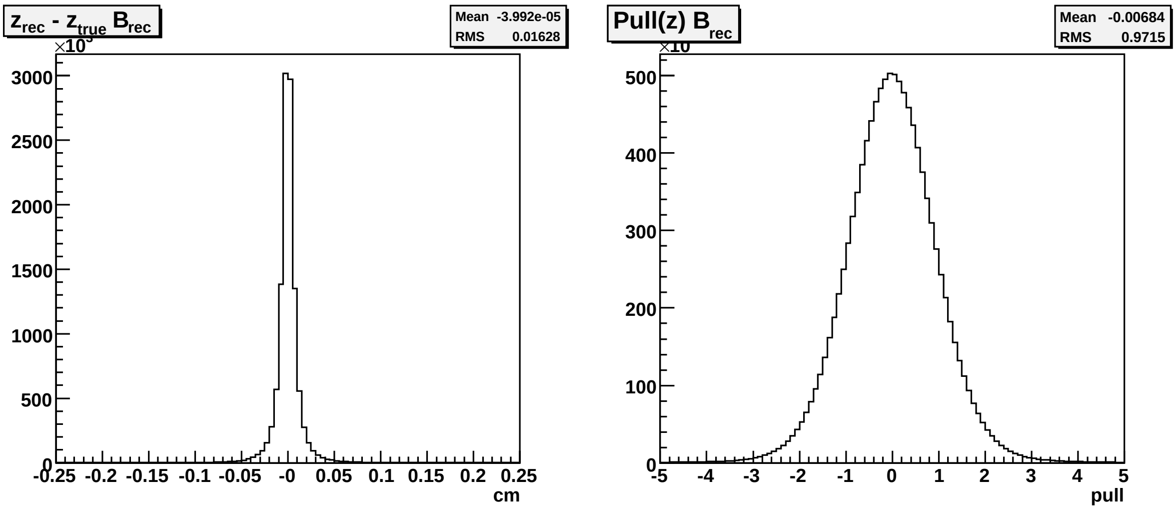

Figure 5.2: Measured z - true z (left plot) and pull (right) distributions for B_{rec} mesons.

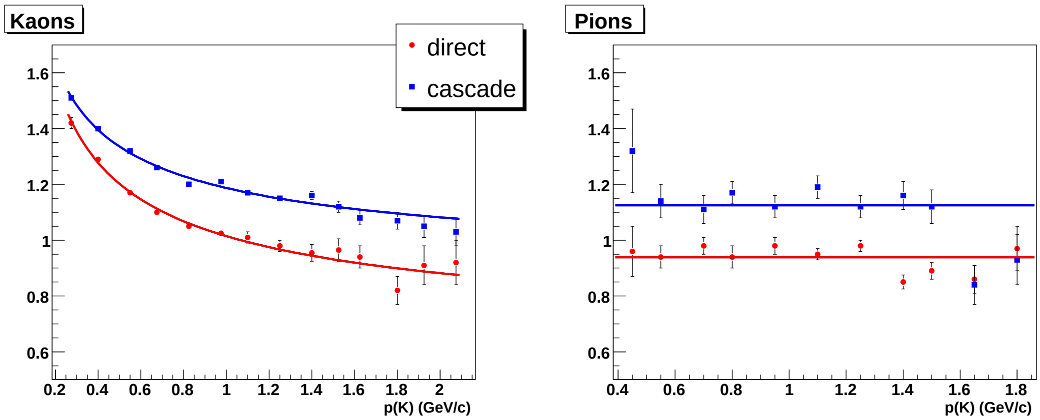

Figure 5.3: Pull of the narrow component in the resolution model for signal B_{tag} events for true kaons (left) and mid-identified pions (right). Direct decays (red circles) are shown separately from cascades (blue squares).

1 because of the contribution of charmed mesons, whose finite lifetime affects the measurement of the z coordinate.

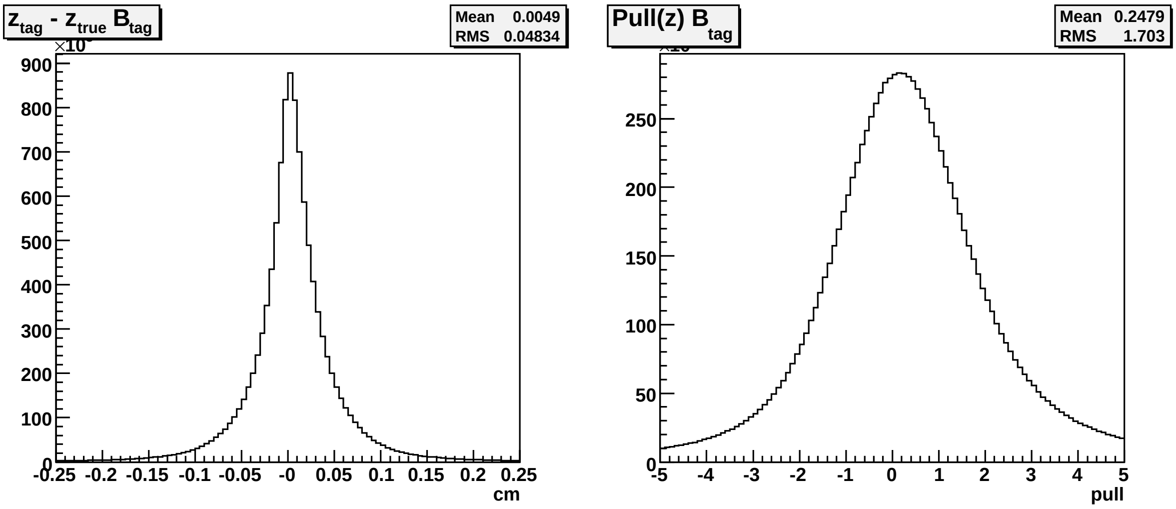

Figure 5.4: Measured z - true z (left plot) and pull (right) distributions for B_{tag} mesons.

The separation between the two B vertices Δz is defined as $\Delta z = z(B_{rec}) - z(B_{tag})$ and its uncertainty $\sigma(\Delta z)$ is computed by propagating the uncertainties on the determinations of the two vertices.

$K^{\pm}$ tracks are requested to pass the `LooseKaonMicro` PID selector (see 4.2.8). Furthermore, we request $|\Delta z| < 0.3$ cm and $\sigma(\Delta z) < 0.05$ cm.

The proper time difference Δt between the decays of B_{rec} and B_{tag} is computed neglecting the motion of the B mesons along the plane perpendicular to the beam axis (*boost approximation*). Thus it is given by:

$$\Delta t = \Delta z / \beta\gamma c\,, \tag{5.1}$$

with $\beta\gamma \simeq 0.56$ being the experimental boost of PEP-II and c is the speed of light.

5.5 Sample Composition

The selected data originate from several different sources, listed below.

1. $\overline{B}^0 \to D^{*+}\ell^-\bar{\nu}_\ell$ (direct) decays;
2. $\overline{B}^0 \to D^{**+}\ell^-\bar{\nu}_\ell,\ \ D^{**+} \to D^{*+}X$ (D^{**}) decays ;
3. $\overline{B}^0 \to D^{*+}\tau^-\bar{\nu}_\tau,\ \ \tau^- \to \ell^-\bar{\nu}_\ell\nu_\tau$ (τ cascade) decays;
4. $\overline{B}^0 \to D^{*+}D_s^-X,\ \ D_s^- \to \ell^-\bar{\nu}_\ell X'$ (D_s cascade) decays;
5. $\overline{B}^0 \to D^{*+}D^-X,\ \ D^- \to \ell^-\bar{\nu}_\ell X'$ (CP-eigenstate) decays;
6. $\overline{B}^0 \to D^{*+}h^-,\ \ h^- \to \ell^-$ (fake hadron), where a pion or a kaon are wrongly identified as a lepton, most frequently a muon;
7. $B^- \to D^{**0}\ell^-\bar{\nu}_\ell,\ \ D^{**0} \to D^{*+}X$ (D^{**}) decays;
8. $\overline{B}^0$ combinatorial, where a lepton is combined randomly with a low-momentum track in a $e^+e^- \to B^0\overline{B}^0$ event;
9. B^- combinatorial;
10. continuum events, where the lepton and the soft pion candidates are produced in a non-$B\overline{B}$ event.

It must be noted that events from different sources might be distinguished by either their different kinematic properties or by their different dependence on Δt. All the $\overline{B}^0$ states listed above share in fact approximately the same time distributions, except the CP-eigenstates; similar considerations hold for all B^- states. The situation for continuum events is more entangled (as four light quarks, leptons, and $\gamma\gamma$ events all contribute), but we take all their properties from rescaled off-peak events.

To determine the sample composition at this stage of the analysis, we rely on the kinematical properties of the decays, and we group events accordingly.

We first note that all the events in the list above, excepted the last three, exhibit a peak near to zero in the m_ν^2 distribution (defined as above). This is obvious for direct decays (item 1), where m_ν^2 represents in fact the mass of the unobserved neutrino, and for fake hadrons (item 6), where no further particles are produced. It is also true for the other events (items 2, 3, 4, 5 and 7), although, due to the production of other particles in addition to the leptons and the D^{*+}, the peak of the distribution is displaced towards positive values. In fact, decays from sources 2 and 7 are indistinguishable on a kinematical basis, whereas the peak in m_ν^2 is displaced by $\sim +0.5$ Gev$^2/c^4$ with respect to the primary decays. Combinatorial (8 and 9) events do not present any peak at all.

We exploit these differences to compute the individual contributions to our data set. We group events in the list above in six basic classes, according to the shape of m_ν^2:

- D^*, corresponding to category (1) above;
- D^{**}, corresponding to the sum of (2)+(7);
- CPeigenstates corresponding to item (5);
- $Other - P$eaking, corresponding to the sum of (3)+(4)+(6);
- $B\overline{B} - c$ombinatorial, (9)+(8);
- *continuum.*

We fit the m_ν^2 data distribution with the sum of the sources defined above, with shapes assumed from the simulation. In the fit we determine the relative amounts of D^*, D^{**}, and $B\overline{B} - c$, while we get the shape and the fraction of *continuum* from the rescaled off-peak events. The contributions from $Other - P$ and CPe are fixed to the simulation. The relative amounts of $\overline{B}^0$ and B^- in the D^{**} and in the $B\overline{B} - c$, at this stage of the analysis, are obtained from the Monte Carlo.

Before fitting, we tune the simulation to the data, correcting for some slight discrepancies in the lepton (p_ℓ) and soft pion ($p_{\pi_{soft}}$) momentum spectra of combinatorial events. For this purpose, we use events in the side band region $-10 < m_\nu^2 < -4$ GeV$^2/c^4$, where very few peaking events are left (see plots in the next pages). We proceed as follows:

- we normalize the simulation to the data using luminosity information ($w_{\mathcal{L}}$);
- we then compare the simulated $p_{\pi_{soft}}$ spectrum to the continuum-subtracted data. We interpolate the ratio between the data and the Monte Carlo with a second order polynomial, $w_{p^*}(p_{\pi_{soft}})$. We determine two separate functions, depending on whether the pion has the same electric-charge as the tag-kaon or the opposite charge;
- subsequently we analyze again the same data, weighting each simulated event with the function obtained above. We compare now the p_ℓ spectra, and we determine a second function $w_\ell(p_\ell)$. We split the data into four sets, separating e from μ and equal from opposite charges;
- finally, we perform the fit to m_ν^2 in the full range ($[-10, +2]$ GeV$^2/c^4$) to compute the sample composition. In the fit, each event from $B\overline{B} - c$ decays has a weight equal to the product: $w_{\mathcal{L}} \times w_{p^*}(p_{\pi_{soft}}) \times w_\ell(p_\ell)$, while peaking events and off-peak events are weighted by the relative luminosities only. At this last stage, we perform in fact eight different fits, splitting the data according to the lepton type and the charge correlations: e^+K^+, e^-K^+, e^+K^-, e^-K^- and μ^+K^+, μ^-K^+, μ^+K^-, μ^-K^-.

As stated above, the fits determine the amount of D^*, D^{**} and $B\overline{B} - c$ in each data set, by computing the scaling factors which must be applied to events from those sources to obtain the best matching. By definition, the scaling factor for the combinatorial events is very well consistent with unity, while it is about 0.95 for D^* and 1.10 for D^{**}. In the full m_ν^2 range, D^* account for about 25% of the sample, D^{**} for about 4%, continuum for about 10% , and $B\overline{B} - c$ for about 55%. Only few per mille is due to other sources. Figures 5.5 and 5.6 show a comparison between the data and the best fit for each of the eight data sets considered.

Sample	Function	Sample	Function
$f_{D^{**}}(x)$	$e^{\mathcal{P}_5(x)}$	$f_{cont.}(x)$	$\mathcal{P}_0(x) + \mathcal{G}(x)$
$f_{Other-P}(x)$	$e^{\mathcal{P}_3(x)}$	$f_{B\overline{B}-c}(x)$	$\mathcal{P}_1(x) + \mathcal{G}(x) + \mathcal{G}(x)$
$f_{CPe}(x)$	$\mathcal{G}(x)$	$f_{D^*}(x)$	$1 - (f_{D^{**}} + f_{Other-P} + f_{CPe} + f_{cont.} + f_{B\overline{B}-c})(x)$

Table 5.3: Parametric functions describing the fraction of events from each source considered. The symbol $\mathcal{P}_n$ indicates a polynomial of degree n, $\mathcal{G}$ is a Gauss function. The variable x is in fact m_ν^2.

We finally determine the fraction of events from each of the sources defined above as a function of m_ν^2. We interpolate the corresponding distributions with some ad-hoc parametric function, listed in table 5.3. These functions are also displayed in figures 5.7-5.14, for $B^0\overline{B}^0$ peaking (top left plot of each figure), B^+B^- peaking (center left), CP-eigenstates (bottom left), continuum (top right), $B^0\overline{B}^0$ combinatorial (center right) and the total combinatorial (bottom right).

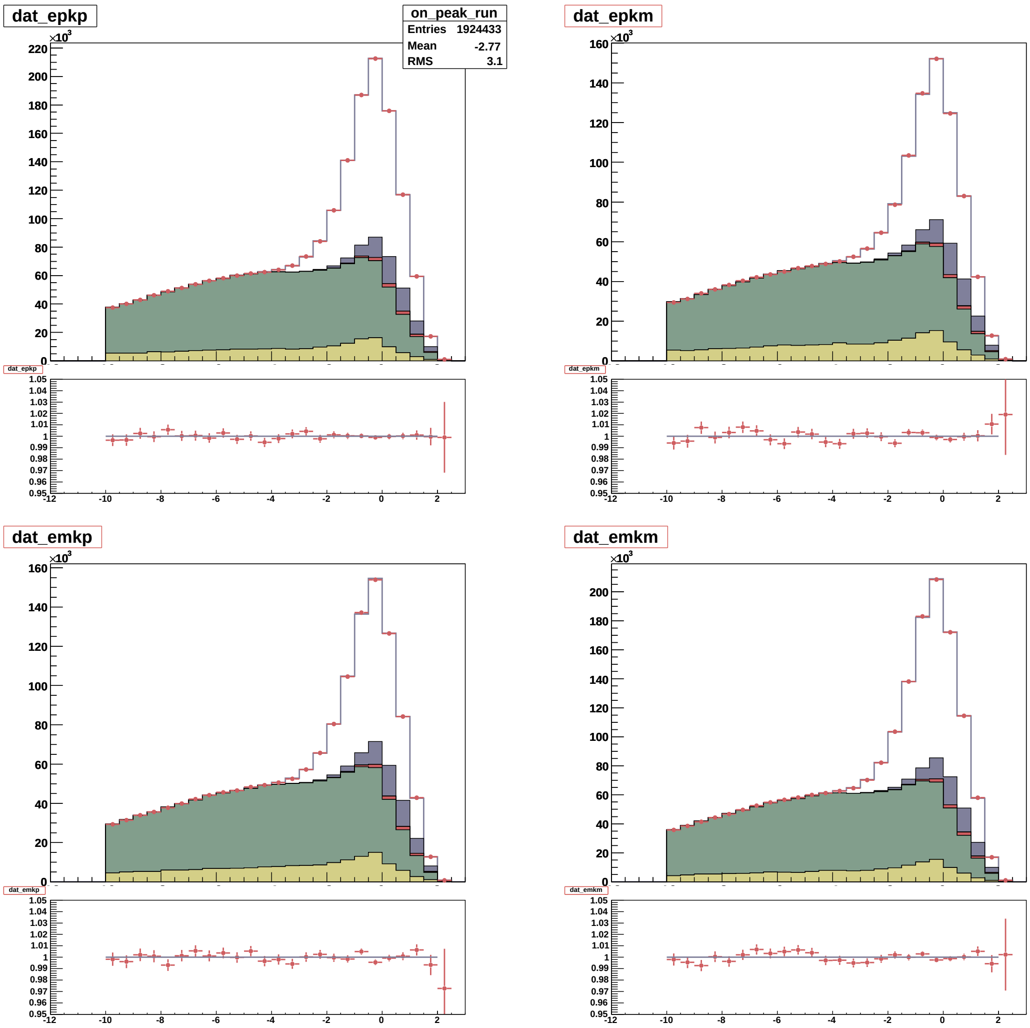

Figure 5.5: m_ν^2 distributions for data (points) and fit results (histogram), electron sample. In each plot we overlay, bottom to top, the contributions from: continuum, combinatoric, other peaking, D**, and D*. Below each plot, we show also the ratio between the data and the fit result. Top left: e^+K^+; top right: e^+K^-; bottom left: e^-K^+; bottom right: e^-K^-.

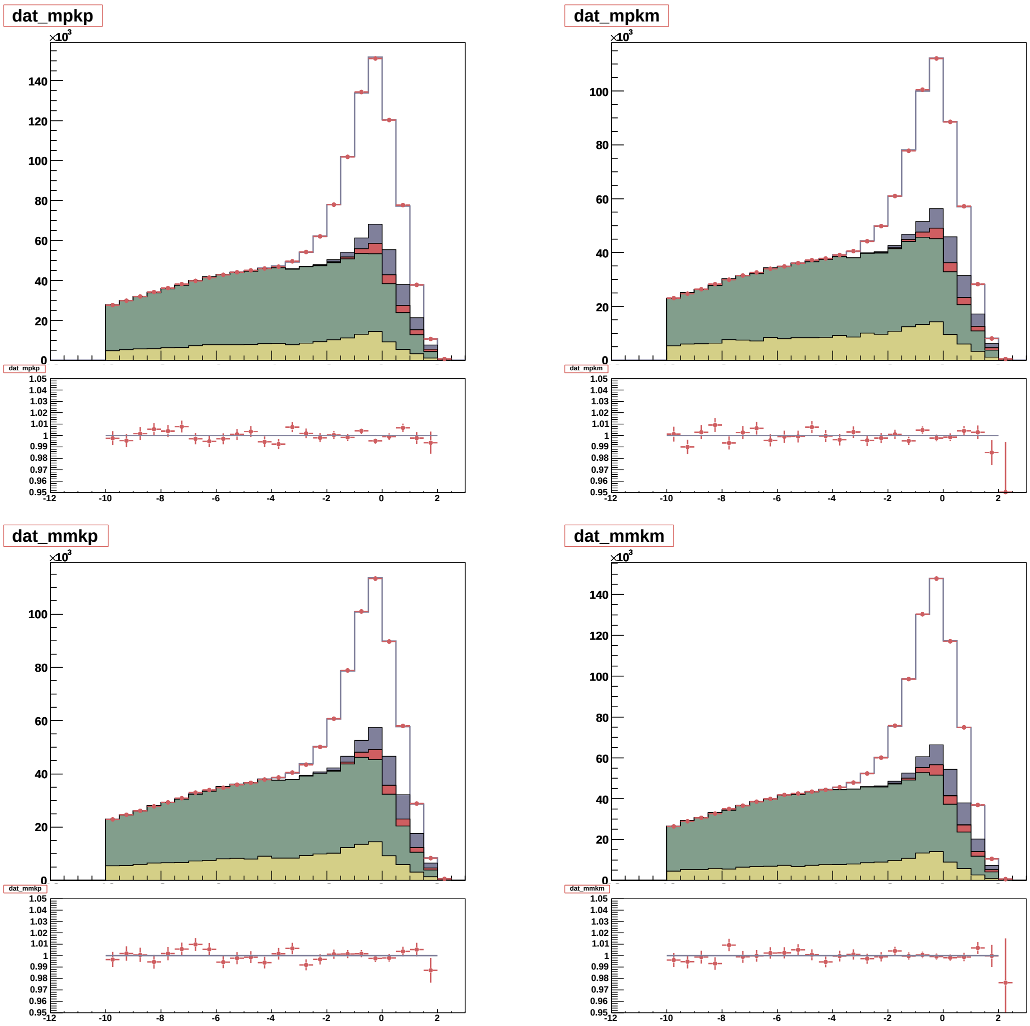

Figure 5.6: m_ν^2 distributions for data (points) and fit results (histogram), muon sample. In each plot we overlay, bottom to top, the contributions from: continuum, combinatoric, other peaking, D**, and D*. Below each plot, we show also the ratio between the data and the fit result. Top left: μ^+K^+; top right: μ^+K^-; bottom left: μ^-K^+; bottom right: μ^-K^-.

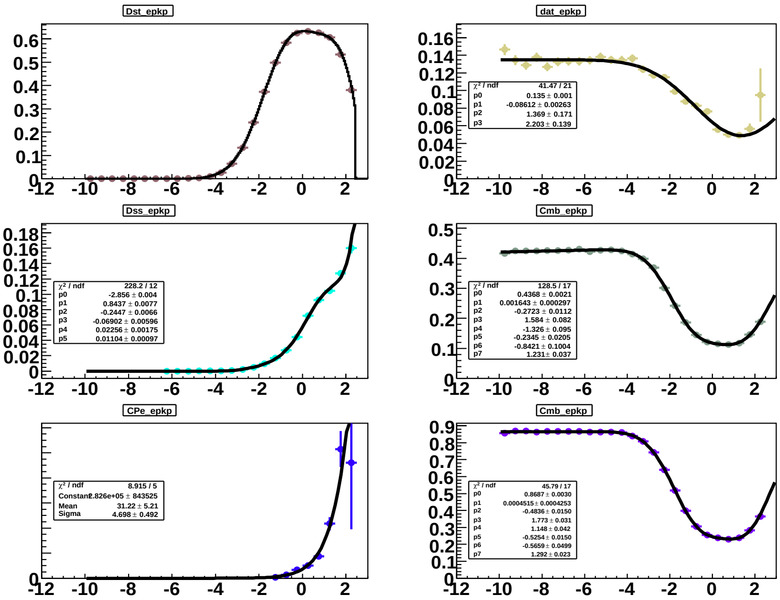

Figure 5.7: Sample composition, e^+K^+. We show the fraction of peaking $B^0\overline{B}^0$ (top left plot), peaking B^+B^- (center left), CP-eigenstates (bottom left), continuum (top right), $B^0\overline{B}^0$ combinatorial (center right) and the total combinatorial (bottom right) as a function of m_ν^2.

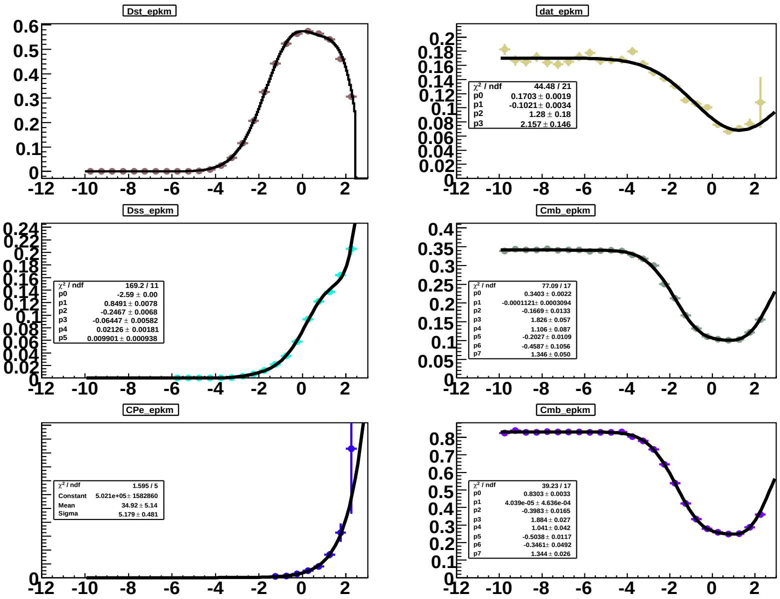

Figure 5.8: Sample composition, e^+K^-. We show the fraction of peaking $B^0\overline{B}^0$ (top left plot), peaking B^+B^- (center left), CP-eigenstates (bottom left), continuum (top right), $B^0\overline{B}^0$ combinatorial (center right) and the total combinatorial (bottom right) as a function of m_ν^2.

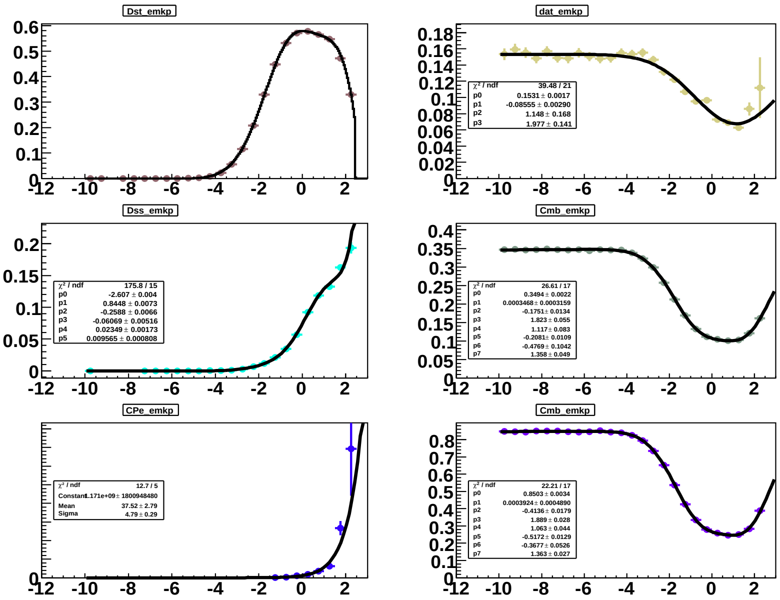

Figure 5.9: Sample composition, e^-K^+. We show the fraction of peaking $B^0\overline{B}^0$ (top left plot), peaking B^+B^- (center left), CP-eigenstates (bottom left), continuum (top right), $B^0\overline{B}^0$ combinatorial (center right) and the total combinatorial (bottom right) as a function of m_ν^2.

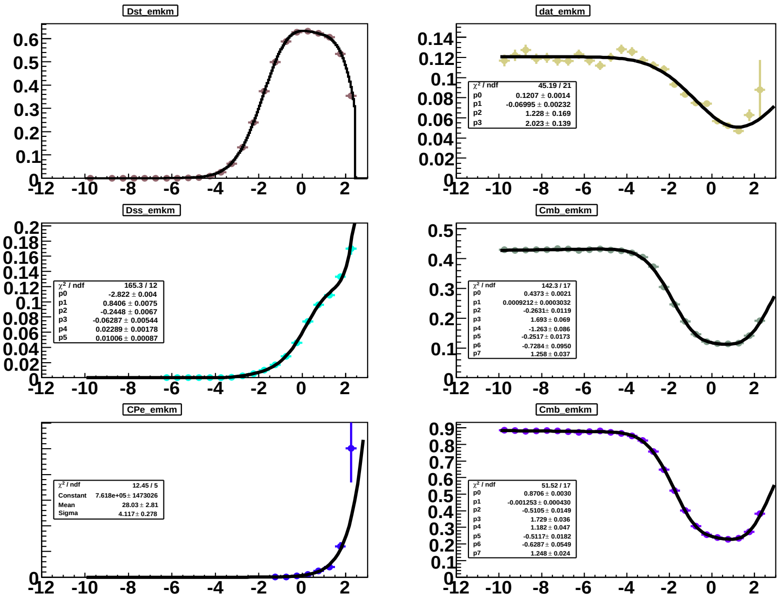

Figure 5.10: Sample composition, e^-K^-. We show the fraction of peaking $B^0\overline{B}^0$ (top left plot), peaking B^+B^- (center left), CP-eigenstates (bottom left), continuum (top right), $B^0\overline{B}^0$ combinatorial (center right) and the total combinatorial (bottom right) as a function of m_ν^2.

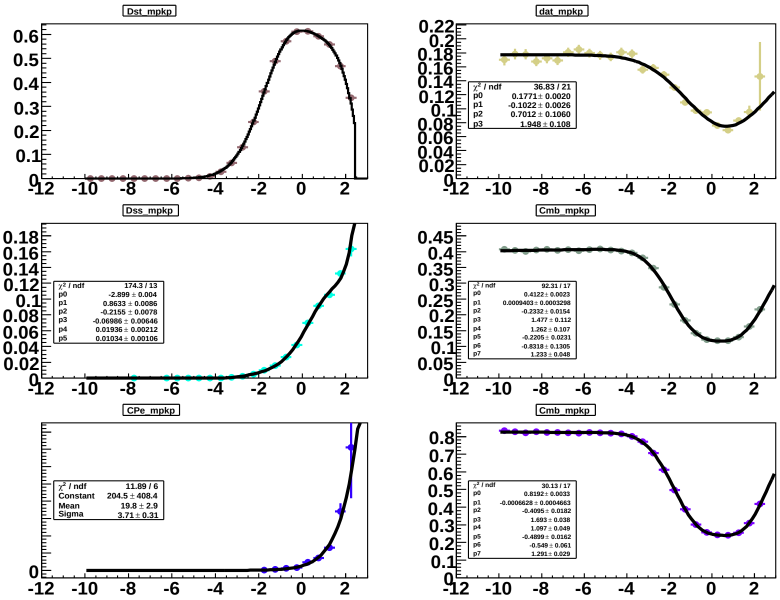

Figure 5.11: Sample composition, μ^+K^+. We show the fraction of peaking $B^0\overline{B}^0$ (top left plot), peaking B^+B^- (center left), CP-eigenstates (bottom left), continuum (top right), $B^0\overline{B}^0$ combinatorial (center right) and the total combinatorial (bottom right) as a function of m_ν^2.

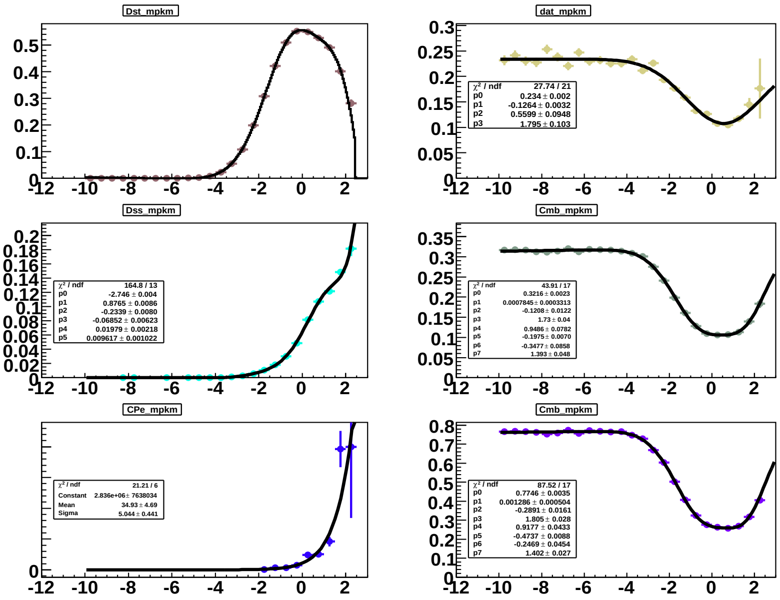

Figure 5.12: Sample composition, μ^+K^-. We show the fraction of peaking $B^0\overline{B}^0$ (top left plot), peaking B^+B^- (center left), CP-eigenstates (bottom left), continuum (top right), $B^0\overline{B}^0$ combinatorial (center right) and the total combinatorial (bottom right) as a function of m_ν^2.

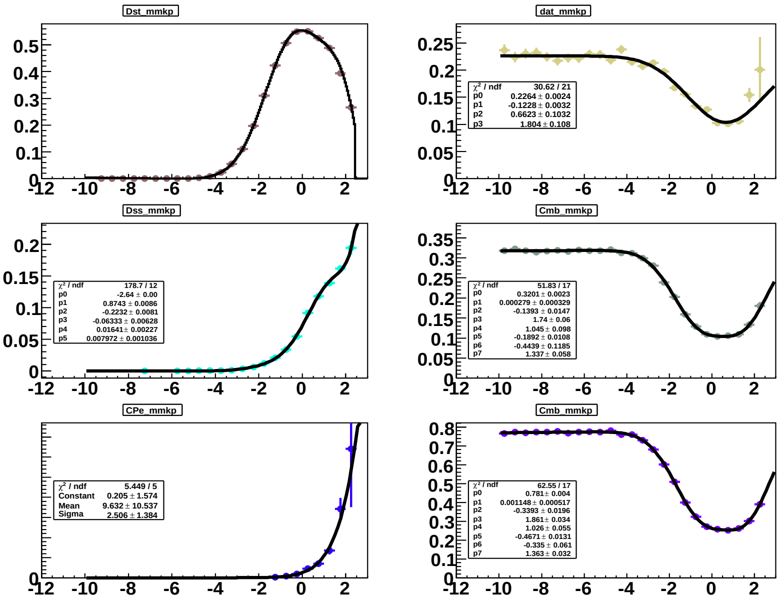

Figure 5.13: Sample composition, $\mu^- K^+$. We show the fraction of peaking $B^0\overline{B}^0$ (top left plot), peaking B^+B^- (center left), CP-eigenstates (bottom left), continuum (top right), $B^0\overline{B}^0$ combinatorial (center right) and the total combinatorial (bottom right) as a function of m_ν^2.

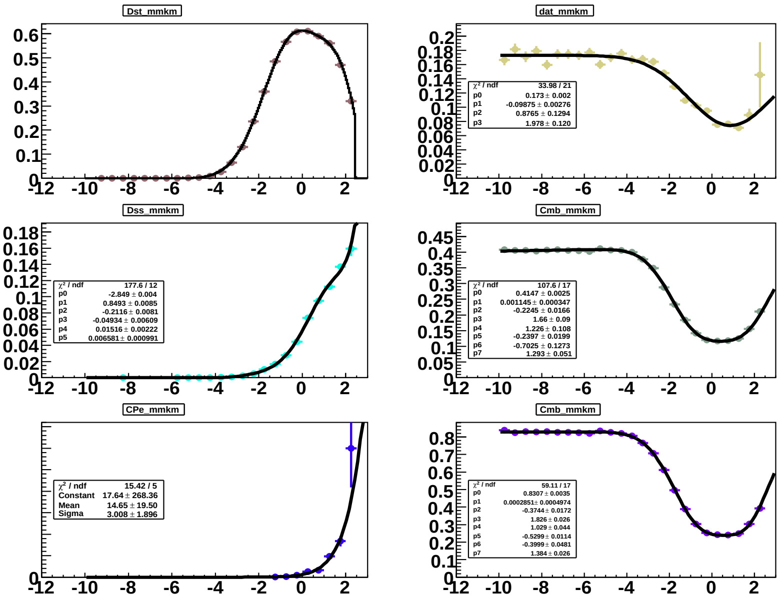

Figure 5.14: Sample composition, $\mu^- K^-$. We show the fraction of peaking $B^0\overline{B}^0$ (top left plot), peaking B^+B^- (center left), CP-eigenstates (bottom left), continuum (top right), $B^0\overline{B}^0$ combinatorial (center right) and the total combinatorial (bottom right) as a function of m_ν^2.

Chapter 6

Measurement technique and charge asymmetries

In this chapter, we will discuss in detail the main physical assumption we make to measure simultaneously $|q/p|$ and the detector related charge asymmetries, without relying on the predictions of the Monte Carlo. After the introduction on the analysis technique (sections 6.1 and 6.2), we will discuss the crucial topic of charge asymmetries in the detection and identification of charged particles (6.3) and present the results we obtained in the feasibility study of this analysis. Finally, in section 6.4 we will show a study (aside from the main analysis stream) on the reduction of proton contamination in our kaon sample, which constitutes a potential source of systematic error in our analysis.

6.1 Analysis Method

In case of CP Violation in $B^0\overline{B}^0$ Mixing, the probability of oscillation of a B^0 state into a $\overline{B}^0$ is different from the probability of the inverse process. Therefore the number of B^0B^0 decays, integrated over the decay times, is different from the number of $\overline{B}^0\overline{B}^0$ events.

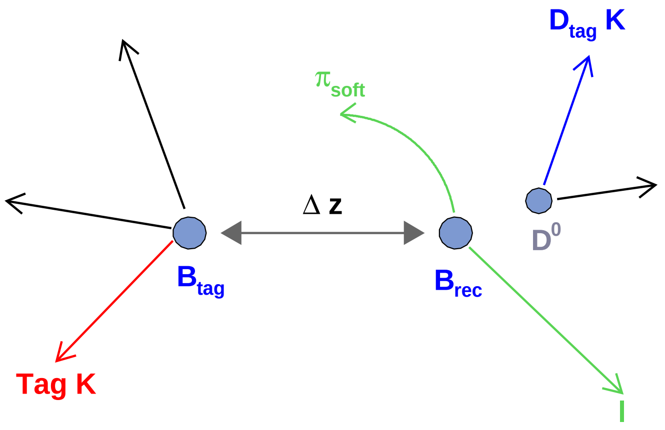

Figure 6.1: Schematic drawing of a possible signal event

Figure 6.1 shows a schematic picture of a possible signal event. We flag as B_{rec} the B-meson partially reconstructed by using only the $(\pi_{soft},\, \ell)$ pair.

Charged kaons may originate from the decay of the unreconstructed B_{tag} and are used to tag its flavor; we will call them B_{tag} *kaons*. Kaons could also come from the decay of the D^0 on the B_{rec} side (D_{tag} *kaons*); most of them have the same charge of the lepton coming from B_{rec}. The small fraction of D_{tag} kaons having opposite charge with respect to the lepton originate from (doubly) Cabibbo Suppressed decays ($D^0 \to K^+K^-, K^+\pi^-, ...$), mistags ($D^0 \to K^-\pi^+X, \pi^+ \to$ fake K^+).

Given the difference between D^0 and B^0 lifetimes and the fact that the B_{tag} decay vertex is computed by using only the K track, D_{tag} and B_{tag} kaons exhibit different Δz distributions, the former being much narrower than the latter (see figure 6.2).

There is then (at least) another difference between the two samples. A D_{tag} kaon is emitted preferentially in the direction opposite to the lepton, whereas a B_{tag} kaon is emitted randomly. Therefore we can separate the two event sets from the different distributions of $\cos(\theta_{K\ell})$, where $\theta_{K\ell}$ is the angle between the lepton and the charged kaon.

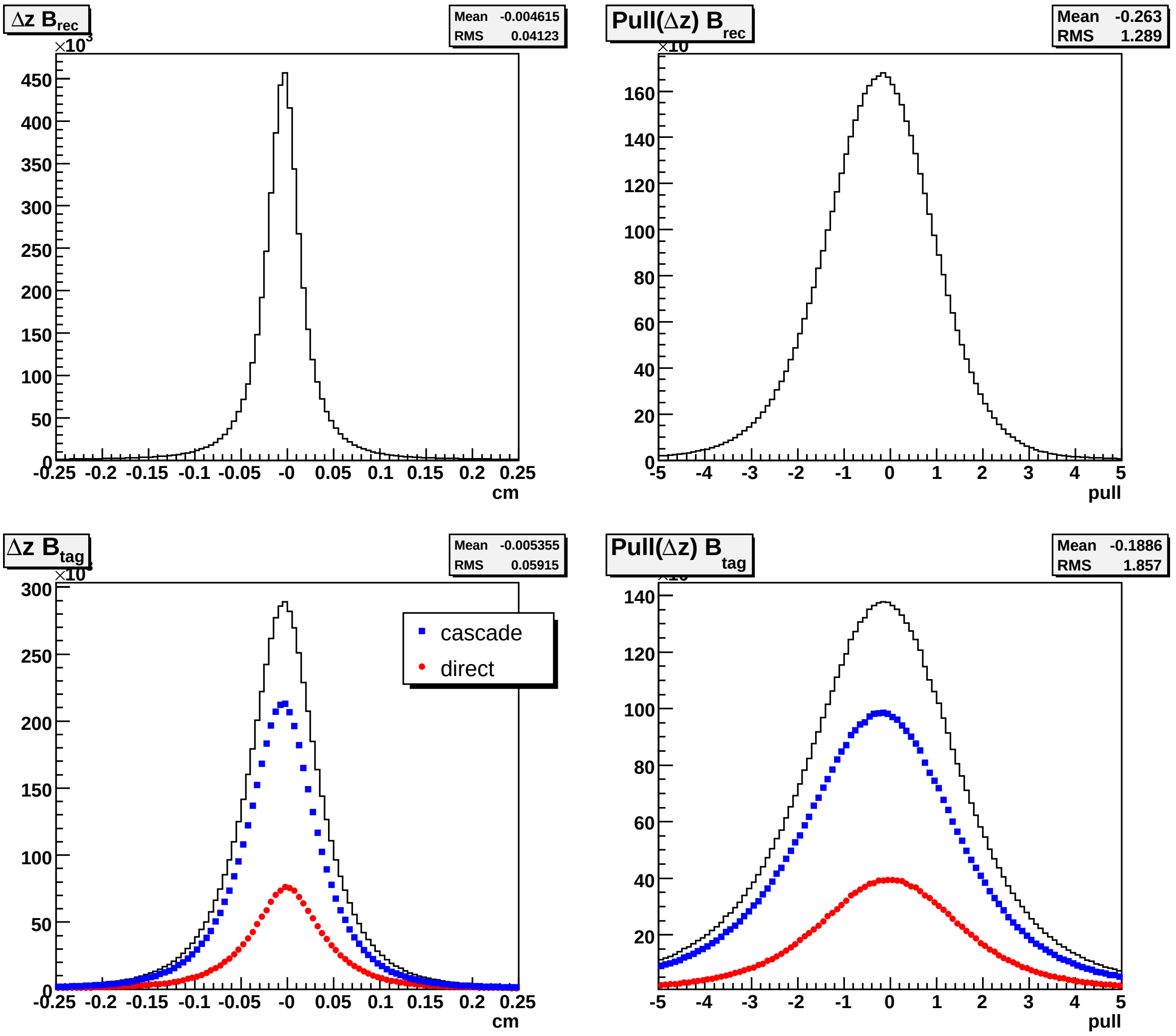

Figure 6.2: Δz distributions (left plots) and relative pull (right) for D_{tag} (top) and B_{tag} (bottom) events. In the computation of D_{tag} pull the true value of Δz is 0 by definition, since the kaon and the ℓ, π_{soft} pair originate from the same B meson. For the B_{tag} events, we show the contributions of direct $b \to K$ decays (red circles) and of the cascade $b \to c \to K$ decays (blue squares).

Under the hypothesis that CP-violation in D^0 decays is negligible, we use the D_{tag} K sample to measure directly on data the charge asymmetries induced by event reconstruction and particle identification, which give a different probability of reconstructing a B^0B^0 event rather than a $\overline{B}^0\overline{B}^0$ one.

Basically, we compare the asymmetry in the yield of "mixed" ℓ^+K^+ events to ℓ^-K^- events in the B_{tag} and in the D_{tag} sample. The observed asymmetries can be expressed in terms of $\mathcal{A}_{SL}$ and of the detector related effects according to the relations:

$$
\begin{aligned}
A(B_{tag}) &\simeq A_{rec} + A_{tag} + \mathcal{A}_{SL} && (6.1)\\
A(D_{tag}) &\simeq A_{rec} + A_{tag} + \chi_d \mathcal{A}_{SL}, && (6.2)
\end{aligned}
$$

where we neglect mistags and all the terms containing a product of asymmetries. A_{rec} is the asymmetry induced by event reconstruction, A_{tag} is the asymmetry introduced by charged kaon tagging (see also details in section 7.1), and χ_d is the integrated mixing probability. If the experimental asymmetries are the same in the B_{tag} and in the D_{tag} samples (this hypothesis is inspected in detail as explained in section 6.3), we can invert equations 6.1, 6.2 and solve for $\mathcal{A}_{SL}$.

In practice, B_{tag} and D_{tag} events can be separated only on a statistical basis, exploiting differences in proper time distribution and in other kinematical variables. For this reason, we determine $\mathcal{A}_{SL}$ with a fit to several experimental distributions sensitive to differences between B_{tag} and D_{tag} events. The fit functions provide a precise analytical description of our data, including mistags and higher order terms neglected in the formulas above, which are introduced in this section only for illustration. In addition to the events where the lepton and the kaon have the same electric charge ("mixed events"), we fit also opposite charge ("unmixed") events, $\ell^\pm K^\mp$. We use this sample mainly to measure mistags, but it also provides additional constraints on the detector related asymmetries. In particular, its use permits to disentangle A_{tag} from A_{rec}.

We describe briefly in the next section the variables that we use in our fit, while the next section of this chapter is reserved for a discussion of detector related asymmetries. A detailed description of the pdf's used to characterize the signal and the backgrounds is reported in the next chapter.

6.2 Fitting technique

The main physics parameters, along with the ones related to detector response and resolution are fitted simultaneously in a binned Maximum Likelihood fit on the variables Δt, $\sigma(\Delta t)$. In the fit, we account explicitly for the dependence of Δt and $\sigma(\Delta t)$ on the kaon momentum $|\vec{p}_K|$.

We use 100 bins for Δt, 25 bins for $\sigma(\Delta t)$ and 5 bins for $|\vec{p}_K|$. The Likelihood value is computed at the center of each bin. Several constraints (e.g. that the fraction of mixed events should be equal to $\chi_d^2/[2(1+\chi_d^2)]$, where $\chi_d = \Delta m_d \tau_{B^0}$) are applied to the Likelihood; this is equivalent to the use of an Extended Maximum Likelihood formalism.

The fractions of $B^0\overline{B}^0$ and B^+B^- peaking and combinatorial events, of CP-eigenstates and continuum are determined from an external fit to the m_ν^2 distributions, as shown in section 5.5.

The fraction of D_{tag} kaons is extracted by exploiting their correlation with the B_{rec} side ℓ flight direction. Figure 6.3 shows the cosine of the angle between the candidate K and the ℓ ($\cos(\theta_{K\ell})$) for signal and background B_{tag} and D_{tag} events.

As the kaon and the lepton originate from different B-mesons in B_{tag} events, their flight directions are un-correlated and thus the $\cos(\theta_{K\ell})$ distributions are roughly constant.

On the other hand, for D_{tag} events, K and ℓ tracks originate from the decay of the same B meson, which has a very little momentum in the $\Upsilon(4S)$ rest frame. The kinematics of the $B^0 \to D^{*-}\ell^+\nu$, $D^{*-} \to \bar{D}^0\pi^-_{soft}$, $\bar{D}^0 \to K^+X$ decay chain is such that the angle between the kaon and the lepton is preferentially large. Figure 6.3 shows that $\cos(\theta_{K\ell})$ peaks towards -1 for both signal and background events and that there is a very small dependence on the value of m_ν^2.

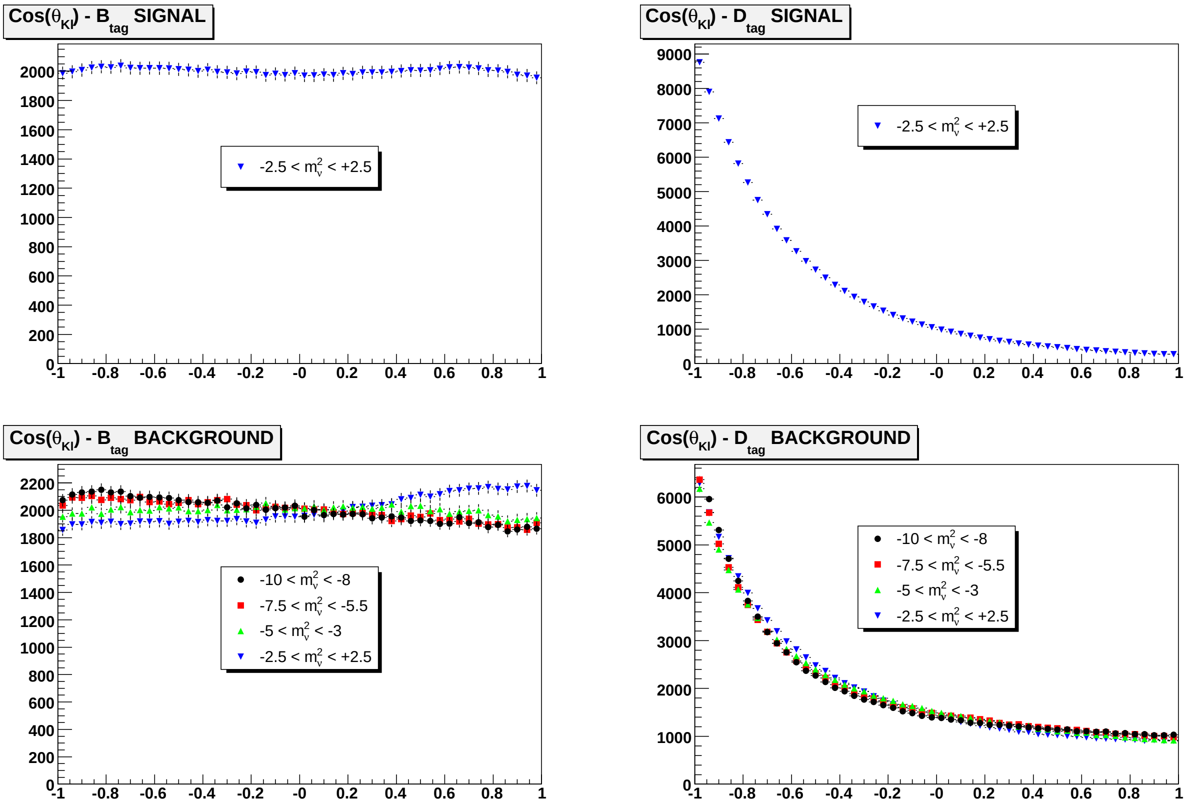

Figure 6.3: $\cos(\theta_{K\ell})$ for B_{tag} (left plots) and D_{tag} (right) events. Top plots show the distributions for events where the (ℓ, π_{soft}) pair is a signal one, while bottom plots show $B^0\overline{B}^0$ combinatorial events in four different ranges of m_{ν}^2. All distributions are normalized to the same arbitrary area.

The D_{tag} fraction is determined from a fit to the $\cos(\theta_{K\ell})$ distribution, where the D_{tag} and B_{tag} shapes are modeled using a polynomial function.

6.3 Charge Asymmetries

Detector related charge asymmetries on the B_{tag} and D_{tag} samples can be measured on generic Monte Carlo (which is generated with no physical source of charge asymmetry) by simply counting K^+ and K^- and using the MC truth.

The results for this test, run over Run1-5 generic $B^0\overline{B}^0$ MC, are presented in table 6.1, where we show the quantity:

$$A_{\ell K} = \frac{N(\ell^+K^+) - N(\ell^-K^-)}{N(\ell^+K^+) + N(\ell^-K^-)}, \tag{6.3}$$

separately for K from the tag side and from the decay side. Only signal events and true kaons are considered and events where the B_{rec} lepton is identified as a muon are separated from the electron case ($A_{\ell K}$ includes also the asymmetry in the reconstruction of B_{rec}).

Table 6.1: Results of the test of charge asymmetries on Run1-5 generic $B^0\overline{B}^0$ MC. Only true kaons have been selected.

	Electrons	Muons
$A_{\ell K}(B_{tag})$	0.0149 ± 0.0013	0.0196 ± 0.0016
$A_{\ell K}(D_{tag})$	0.0152 ± 0.0009	0.0205 ± 0.0010
$A_{\ell K}(B_{tag})$ - $A_{\ell K}(D_{tag})$	-0.0003 ± 0.0016	-0.0009 ± 0.0019

There is a very good agreement between the charge asymmetries measured in B_{tag} and D_{tag} samples for separately electrons and muons, so the method of constraining the detector related asymmetries to the ones found on the D_{tag} sample looks feasible.

As the momentum ($|\vec{p}_L|$) and the polar angle (ϑ_L) spectra are different for B_{tag} and D_{tag} kaons (see figures 6.4 and 6.5) and charge asymmetries depend on those variables, we need to check that there is not a strong dependence of the asymmetries on small variations of the spectra predicted by our Monte Carlo.

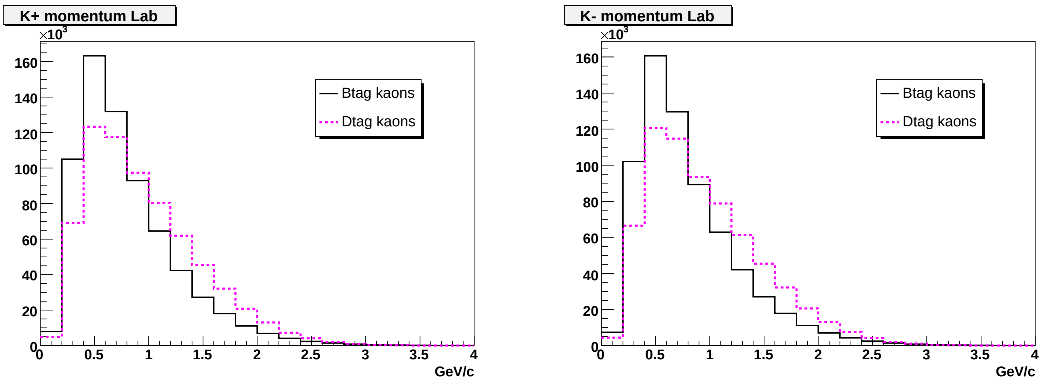

Figure 6.4: Distributions of B_{tag} and D_{tag} momenta in the laboratory frame, separately for K^+ (left plot) and K^- (right). D_{tag} spectra have been normalized to B_{tag} ones.

First of all we check that the charge asymmetry for B_{tag} and D_{tag} detection is the same in a given (small) range of $|\vec{p}_L|$ and ϑ_L. We divide the ($|\vec{p}_L|$, ϑ_L) 2-dimensional spectrum in 400

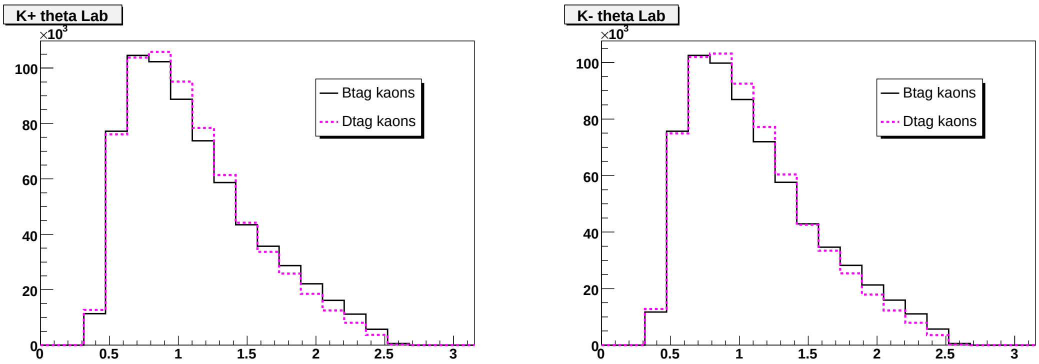

Figure 6.5: Distributions of B_{tag} and D_{tag} polar angles in the laboratory frame (ϑ_L), separately for K^+ (left plot) and K^- (right). D_{tag} spectra have been normalized to B_{tag} ones.

squared bins and for each of them (if it contains at least 50 events), compute the quantity:

$$pull(Asy) = \frac{A_{Btag} - A_{Dtag}}{\sqrt{\sigma^2(A_{Btag}) + \sigma^2(A_{Dtag})}}.$$

The result is shown in figures 6.6 and 6.7; it can be seen that, as expected, the two charge asymmetries are well compatible with each other within statistical uncertainties.

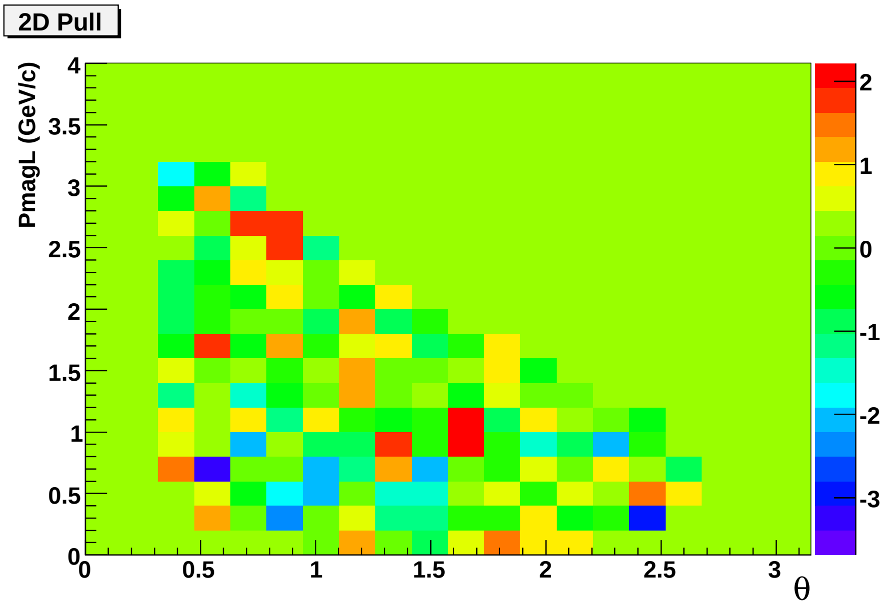

Figure 6.6: Distribution of *pull(Asy)* for Run1-4 generic $B^0\overline{B}^0$ Monte Carlo as a function of $(|\vec{p}_L|, \vartheta_L)$.

To check the dependence of charge asymmetries on the shapes of $|\vec{p}_L|$ and ϑ_L spectra, we generate 11 datasets with modified spectra, according to the following procedure. To generate a dataset with modified $|\vec{p}_L|$ spectra, we randomly select, from the initial sample, D_{tag} kaons with a probability:

$$prob(|\vec{p}_L|) = 0.9 + m(|\vec{p}_L| \ - 2),$$

(with $|\vec{p}_L|$ in GeV/c), independently of ϑ_L and regardless of the kaon charge. m is specific for

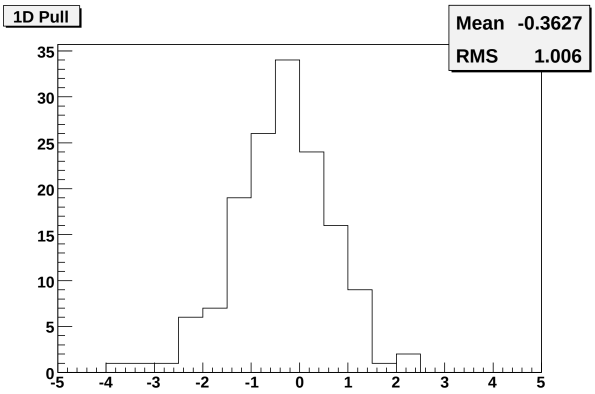

Figure 6.7: Distribution of *pull(Asy)* for bins containing at least 50 events of B_{tag} and D_{tag} kaons.

each dataset and is chosen from $[-0.5, \ldots, +0.5]$ at steps of 0.1. We do the same generating datasets with ϑ_L spectra modified according to the probability:

$$prob(\vartheta_L) = 0.9 + m(\vartheta_L \ - 1.575),$$

and m chosen as before. Figure 6.8 shows the modified $|\vec{p}_L|$ and ϑ_L spectra for the extreme cases and the unmodified shapes. The difference between the original and the modified samples is at the level of a few % and should cover the uncertainty of our generic MC.

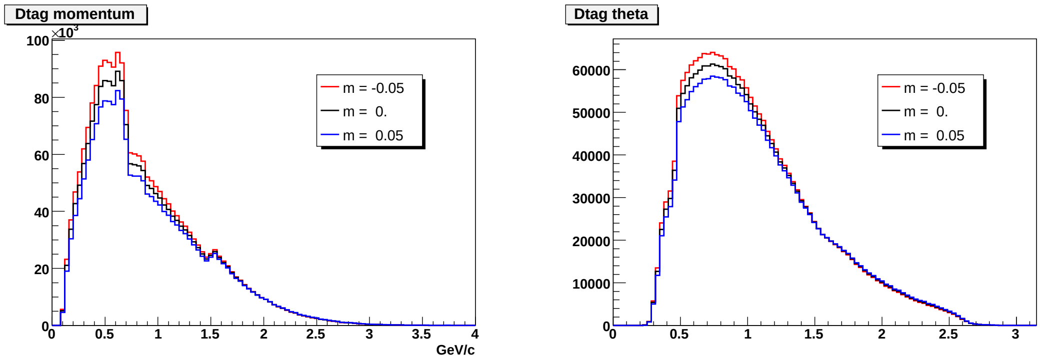

Figure 6.8: Modified $|\vec{p}_L|$ (left plot) and ϑ_L (right) spectra for the extreme cases ($m = \pm 0.5$, red and blue histograms) and the original shape ($m = 0$, black histogram).

For each generated dataset, we compute the charge asymmetries (separately for electrons and muons). The results are reported in figure 6.9.

No sizable deviations appear on the modified spectra with respect to the original case. We conclude that the method of constraining detector related charge asymmetries to the ones measured on the D_{tag} sample is reliable, within the uncertainties on the generic Monte Carlo.

6.4 Charge Asymmetries due to proton contamination

Early studies on our Monte Carlo sample showed that the tracks sample passing the `LooseKaonMicro` selector is affected by a significant contamination of (anti)protons. Furthermore we observe a large charge-asymmetry on this sub-sample, with the number of positive tracks being several times larger than the number of negative ones.

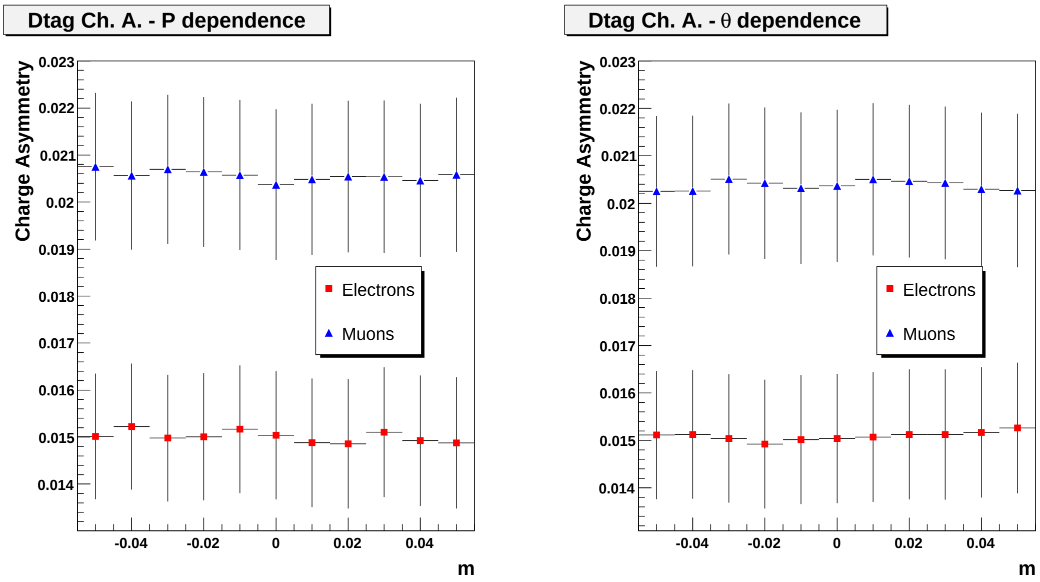

Figure 6.9: Charge asymmetries for modified $|\vec{p}_L|$ spectra (left plot) and ϑ_L (right) separately for electrons (red squares) and muons (blue triangles). We stress the fact that there is a strong overlap among the generated samples, thus the differences between the computed asymmetries are much smaller than the associated statistical uncertainty.

This effect can be explained (and Monte Carlo studies confirm this) by taking into account the interaction of particles and anti-particles coming from the decays of B mesons (or other particles produced in the e^+e^- collisions) with a detector made up by matter only. Nuclear interactions involving particles coming from the beam spot with the detector material may produce detectable protons, while nuclear interactions producing anti-protons are strongly suppressed.

Our simulation shows that only $\sim$ 16% of the (anti)proton tracks (p and $\bar{p}$ in roughly the same amount as expected) come from a B^0 decay chain, while the remaining ($\sim$ 84%) are p produced by the interaction of particles coming from the beam spot with the detector material; $\bar{p}$ production in the matter is confirmed to be negligibly small.

In this section, we use the Monte Carlo truth to subdivide our sample into kaon ($K^\pm$) tracks, protons and anti-protons (p and $\bar{p}$) and other particles ($O^\pm$). Also, we assign the charge sign to each particle according to its generated value.

We use the Monte Carlo truth to separate the non-K particles coming from a decay chain of a B^0 meson (suffix *int*) from the ones produced inside the detector material (suffix *mat*). Table 6.2 summarizes the yields we get on our generic $B^0\overline{B}^0$ Monte Carlo samples. In each sample we also compute the charge asymmetry, defined as $A = (N^+ - N^-)/(N^+ + N^-)$.

Figure 6.10 shows the production vertices in the (x, y) plane for protons separated into p_{int} and p_{mat}. The structure of the beam pipe and of the SVT appears clearly for protons coming from interactions in the material. A significant number of p_{int} and $\bar{p}_{int}$ come from decays of long lived Λ baryons, hence the large fraction of tracks originating several centimeters away from the beam spot.

Concerning the $O^\pm$ sample, the dominant contribution is coming from $\pi^\pm$ (56.6 %), followed by $e^\pm$ (22.4 %) and $\mu^\pm$ (21.0 %). There is also a small, but not negligible contribution coming from deuterons (d) and alpha particles (α); we do not observe $\bar{d}$ or $\bar{\alpha}$, hence the small charge asymmetry in the $O^\pm$ sample. For more details, see table 6.4.

The only use of vetoes on particle selectors passed or not passed by the tracks is not efficient in suppressing the proton component while retaining most of $K^\pm$, hence the need of considering a wider set of variables with more or less sophisticated statistical tools.

Table 6.2: Number of selected tracks, divided by category, for generic $B^0\overline{B}^0$. Monte Carlo truth has been used to separate protons coming from a decay chain of a B^0 meson (p_{int}) from the ones produced inside the detector material (p_{mat}), and the same applies for the other particles: $O^{\pm}_{int}$ and $O^{\pm}_{mat}$. The charge asymmetry A in each sample is also reported.

	Run1	Run2	Run3	Run4
K^+	660 674	2 004 618	1 006 139	3 033 202
K^-	639 575	1 937 999	963 601	2 903 872
$A(K^{\pm})$	1.62 ± 0.09 %	1.69 ± 0.05 %	2.16 ± 0.07 %	2.18 ± 0.04 %
p_{int}	6 168	18 566	9 553	28 972
$\bar{p}_{int}$	6 413	19 350	10 048	30 129
$A(p_{int} - \bar{p}_{int})$	-1.95 ± 0.89 %	-2.07 ± 0.51 %	-2.52 ± 0.71	-1.96 ± 0.41 %
p_{mat}	33 995	102 581	52 565	157 116
$\bar{p}_{mat}$	10	27	22	38
$A(p_{mat} - \bar{p}_{mat})$	99.94 ± 0.54 %	99,95 ± 0.31 %	99.92 ± 0.44 %	99.95 ± 0.25 %
O^+_{int}	49 371	150 616	70 646	219 065
O^-_{int}	49 902	151 698	71 008	217 552
$A(O^{\pm}_{int})$	-0.53 ± 0.32 %	-0.36 ± 0.18 %	-0.25 ± 0.27 %	0.35 ± 0.15 %
O^+_{mat}	40 828	126 923	62 701	199 823
O^-_{mat}	36 998	114 966	56 227	181 922
$A(O^{\pm}_{mat})$	4.92 ± 0.36 %	4.94 ± 0.20 %	5.44 ± 0.29 %	4.69 ± 0.16 %
Total A	3.81 ± 0.08 %	3.87 ± 0.05 %	4.37 ± 0.07 %	4.37 ± 0.04 %

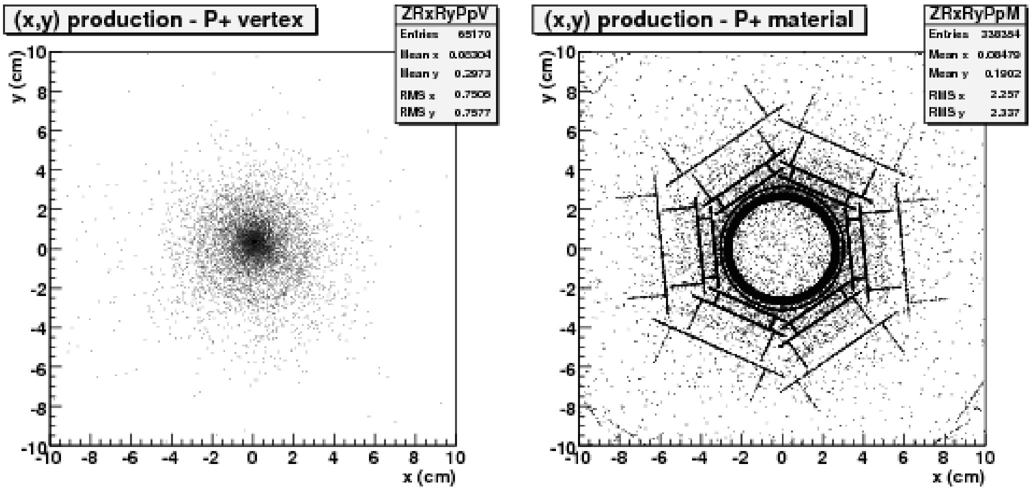

Figure 6.10: Positions in the (x, y) plane of the production vertex for p_{int} (left plot) and p_{mat} (right).

The tracking variables (available in our rootuples) considered in the various analyses are listed below:

- $|\vec{p}_L|$, the magnitude of the particle momentum in the Laboratory frame;
- θ_L, the polar angle in the Laboratory frame of the track;
- ϕ_L, the azimuthal angle of the track;
- $DOCA$ and $eDOCA$: Distance Of Closest Approach (to the beam spot) and its error;
- $POCA$ and $ePOCA$: z coordinate of the Point Of Closest Approach and its error;
- dE/dX_{SVT}, the ionization energy loss measured by the SVT;
- $nHit_{SVT}$, number of hits in the SVT;
- $nHit_{DCH}$, number of hits in the DCH;
- $PidL$: a PID word containing the information of all the available electron and muon selectors;
- $PidH$: a PID word containing the information of all the available kaon, pion and proton selectors;

Figure 6.11-6.17 show the distributions of some of those variables for $K^{\pm}$, p and $\bar{p}$ (either p_{int} or p_{mat}) and $O^{\pm}$.

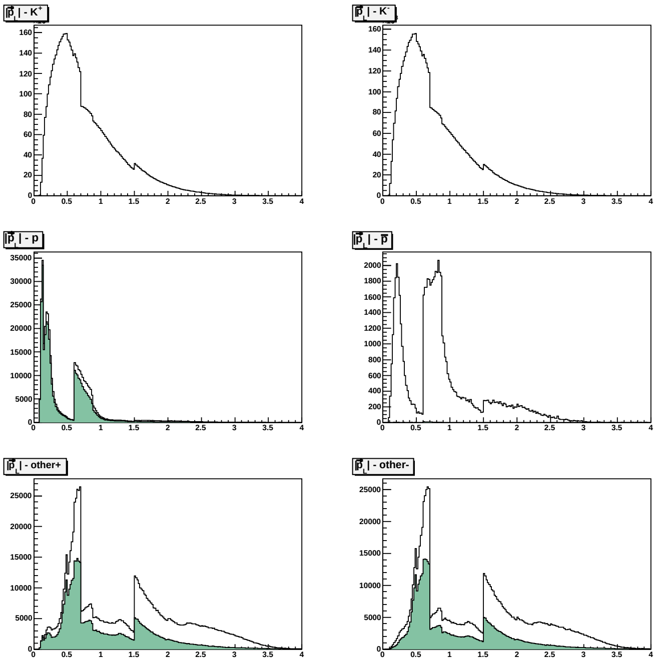

Figure 6.11: $|\vec{p}_L|$ for K^+ (upper left), K^- (upper right), p (middle left), $\bar{p}$ (middle right), O^+ (bottom left) and O^- (bottom right). The shaded histograms show the contributions of particles produced in the detector material.

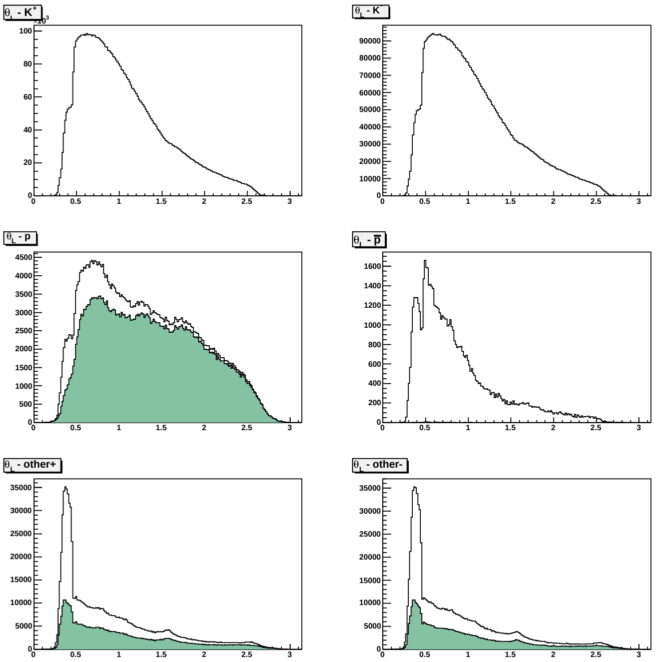

Figure 6.12: θ_L for K^+ (upper left), K^- (upper right), p (middle left), $\bar{p}$ (middle right), O^+ (bottom left) and O^- (bottom right). The shaded histograms show the contributions of particles produced in the detector material.

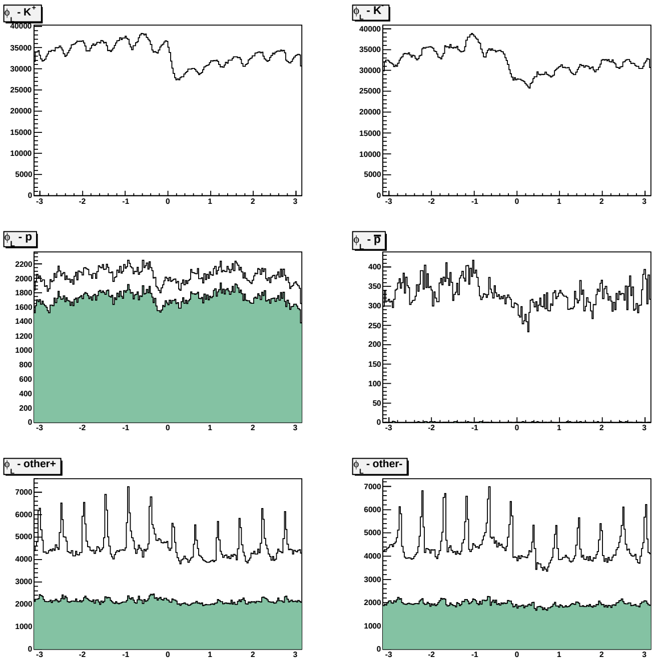

Figure 6.13: ϕ_L for K^+ (upper left), K^- (upper right), p (middle left), $\bar{p}$ (middle right), O^+ (bottom left) and O^- (bottom right). The shaded histograms show the contributions of particles produced in the detector material.

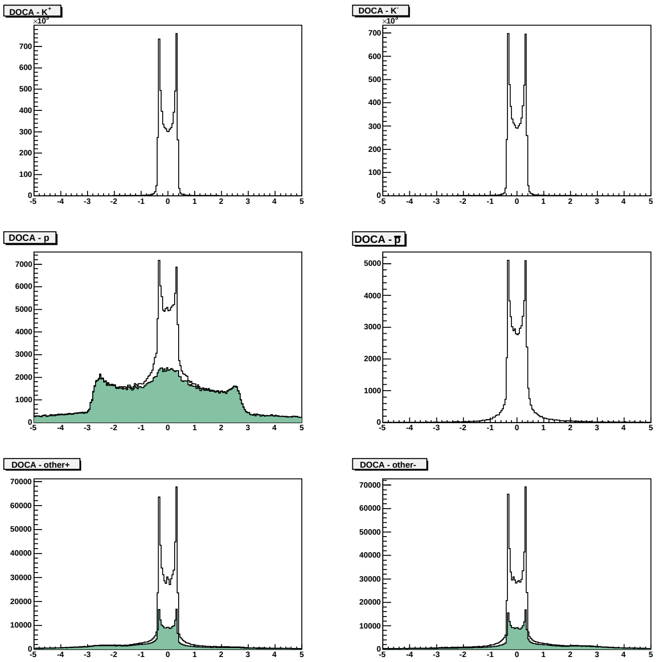

Figure 6.14: *DOCA* for K^+ (upper left), K^- (upper right), p (middle left), $\bar{p}$ (middle right), O^+ (bottom left) and O^- (bottom right). The shaded histograms show the contributions of particles produced in the detector material.

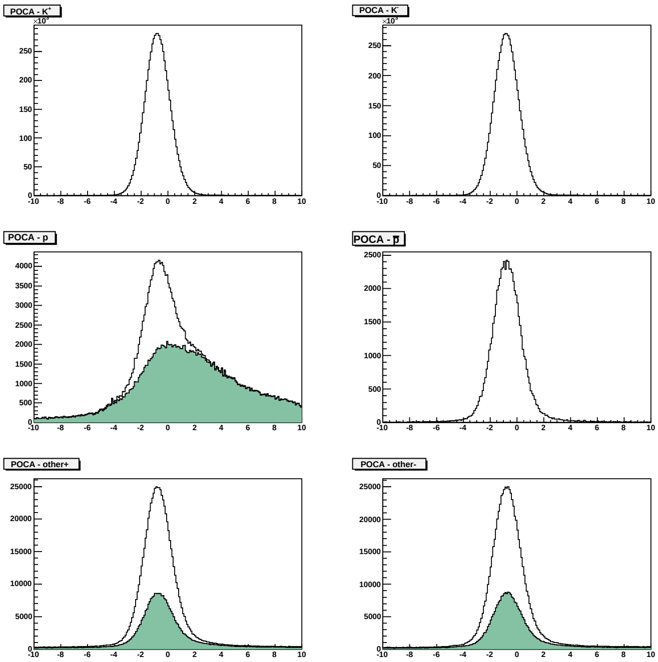

Figure 6.15: *POCA* for K^+ (upper left), K^- (upper right), p (middle left), $\bar{p}$ (middle right), O^+ (bottom left) and O^- (bottom right). The shaded histograms show the contributions of particles produced in the detector material.

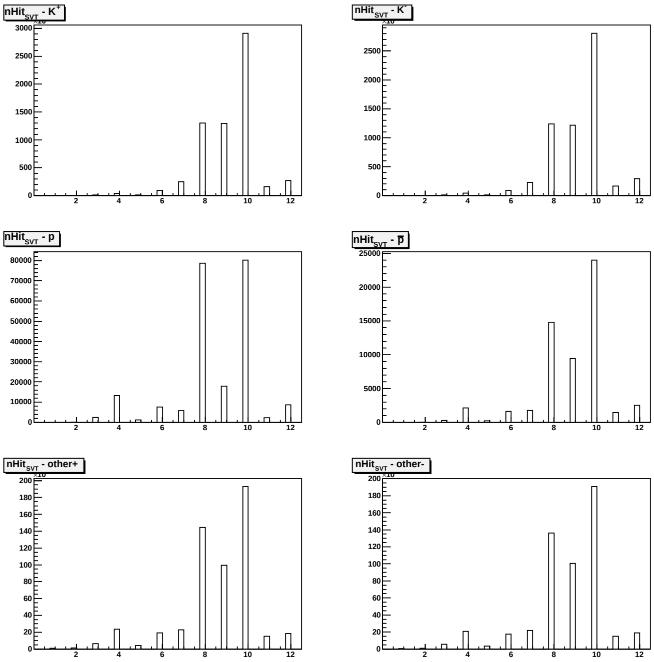

Figure 6.16: $nHit_{SVT}$ for K^+ (upper left), K^- (upper right), p (middle left), $\bar{p}$ (middle right), O^+ (bottom left) and O^- (bottom right).

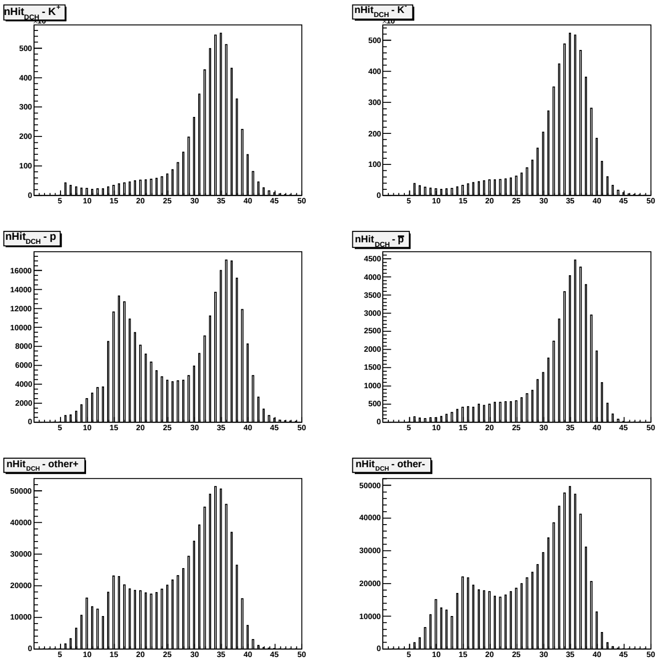

Figure 6.17: $nHit_{DCH}$ for K^+ (upper left), K^- (upper right), p (middle left), $\bar{p}$ (middle right), O^+ (bottom left) and O^- (bottom right).

6.4.1 Cut and count analysis

A quick and transparent reduction of the contamination from non-K tracks in our sample can be achieved by imposing a small set of cuts on the variables considered.

An acceptable trade-off between purity and efficiency is given by the following requests:

- the track is requested to pass the `VeryLooseLHProtonSelection` selector;
- $nHit_{SVT} \geq 6$;
- $|DOCA| < 0.4$;
- $-3 < POCA < 1.5$;

The above cuts have been set trying to suppress the p_{mat} component while retaining most of the $K^{\pm}$ component and indeed we reject $\sim 95\%$ of the $p_{mat} - \bar{p}_{mat}$ component while retaining about 89% of genuine kaons. Furthermore, we achieve a significant suppression also on the p_{int} and $O^{\pm}$ components. Details about the performance of our selection can be found in table 6.3.

Table 6.3: Rejection efficiencies of our set of cuts on each subsample. The whole Run1-4 $B^0\overline{B}^0$ generic Monte Carlo has been taken into account.

	Before cuts	After Cuts	1 - ε
K^+	6 704 633	5 978 030	10.84 ± 0.01 %
K^-	6 445 047	5 740 580	10.93 ± 0.01 %
p_{int}	63 259	23 327	63.12 ± 0.19 %
p_{mat}	346 257	15 546	95.51 ± 0.04 %
$\bar{p}_{int}$	65 940	26 037	60.51 ± 0.19 %
$\bar{p}_{mat}$	97	6	93.81 ± 2.45 %
O^+_{int}	490 058	272 212	44.45 ± 0.07 %
O^+_{mat}	430 275	110 515	74.31 ± 0.07 %
O^-_{int}	490 160	272 220	44.46 ± 0.07 %
O^-_{mat}	390 113	110 490	71.67 ± 0.07 %
Total A	4.169 ± 0.025 %	1.995 ± 0.028 %	-

On the backgrounds only, our set of cuts reduces the charge asymmetry from 16.85 ± 0.07 % to 1.55 ± 0.11 %; the global asymmetry we observe after the cuts is therefore almost entirely due to the detection asymmetry of $K^{\pm}$ tracks.

The performances of the above set of cuts on the single components of the $O^{\pm}$ sample are illustrated on table 6.4. The cuts suppress most of d and α and significantly reduce the background from $e^{\pm}$, $\mu^{\pm}$ and $\pi^{\pm}$ and the charge asymmetry of the whole $O^{\pm}$ sample.

While it is apparent that this small set of cuts significantly improves the quality of our $K^{\pm}$ sample, it is also evident that only a limited part of the available information is used and even on the variables involved in the cuts some more rejection power is left.

In the following sections we will apply more sophisticated and powerful statistical tools, beginning (subsection 6.4.2) with Neural Networks in one of the most popular implementations in HEP and then applying some of the less popular (in HEP) tools available in the `StatPatternRecognition` package (subsection 6.4.3).

Table 6.4: Breakdown of the $O^{\pm}$ components, before and after applying the set of cuts; selection efficiencies are also reported.

	Before cuts	After Cuts	Efficiency
e^+	197 811	82 283	41.6 ± 0.1 %
e^-	203 338	81 623	40.1 ± 0.1 %
μ^+	186 967	75 005	40.1 ± 0.1 %
μ^-	188 462	77 102	40.9 ± 0.1 %
π^+	490 454	224 824	45.8 ± 0.1 %
π^-	488 301	223 880	45.8 ± 0.1 %
d	16 662	163	1.0 ± 0.1 %
$\bar{d}$	0	0	n.a.
α	19 698	258	1.3 ± 0.1 %
$\bar{\alpha}$	0	0	n.a.

6.4.2 Neural Network Analysis

In this section we will apply to our selection problem a feedforward with backpropagation neural network, implemented in the `TMultiLayerPerceptron` class, available in the most recent ROOT distributions.

Given the size of our data sets, we can produce many independent samples to be used for training and validation. We start by considering only positive kaons and protons; the performance of the network will be tested on the negative tracks and on the $O^{\pm}$ sample once the setup has been optimized and frozen.

Learning Methods

The `TMultiLayerPerceptron` package offers six *Learning Methods*. The choice of the optimal one for our purposes has been made by building a neural network with one hidden layer (8 nodes) and one output node utilizing each real variable considered. The network has been trained and validated by using a sample of 30k K^+ tracks and 10k p (either p_{int} or p_{mat}) split in two samples (*Training* and *Validation*) having the same size. 300 training cycles have been run for each learning method; to compare the efficiencies of the different learning methods, we compare the fractions of protons rejected with a cut on the output value which keeps $\sim 90\,\%$ of K^+ tracks.

In the following we list the results of our tests and the reasons which motivated our choice:

- **Steepest Descent with Fixed Step Size (Batch Learning)**: the algorithm fails during the validation process after a few tens of cycles;
- **Steepest Descent**: this algorithm terminates successfully the training cycles, but the fraction of rejected protons is rather poor: $73.5 \pm 0.4\%$;
- **Conjugate Gradients with Fletcher-Reeves Updating Formula**: the fraction of rejected protons is $86.8 \pm 0.3\%$;
- **Conjugate Gradients with Polach-Ribiere Updating Formula**: the fraction of rejected protons is $88.5 \pm 0.3\%$;
- **Stochastic Minimization**: this method gives a very good proton rejection efficiency ($93.4 \pm 0.2\%$) but the validation error curve (see fig. 6.18, left) is rather spiky;

- **Broyden, Fletcher, Goldfarb, Shanno Method (BFGS)**: this method achieves the best performance (94.8 ± 0.2%) and the training and validation error curves look well behaved (see fig. 6.18, right);

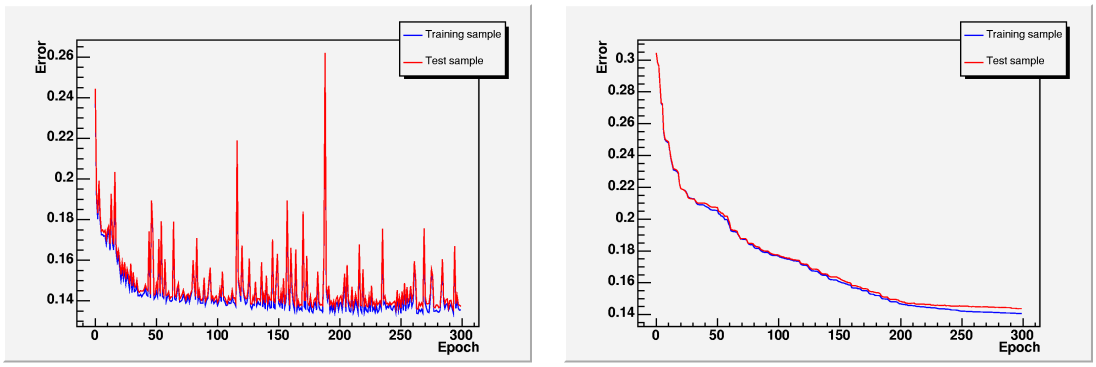

Figure 6.18: Training and validation errors as a function of the training cycle for Stochastic Minimization (left) and BGFS (right) learning methods.

Given its performance and stability, we choose the BFGS learning method for the following refinements and optimizations of the network. In this method, the search precision (and training speed) is set by the parameter τ (the lower it is, the more precise and slower is the search).

We perform a brief scan on the same training and validation samples to look for any optimal setting of the τ parameter; results are shown in figure 6.19.

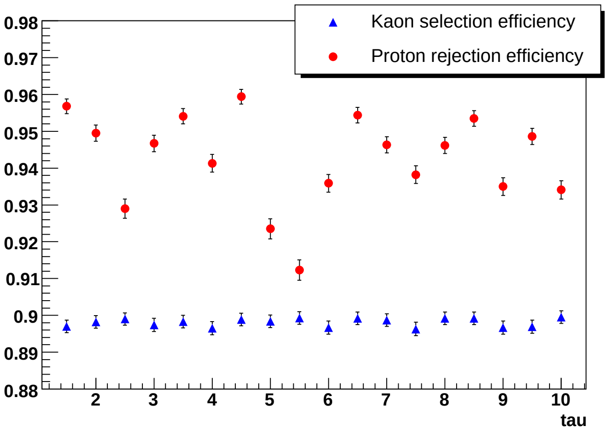

Figure 6.19: Results of the scan on the τ parameter of the BFGS learning method. We compare the proton rejection efficiencies (red dots) achieved by a cut on the NN output which preserves $\sim 90\%$ of K^+.

As no evident trend is visible in the scan, we conservatively keep the default value of $\tau = 3$.

Network Optimization

We use a sample of 100k K^+ and 17k p to test if the rejection efficiency of protons produced in the material could be improved by training the network only on a sample of p_{mat}.

This quick test actually shows that the p_{mat} rejection efficiency is slightly degraded (it moves from 97.00 ± 0.13 % to 96.22 ± 0.15 %) by training on the p_{mat} component only. On the other side, the p_{int} rejection efficiency drops from 77.9 ± 0.7 % to 65.6 ± 0.8 %.

In order to preserve the performance and the stability of the neural network (also in sight of an effective reduction of the $\bar{p}_{int}$ component), we decide to keep training the network on both components.

We then vary the number of nodes in the hidden layer and compare the efficiency of each network. As before, we cut on the output value of the network in order to preserve $\sim 90\,\%$ of K^+; results are shown in figure 6.20.

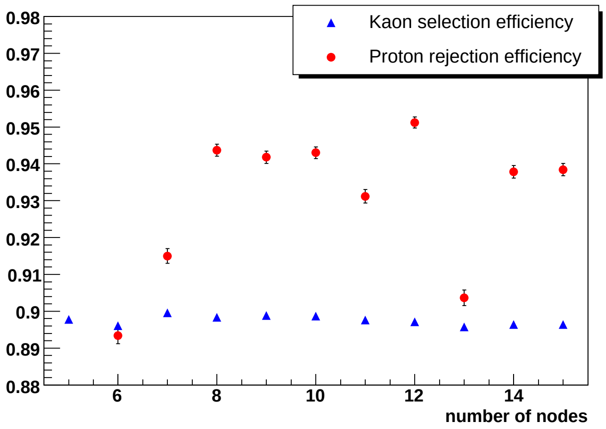

Figure 6.20: Results of the scan on the *number of nodes* in the hidden layer of NN. the BFGS learning method.

We choose 12 as the optimal number of hidden nodes; some concern on the stability of this choice could arise from the fact that the solutions with 11 and 13 hidden nodes give results significantly worse than the optimal solution and the average over the scanned range: some thorough study on this will be necessary, should we actually use this tool in the actual analysis.

We also try to put a second hidden layer, but we quickly discard this kind of networks because, while having roughly the same efficiency on the rejection of the p_{mat} component, they reach significantly worse results with p_{int}.

In figure 6.21 we show the output of our optimized Neural Network for K^+, p_{int} and p_{mat}.

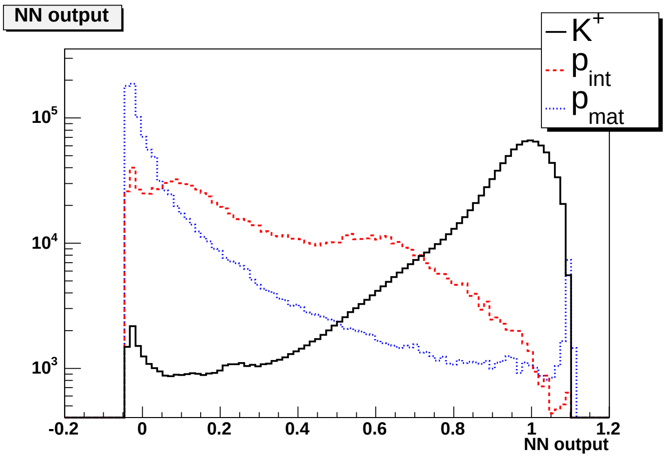

Figure 6.21: Output of the optimized neural network for K^+ (continuous black line), p_{int} (red dashed) and p_{mat} (blue dots). The histograms have been normalized to the same area.

Table 6.5 shows the efficiencies of the cut on Neural Network output for e, μ and π and figure 6.22 shows its distributions separately for positive and negative tracks.

With respect to the cut based strategy, while there is a substantial improvement on the rejection of $\mu^{\pm}$, the Neural Network has a significantly poorer performance on $e^{\pm}$ and works slightly worse for $\pi^{\pm}$.

Table 6.5: Breakdown of the $O^{\pm}$ components, before and after applying the cut on Neural Network output; selection efficiencies are also reported.

	Before cuts	After Cuts	Efficiency
e^+	197 811	122 340	60.2 ± 0.1 %
e^-	203 338	119 749	60.5 ± 0.1 %
μ^+	186 967	49 100	26.1 ± 0.1 %
μ^-	188 462	48 289	25.8 ± 0.1 %
π^+	490 454	230 536	47.0 ± 0.1 %
π^-	488 301	229 079	46.9 ± 0.1 %

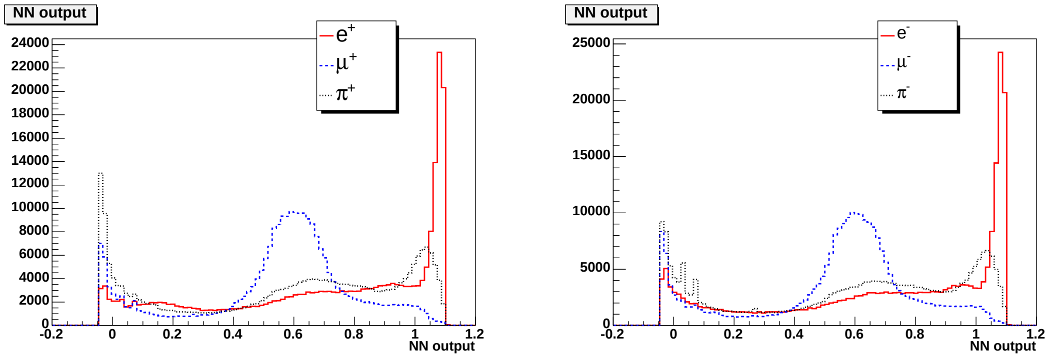

Figure 6.22: Neural Network output for positive (left plot) and negative (right) e, μ and π. The distributions have been normalized to the same conventional area.

6.4.3 StatPatternRecognition Analysis

In this subsection we apply to our selection the more sophisticated (and less popular in HEP) statistical tools available in the package `StatPatternRecognition`. Extensive documentation on this package and the statistical techniques involved can be found in [61], [62] and references therein.

We will use the *AdaBoost* technique, which can handle several elementary classifiers in a very flexible way. The hard split decision (signal or background) which is used e.g. in *Bump Hunting* and simple *Decision Trees* is replaced here by soft splits.

At each training cycle, the algorithm performs a series of splits minimizing the fraction of misclassified events; the weight of misclassified events is enhanced with respect to the weight of correctly classified ones and a new training cycle is performed. The procedure is repeated until a stopping criterion is satisfied. The final classification of an event is given by a weighted vote of all the binary splits; given the large number of splits in practice we get a continuous output, similar to the one we get from a Neural Network.

For our analysis, we will use the `SprAdaBoostDecisionTreeApp` implementation of *AdaBoost*. We choose the *Gini index* as the FOM to be maximized, as highly recommended by the Author.

One of the main advantages of *AdaBoost* with respect to Neural Networks is the possibility to efficiently exploit integer variables as well as floats in the same analysis. We therefore use, in addition to the variables used in the Neural Network analysis, $nHit_{SVT}$, and $nHit_{DCH}$. We leave out the PID information in order to apply vetoes or select control sample using variables independent from the ones used in the *AdaBoost*.

Number of Classifiers

There are basically two parameters to be optimized in using `SprAdaBoostDecisionTrees`: the minimum number of events per node in each decision trees and the number of classifiers to be used in the whole process.

In order to avoid the possibility of overtraining, we conservatively set the minimum number of events per node to 1000. We then perform a scan by varying the number of classifiers to be used in order to find the optimal setting.

The training sample contains 67 046 K^+ and 20 480 p, the validation and test samples are independent from the training sample and have half its size. We evaluate the performance on the test sample by setting a cut on the AdaBoost output variable which preserves $\sim 90\%$ of K^+ and computing the rejection efficiency of the protons.

The results of this scan are reported in figure 6.23.

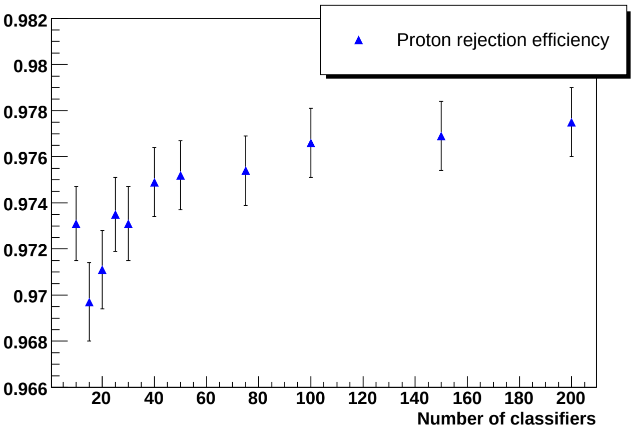

Figure 6.23: Scan over the number of classifiers used by *AdaBoost*

As we can see, the performance increases with the number of classifiers. As the improvement over 100 is marginal compared to the additional computing time requested, we choose 100 as default value for the following studies.

Figure 6.24 shows the output of AdaBoost for K^+, p_{int} and p_{mat}. The plot has been drawn on a sample (independent from the ones previously used for training, validation and test) of $67k$ K^+, $13k$ p_{int} and $69k$ p_{mat}; the training and the cut position have been kept frozen.

On this sample we get a K^+ selection efficiency of $90.45 \pm 0.11\,\%$ while the protons rejection efficiencies are $92.87 \pm 0.23\,\%$ for p_{int} and $99.10 \pm 0.04\,\%$ for p_{mat}.

Figure 6.25 shows the output distributions of the same AdaBoost on $e^\pm$, $\mu^\pm$ and $\pi^\pm$. A summary of the performance on those tracks with the same cut on the *AdaBoost* output is given in table 6.6.

Comparison with Neural Network

As it is apparent from the preliminary checks done so far, the AdaBoost technique is significantly more powerful than the Neural Network set up on the same problem. We may ask how much this additional power is due to the inclusion of the integer variables $nHit_{SVT}$ and $nHit_{DCH}$.

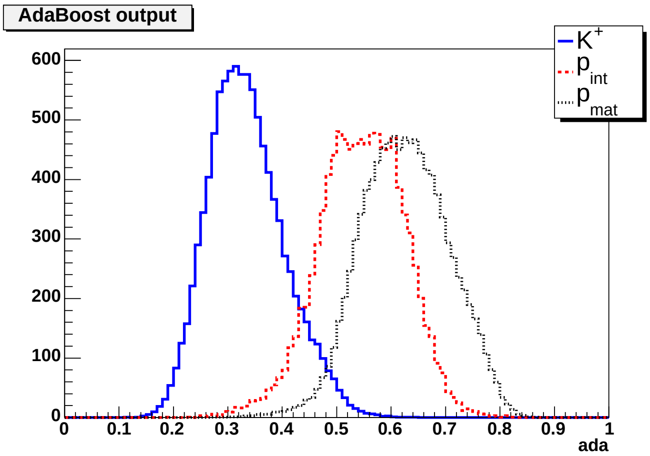

Figure 6.24: Output of *AdaBoost* for K^+ and separately for p_{int} and p_{mat}. The distributions have been normalized to the same area.

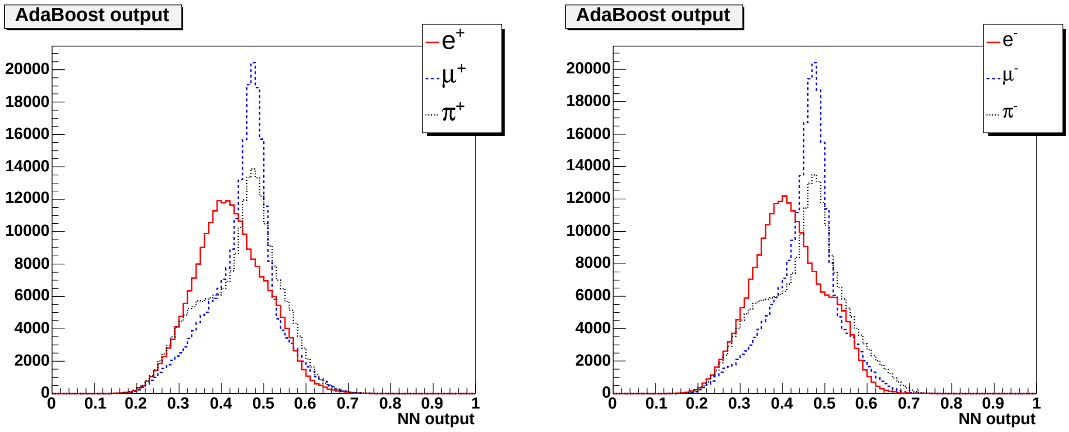

Figure 6.25: AdaBoost output for positive (left plot) and negative (right) e, μ and π.

Table 6.6: Breakdown of the $O^\pm$ components, before and after applying the cut on the AdaBoost output; selection efficiencies are also reported.

	Before cuts	After Cuts	Efficiency
e^+	197 811	114 606	56.4 ± 0.1 %
e^-	203 338	117 115	59.2 ± 0.1 %
μ^+	186 967	62 613	33.2 ± 0.1 %
μ^-	188 462	60 679	32.5 ± 0.1 %
π^+	490 454	191 350	39.0 ± 0.1 %
π^-	488 301	188 761	38.7 ± 0.1 %

To quickly answer this question, we re-train, on the same samples used before and again using 100 classifiers, a new `SprAdaBoostDecisionTree` which does not take into account the two integer variables.

The results on the test sample (33 523 K^+ and 10 240 p) show that with a K^+ selection efficiency of 89.94 ± 0.16 %, we reject 97.78 ± 0.0015 % of the protons, a result perfectly compatible with the one obtained by using the two discarded variables.

Charge Asymmetries

We compute the charge asymmetry on the selection of $K^\pm$ tracks on a large ($\sim 670k$ K^+ and $\sim 645k$ K^-) Monte Carlo sample, with the usual selection technique.

The results are: $\varepsilon(K^+) = 89.88 \pm 0.04\,\%$ and $\varepsilon(K^-) = 89.41 \pm 0.04\,\%$, the ratio between the two being 1.0054 ± 0.0006.

Figure 6.26 shows the output of the AdaBoost for K^+ and K^- separately. While there is an overall consistency between the two distributions, some differences are apparent on the tails. Fitting the ratio histogram with a constant, we get $c = 0.9964 \pm 0.0018$ with $\chi^2/NDOF = 769.2/64$.

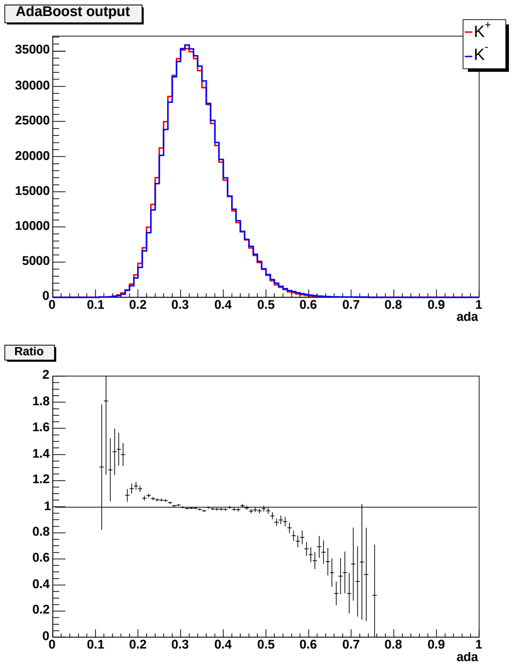

Figure 6.26: Output of AdaBoost **trained only on** K^+, separately for K^+ and K^- (upper plot) and ratio $\varepsilon(K^+)/\varepsilon(K^-)$ between the two (lower plot). The distributions have been normalized to the same area.

The charge asymmetry in $K^\pm$ selection is significantly reduced by training the AdaBoost on a sample containing K^+ and K^- in roughly the same amount. By repeating the whole procedure on training, validation and test samples of comparable in size to the ones used above, we get: $\varepsilon(K^+) = 89.84 \pm 0.04\,\%$, $\varepsilon(K^-) = 89.72 \pm 0.04\,\%$, and the ratio between the two: 1.0013 ± 0.0006. The fit with a constant gives $c = 0.9984 \pm 0.0018$, $\chi^2/NDOF = 321.4/64$.

If we train by using only K^- what we get is: $\varepsilon(K^+) = 89.50 \pm 0.04\,\%$, $\varepsilon(K^-) = 89.80 \pm 0.04\,\%$, and the ratio is 0.9967 ± 0.0006. The fit result is: $c = 0.9995 \pm 0.0018$ with $\chi^2/NDOF = 96.5/64$.

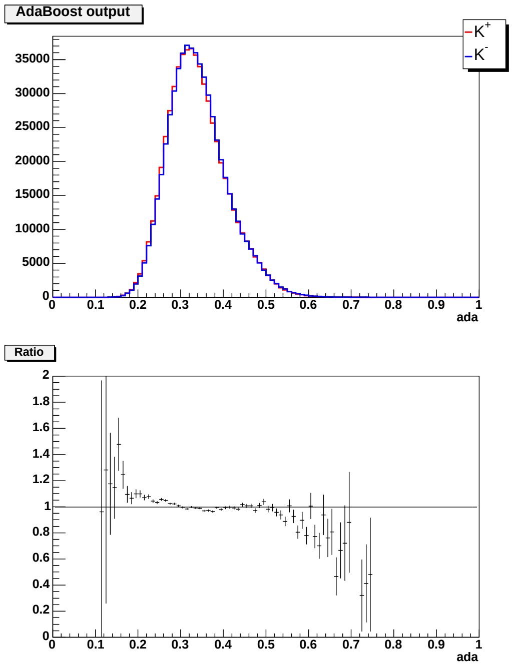

Figure 6.27: Output of AdaBoost **trained on both K^+ and K^-**, separately for K^+ and K^- (upper plot) and ratio $\varepsilon(K^+)/\varepsilon(K^-)$ between the two (lower plot). The distributions have been normalized to the same area.

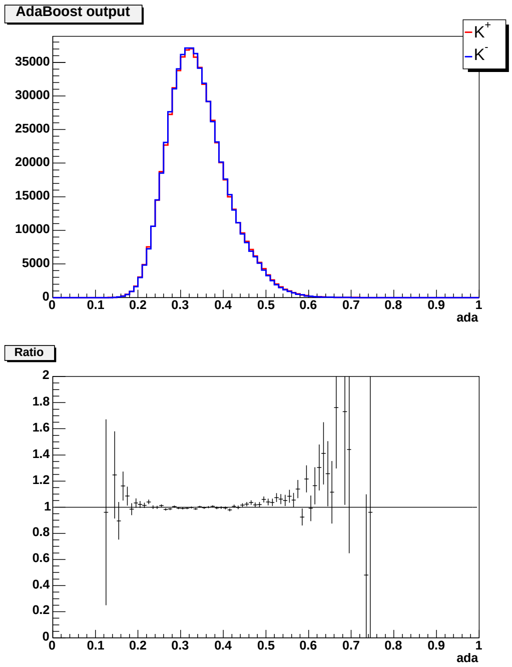

Figure 6.28: Output of AdaBoost **trained only on K^-**, separately for K^+ and K^- (upper plot) and ratio $\varepsilon(K^+)/\varepsilon(K^-)$ between the two (lower plot). The distributions have been normalized to the same area.

6.4.4 Conclusions

The optimization on the selection of $K^{\pm}$ tracks to be used in the CP-violation analysis showed that the contamination from protons (and in particular from protons produced in the interaction with the detector material) is already reduced to negligible levels, so we do not need to apply the algorithms developed in this separate study to the main analysis stream.

Chapter 7

Probability density functions

In this chapter we describe the *probability density functions* (pdf's) we use to parametrize the $(\Delta t, \sigma(\Delta t))$ distributions for the various components entering our fit.

We will not use the parametrization here defined for the D_{tag} kaons in peaking $B^0\overline{B}^0$ and B^+B^- events and B^+B^- combinatorial due to the fact that it is possible to obtain a more reliable description based on the data of these components. The parametrization given in this chapter will be used anyway to estimate the systematic uncertainties.

7.1 Reconstruction and tagging asymmetries

Theoretical signal and background pdf's have to be properly modified in order to take into account physical and detector related asymmetries. These can be schematically grouped as follows:

1. *Reconstruction Asymmetry.* If ρ is the reconstruction efficiency of a (ℓ^+, π_s^-) pair and $\bar{\rho}$ is the reconstruction efficiency for its conjugate, we define the reconstruction asymmetry $A_{rec} = (\rho - \bar{\rho})/(\rho + \bar{\rho})$ and the average reconstruction efficiency $R = (\rho + \bar{\rho})/2$. ρ and $\bar{\rho}$ can then be expressed as:

$$\begin{aligned}\rho &= R(1 + A_{rec})\\ \bar{\rho} &= R(1 - A_{rec})\end{aligned} \tag{7.1}$$

   Given that the reconstruction efficiencies for $(e^\pm, \pi_s^\mp)$ pairs is different from the ones for $(\mu^\pm, \pi_s^\mp)$, we will distinguish the two lepton flavors in the fit and quote $A_{rec}(e)$ and $A_{rec}(\mu)$.

2. *Tagging Asymmetry (Physics).* We define ω^+ the probability for a B^0 to have among its decay products the hadron h^- and ω^- the probability for a $\overline{B}^0$ to decay to h^+. We have $\Delta\omega = \omega^+ - \omega^-$ and $\omega = (\omega^+ + \omega^-)/2$.

3. *Tagging Asymmetry (Detector).* If τ is the probability that the hadron h^+ is identified as a K^+ and $\bar{\tau}$ the probability that h^- is identified as K^-, we define: $A_{tag} = (\tau - \bar{\tau})/(\tau + \bar{\tau})$ and $T = (\tau + \bar{\tau})/2$. τ and $\bar{\tau}$ can be written as:

$$\begin{aligned}\tau &= T(1 + A_{tag})\\ \bar{\tau} &= T(1 - A_{tag})\end{aligned} \tag{7.2}$$

We will assume that B_{tag} and D_{tag} samples share the same A_{rec} and A_{tag} asymmetries, while ω and $\Delta\omega$ are kept separated because they originate from different underlying physical processes.

Because of these effects, the theoretical pdf's $\mathcal{F}_\chi(s_t, s_m)$, where χ defines the different components (*signal* B_{tag}*, signal* D_{tag}*, combinatorial* B_{tag}*, combinatorial* D_{tag}*, peaking and continuum*), are related to measured pdf's $\mathcal{F}_\chi^{meas}(s_t, s_m)$, in this way:

$$\begin{aligned}\mathcal{F}_\chi^{meas}(\Delta t, s_t=1, s_m=-1) &= \rho\tau\left[(1-\omega_\chi^+)\mathcal{F}_\chi(\Delta t,1,-1)+\omega_\chi^-\mathcal{F}_\chi(\Delta t,-1,1)\right] = \\ &= RT(1+A_{rec})(1+A_{tag})\left[(1-\omega_\chi^+)\mathcal{F}_\chi(\Delta t,1,-1)+\omega_\chi^-\mathcal{F}_\chi(\Delta t,-1,1)\right]\end{aligned} \tag{7.3}$$

$$\begin{aligned}\mathcal{F}_\chi^{meas}(\Delta t, s_t=1, s_m=1) &= \bar{\rho}\tau\left[(1-\omega_\chi^+)\mathcal{F}_\chi(\Delta t,1,1)+\omega_\chi^-\mathcal{F}_\chi(\Delta t,-1,-1)\right] = \\ &= RT(1-A_{rec})(1+A_{tag})\left[(1-\omega_\chi^+)\mathcal{F}_\chi(\Delta t,1,1)+\omega_\chi^-\mathcal{F}_\chi(\Delta t,-1,-1)\right]\end{aligned} \tag{7.4}$$

$$\begin{aligned}\mathcal{F}_\chi^{meas}(\Delta t, s_t=-1, s_m=-1) &= \bar{\rho}\bar{\tau}\left[(1-\omega_\chi^-)\mathcal{F}_\chi(\Delta t,-1,-1)+\omega_\chi^+\mathcal{F}_\chi(\Delta t,1,1)\right] = \\ &= RT(1-A_{rec})(1-A_{tag})\left[(1-\omega_\chi^-)\mathcal{F}_\chi(\Delta t,-1,-1)+\omega_\chi^+\mathcal{F}_\chi(\Delta t,1,1)\right]\end{aligned} \tag{7.5}$$

$$\begin{aligned}\mathcal{F}_\chi^{meas}(\Delta t, s_t=-1, s_m=1) &= \rho\bar{\tau}\left[(1-\omega_\chi^-)\mathcal{F}_\chi(\Delta t,-1,1)+\omega_\chi^+\mathcal{F}_\chi(\Delta t,1,-1)\right] = \\ &= RT(1+A_{rec})(1-A_{tag})\left[(1-\omega_\chi^-)\mathcal{F}_\chi(\Delta t,-1,1)+\omega_\chi^+\mathcal{F}_\chi(\Delta t,1,-1)\right]\end{aligned} \tag{7.6}$$

where s_t and s_m have been defined in chapter 2.

The observed distributions are obtained from the convolution of the resolution functions with the $\mathcal{F}_\chi^{meas}(s_t, s_m)$ defined above, as discussed in the following sections 7.2- 7.10 for each component of the global pdf.

Even if for D_{tag} kaons in $B^0\overline{B}^0$ signal and B^+B^- signal and combinatorial we will get the pdf's from the data (see chapter 10), we describe the analytical pdf's and resolution models, since these will be used in the evaluation of systematic uncertainties.

7.2 Signal B_{tag}

The theoretical pdf's $\mathcal{F}_{B_{tag},sig}(s_t, s_m)$ for signal B_{tag} events are those described in section 2.

The resolution model we need to use is complicated by the fact that a large fraction of B_{tag} kaons originate from *cascade* decays ($b \to c \to K$); the effect of the finite lifetime of the charmed meson and the experimental boost cause a distortion towards negative values of the Δt distribution. This effect is accounted for by using gaussians convoluted with a decaying exponential (Gexp's) instead of simple gaussians in the resolution model.

Moreover, the dependence on $|\vec{p}_K|$ of the resolution function has to be parametrized. The resolution model, for *signal* B_{tag} events, is defined as follows:

$$\begin{aligned}R_{B_{tag},sig}(\delta\Delta t, \sigma\Delta t, |\vec{p}_K|) &= f_n\, exp\left(-\frac{(\delta\Delta t - o_n)^2}{2(s_n(|\vec{p}_K|)\,\sigma\Delta t)^2}\right) + \\ &+ |1-f_n-f_o|\, exp\left(-\frac{(\delta\Delta t - o_w)^2}{2(s_w(|\vec{p}_K|)\,\sigma\Delta t)^2}\right) + \\ &+ f_o\, exp\left(-\frac{(\delta\Delta t - o_o)^2}{2s_o^2}\right)\end{aligned} \tag{7.7}$$

where $\delta\Delta t = \Delta t_{true} - \Delta t_{meas}$ and s_x and o_x ($x = n, w, o$) are the offsets and widths, respectively, of the gaussian components.

$R_{B_{tag},sig}(\delta\Delta t, \sigma\Delta t, |\vec{p}_K|)$ is convoluted with two decaying exponentials:

$$\begin{aligned} \mathcal{R}_{B_{tag},sig}(\delta\Delta t, \sigma\Delta t, |\vec{p}_K|) &= (1 - f_{G2}(|\vec{p}_K|))\, R_{B_{tag},sig}(\delta\Delta t, \sigma\Delta t, |\vec{p}_K|) \otimes exp\left(-\frac{\delta\Delta t}{\tau_{G1}}\right) + \\ &+ f_{G2}(|\vec{p}_K|)\, R_{B_{tag},sig}(\delta\Delta t, \sigma\Delta t, |\vec{p}_K|) \otimes exp\left(-\frac{\delta\Delta t}{\tau_{G2}(|\vec{p}_K|)}\right) \end{aligned} \tag{7.8}$$

The dependence on $|\vec{p}_K|$ of some of the parameters entering the resolution model is

$$s_x(|\vec{p}_K|) = s_{x,0} + \frac{s_{x,1}}{\sqrt{|\vec{p}_K|}} \qquad x = n, w \tag{7.9}$$

$$\tau_{G2}(|\vec{p}_K|) = \tau_{G2,0} + \frac{\tau_{G2,1}}{\sqrt{|\vec{p}_K|}} \tag{7.10}$$

$$f_{G2}(|\vec{p}_K|) = f_{G2,0} + f_{G2,1}|\vec{p}_K| \tag{7.11}$$

The left plot of figure 7.1 shows the resulting resolution model for a kaon with $|\vec{p}_K| = 1$ GeV/c.

The mistag probability ω^+ (ω^-) of incorrectly tagging a B^0 ($\overline{B}^0$) reduces the statistical significance of our measurement by the dilution factor $D = (1 - 2\omega)$. The dilution is also dependent linearly on $|\vec{p}_K|$:

$$D(|\vec{p}_K|) = D_0 + D_1\, |\vec{p}_K|\,, \tag{7.12}$$

that is:

$$\omega^{\pm} = \frac{1 - D}{2} \pm \Delta\omega\,. \tag{7.13}$$

7.3 Signal D_{tag}

Signal D_{tag} events are parametrized by using a double exponential with an effective D^0 lifetime τ_{D^0}. This pdf is convoluted with the following resolution model:

$$\begin{aligned} R_{D_{tag},sig}(\delta\Delta t, \sigma\Delta t, |\vec{p}_K|) &= f_{nn}\, exp\left(-\frac{(\delta\Delta t - o_{nn})^2}{2(s_{nn}\,\sigma\Delta t)^2}\right) + \\ &+ f_n\, exp\left(-\frac{(\delta\Delta t - o_n)^2}{2(s_n(|\vec{p}_K|)\,\sigma\Delta t)^2}\right) + \\ &+ f_w\, exp\left(-\frac{(\delta\Delta t - o_w)^2}{2(s_w(|\vec{p}_K|)\,\sigma\Delta t)^2}\right) + \\ &+ f_o\, exp\left(-\frac{(\delta\Delta t - o_o)^2}{2s_o^2}\right), \end{aligned} \tag{7.14}$$

where f_{nn}, f_n, f_w and f_o are normalized to unity.

The resolution function $\mathcal{R}_{D_{tag},sig}(\delta\Delta t, \sigma\Delta t, |\vec{p}_K|)$ is computed by convoluting each of the gaussian components with a Gexp with lifetimes τ_{nn}, τ_n, τ_w and $\tau_o(|\vec{p}_K|)$.

As in the B_{tag} case, we allow a dependence on $|\vec{p}_K|$ for the widths of the narrow and the wide components; moreover we allow the lifetime of the outlier Gexp to have a dependence on the kaon momentum:

$$s_x(|\vec{p}_K|) = s_{x,0} + \frac{s_{x,1}}{\sqrt{|\vec{p}_K|}} \qquad x = n, w \tag{7.15}$$

$$\tau_o(|\vec{p}_K|) = \tau_{o,0} + \frac{\tau_{o,1}}{|\vec{p}_K|}. \tag{7.16}$$

The right plot of figure 7.1 shows the resulting resolution model for a kaon with $|\vec{p}_K| = 1$ GeV/c.

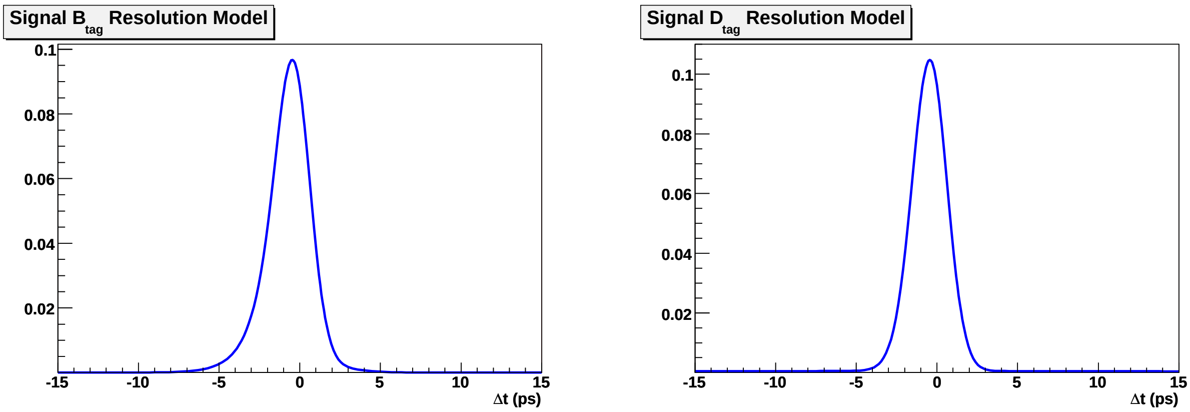

Figure 7.1: Resolution models for B_{tag} (left plot) and D_{tag} (right) signal events. The models shown are referred to a kaon with $|\vec{p}_K| = 1$ GeV/c.

7.4 Combinatorial B_{tag} ($B^0\overline{B}^0$)

For this category of events, the same pdf and resolution model described in section 7.2 is used. Given that in this case the (ℓ, π_{soft}) are uncorrelated the parameters τ_{B^0} and Δm_d have no direct physical interpretation but are used as two effective parameters.

7.5 Combinatorial B_{tag} (B^+B^-)

The pdf is a double exponential, decaying with an effective lifetime $\tau_{Bch,bkg}$.

The resolution model is defined as follows:

$$\begin{aligned} R_{Bch,bkg}(\delta\Delta t, \sigma\Delta t, |\vec{p}_K|) &= f_n\, exp\left(-\frac{(\delta\Delta t - o_n)^2}{2(s_n(|\vec{p}_K|)\,\sigma\Delta t)^2}\right) + \\ &+ f_w\, exp\left(-\frac{(\delta\Delta t - o_w)^2}{2(s_w(|\vec{p}_K|)\,\sigma\Delta t)^2}\right) + \\ &+ f_o\, exp\left(-\frac{(\delta\Delta t - o_o)^2}{2s_o^2}\right) \end{aligned} \tag{7.17}$$

$R_{Bch,bkg}(\delta\Delta t, \sigma\Delta t, |\vec{p}_K|)$ is convoluted with an exponential:

$$\mathcal{R}_{Bch,bkg}(\delta\Delta t, \sigma\Delta t, |\vec{p}_K|) = R_{Bch,bkg}(\delta\Delta t, \sigma\Delta t, |\vec{p}_K|) \otimes exp\left(-\frac{\delta\Delta t}{\tau_G}\right)$$

The only parameters depending on $|\vec{p}_K|$ are:

$$s_x(|\vec{p}_K|) = s_{x,0} + \frac{s_{x,1}}{\sqrt{|\vec{p}_K|}} \qquad x = n, w$$

7.6 Combinatorial D_{tag}

We use the same pdf found for signal D_{tag} events for both $B^0\overline{B}^0$ and B^+B^- combinatorial events. While we can use the same parameters for B^+B^- as for signal D_{tag}, we must use independent parameters for $B^0\overline{B}^0$ combinatorial events.

7.7 Peaking B_{tag}

The same pdf and resolution model used in 7.5 is also used for peaking background B_{tag} events, with the same dependence on $|\vec{p}_K|$ for s_n and s_o.

7.8 Peaking D_{tag}

The same resolution model used for signal D_{tag} is used (see section 7.3), forcing all the parameters to be the same for the two samples.

7.9 Continuum background

The pdf used for modeling the background originating from continuum events is a decaying exponential with effective lifetime τ_{off}.

The resolution model is very similar to the one used for signal B_{tag}:

$$\begin{aligned} R_{off}(\delta\Delta t, \sigma\Delta t, |\vec{p}_K|) &= f_n\, exp\left(-\frac{(\delta\Delta t - o_n)^2}{2(s_n(|\vec{p}_K|)\,\sigma\Delta t)^2}\right) + \\ &+ |1 - f_n - f_o|\, exp\left(-\frac{(\delta\Delta t - o_w)^2}{2(s_w(|\vec{p}_K|)\,\sigma\Delta t)^2}\right) + \\ &+ f_o\, exp\left(-\frac{(\delta\Delta t - o_o)^2}{2s_o^2}\right) \end{aligned} \tag{7.18}$$

$R_{off}(\delta\Delta t, \sigma\Delta t, |\vec{p}_K|)$ is convoluted with two exponentials:

$$\begin{aligned} \mathcal{R}_{off}(\delta\Delta t, \sigma\Delta t, |\vec{p}_K|) &= (1 - f_{G2})\, R_{off}(\delta\Delta t, \sigma\Delta t, |\vec{p}_K|) \otimes exp\left(-\frac{\delta\Delta t}{\tau_{G1}}\right) + \\ &+ f_{G2}\, R_{off}(\delta\Delta t, \sigma\Delta t, |\vec{p}_K|) \otimes exp\left(-\frac{\delta\Delta t}{\tau_{G2}}\right) \end{aligned} \tag{7.19}$$

The basic difference with respect to the resolution model used in signal B_{tag} events is that the only parameters depending on $|\vec{p}_K|$ are the widths of the narrow and wide gaussians:

$$s_x(|\vec{p}_K|) = s_{x,0} + \frac{s_{x,1}}{\sqrt{|\vec{p}_K|}} \qquad x = n, w$$

7.10 CP-eigenstates

A small subsample (roughly 1.2% of $B^0\overline{B}^0$) of our selected events originate from B^0 (either on the reconstructed or on the tag side) decays to CP-eigenstates (mostly $B^0 \to D^*\bar{D}^{(*)}$). Given that the probability of having a K^+ is equal to the one of having a K^- among its decay products and that there is interference between mixing and decay, these events need to be treated separately from the rest of B_{tag} B^0 decays.

When the kaon comes from the tag side, we model these decays with the usual pdf:

$$\mathcal{F}_{CP-eigen} = \frac{\Gamma}{4}e^{-\Gamma|\Delta t|}\left[1 \pm S_{eff}\sin(\Delta m_d \Delta t) \pm C_{eff}\cos(\Delta m_d \Delta t)\right] . \tag{7.20}$$

The + sign is used when the other B is tagged as a B^0 and - to the other B tagged as a $\overline{B}^0$ by means of the charge sign of either the lepton or the kaon. We take the same resolution model we use for the other B^0 B_{tag} events.

When the kaon is a D_{tag} one, we use the same pdf's and resolution models used for (peaking or combinatorial) non-CP decays.

Given the smallness of this sample, we fit the C_{eff} and S_{eff} parameters to the Monte Carlo and fix their values on the nominal fit to the data.

Chapter 8

Validation on Monte Carlo

In this chapter, we describe the different steps of the validation of our fit model on Monte Carlo. Apart from sub-sections 8.8 and 8.9, the samples used in this section correspond to generic Run1-4 Monte Carlo.

Throughout this chapter, every fit is performed keeping $|q/p|-1$, $\Delta\Gamma$, b and c fixed to 0, the value used in the generation of generic MC.

We also report the values of tagging and reconstruction asymmetries; for the latter, we separate the cases when the B_{rec} lepton is an electron from the muon case.

The purpose of some of the fits which are shown here, is just to debug our fit code, therefore we report the results even if a fit has not properly converged and the errors associated to the parameters are not realistic.

8.1 Signal B_{tag} - true Δt, true tag

As a first step of the validation process, we fit signal B_{tag} events using the Monte Carlo truth for both Δt and the flavor of B_{tag}.

Table 8.1: Results of the fit to generic B_{tag} Run1-4 MC, using true Δt and the true flavor of B_{tag}.

Parameter	Generated value	Fit result
τ_{B^0}	1.540	1.5303 ± 0.0008
Δm_d	0.489	0.4856 ± 0.0002
A_{tag}	-	0.0130 (fixed)
$A_{rec}(e)$	-	0.0020 (fixed)
$A_{rec}(\mu)$	-	0.0070 (fixed)

We let τ_{B^0} and Δm_d as the only free parameters in the fit. Results are in good agreement with expectations and are reported in table 8.1 and in figure 8.1.

8.2 Signal B_{tag} - true Δt, experimental tag

Table 8.2 and figure 8.2 summarize the results of the fit on signal B_{tag} sample, using the MC truth for Δt, but considering the experimental dilution.

Besides τ_{B^0} and Δm_d only the parameters D_0, D_1 and $\Delta\omega$ are left floating in the fit. Again, the fit results are consistent with expectations.

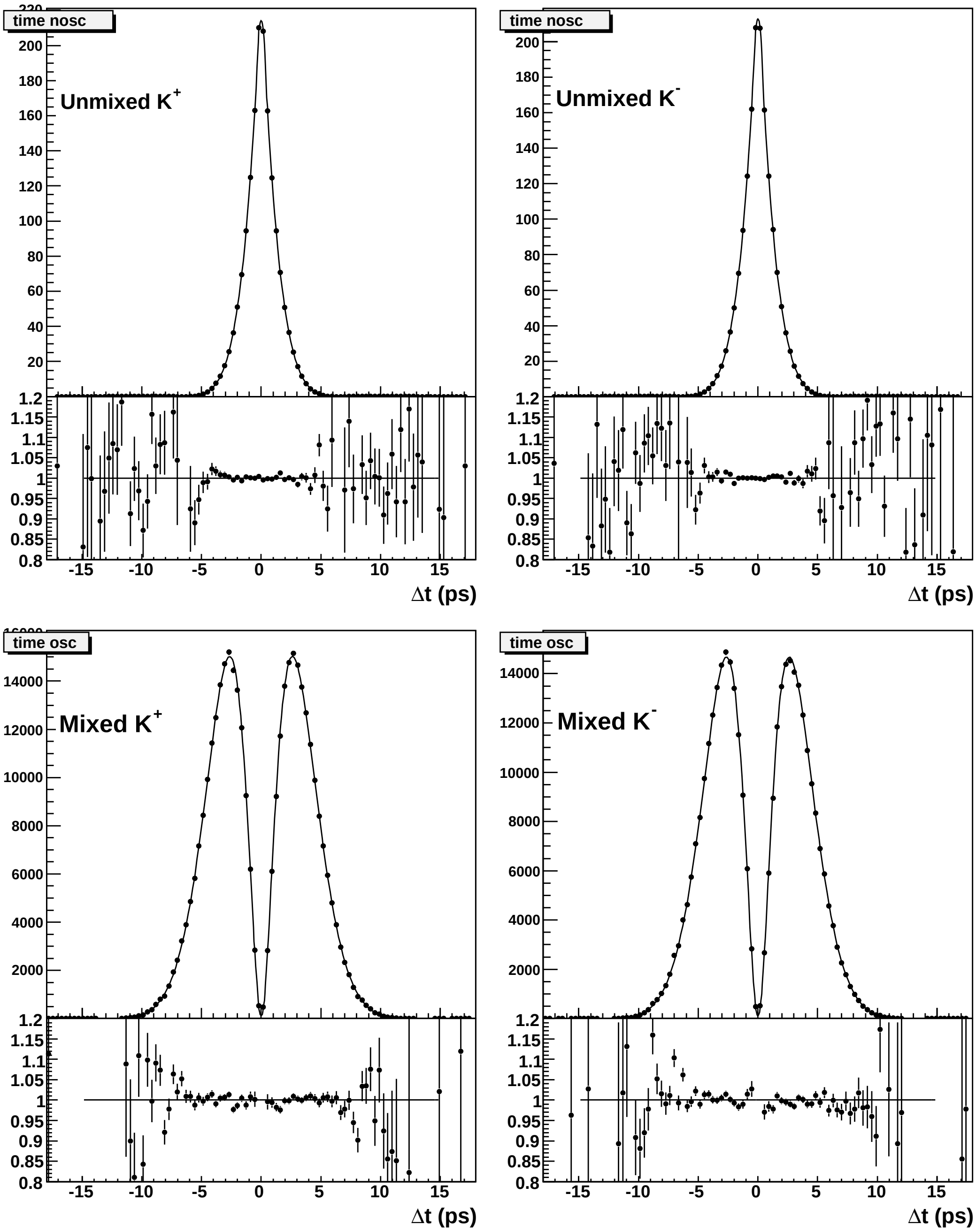

Figure 8.1: Fitted distributions for the four samples (top plots). The generated Δt value has been used and B_{tag} has been tagged using the MC truth. The box at the bottom of each plot shows the ratio between the histograms and the fitted pdf's.

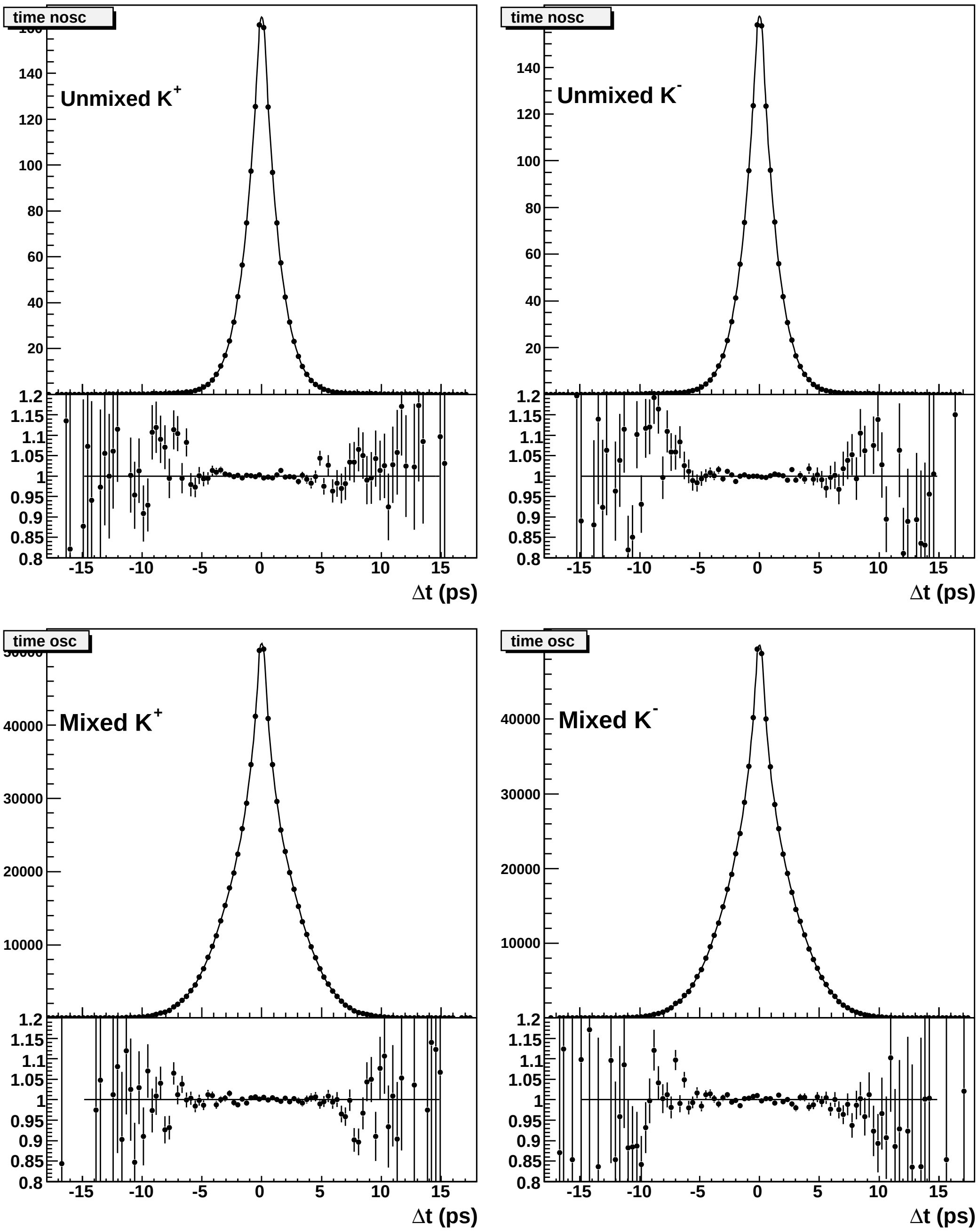

Figure 8.2: Fitted distributions for the four samples (top plots). The generated Δt value has been used, while the flavor of B_{tag} is determined with the experimental dilution. The box at the bottom of each plot shows the ratio between the histograms and the fitted pdf's.

Table 8.2: Results of the fit to generic B_{tag} Run1-4 MC, using true Δt and the flavor of $B_{tag}$is determined considering the experimental dilution.

Parameter	Fit result
τ_{B^0}	1.5298 ± 0.0009
Δm_d	0.4824 ± 0.0006
A_{tag}	0.0146 ± 0.0018
$A_{rec}(e)$	0.0029 ± 0.0009
$A_{rec}(\mu)$	0.0074 ± 0.0010
D_0	0.3988 ± 0.0017
D_1	0.1731 ± 0.0021
$\Delta\omega$	0.0033 ± 0.0015

8.3 Signal B_{tag} - measured Δt, true tag

We repeat the fit by using the Monte Carlo truth information for the flavor of B_{tag} and the measured value of Δt, leaving the parameters of the resolution floating. Results are reported in table 8.3 and figure 8.3.

Table 8.3: Results of the fit to generic B_{tag} Run1-4 MC, using measured Δt and the true flavor of B_{tag}.

Parameter	Fit result
τ_{B^0}	1.5286 ± 0.0013
Δm_d	0.4839 ± 0.0006
A_{tag}	0.0113 (fixed)
$A_{rec}(e)$	-0.0002 (fixed)
$A_{rec}(\mu)$	0.0090 (fixed)
f_n	0.9050 ± 0.0022
f_o	0.0048 (fixed)
o_n	0.0114 ± 0.0012
o_w	-0.1862 ± 0.0113
o_o	0.0000 (fixed)
$s_{n,0}$	0.5911 ± 0.0050
$s_{n,1}$	0.3838 ± 0.0037
$s_{w,0}$	1.1537 ± 0.0360
$s_{w,1}$	1.0881 ± 0.0275
s_o	11.35 (fixed)
f_{G2}	0.3973 ± 0.0029
τ_{G1}	0.0996 ± 0.0057
$\tau_{G2,0}$	0.9925 ± 0.0088
$\tau_{G2,1}$	-0.0752 ± 0.0033

8.4 Signal B_{tag} - measured Δt, experimental tag

We now fit the B_{tag} sample using the reconstructed Δt and the realistic tagging. All the parameters separately left free in the two previous stages of the validation are floating.

The results are reported in table 8.4 and figure 8.4.

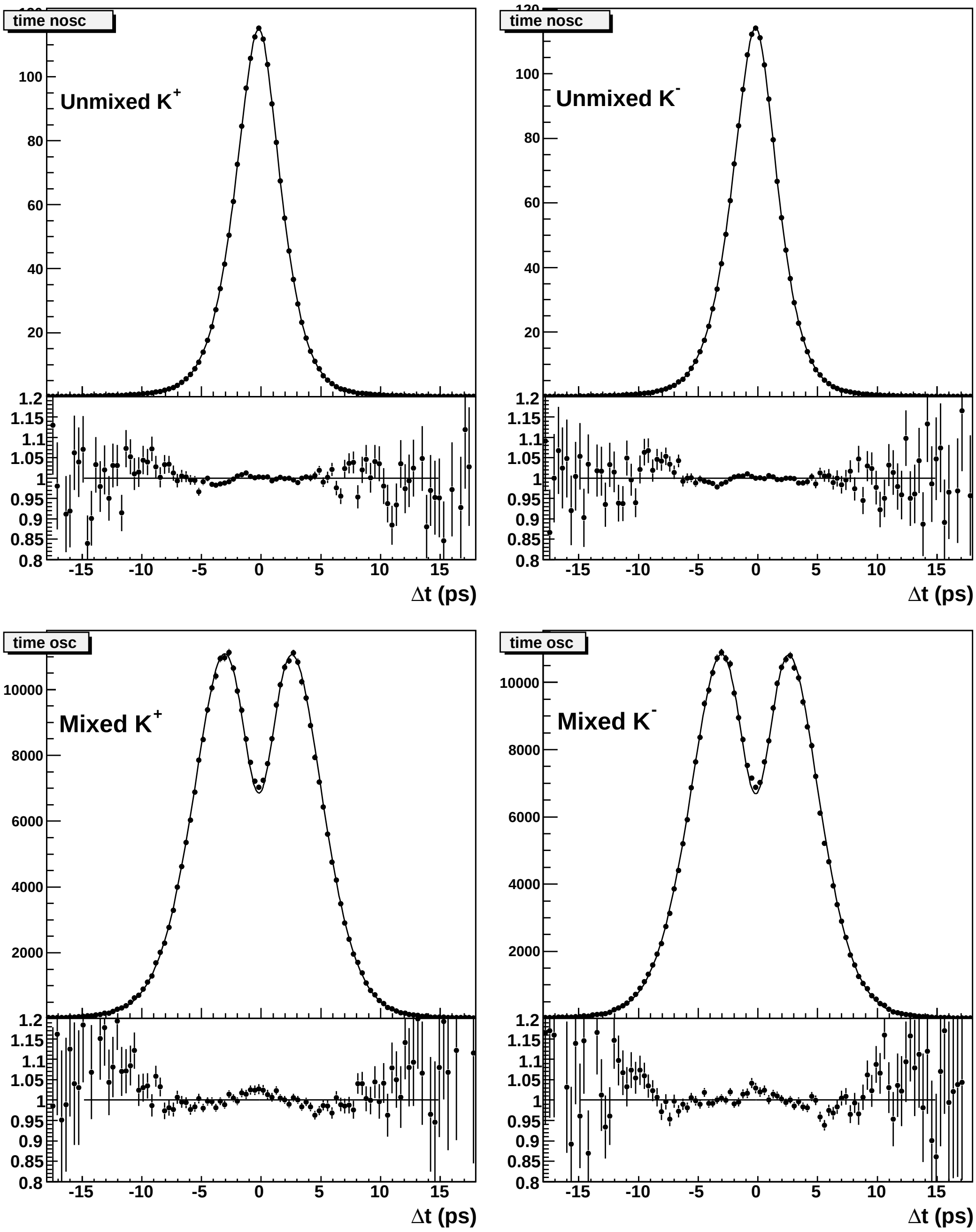

Figure 8.3: Fitted distributions for the four samples (top plots). The measured Δt value has been used, while the flavor of B_{tag} is got from MC truth. The box at the bottom of each plot shows the ratio between the histograms and the fitted pdf's.

Table 8.4: Results of the fit to generic B_{tag} Run1-4 MC, using measured Δt and realistic tagging.

Parameter	Fit result
τ_{B^0}	1.5324 ± 0.0016
Δm_d	0.4786 ± 0.0011
A_{tag}	0.0134 ± 0.0023
$A_{rec}(e)$	0.0025 ± 0.0010
$A_{rec}(\mu)$	0.0070 ± 0.0011
D_0	0.3720 ± 0.0032
D_1	0.2089 ± 0.0038
$\Delta\omega$	-0.0087 ± 0.0003
f_n	0.9071 ± 0.0026
f_o	0.0048 (fixed)
o_n	0.0122 ± 0.0014
o_w	-0.1848 ± 0.0128
o_o	0.0000 (fixed)
$s_{n,0}$	0.5639 ± 0.0046
$s_{n,1}$	0.3997 ± 0.0034
$s_{w,0}$	1.0895 ± 0.0328
$s_{w,1}$	1.1615 ± 0.0224
s_o	11.35 (fixed)
f_{G2}	0.3964 ± 0.0032
τ_{G1}	0.1003 ± 0.0068
$\tau_{G2,0}$	0.9915 ± 0.0102
$\tau_{G2,1}$	-0.0674 ± 0.0042

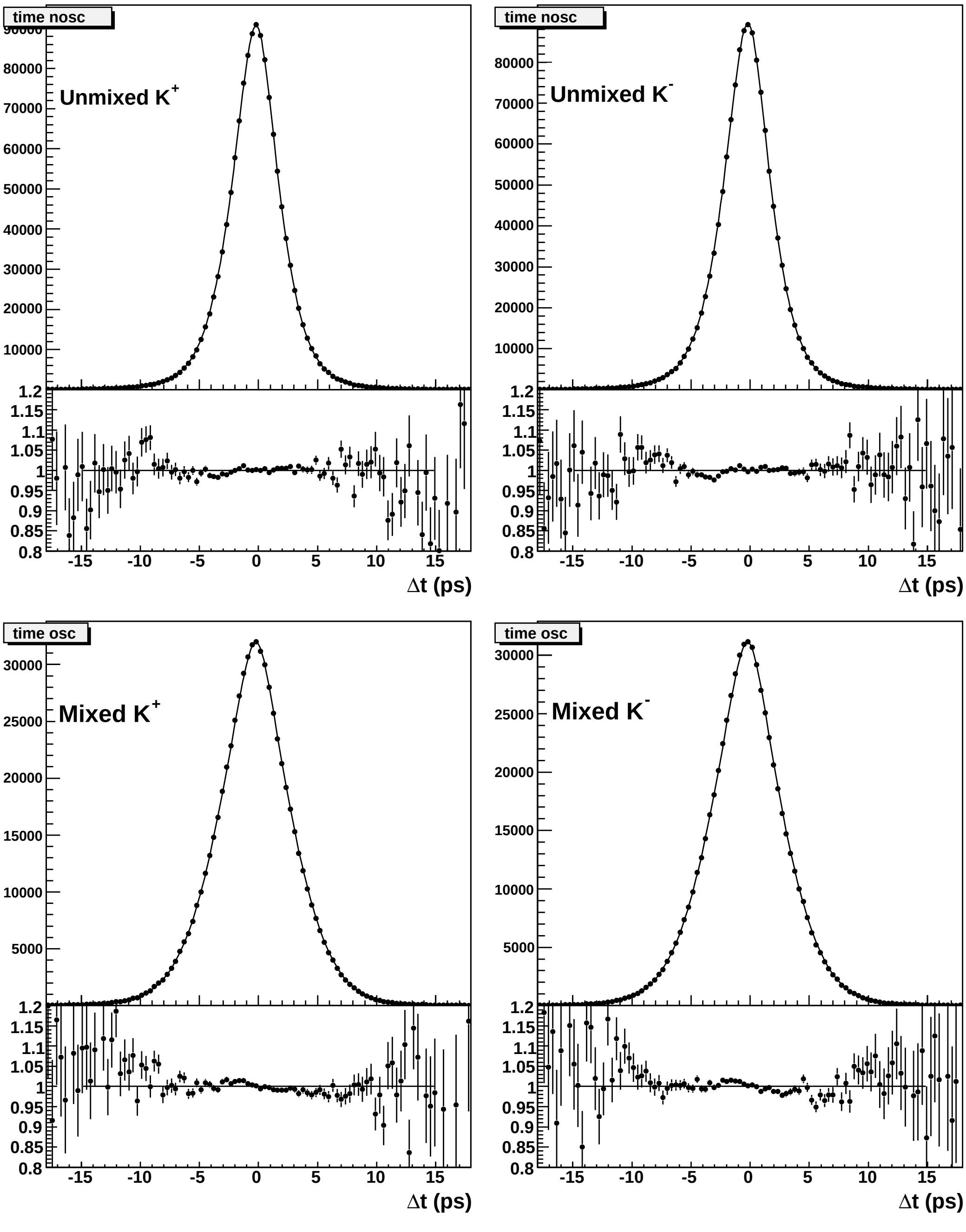

Figure 8.4: Fitted distributions for the four samples (top plots). The measured Δt value has been used and the flavor of B_{tag} is determined with the experimental dilution. The box at the bottom of each plot shows the ratio between the histograms and the fitted pdf's.

8.5 Signal D_{tag} - measured Δt, experimental tag

We apply the pdf and the resolution model described in section 7.3 to fit only signal D_{tag} events. The generic Run1-4 Monte Carlo has been used; results are shown in table 8.5 and figure 8.5.

Table 8.5: Results of the fit to signal D_{tag} on generic Run1-4 MC, using measured Δt and realistic tagging.

Parameter	Fit result
A_{tag}	0.0071 ± 0.0006
$A_{rec}(e)$	0.0062 ± 0.0008
$A_{rec}(\mu)$	0.0122 ± 0.0010
D_0	0.4083 (fixed)
D_1	0.1961 (fixed)
$\Delta\omega$	-0.0092 (fixed)
f_{nn}	0.0980 ± 0.0002
f_n	0.9237 ± 0.0003
f_o	0.0351 ± 0.0003
o_{nn}	0.0714 ± 0.0048
o_n	-0.1051 ± 0.0013
o_w	-0.3251 ± 0.0136
o_o	1.4675 ± 1.1398
s_{nn}	0.7028 ± 0.0017
$s_{n,0}$	0.6044 ± 0.0009
$s_{n,1}$	0.4330 ± 0.0006
$s_{w,0}$	1.0922 ± 0.0113
$s_{w,1}$	1.2415 ± 0.0097
s_o	24.212 ± 0.0034
τ_{nn}	0.0441 ± 0.0006
τ_n	0.3992 ± 0.0012
τ_w	0.8403 ± 0.0103
$\tau_{o,0}$	1.6898 ± 0.0002
$\tau_{o,1}$	0.0029 ± 0.0002

8.6 $B\overline{B}$ combinatorial - measured Δt, experimental tag

In this section we show (without numerical outputs) the results of the fits of each background components, using the pdf's and the resolution models described in section 7.

Figures 8.6-8.9 show the fitted distributions for the various $B\overline{B}$ combinatorial samples.

8.7 Peaking B^+B^- - measured Δt, experimental tag

Figure 8.10 shows the fitted distributions of peaking B^+B^- B_{tag} events.

We fit the distributions of D_{tag} events coming from $B^\pm$ decays using the same model which describes the signal D_{tag} sample.

Figure 8.11 shows the Δt distributions of peaking D_{tag} events with overlaid the fitting function obtained for the signal D_{tag} sample. It can be seen that the agreement is pretty good and justifies the choice of using the same model for the two parameters.

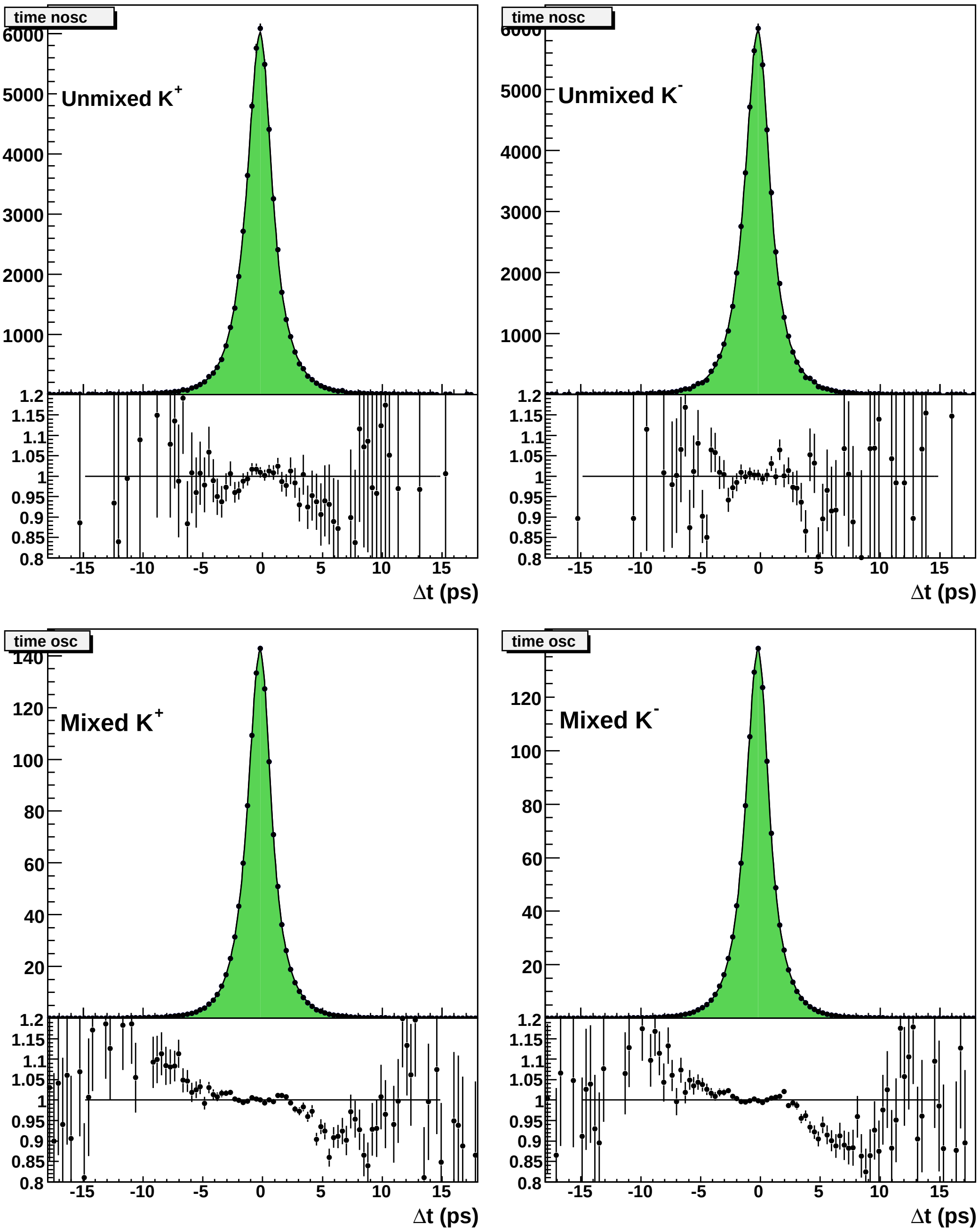

Figure 8.5: Fitted distributions for the four samples (top plots) of signal D_{tag} events. The bottom box under each plot shows the ratio between the histograms and the fitted pdf's.

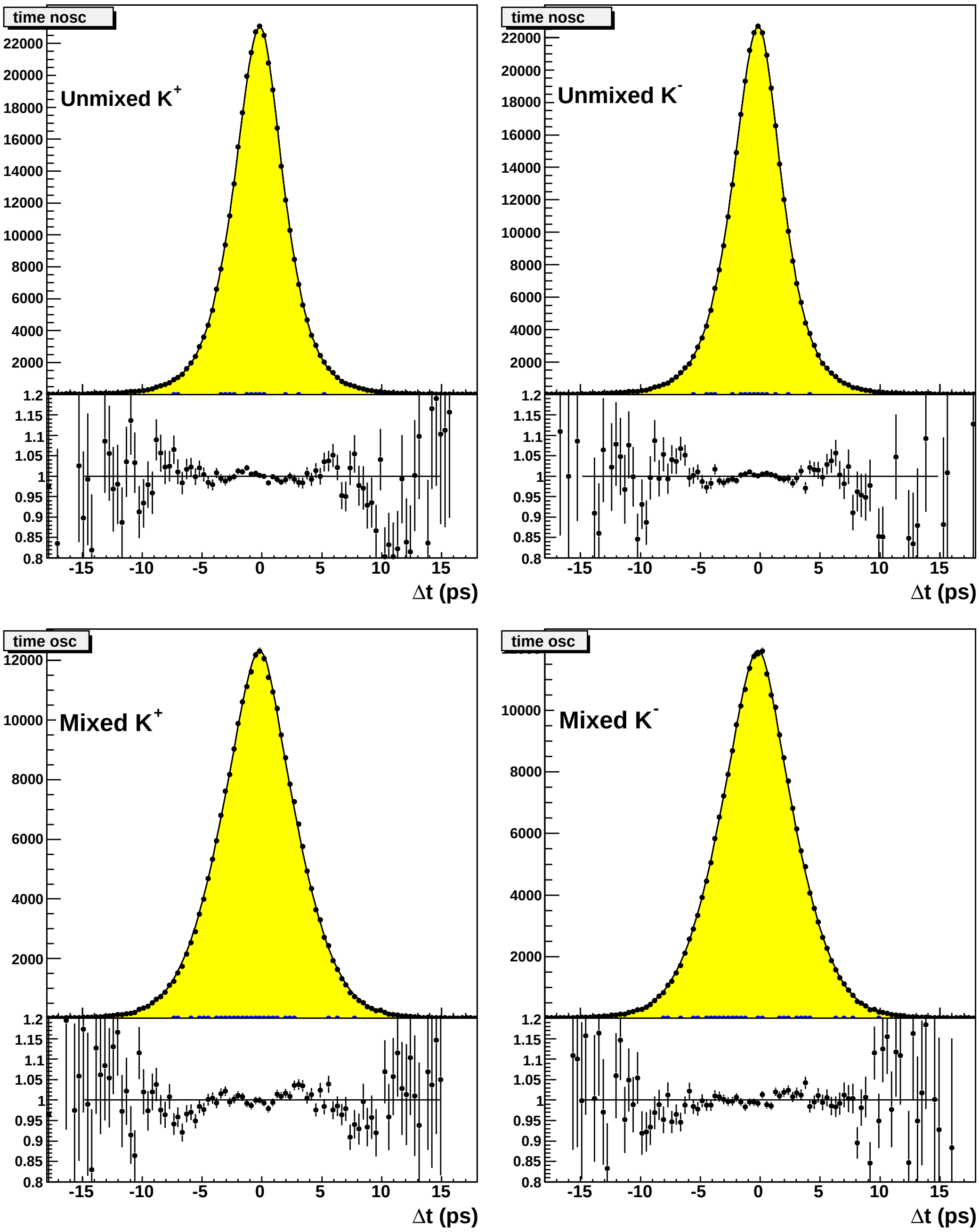

Figure 8.6: Fitted distributions for $B^0\overline{B}^0$ combinatorial B_{tag} events. The bottom box under each plot shows the ratio between the histograms and the fitted pdf's.

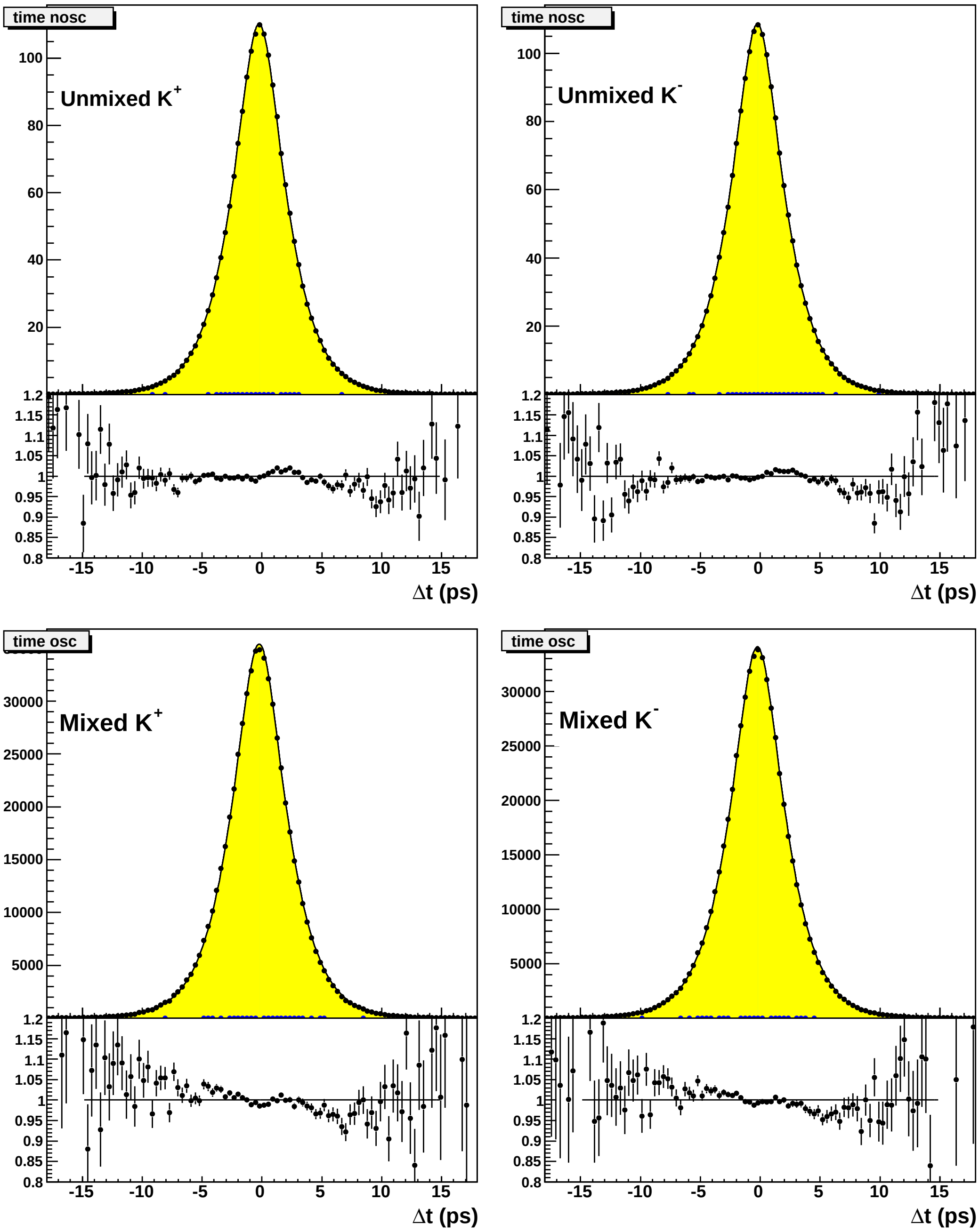

Figure 8.7: Fitted distributions for B^+B^- combinatorial B_{tag} events. The bottom box under each plot shows the ratio between the histograms and the fitted pdf's.

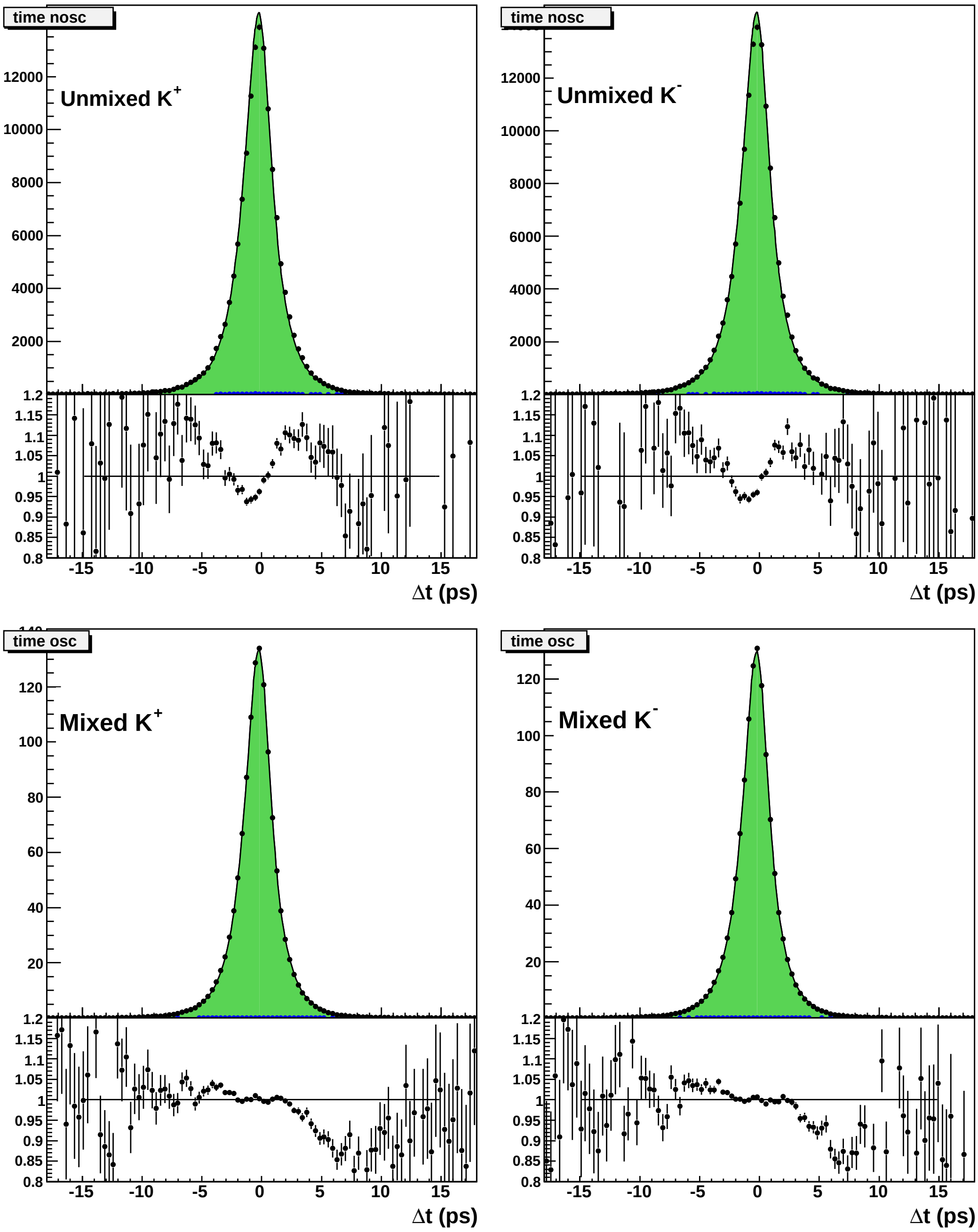

Figure 8.8: Fitted distributions for $B^0\overline{B}^0$ combinatorial D_{tag} events.

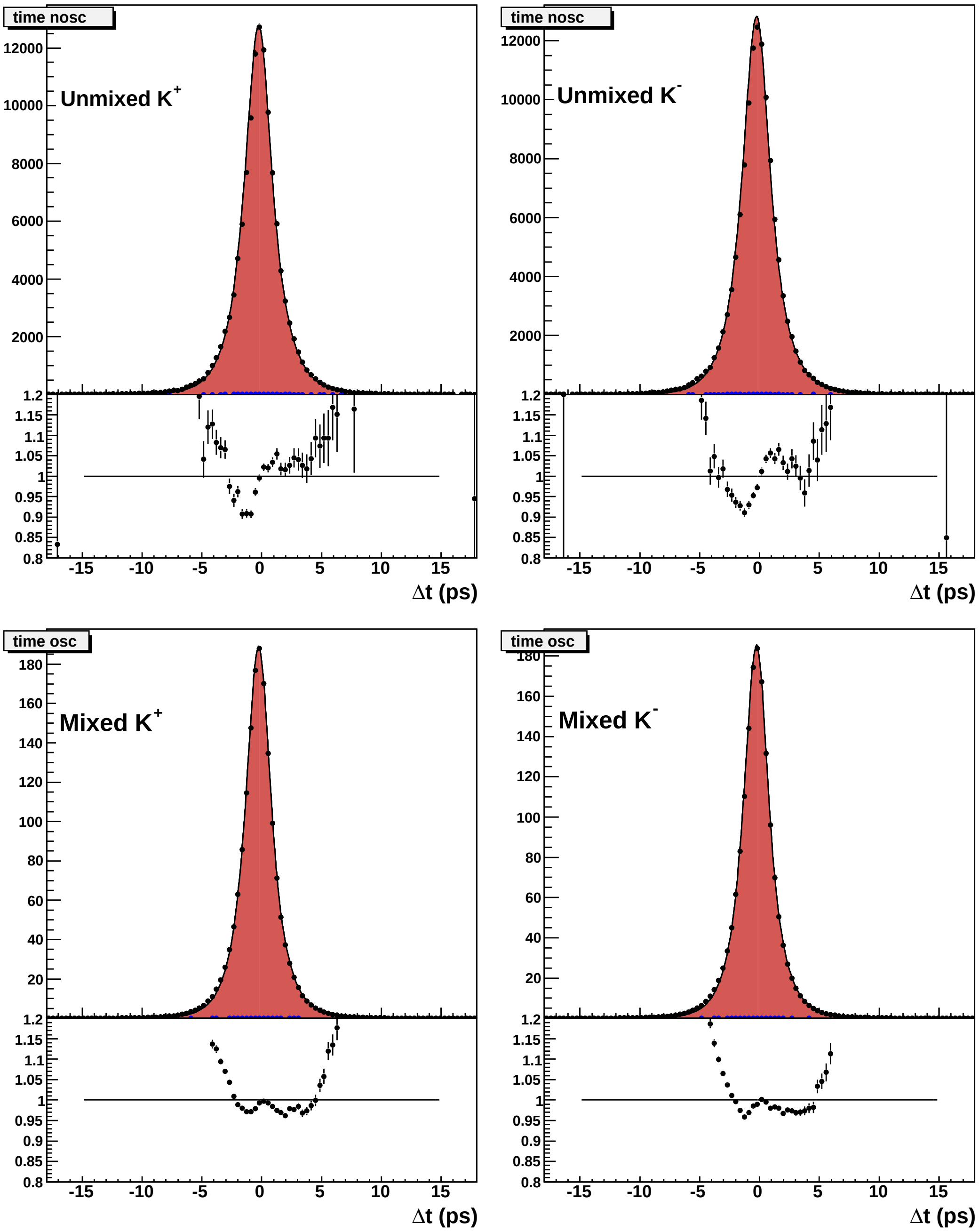

Figure 8.9: Fitted distributions for B^+B^- combinatorial D_{tag} events. The bottom box under each plot shows the ratio between the histograms and the fitted pdf's.

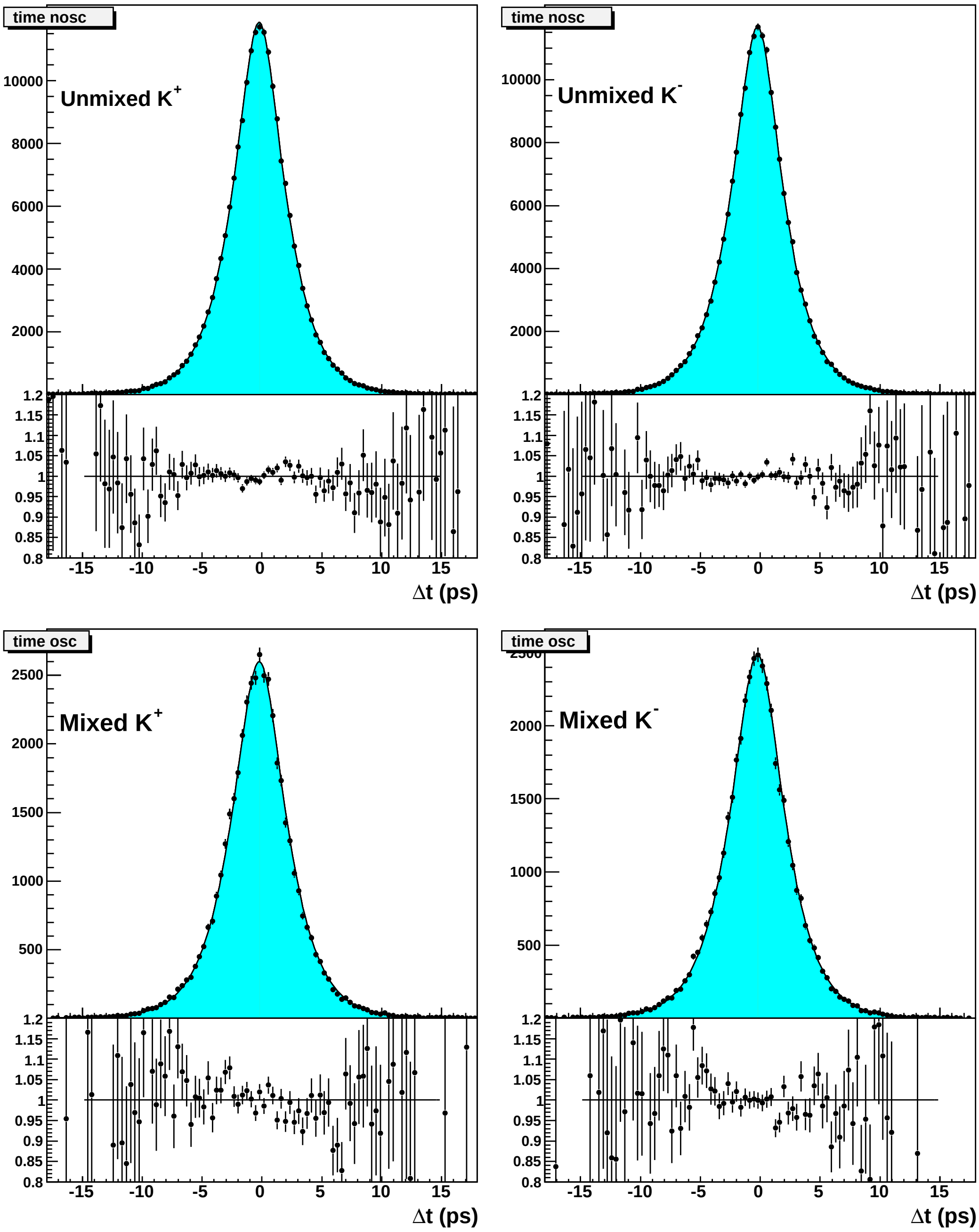

Figure 8.10: Fitted distributions for B^+B^- peaking B_{tag} events. The bottom box under each plot shows the ratio between the histograms and the fitted pdf's.

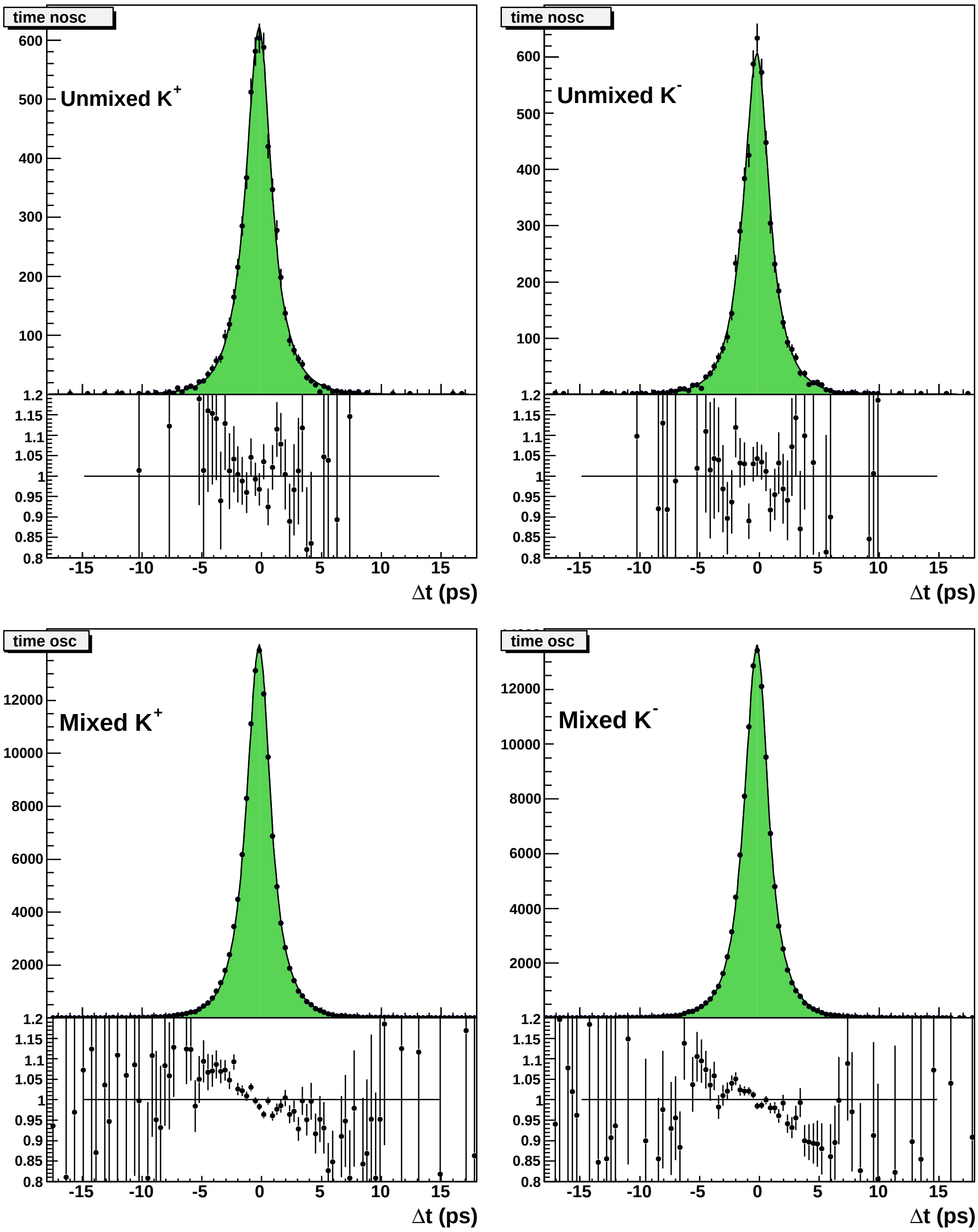

Figure 8.11: Distributions for the four samples (top plots) of B^+B^- peaking D_{tag} events with overloaded the fitting function found for the signal D_{tag} sample. The bottom box under each plot shows the ratio between the histograms and the fitted pdf's.

We conclude the discussion on the $B\overline{B}$ components observing that, while the description is satisfactory for the B_{tag} components, the discrepancies in the tails and in the position of the maxima in the D_{tag} components are quite sizable. This motivated the choice to model the shape of the D_{tag} components from the data, as explained in chapter 10.

8.8 Continuum background

We use the off-peak data sample to study the contribution of *continuum* events.

Table 8.6 and figure 8.12 show the results of a fit to off-peak Run1-4 events, using the pdf and the resolution model described in 7.9.

Table 8.6: Results of the fit to off-peak events. The bottom box under each plot shows the ratio between the histograms and the fitted pdf's.

Parameter	Fit result
τ_{off}	0.4431 ± 0.0055
f_n	0.8097 ± 0.0087
f_o	0.0200 ± 0.0006
o_n	-0.0249 ± 0.0050
o_w	-0.1442 ± 0.0283
o_o	0. (fixed)
$s_{n,0}$	0.5840 ± 0.0200
$s_{n,1}$	0.3610 ± 0.0167
$s_{w,0}$	2.1348 ± 0.0263
$s_{w,1}$	0.0000 ± 0.0006
s_o	6.1610 ± 0.0001
f_{G2}	0.2997 ± 0.3856
τ_{G1}	0.0000 ± 0.0025
τ_{G2}	0.1000 ± 1.1033

8.9 CP-eigenstates

Several components of B decays to CP-eigenstates are present in our sample: the $(\ell,\ \pi_{soft})$ pair can be either signal or combinatorial, the B decaying to a CP-eigenstate can be in the tag side or in the decay side and finally the candidate kaon can be either a B_{tag} one or a D_{tag} one.

As explained in section 7.10, D_{tag} kaons are fitted with the same pdf's used for non-CP B decays, while for B_{tag} kaons we use a pdf containing the two effective parameters C_{eff} and S_{eff}.

In figure 8.13 we show the result of our fit to the CP-eigenstates on the decay side on the full Run1-5 Monte Carlo statistics. In figure 8.14 we show the same plots for CP-eigenstates on the tag side.

Finally, in figure 8.15 we show the fit on the sum of all CP-eigenstates events. The results we get on C_{eff} and S_{eff} (reported in table 8.7) are the ones we actually use (keeping them fixed) in the nominal fit.

Systematic uncertainties will be estimated by varying those parameters inside an interval which covers our uncertainty in their determination (see section 12.7).

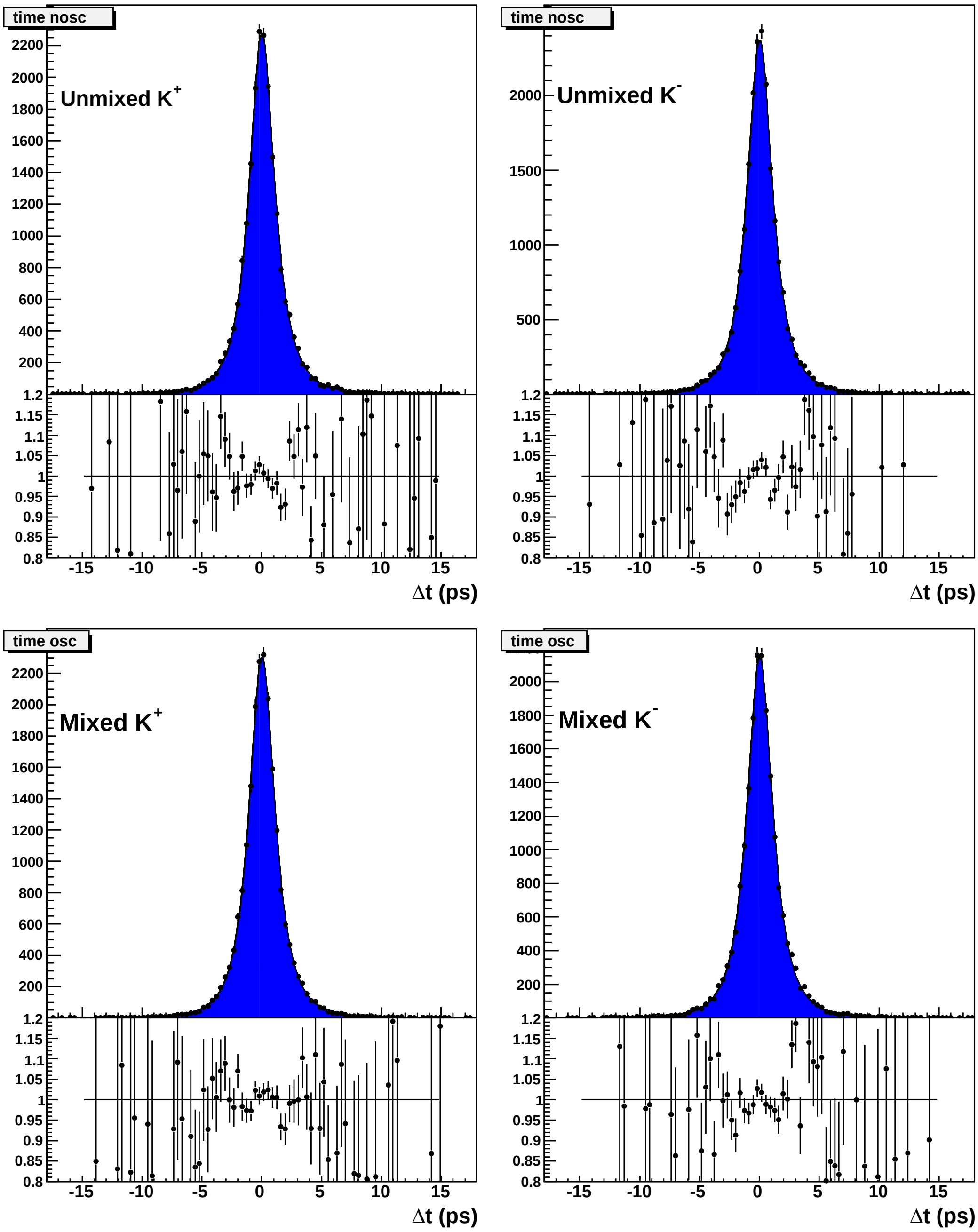

Figure 8.12: Fitted distributions for the four samples and the asymmetry for off-peak events.

Table 8.7: Results of the fit to CP-eigenstates.

Parameter	Fit result
C_{eff}	-0.0144 ± 0.0066
S_{eff}	-0.0780 ± 0.0056

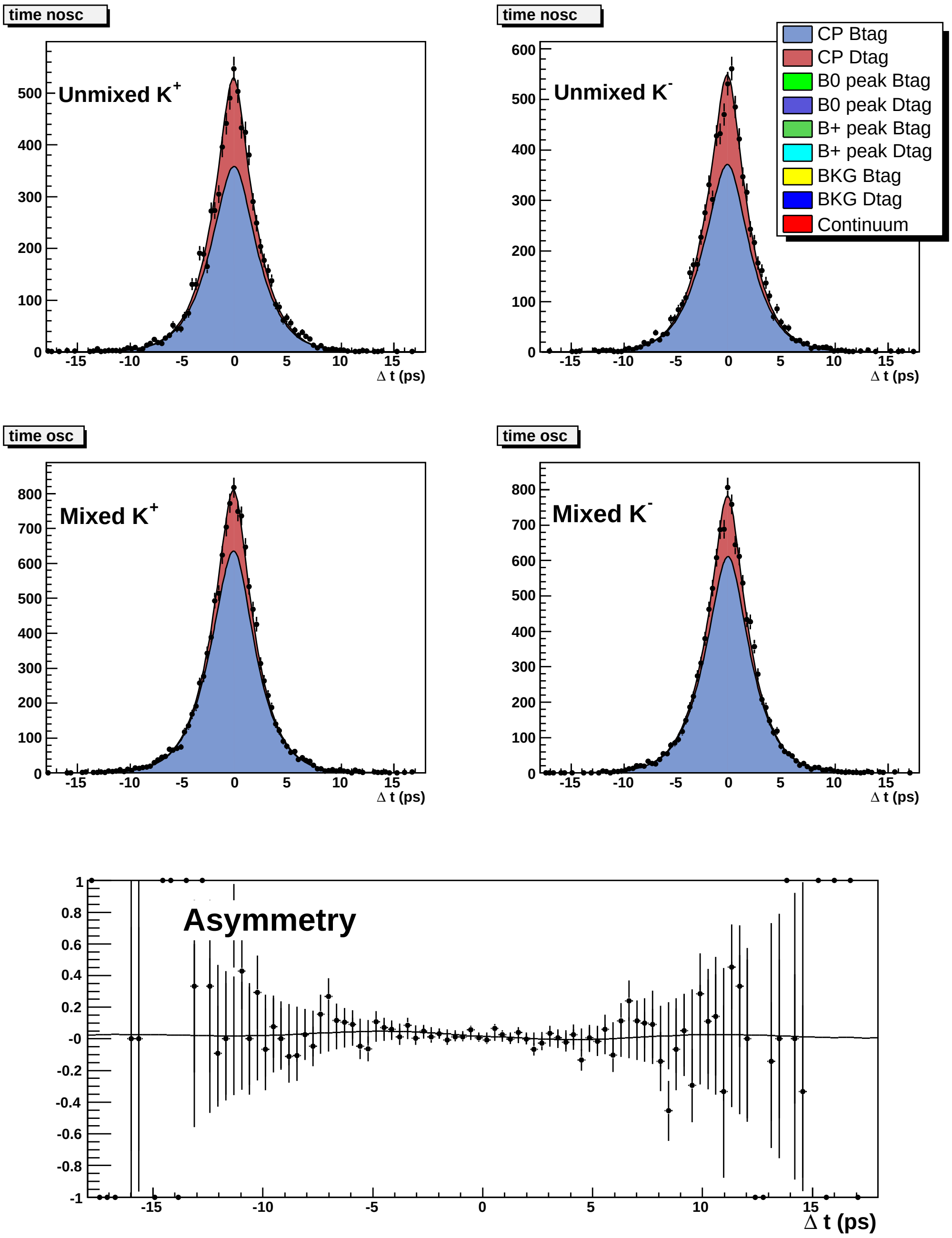

Figure 8.13: Fitted distributions for the four samples and the asymmetry for CP-eigenstates events in the decay side.

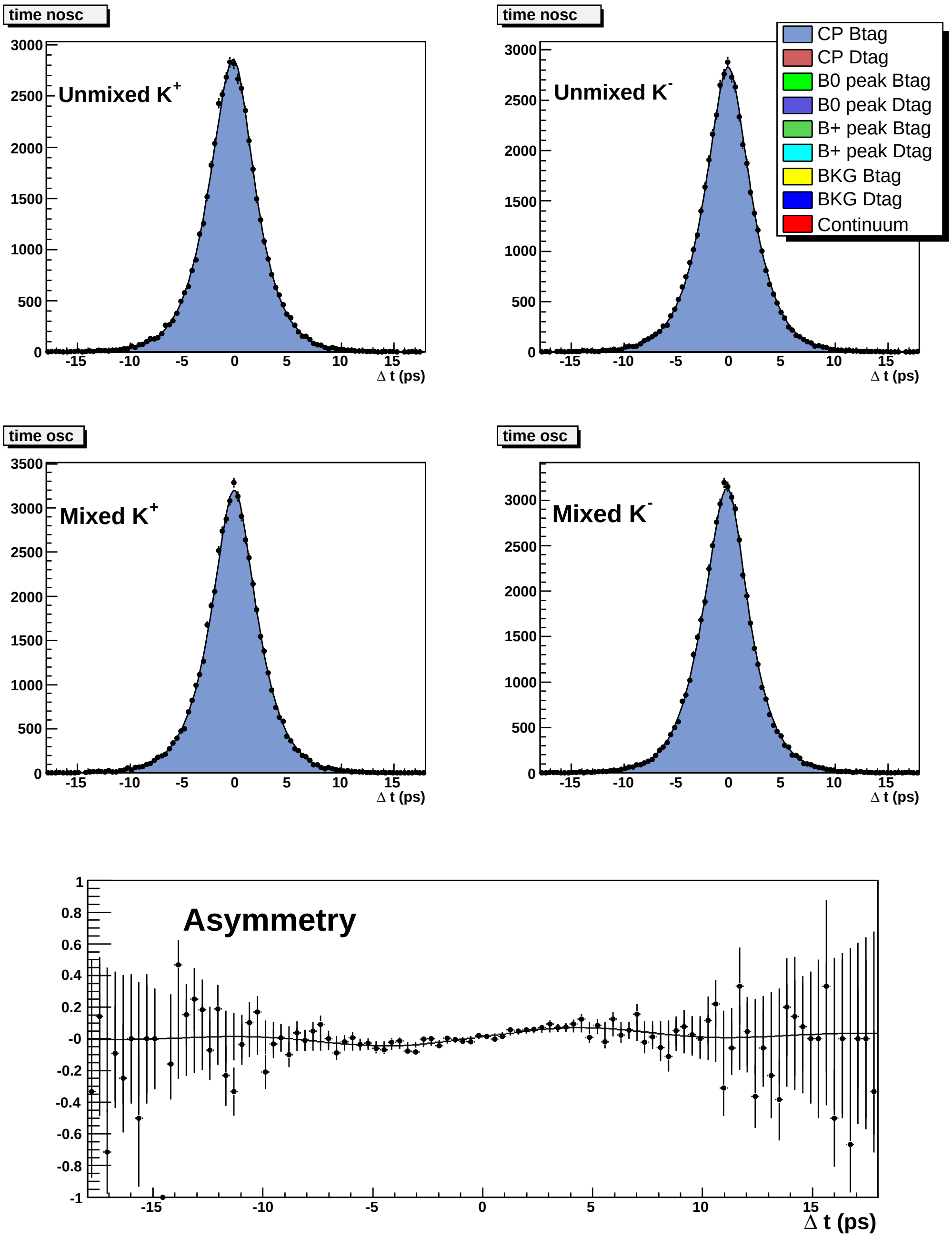

Figure 8.14: Fitted distributions for the four samples and the asymmetry for CP-eigenstates events in the tag side.

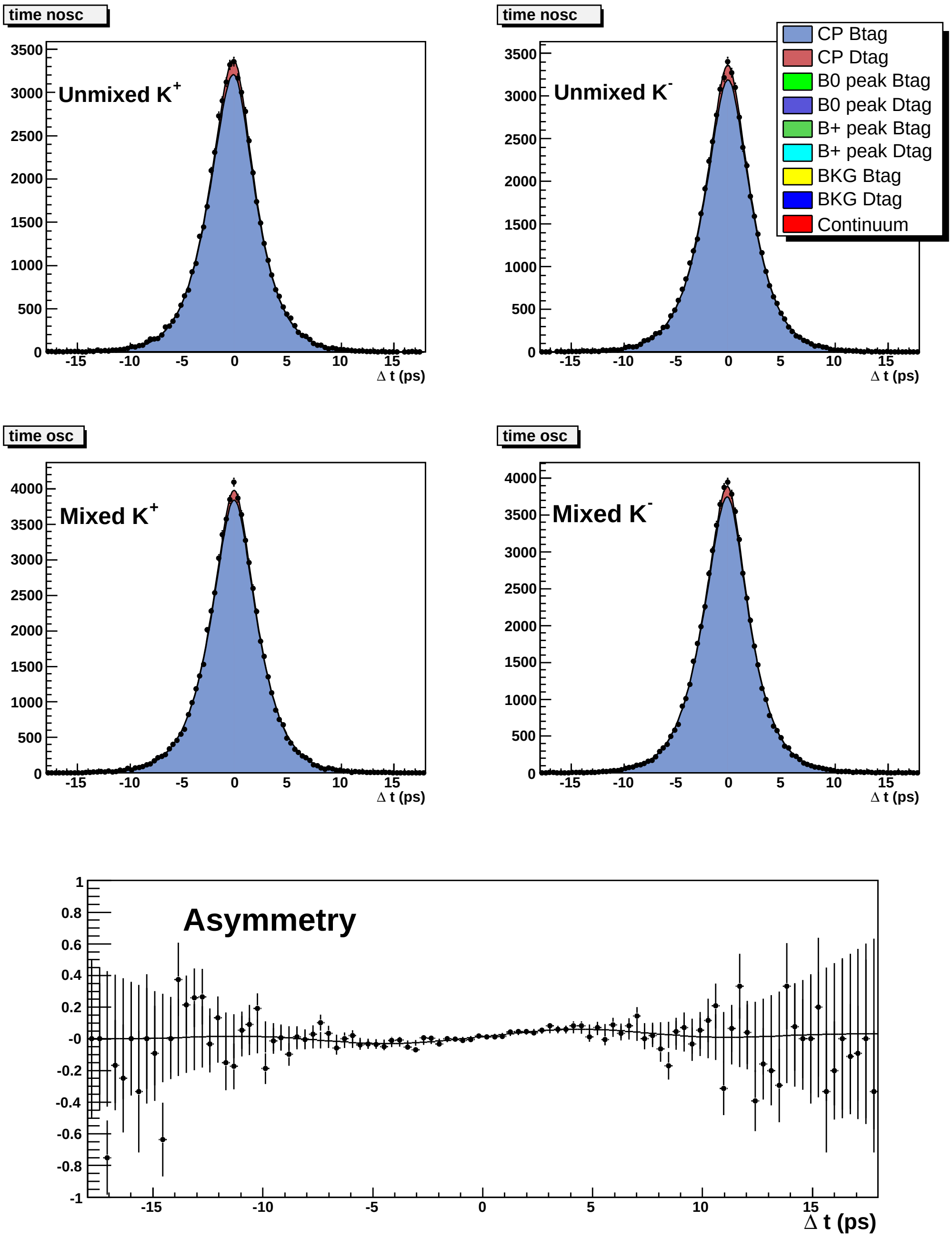

Figure 8.15: Fitted distributions for the four samples and the asymmetry for the sum of all the CP-eigenstates events.

8.10 Test on Fitted Asymmetries

We validate the test on charge asymmetries performed on section 6.3, by comparing the fit results for $A_{rec}(e)$, $A_{rec}(\mu)$ and A_{tag} obtained by separately fitting each of the eight Monte Carlo samples, keeping $|q/p|$ fixed to 1.

Results are shown in figures 8.16 and 8.17. The agreement we find for every sample is impressively good, with deviations with respect to the average well within 2.5 σ.

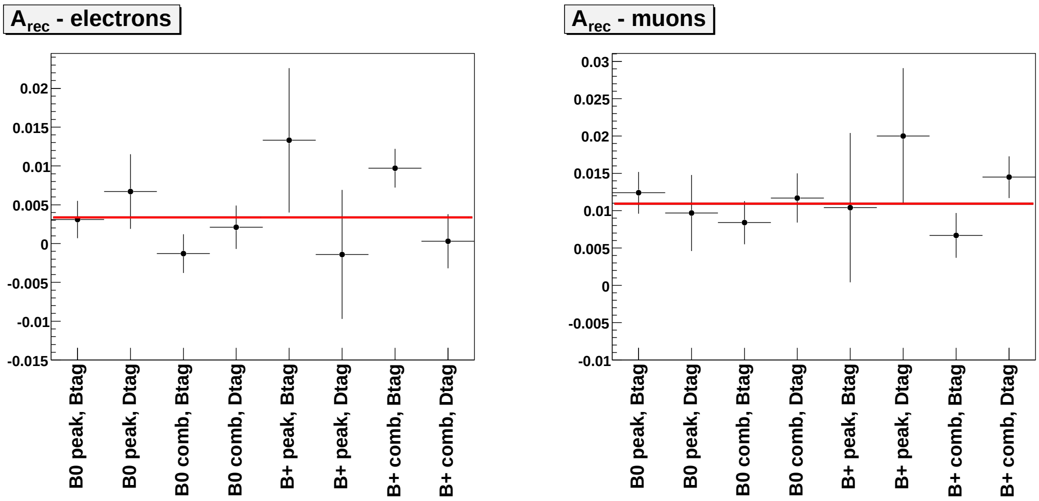

Figure 8.16: Reconstruction asymmetries $A_{rec}(e)$ (left plot) and $A_{rec}(\mu)$ (right) for the 8 Monte Carlo samples. The red line represents the weighted average of the asymmetries.

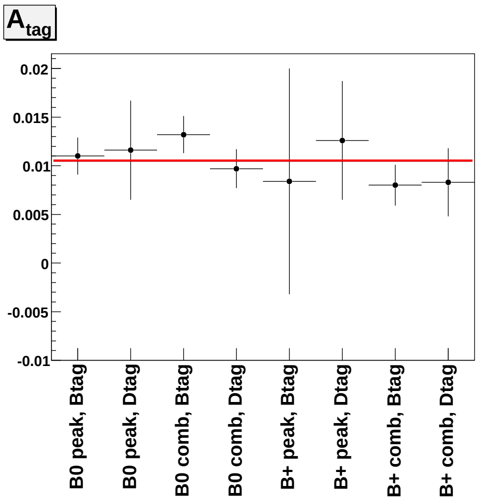

Figure 8.17: Reconstruction asymmetries A_{tag} for the 8 Monte Carlo samples. The red line represents the weighted average of the asymmetries.

Chapter 9

Validation on Toy and Reweighted Monte Carlo

Given the very large number of events we select in our analysis, it is not possible to generate signal Monte Carlo samples of adequate size. The validation of the fitting technique therefore proceeds on Toy or Reweighted Monte Carlo generated data samples.

9.1 Continuum

Monte Carlo samples of continuum events are generated from real off-peak data events according to the procedure which is explained in the following.

For each event, we consider the variables: $|\vec{p}_K|$, Δt, $\cos(\theta_{K\ell})$ and m_ν^2. For each of the above variables x_i, we define a gaussian pdf $G_i(x_i, \sigma_i)$, with mean value x_i and width σ_i. The value of σ_i is fixed for every event and is chosen empirically as the bin width of a histogram where the statistical fluctuations of x_i become evident. Each $G_i(x_i, \sigma_i)$ is used to generate the variable x_i'.

With this procedure, the generated event, with variables ($|\vec{p}_K|'$, $\Delta t'$, $\cos(\theta_{K\ell})'$, $m_\nu^2{}'$), is *close* to the original one in the 4-dimensional parameter space and the correlations between the variables are preserved.

Figure 9.1 shows the comparison between the original distributions got from *off-peak* data events and the generated ones for the four variables of interest.

9.2 Generation of Toy MC with non-zero CP-violating parameters

We select several samples of Monte Carlo events with non-zero CP-violating parameters by selectively discarding events from the initial generic MC sample.

The probability of keeping a $B\overline{B}$ event with generated difference of decay times of the two B mesons Δt_{true} is computed from the ratio of the Δt pdf with non-zero CP-violating parameters with the original one ($|q/p| = 1$, $b = c = 0$). In order to avoid the divergences which arise where the original pdf is zero and the modified one is not, we compute the ratio of the integrals of the two pdf's in 0.5 ps wide bins (significantly smaller than our resolution in Δt).

Figure 9.2 shows the distributions of the probability of keeping a $B^0\overline{B}^0$ event as a function of (the generated) Δt. No significant effects are expected to originate from the pretty large discontinuities in correspondence of the zeroes of the original pdf, as long as the realistic resolution is used in the fits.

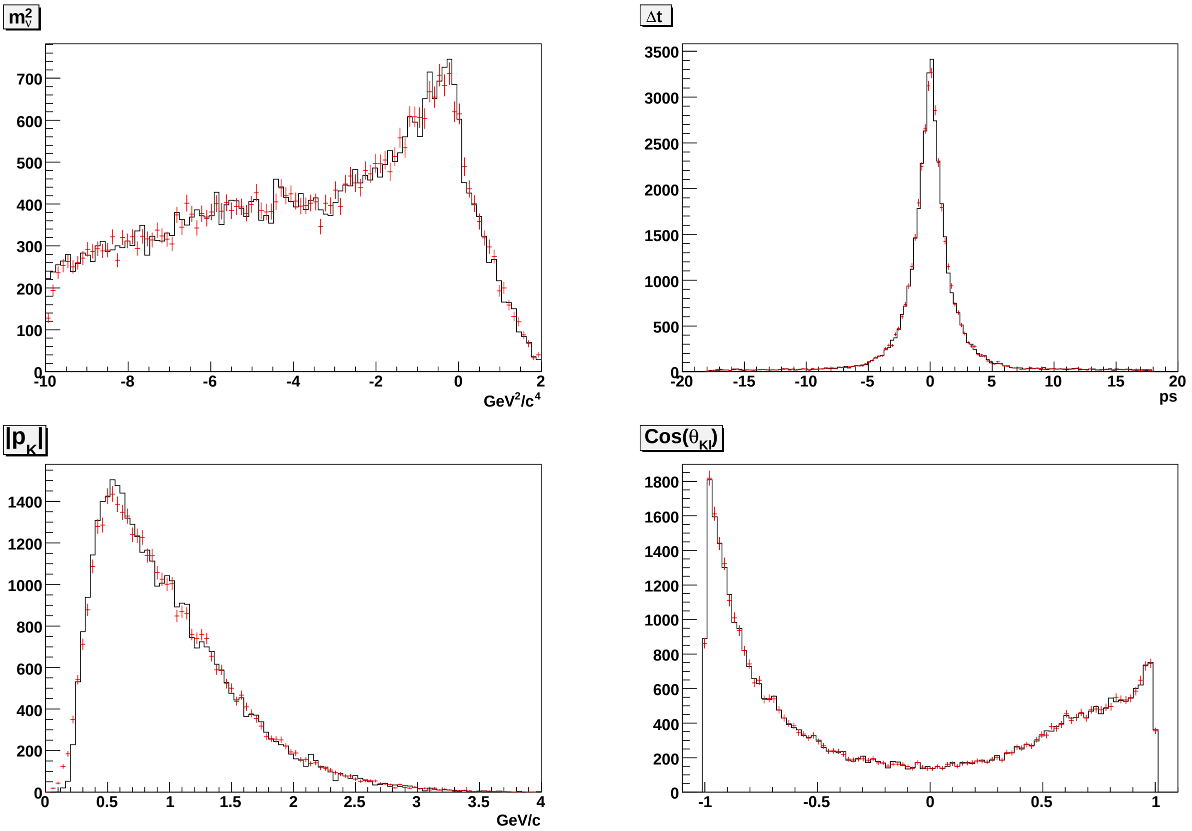

Figure 9.1: Original *off-peak* distributions (histograms) and modified ones (data points) for m_ν^2 (top left plot), Δt (top right), $|\vec{p}_K|$ (bottom left) and $\cos(\theta_{K\ell})$ (bottom right).

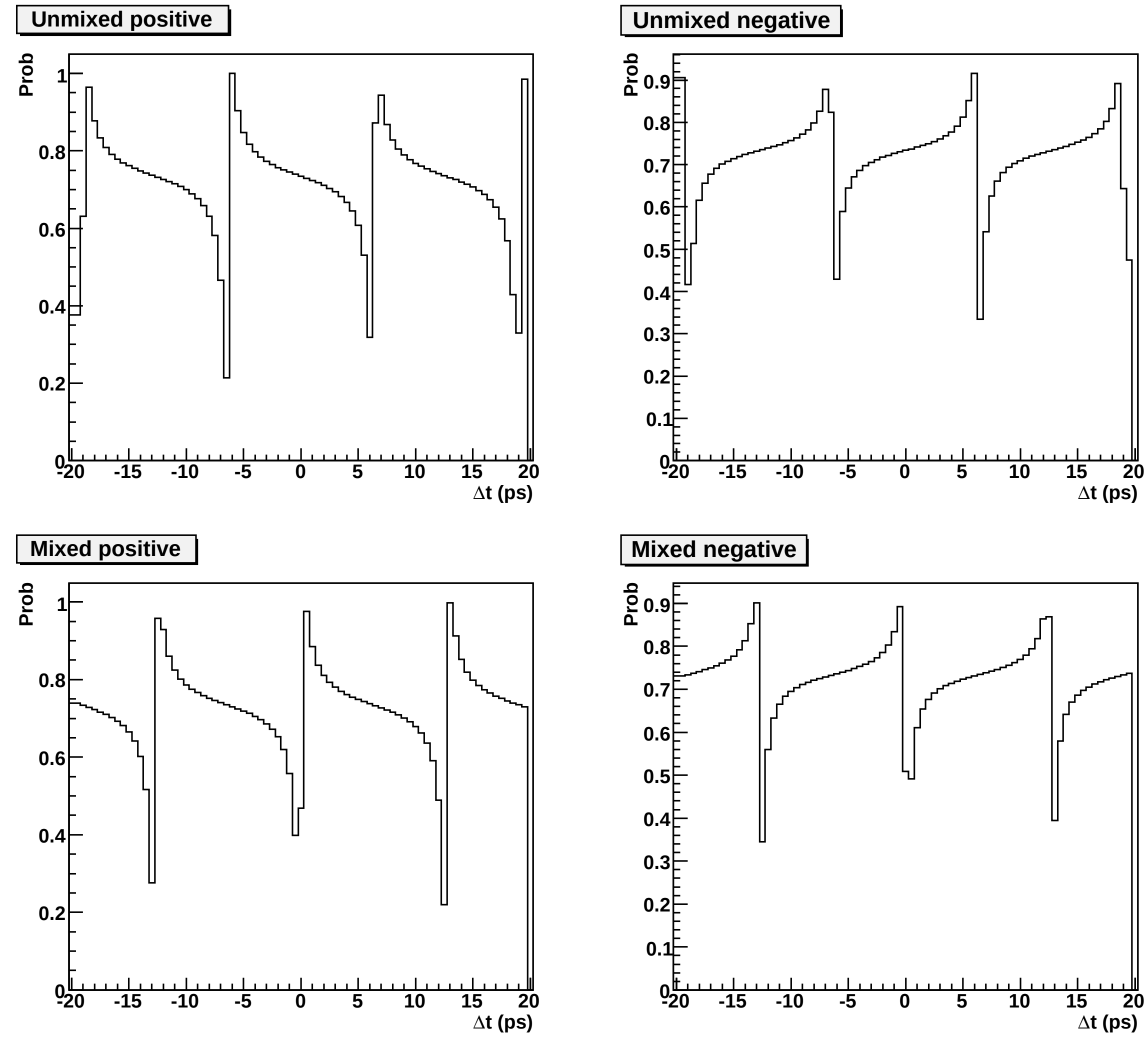

Figure 9.2: Probability of keeping a $B^0\overline{B}^0$ event for Unmixed Positive (top left plot), Unmixed Negative (top right), Mixed Positive (bottom left) and Mixed Negative (bottom right) as a function of Δt. The generated CP-violating parameters which have been used are: $(|q/p|, r', \delta') = (1., 0.03, 0.5)$.

9.3 Fits of Reweighted MC with non-zero DCS decays parameters

We begin with generating 13 samples of generic $B^0\overline{B}^0$ MC, with $r' = 0.05$ and δ' varying from 0 to 6 by steps of 0.5. We fit each sample (separating the data-taking periods Run1-3, Run4 and Run5), requesting the (ℓ, π_{soft}) pair to be a signal one, using realistic tagging and resolution.

The results of this sequence of fits are graphically represented in figure 9.3.

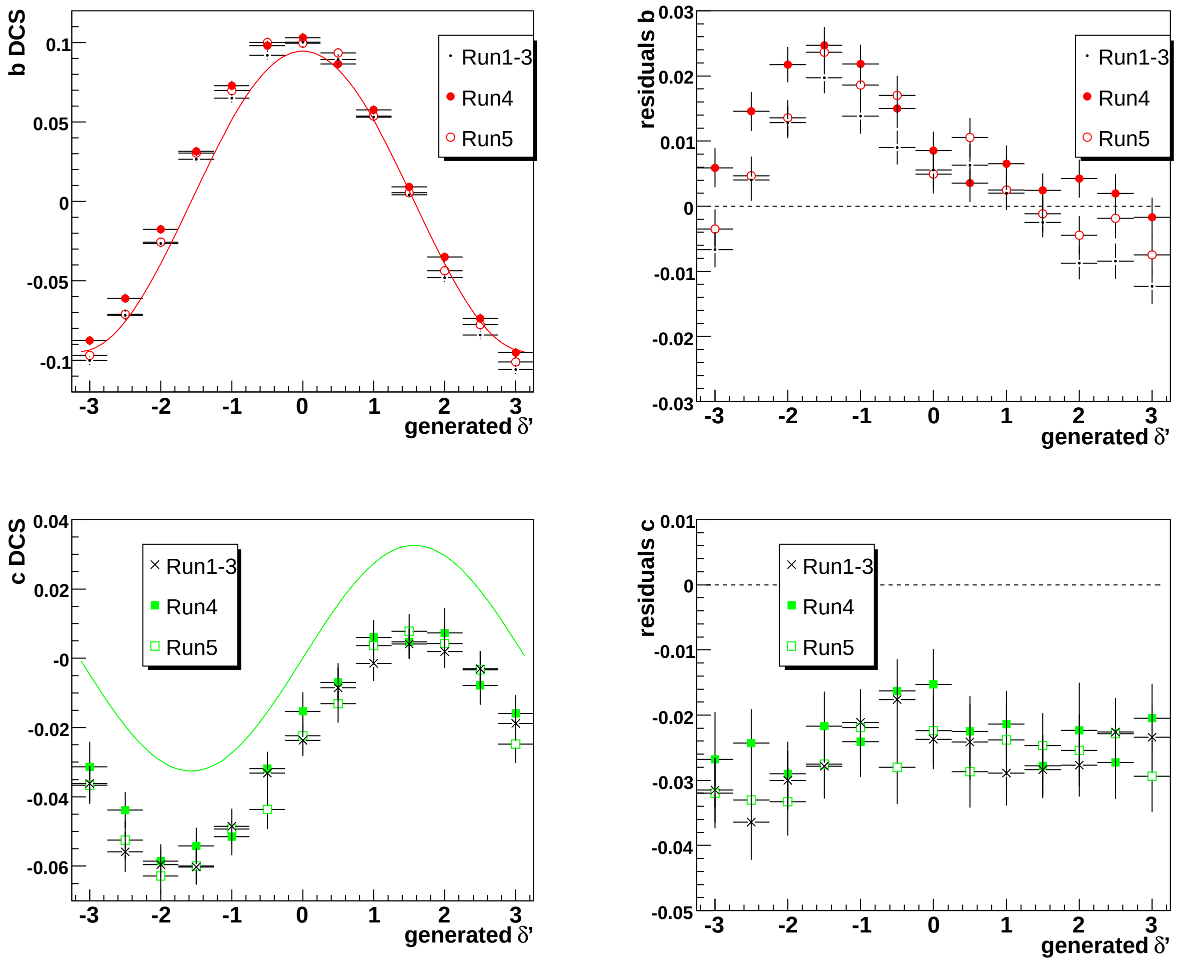

Figure 9.3: Fit results (left plots) and residuals with respect to the generated values (right) for the DCS decays parameters b (top) and c (bottom), with $r' = 0.05$. The data points correspond to the fit results, while the continuous lines represent the predicted values.

It can be seen that the predicted behavior of the two fitted parameters roughly follows the expected values, although with a pretty large bias on c which does not show any dependence on δ'. The results on b are closer to the expectations, but a significant dependence on δ' is seen.

To investigate deeper on these biases, we repeat this kind of fits on 13 samples (Run1-3 only), generated with $r' = 0.01$ (a value much closer to the expected one on our data) and δ' varying as before.

The bias we observe on c remains basically the same as in the case with $r' = 0.05$ and it is roughly at -0.026. As we can see from the theoretical pdf's in chapter 1, a negative value of c tends to enhance the peak at negative values of Δt for mixed events, where the effects of DCS decays are larger. This effect goes on the same direction of the finite lifetime of the charmed

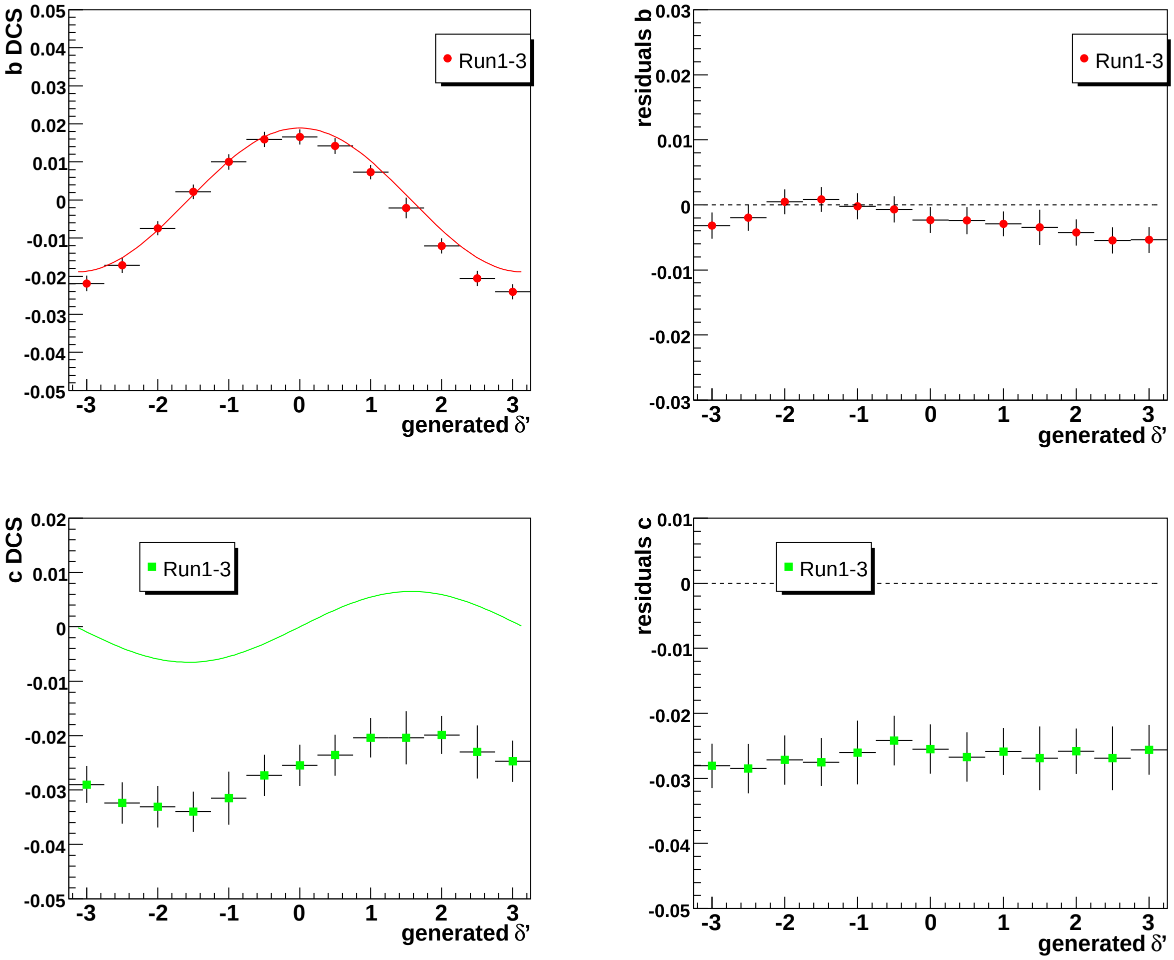

Figure 9.4: Fit results (left plots) and residuals with respect to the generated values (right) for the DCS decays parameters b (top) and c (bottom), with $r' = 0.01$. The data points correspond to the fit results, while the continuous lines represent the predicted values.

mesons, which causes a tail towards negative Δt. The interplay of these two effects causes the bias we observe.

On the other side, the bias on b shrinks significantly with respect to the previous case.

We repeat the same kind of study adding the B_{tag} $B^0\overline{B}^0$ combinatorial background component. We begin by floating all the main physical and resolution parameters both for the peaking and the combinatorial components. Results are shown in figures 9.5 and 9.6. While the bias on b shows the same behavior exhibited on the signal-only fits, the bias on c is now strongly dependent on the strong phase δ'.

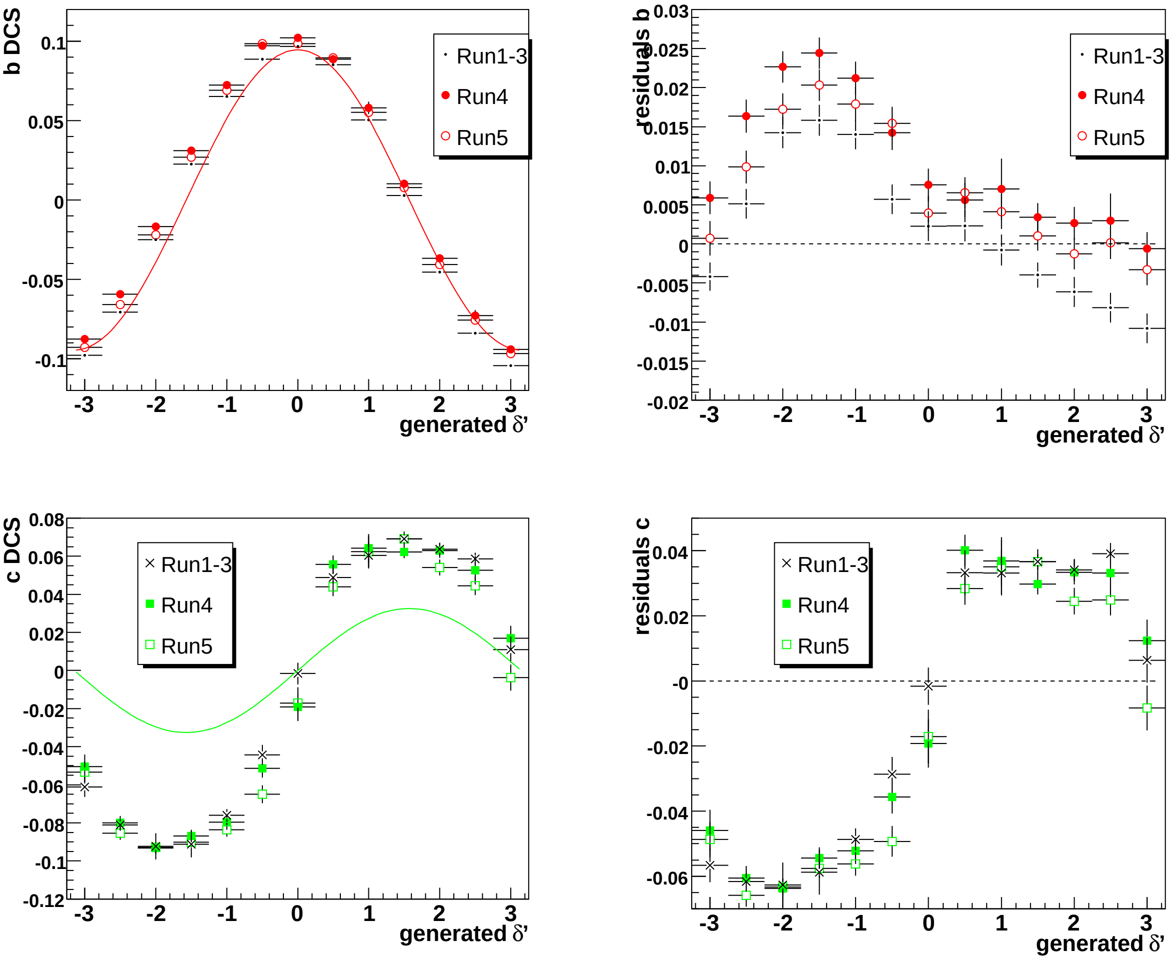

Figure 9.5: Fit results (left plots) and residuals with respect to the generated values (right) for the DCS decays parameters b (top) and c (bottom), with $r' = 0.05$. The sample used in the fit carries both the peaking and combinatorial components; the parameters of the two components have been floated.

In order to investigate deeper on the source of the large biases on c, we repeat the fits, fixing the parameters of the combinatorial background to the ones we found in the fits of chapter 8. Results are shown in figures 9.7 and 9.8. No significant variations are seen on b central values, while the bias on c continues to be unmanageable.

We therefore conclude that even giving a rough estimate on c will not be possible in our analysis.

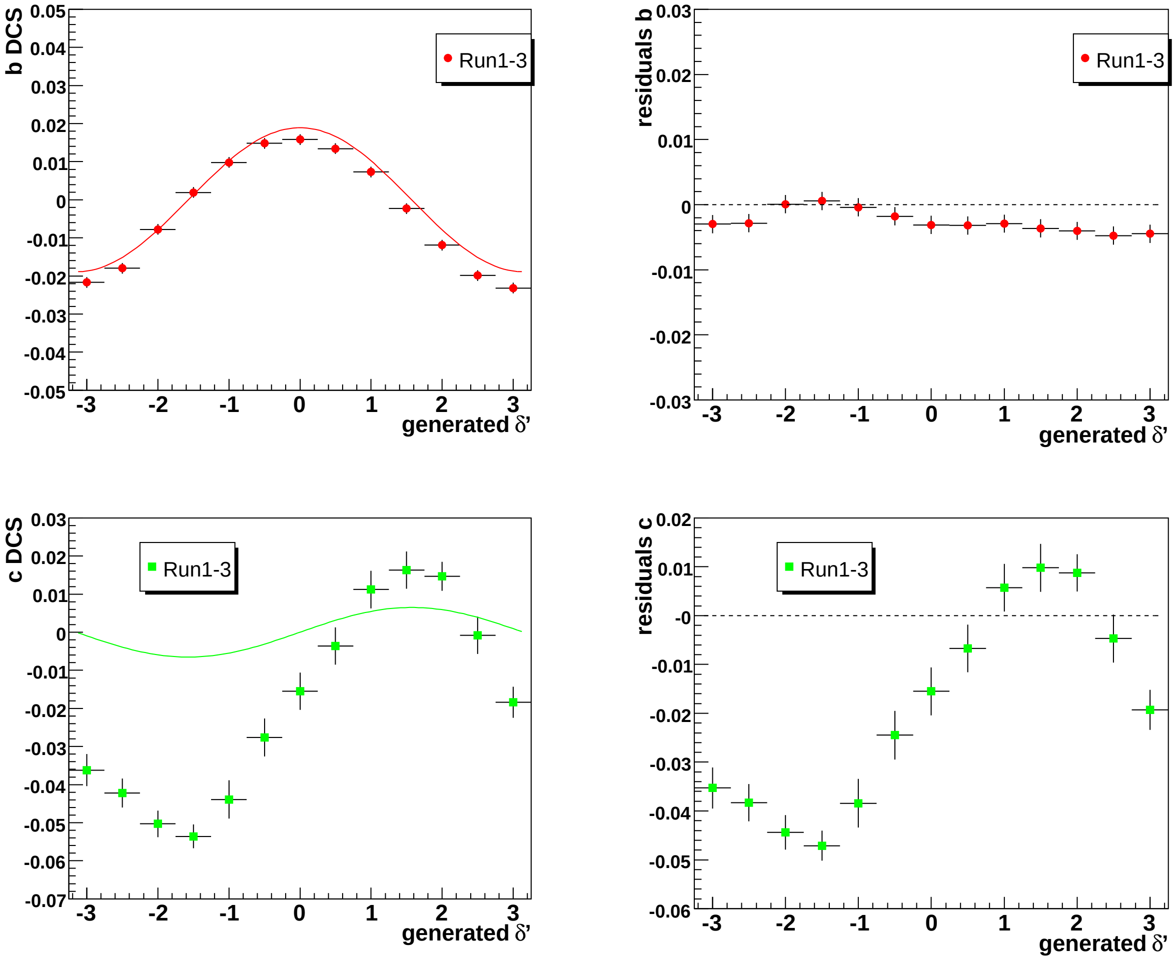

Figure 9.6: Fit results (left plots) and residuals with respect to the generated values (right) for the DCS decays parameters b (top) and c (bottom), with $r' = 0.01$. The sample used in the fit carries both the peaking and combinatorial components; the parameters of the two components have been floated.

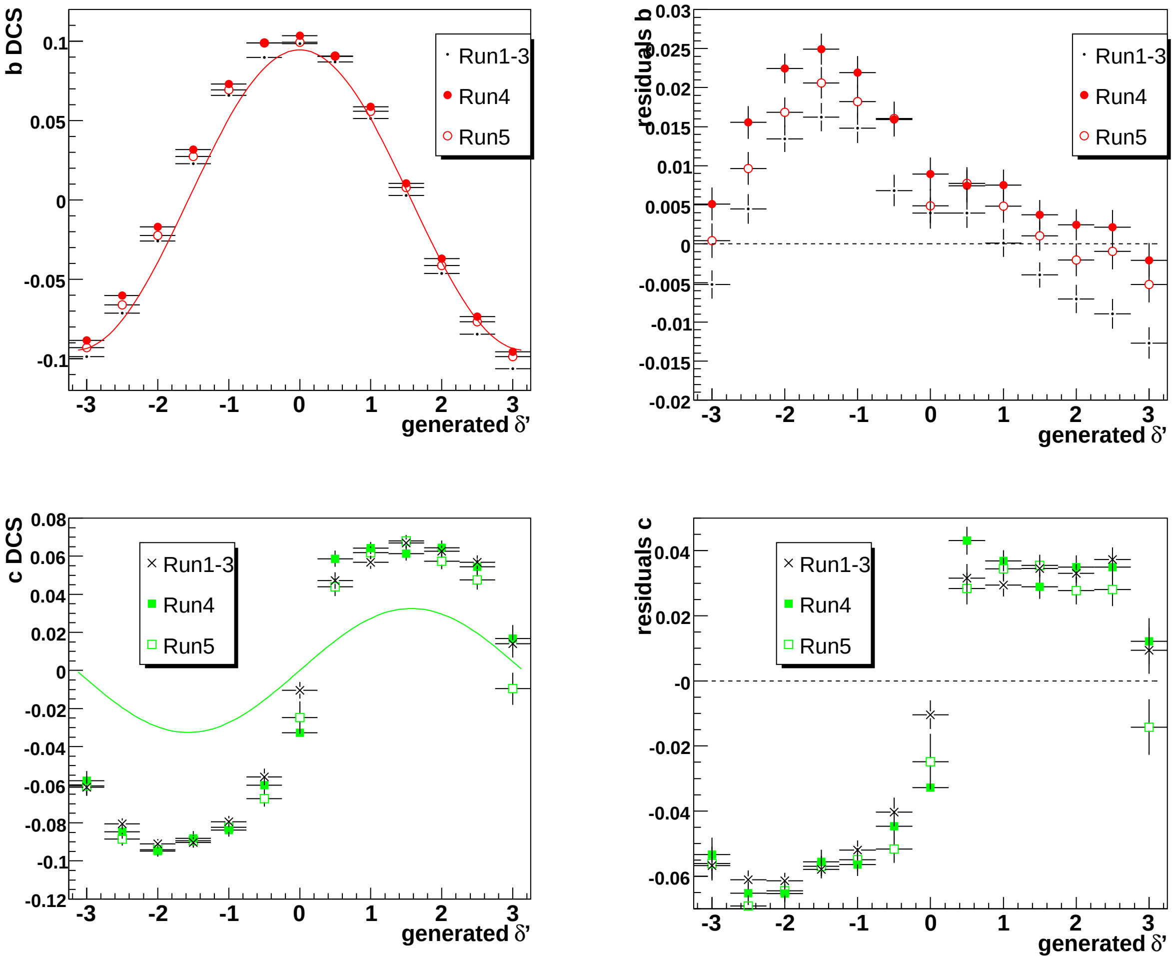

Figure 9.7: Fit results (left plots) and residuals with respect to the generated values (right) for the DCS decays parameters b (top) and c (bottom), with $r' = 0.05$. The sample used in the fit carries both the peaking and combinatorial components; the parameters of the combinatorial background have been fixed.

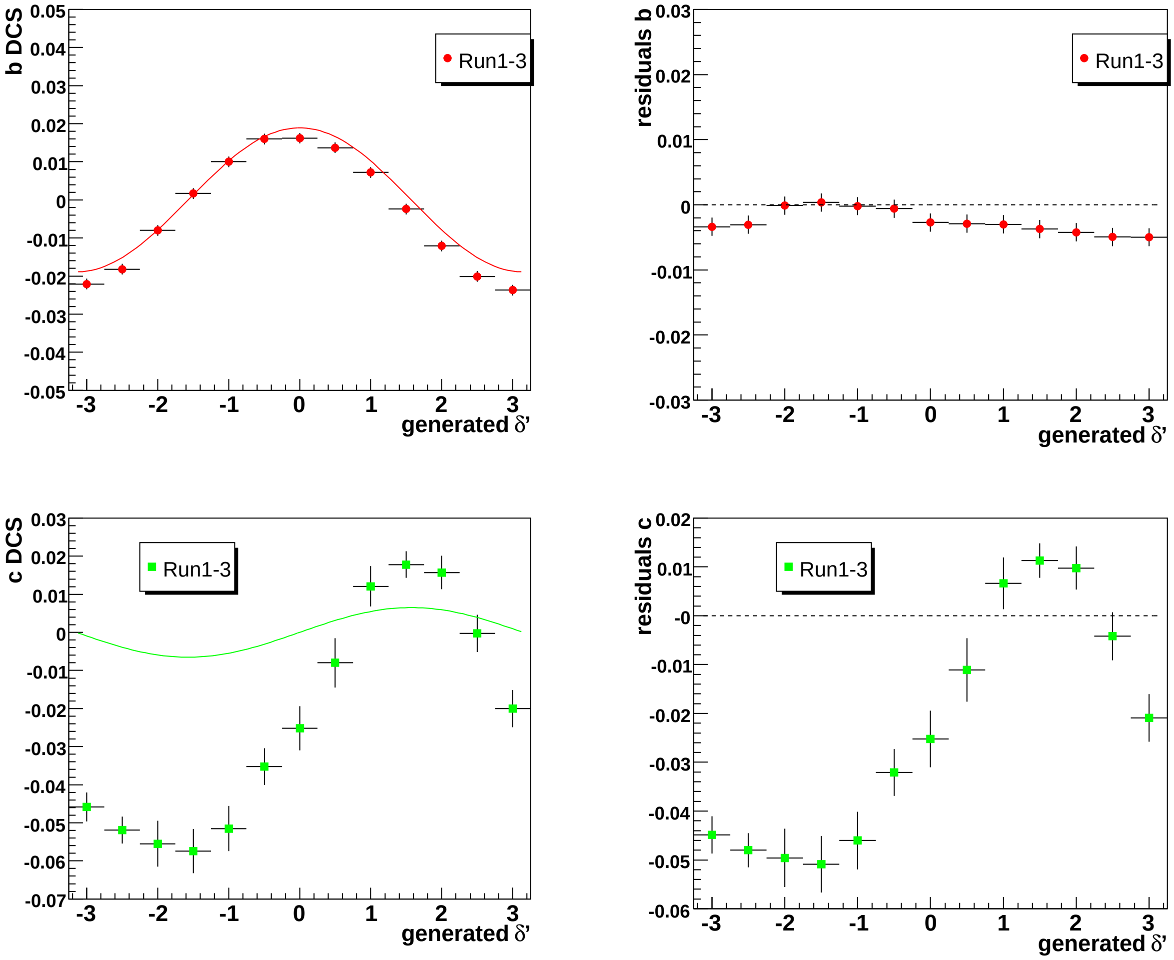

Figure 9.8: Fit results (left plots) and residuals with respect to the generated values (right) for the DCS decays parameters b (top) and c (bottom), with $r' = 0.01$. The sample used in the fit carries both the peaking and combinatorial components; the parameters of the combinatorial background have been fixed.

9.4 Fits of Reweighted MC with non-zero $|q/p|-1$

We generate sub-samples of Reweighted MC, with $|q/p|-1$ varying in the range $[-0.05, +0.05]$ (at steps of 0.01) for the three data-taking periods Run1-3, Run4, Run5. $B^0\overline{B}^0$ samples have been produced using the procedure explained in section 9.2. Since the variation of $|q/p|$ does not affect the properties of charged B's events, B^+B^- MC has been rescaled (by randomly discarding events) in order to keep the fraction of neutral/charged B's equal to the generic MC. We stress here that, since every selected sample is a (pretty large) subsample of the original one, there is a very strong statistical correlation among the generated samples of each data-taking period.

Varying $|q/p|$ produces an imbalance of the number of B^0B^0 events with respect to the number of $\overline{B}^0\overline{B}^0$ and thus the yields of both B_{tag} and D_{tag} kaons vary as a function of $|q/p|$ for the four categories of Unmixed/Mixed and Positive/Negative events.

The basic idea of this measurement is that the simultaneous determination of $|q/p|$ and of the detector related asymmetries can be performed because the B_{tag} mixed, B_{tag} unmixed and D_{tag} samples have different sensitivities to these variables (see equations 6.1, 6.2).

To check the correctness of our model, we first perform a series of exercise fits separately to D_{tag} and B_{tag} events. In these fits we allow to float only the tagging asymmetry A_{tag}, the dilutions and $|q/p|$ for the B_{tag} case. The reconstruction asymmetries are kept fixed to the values derived by counting the reconstructed events on generic MC.

Results for peaking $B^0\overline{B}^0$ events are shown in figure 9.9. No dependence on the generated value of $|q/p|-1$ is seen, as we would expect if the modeling of our pdf's is correct.

We then fit together D_{tag} and B_{tag} (mixed and unmixed) events and repeat the exercise. In this case, we are able to measure both A_{tag} and A_{rec} in addition to $|q/p|$. The left plot of figure 9.10 shows the result for a test case, where we neglect in the fit the dependence of the D_{tag} asymmetry on $|q/p|$. (We do that by fixing the fractions of D_{tag} events over the total for each charge correlation to the value obtained for $|q/p|=1$). As a consequence A_{tag} and A_{rec} vary almost linearly with $|q/p|$. If we restore in the fit the correct dependence, we obtain the results shown in the right plot of figure 9.10, which do no exhibit any sensible variation of the detector-induced asymmetries with the value of $|q/p|$.

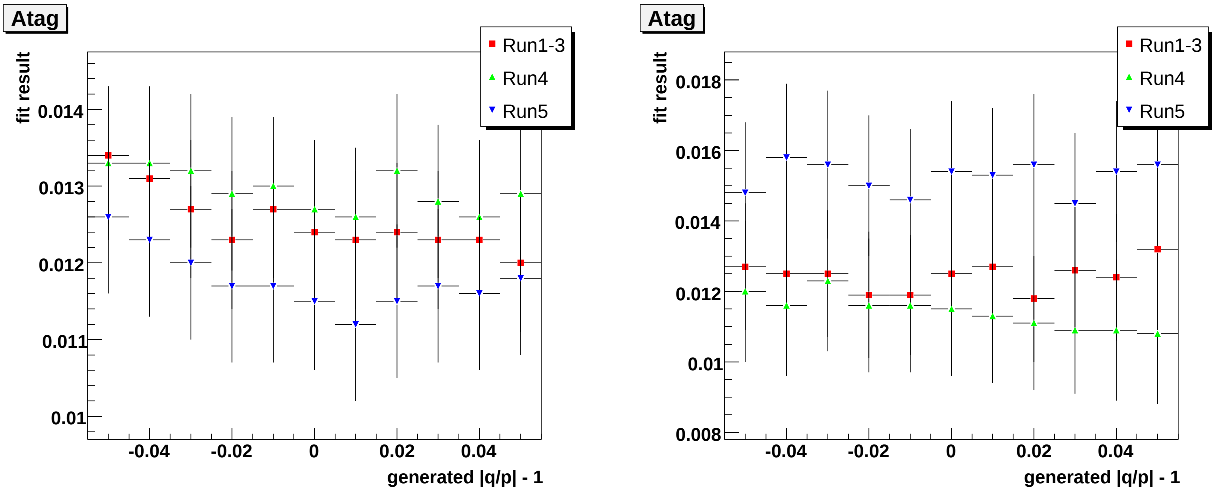

Figure 9.9: Fit results of A_{tag} for D_{tag} kaons (left plot) and B_{tag} (right) as a function of the generated value of $|q/p|-1$ for peaking $B^0\overline{B}^0$ events.

The results for combinatorial $B^0\overline{B}^0$ events are shown in figure 9.11. With respect to $B^0\overline{B}^0$ peaking, in the combinatorial case the treatment of the dependence on $|q/p|$ of the asymmetries

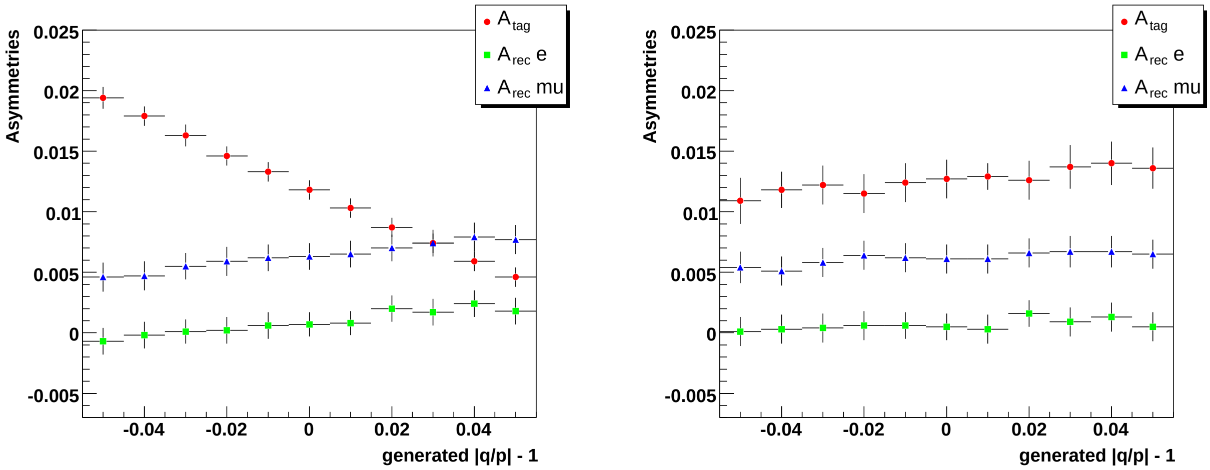

Figure 9.10: Fit results of A_{tag}, $A_{rec}(e)$ and $A_{rec}(\mu)$ in a simultaneous fit of D_{tag} and B_{tag} kaons in $B^0\overline{B}^0$ peaking events. In the left plot, the fractions of D_{tag} events over the total have been kept fixed to the value obtained in the $|q/p|=1$ case, while in the right one these have been floated, as it should be done. The spurious dependence on the asymmetries on the generated values of $|q/p|-1$ is thus removed.

(see equation 6.2) of D_{tag} kaons is less straight-forward. This dependence is proportional, in peaking $B^0\overline{B}^0$ events, to the value of χ_d. In combinatorial events, we combine a lepton and a soft pion (likely to come from the decay of a D^*) originating from two different B's and the probability of doing so is higher in mixed events. Based on our generic Monte Carlo, we apply a correction, and use $\chi_{d,bkg}=\chi_d\cdot 1.41$. After this correction has been applied, no dependence on A_{tag} is visible in the scan over the whole range of variation of $|q/p|$. A discussion of the systematic uncertainty associated to this correction factor will be carried out in section 12.4.

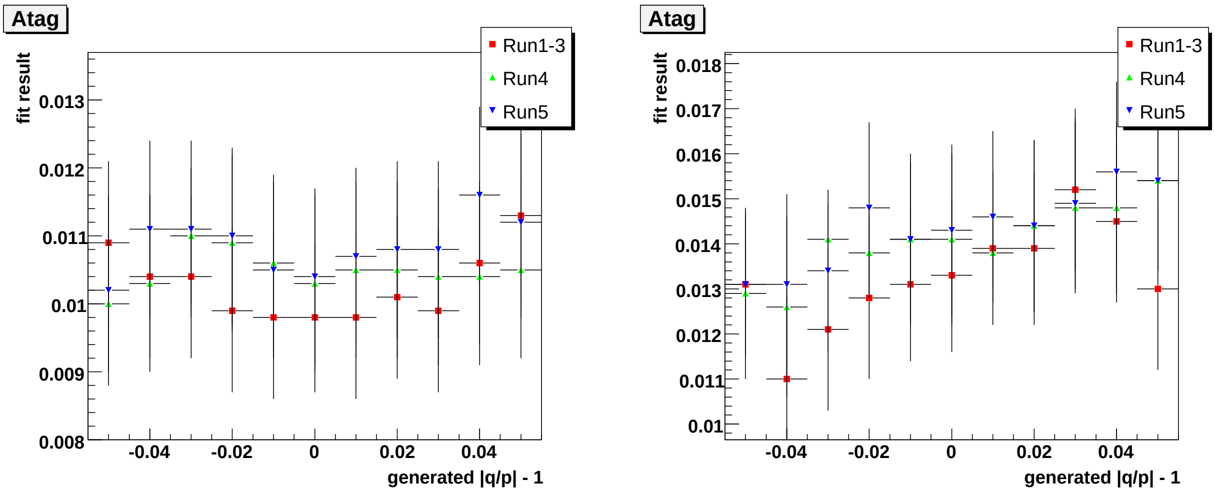

Figure 9.11: Fit results of A_{tag} for D_{tag} kaons (left plot) and B_{tag} (right) as a function of the generated value of $|q/p|-1$ for combinatorial $B^0\overline{B}^0$ events.

The results on fitted $|q/p|-1$, separately for $B^0\overline{B}^0$ peaking and combinatorial events are shown in figure 9.12, in the three considered data taking periods. Reconstruction and tagging asymmetries and mistag probabilities have been left floating in the fits.

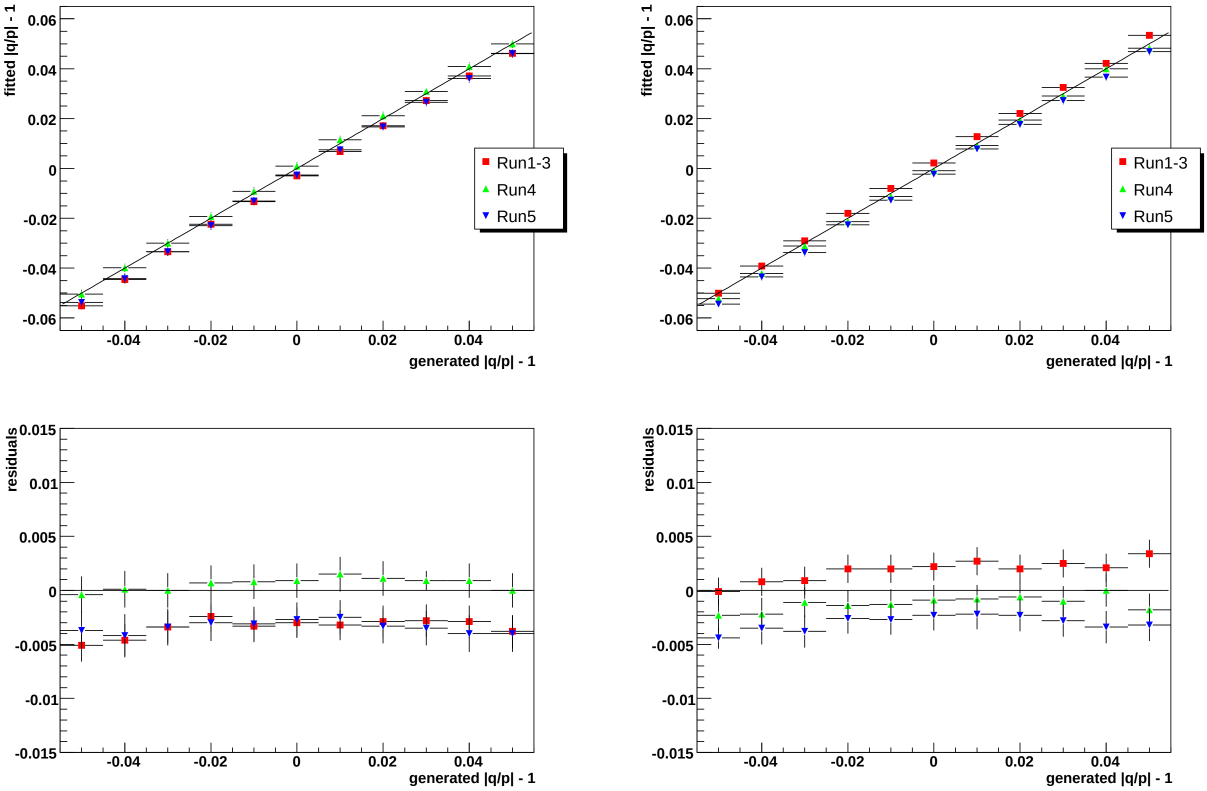

Figure 9.12: Fit results of $|q/p|-1$ for $B^0\overline{B}^0$ peaking (left plots) and combinatorial (right). The top plots show the fitted values of $|q/p|-1$ as a function of the generated one, while the bottom ones display the residuals of fit results with respect to the generated value.

It can be seen that the fit results reproduce correctly the generated values. The slope of both sets of points is very well consistent with unity: in this way we verify that the value of $|q/p|-1$ fitted in combinatorial events coincides with the one fitted on peaking. This result was expected (since the measurement of the reconstructed vertex is dominated by the lepton track), but we could not assume it *a priori*. We stress once more that there is a strong statistical correlation among the reweighted MC samples within the same data-taking period, so a fluctuation (additive bias) on the $|q/p| \equiv 1$ sample is to be seen also in the other samples with non-zero CP-violation parameters.

Finally, we fit together peaking and combinatorial $B^0\overline{B}^0$ events. Results are shown in figure 9.13. Again, we observe a very good linearity of fit results over the wide range scanned and no significant dependence on the generated value of $|q/p|-1$.

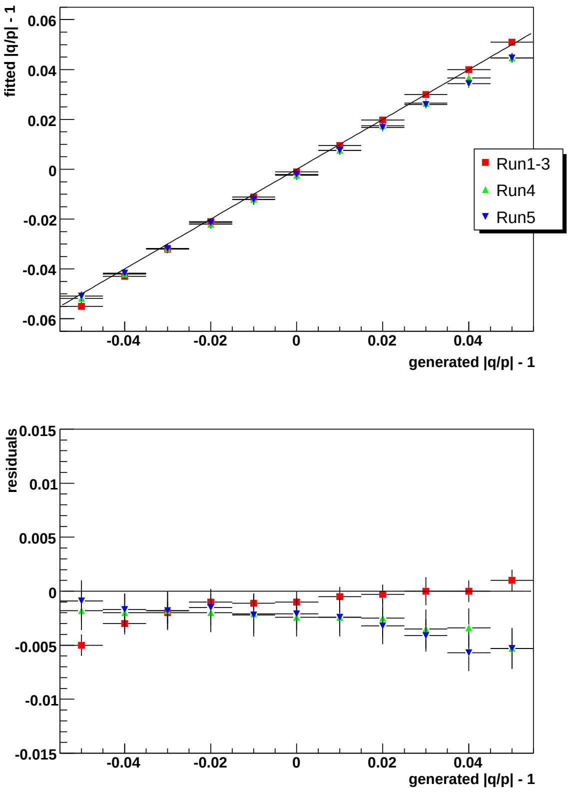

Figure 9.13: Fit results of $|q/p|-1$ for $B^0\overline{B}^0$ peaking and combinatorial events together. The top plot shows the fitted values of $|q/p|-1$ as a function of the generated one, while the bottom ones displays the residuals of fit results with respect to the generated value.

We summarize in table 9.1 the results we get on the three run ranges fitting together all $B^0\overline{B}^0$ components. Given the large correlations between the reweighted Monte Carlo samples within one data-taking period, we limit ourselves to quote the results for generated $|q/p| = 1$ only.

We complete the survey over our reweighted Monte Carlo samples adding also the B^+B^- components.

Figure 9.14 and table 9.2 show the results of the fits run on the data-taking periods Run3, Run4 and Run5. The addition of the B^+B^- component thus does not shift the fitted values of $|q/p|-1$ and the asymmetries by values incompatible with statistical fluctuations.

To further check that the downward shift we observe in the fitted value of $|q/p|-1$ (particularly remarkable in the Run5 sample), we perform another set of fits to study the effects of

Table 9.1: Results of $|q/p| - 1$ and the tagging and reconstruction asymmetries for the fits on all the components of $B^0\overline{B}^0$ Monte Carlo.

Period	$\lvert q/p\rvert - 1$	A_{tag}	$A_{rec}(e)$	$A_{rec}(\mu)$
Run1-3	-0.0010 ± 0.0010	0.0130 ± 0.0010	0.0010 ± 0.0007	0.0090 ± 0.0008
Run4	-0.0024 ± 0.0018	0.0126 ± 0.0014	-0.0011 ± 0.0009	0.0084 ± 0.0009
Run5	-0.0021 ± 0.0015	0.0103 ± 0.0014	-0.0022 ± 0.0009	0.0038 ± 0.0008

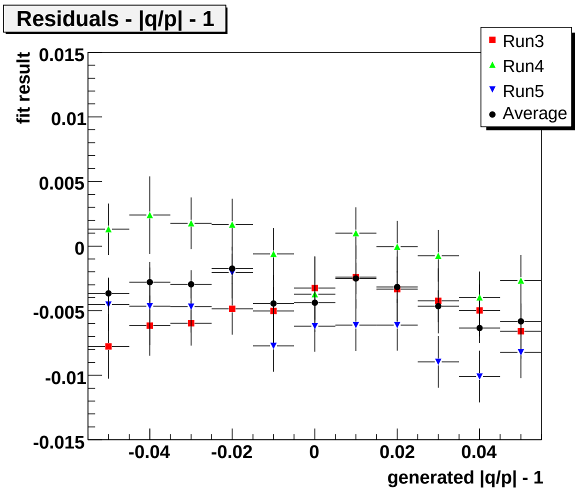

Figure 9.14: Fit results of $|q/p| - 1$ for all the components of our $B\overline{B}$ generic Monte Carlo. We show here only the residuals with respect to the generated value of $|q/p| - 1$ for the three data-taking periods and for the weighted average of these results (black dots).

Table 9.2: Results of $|q/p| - 1$ and the tagging and reconstruction asymmetries for the fits on all the components of $B\overline{B}$ Monte Carlo.

Period	$\lvert q/p\rvert - 1$	A_{tag}	$A_{rec}(e)$	$A_{rec}(\mu)$
Run3	-0.0032 ± 0.0030	0.0090 ± 0.0012	0.0002 ± 0.0010	0.0083 ± 0.0010
Run4	-0.0037 ± 0.0018	0.0110 ± 0.0008	-0.0007 ± 0.0006	0.0096 ± 0.0006
Run5	-0.0062 ± 0.0018	0.0087 ± 0.0008	-0.0009 ± 0.0006	0.0044 ± 0.0006

the addition of the B^+B^- components. Since the sample composition (see section 5.5) has been performed on the complete Run1-5 sample and there could be some slight differences between the data-taking periods, we subdivide our MC sample into 20 equally sized subsamples. These subsamples are homogeneous with respect to data-taking periods, that is they contain the same amount of events from each Run.

We then run the same kind of fits we used to draw the results summarized in tables 9.1 and 9.2 to the $B^0\overline{B}^0$ only components and to all $B\overline{B}$ components and compare each result. Averaging the fit results, we get:

$$\begin{aligned} B^0 \text{ only:} \quad (|q/p|-1) &= -0.0013 \pm 0.0011 & (9.1)\\ \text{all } B\overline{B}\text{:} \quad (|q/p|-1) &= -0.0020 \pm 0.0010\,. & (9.2)\end{aligned}$$

We conclude that the shift we observe after adding the B^+B^- component is compatible with a statistical fluctuation.

9.5 Selection bias

As we have seen, our results on the reweighted MC samples yield results for $|q/p|-1$ typically lower than 0 (at the $\sim 2\,\sigma$ level of significance).

To verify if this deviation is caused by a bias in the fitting procedure, we perform a quick check on the MC truth of the events in our generic $B^0\overline{B}^0$ Monte Carlo sample. We compare the number of events we get in each of the four categories (keeping separated the partially reconstructed and tag sides): $\overline{B}^0B^0$, $B^0\overline{B}^0$, B^0B^0 and $\overline{B}^0\overline{B}^0$. We do not require the presence of a tag kaon in the event.

Table 9.3: Yields for the four categories in the generic Run1-5 $B^0\overline{B}^0$ Monte Carlo. In the second column the raw yields are reported, while in the third, the number of events with a $\overline{B}^0$ on the reconstructed side have been corrected to account for reconstruction asymmetries. MC truth has been used.

Category ($B_{rec}B_{tag}$)	Raw yields	Corrected yields
$\overline{B}^0B^0$	7 210 249	7 286 678
$B^0\overline{B}^0$	7 268 505	7 268 505
B^0B^0	1 890 285	1 890 285
$\overline{B}^0\overline{B}^0$	1 852 486	1 872 122

In order to get rid of the reconstruction asymmetries on the selection of the (ℓ, π_{soft}) pair, we rescale the number of events with a $\overline{B}^0$ on the reco side, so they equal the number of events with a B^0 on the reco side; raw and corrected yields are reported in table 9.3.

We then compare the asymmetries in the tag side for both mixed and unmixed events:

$$\begin{aligned} A_{unmix} &= \frac{N(\overline{B}^0B^0)-N(B^0\overline{B}^0)}{N(\overline{B}^0B^0)+N(B^0\overline{B}^0)} = 0.00125 \pm 0.00026\,, & (9.3)\\ A_{mix} &= \frac{N(B^0B^0)-N(\overline{B}^0\overline{B}^0)}{N(B^0B^0)+N(\overline{B}^0\overline{B}^0)} = 0.0048 \pm 0.0005\,. & (9.4)\end{aligned}$$

The results show that we have a significantly larger number of events with a B^0 in the tag side with respect to a $\overline{B}^0$, even though we did not apply any request besides the selection of an oppositely charged (ℓ, π_{soft}) pair. Recalling equation 2.9, the fit results for $|q/p|-1$ seem to be in good agreement with the asymmetry we measure in our preselected sample.

Concerning the origin of this asymmetry, we verify that it is not present in the `AllEvents` Monte Carlo collections, thus it arises at the preselection level.

The discussion on the treatment of this bias is reported in section 12.13, along with the assignment of its systematic uncertainty.

Chapter 10

D_{tag} modeling from exclusively reconstructed $B^0 \to D^{*-}\ell^+\nu$

In this chapter, we will use a high purity sample of exclusively reconstructed $B^0 \to D^{*-}\ell^+\nu$ events to derive from the on-peak data the modeling of D_{tag} kaons for peaking $B^0\overline{B}^0$ and peaking and combinatorial B^+B^-.

10.1 Selection of $B^0 \to D^{*-}\ell^+\nu$ events

A subsample of exlusively reconstructed $B^0 \to D^{*-}\ell^+\nu$ events can be selected inside our sample of B_{rec} mesons by reconstructing the $\bar{D}^0$ decaying into the final states $K^+\pi^-$, $K^+\pi^-\pi^0$ and $K^+\pi^-\pi^+\pi^-$.

The candidate K is requested to pass the same `LooseKaonMicro` PID selector used for the standard selection of the main sample and to have opposite charge with respect to the π_{soft}. The mass of the D^* candidate has to satisfy the cut $2.008 < m_{D^*} < 2.012$ GeV/c^2 and the probability of the charged D^0 daughters to originate from a common vertex must exceed 1 %. A mode dependent cut on the mass of the D^0 candidate is applied: $1.845 < m_{D^0} < 1.880$ GeV/c^2 ($K\pi$), $1.850 < m_{D^0} < 1.880$ GeV/c^2 ($K\pi\pi^0$) and $1.855 < m_{D^0} < 1.875$ GeV/c^2 ($K3\pi$).

As in the partial reconstruction case, we compute m_ν^2 using equation (2.23). Given that in this case the D^* is fully reconstructed, the resolution on m_ν^2 is considerably better. We do not apply any cut on m_ν^2.

Kaon tracks originating from the D^0 decay are treated in the same way of candidate tag K tracks in the main sample; the variables Δt, $\sigma(\Delta t)$ and $\cos(\theta_{K\ell})$ are computed in the same way.

Figure 10.1 shows the m_ν^2 and Δt distributions for the selected events in generic $B^0\overline{B}^0$ Monte Carlo; the contribution from background is of the order of a few percent in all the three samples.

Table 10.1 summarizes the yields of exclusively reconstructed $\overline{B}^0 \to D^{*+}\ell^-\bar{\nu}_\ell$ events we have in our data samples.

Table 10.1: Number of exclusively reconstructed $\overline{B}^0 \to D^{*+}\ell^-\bar{\nu}_\ell$ events, separated by D^0 decay channel and data kind.

	$B^0\overline{B}^0$ MC	B^+B^- MC	off-peak data	on-peak data
$D \to K\pi$	327 285	42 707	730	119 185
$D \to K\pi\pi^0$	637 810	101 488	1 490	232 445
$D \to K3\pi$	397 939	62 650	999	142 275

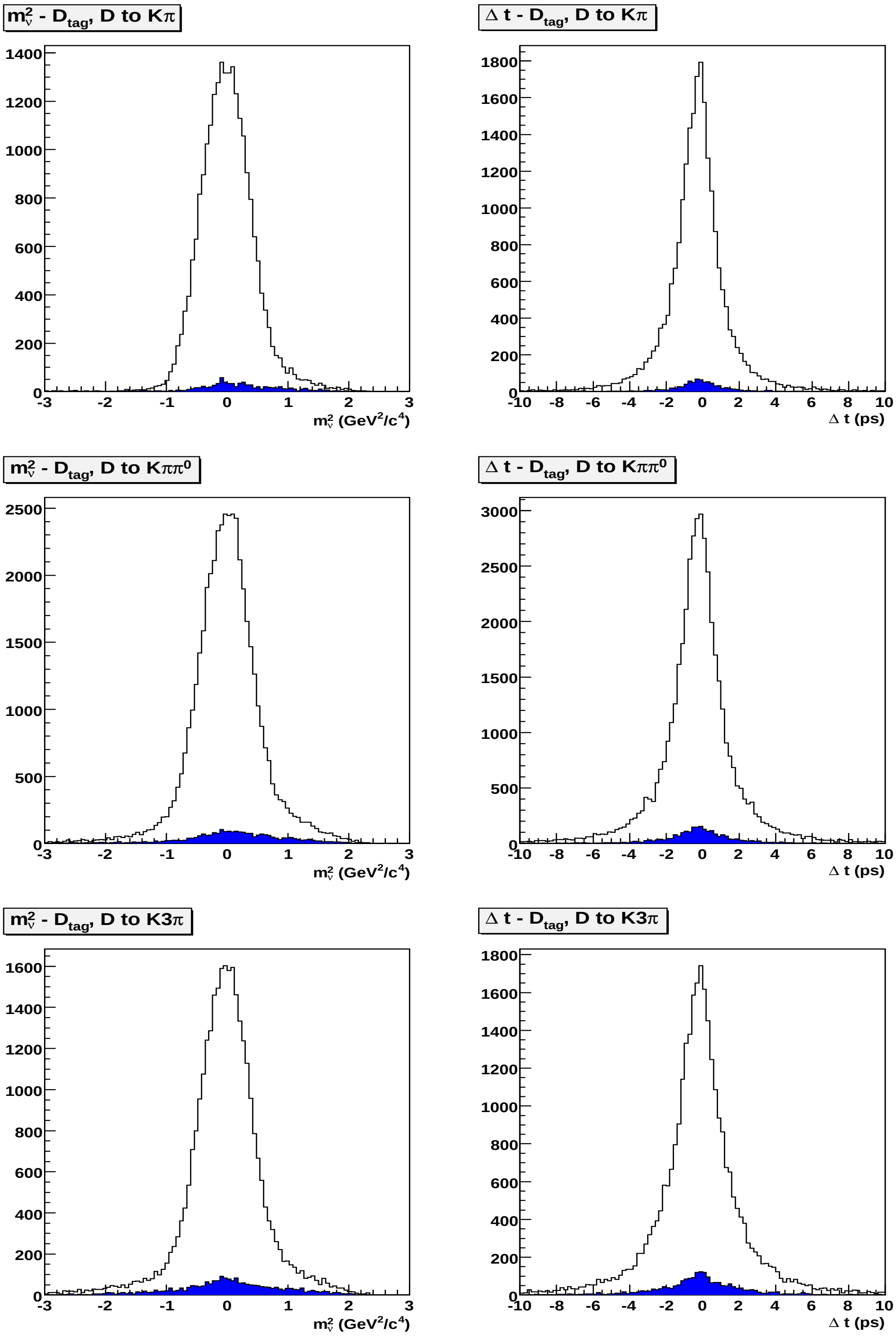

Figure 10.1: m_ν^2 (left plots) and Δt (right) distributions for exclusively reconstructed $B^0 \rightarrow D^{*-}\ell^+\nu$ events with $D^0 \rightarrow K\pi$ (top plots), $D^0 \rightarrow K\pi\pi^0$ (middle) and $D^0 \rightarrow K3\pi$ (bottom) for generic $B^0\overline{B}^0$ MC. The background contribution is shown in blue.

10.2 Fit on the exclusive samples

We begin fitting the peaking and combinatorial $B^0\overline{B}^0$ exclusive samples (requesting the event to be a true D_{tag} event from the MC truth), using the same pdf's defined in chapter 7.

The results of these two fits are shown in figure 10.2. The agreement between the fitted pdf's and data points is satisfactory and most of the fitted parameters are compatible with the ones we find in the inclusive sample.

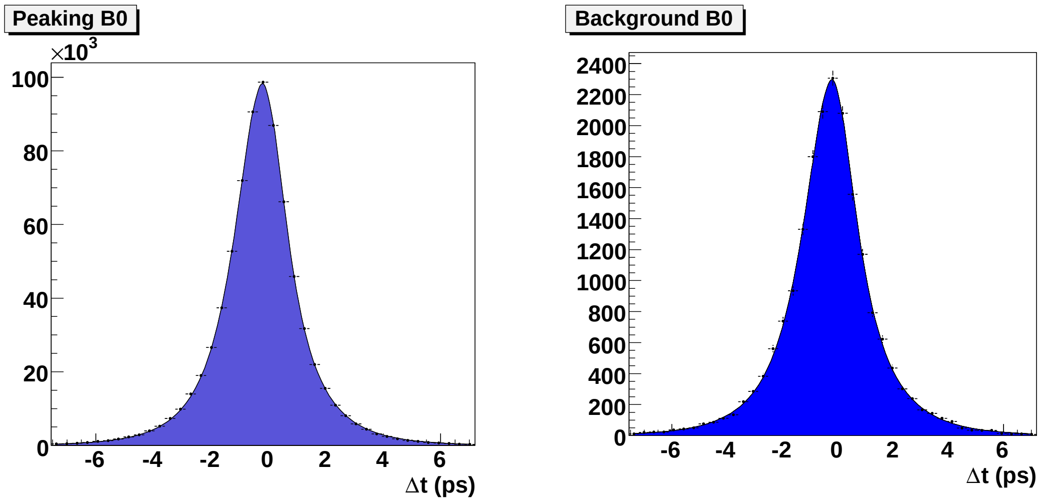

Figure 10.2: Results of the fits on the $B^0\overline{B}^0$ exclusive sample for the peaking component (left plot) and the $B^0\overline{B}^0$ combinatorial (right).

In order to look for any difference between the three D^0 decay channels we are reconstructing, we superimpose the fitted signal D_{tag} pdf to each channel of the peaking $B^0\overline{B}^0$ sample (figure 10.3), the peaking and combinatorial B^+B^- (figure 10.4) and the $B^0\overline{B}^0$ combinatorial (figure 10.5).

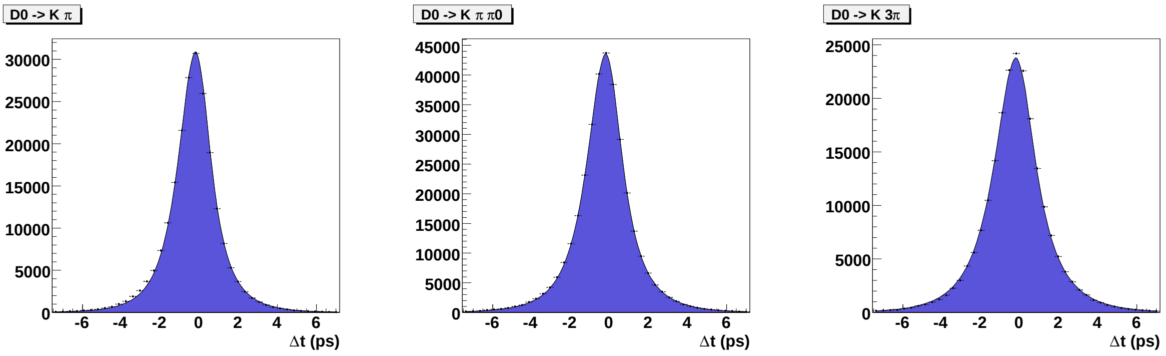

Figure 10.3: Δt distributions for the exclusive D_{tag}samples and $B^0\overline{B}^0$ peaking, separating for $D^0 \to K\pi$ (left plot), $D^0 \to K\pi\pi^0$ (center), and $D^0 \to K3\pi$ (right). The overlaid pdf is the signal D_{tag} pdf whose parameters have been fitted on the sum of the three channels.

We do not see any significant discrepancy between the three channels, thus from now on we will consider the sum of the three D^0 decay modes, whose kaon momentum spectrum is closer to the inclusive one.

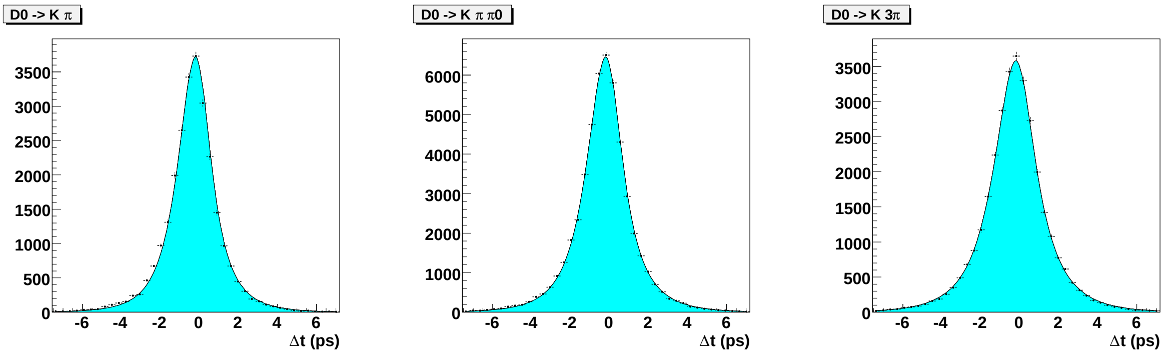

Figure 10.4: Δt distributions for the exclusive D_{tag}samples and B^+B^- peaking + combinatorial, separating for $D^0 \rightarrow K\pi$ (left plot), $D^0 \rightarrow K\pi\pi^0$ (center), and $D^0 \rightarrow K3\pi$ (right). The overlaid pdf is the signal D_{tag} pdf whose parameters have been fitted on the sum of the three channels in $B^0\overline{B}^0$ peaking events.

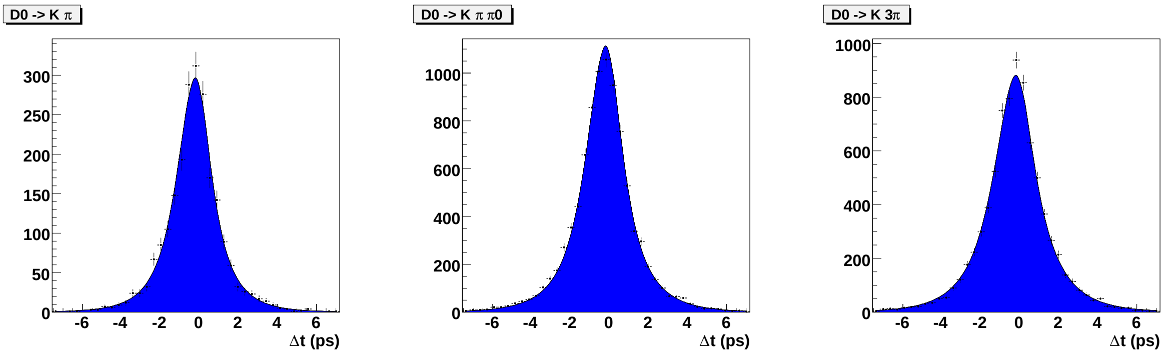

Figure 10.5: Δt distributions for the exclusive D_{tag}samples and $B^0\overline{B}^0$ combinatorial, separating for $D^0 \rightarrow K\pi$ (left plot), $D^0 \rightarrow K\pi\pi^0$ (center), and $D^0 \rightarrow K3\pi$ (right). The overlaid pdf is the $B^0\overline{B}^0$ combinatorial D_{tag} pdf whose parameters have been fitted on the sum of the three channels.

10.3 Modeling of D_{tag} pdf's from the exclusive data sample

In order to verify the possibility to use the exclusive sample to model the inclusive one and then constrain the D_{tag} shapes in the nominal fit, in figure 10.6 we compare the Δt distributions of the two, using $B^0\overline{B}^0$ MC signal events.

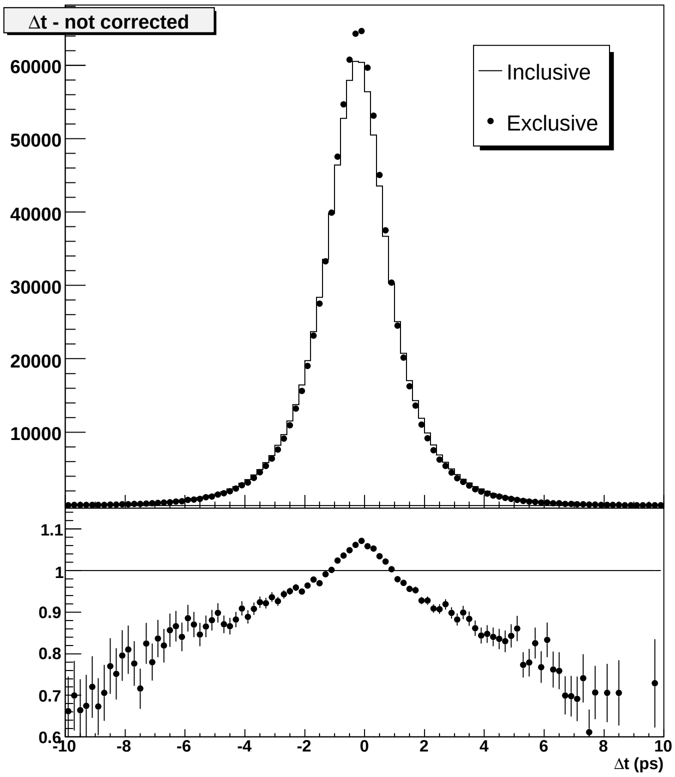

Figure 10.6: Top: comparison of the Δt distributions for the inclusive D_{tag}sample (histogram) and the exclusive one (points with error bars) for $B^0\overline{B}^0$ MC signal events. The histograms have been normalized to the same arbitrary number of events. Bottom: ratio (exclusive/inclusive) of the two distributions.

Significant discrepancies are evident from the comparison of the two distributions. We observe anyway that the $|\vec{p}_K|$ spectra, though similar, still exhibit some differences (see figure 10.7).

Given that Δt distributions are sensitive to the $|\vec{p}_K|$ spectrum, we reweight the exclusive D_{tag} events so that their $|\vec{p}_K|$ spectrum coincides with the inclusive one and perform again the comparison of the Δt distributions (fig. 10.8).

The $|\vec{p}_K|$ reweighting procedure removes most of the discrepancies found in the original Δt distributions, besides some structure at $\Delta t \sim -3$ ps and some disagreement at the very end of the tails. The misagreement is in any case at the level of a few percent and therefore the idea of constraining the inclusive D_{tag} distributions to the exclusive ones looks reasonable.

We repeat the procedure in the MC including also the combinatorial background. Given that the background is characterized by a wider Δt distribution and the fraction of combinatorial is different for the two samples ($\sim$ 35 % for the inclusive and $\sim$ 6 % for the exclusive, see figure 10.9), we have to rescale background events so that the Δt distributions we compare in figure 10.10 have the same fraction of combinatorial.

Again, the comparison between the two samples looks pretty good, with discrepancies at the

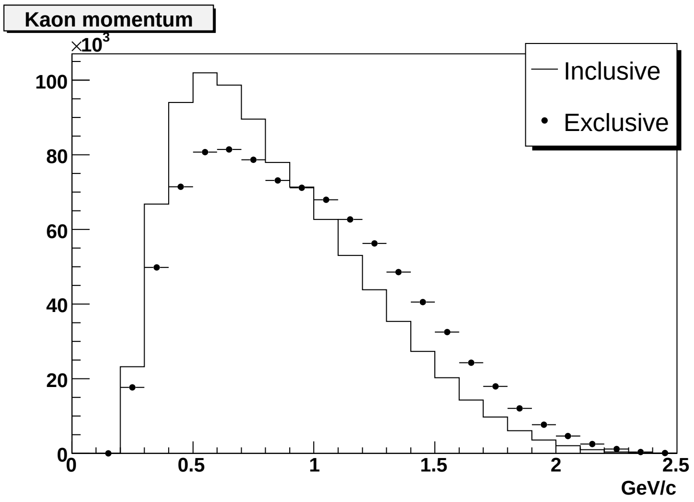

Figure 10.7: Comparison of the $|\vec{p}_K|$ spectra for the inclusive D_{tag} sample (histogram) and the exclusive one (points with error bars) for $B^0\overline{B}^0$ MC signal events. The histograms have been normalized to the same arbitrary number of events.

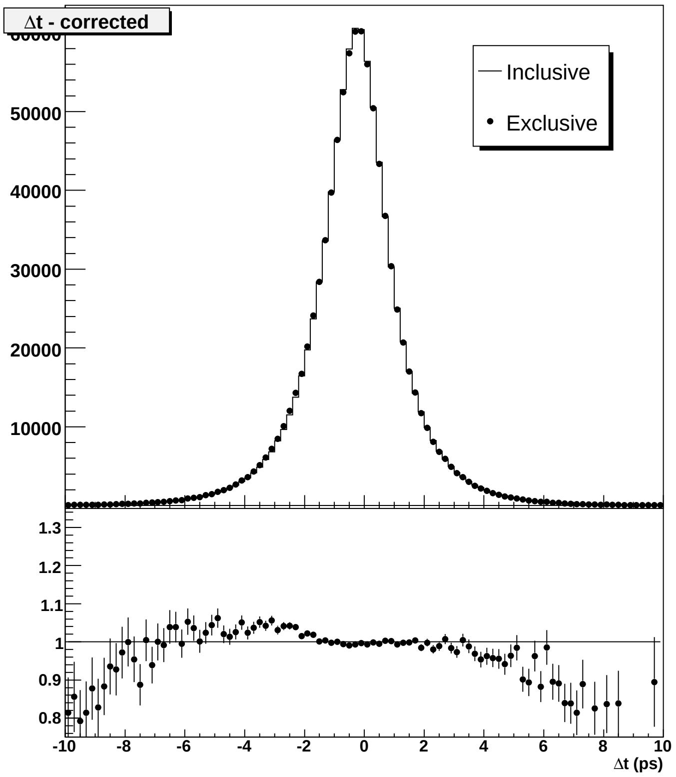

Figure 10.8: Top: comparison of the Δt distributions for the inclusive D_{tag} sample (histogram) and the exclusive one (points with error bars) for $B^0\overline{B}^0$ MC signal events, after the $|\vec{p}_K|$ reweighting procedure has been applied. The histograms have been normalized to the same arbitrary number of events. Bottom: ratio (exclusive/inclusive) of the two distributions.

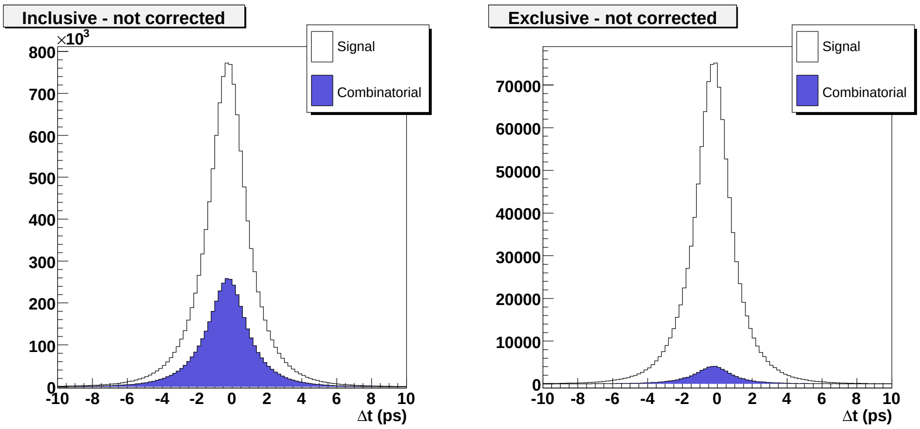

Figure 10.9: Δt distributions for the inclusive sample (left plot) and the exclusive one (right) with highlighted in color the contribution of combinatorial background.

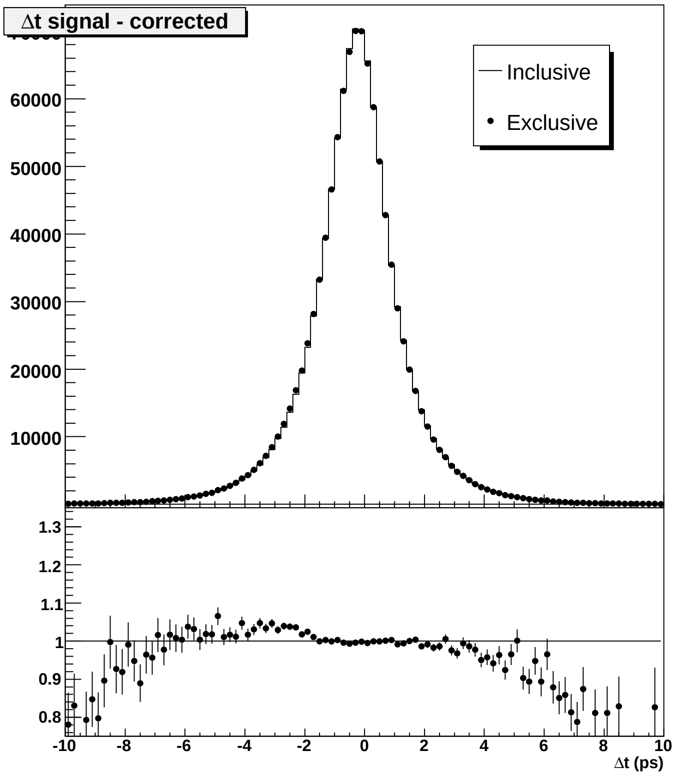

Figure 10.10: Top: comparison of the Δt distributions for the inclusive D_{tag}sample (histogram) and the exclusive one (points with error bars) for $B^0\overline{B}^0$ MC signal+combinatorial events, after the $|\vec{p}_K|$ reweighting procedure has been applied. The histograms have been normalized to the same arbitrary number of events. Bottom: ratio (exclusive/inclusive) of the two distributions.

order of a few percent level.

We would like to model the combinatorial background shapes directly on the data, using wrongly charged (ℓ, π_{soft}) pairs on the m_ν^2 signal region. The comparison between correctly charged (GC) combinatorial events and wrongly charged events (WC) shows unacceptable discrepancies in the m_ν^2 signal region, while such discrepancies vanish in the sideband, see figure 10.11.

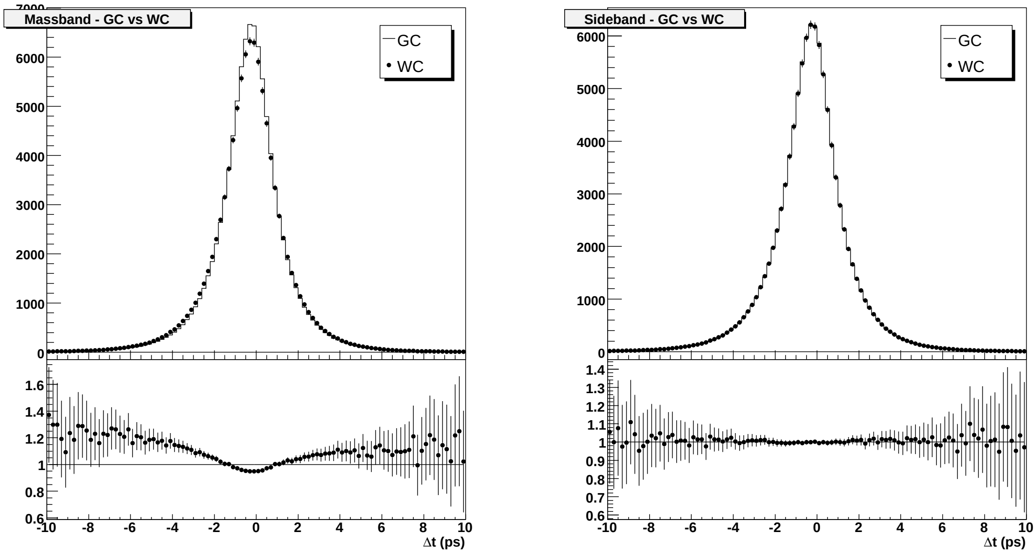

Figure 10.11: Good Charge (histograms) and Wrong Charge (points with error bars) comparisons on Δt distributions for the exclusive sample in the m_ν^2 signal region (left plot) and in the sideband (right plot). All distributions have been normalized to the same arbitrary area.

Given that the combinatorial background is only a small fraction of the exclusive sample and that the data-MC comparison shows good agrement both in the massband WC and the sideband (WC and GC), see figure 10.12, we decide to take the combinatorial background shapes from the Monte Carlo.

To get the signal D_{tag} shapes from the *on-peak* exclusive data sample we adopt the following procedure:

- we split our exclusive data sample into the five sub-samples corresponding to the $|\vec{p}_K|$ bins over which the nominal fit is run;
- we eliminate the continuum background by subtracting the properly rescaled *off-peak* events;
- we subtract the combinatorial background, using the Δt shape predicted by the Monte Carlo;
- we reweight the exclusive events in order to match the inclusive signal D_{tag} spectrum as predicted by the MC;

The effects of varying the MC distributions within the uncertainties will be taken into account in the systematic uncertainties section.

The whole procedure has been successfully tested on a Monte Carlo + *off-peak* sample, where proper luminosity weights have been taken into account. Figure 10.13 shows the comparison of data D_{tag} shapes with signal Monte Carlo; in general we find pretty good consistency, besides the bin with highest $|\vec{p}_K|$, where some discrepancy is apparent.

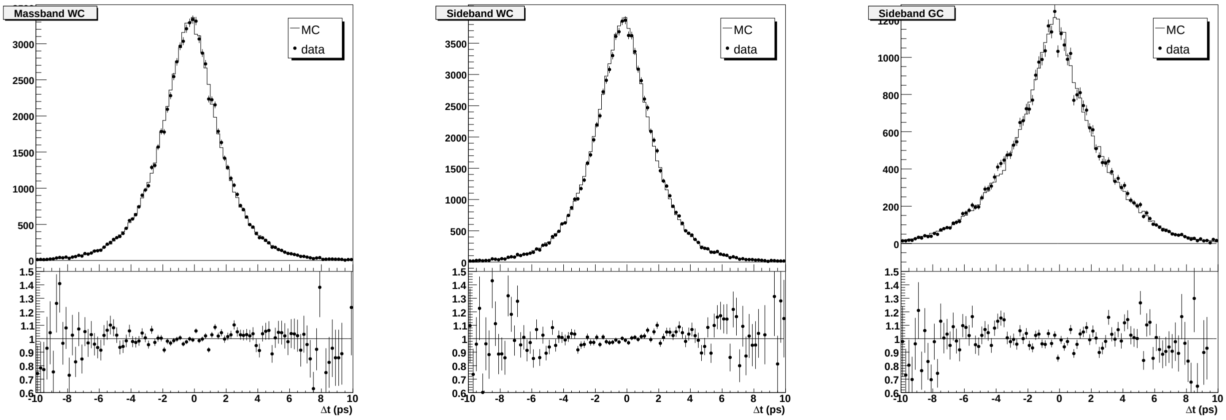

Figure 10.12: Comparisons of data (points with error bars) and Monte Carlo (histograms) for the exclusive D_{tag} sample in the m_ν^2 signal region WC (left plot), in the m_ν^2 sideband WC (center) and GC (right). Properly normalized off-peak data have been subtracted from on-peak data and MC histograms have been normalized to the data.

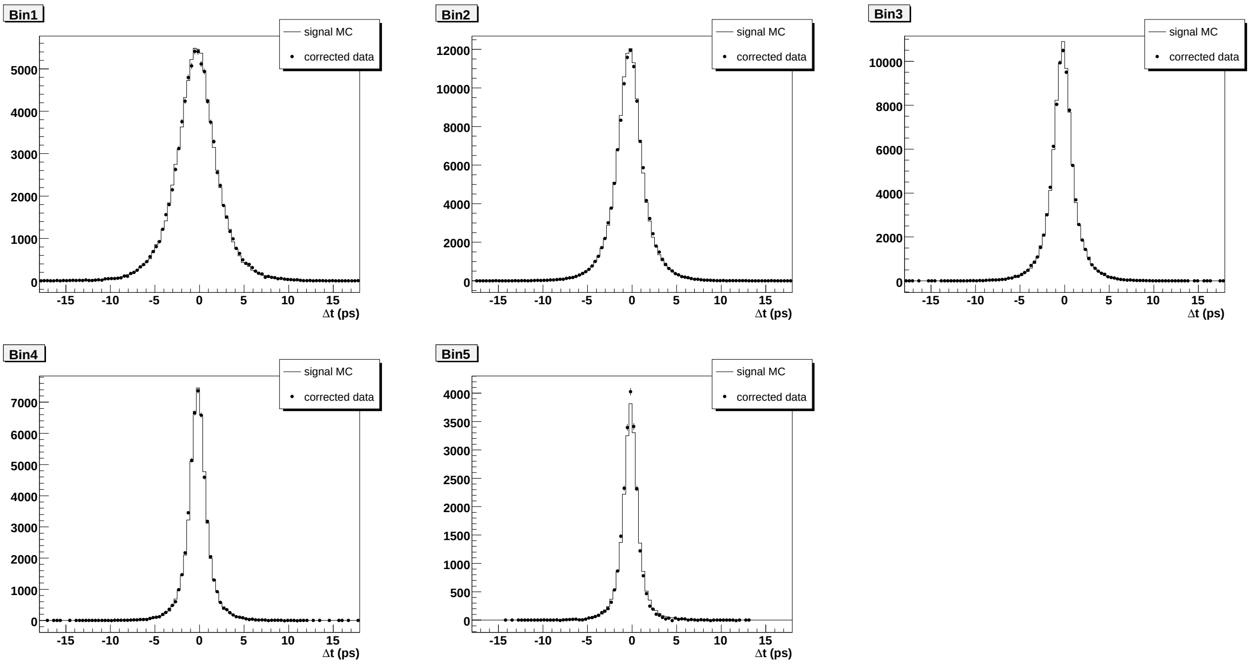

Figure 10.13: Comparison of signal D_{tag} Monte Carlo (histograms) with signal D_{tag} shapes derived from the *on-peak* data (points with error bars) in every bin of $|\vec{p}_K|$(increasing from top left to bottom right). Distributions have been normalized to the same area and events have been reweighted in order to match the inclusive signal D_{tag} $|\vec{p}_K|$ spectrum.

Chapter 11

Fit to data

In this chapter we will overview the procedure used to define our nominal fit to the data, after the validation process on generic and reweighted Monte Carlo samples.

During the whole procedure, the value of $|q/p| - 1$ and some other physically relevant parameters are kept *blind*; this means that randomly generated numbers are added to them and these numbers are disclosed only until the procedure has been completely defined and all the systematic uncertainties are established.

11.1 Data sideband

We begin fitting our data sample limiting ourselves to the m_ν^2 sideband, dominated by continuum and $B\overline{B}$ combinatorial events. Since $B^0\overline{B}^0$ combinatorial events are sensitive to $|q/p|$ in the same way as peaking, we proceed blinding $|q/p|$. The other parameters which are kept blind are τ_{B^0}, Δm, $\Delta\Gamma$ and the two DCSD effective parameters b and c.

Figures 11.1 and 11.2 show the result of a fit to a homogeneous subsample of the available statistics in the Δt and $\cos(\theta_{K\ell})$ projections respectively. The parameters which have been floated are the detector asymmetries, mistags, the effective parameters τ_{B^0} and Δm for $B^0\overline{B}^0$ combinatorial, the main parameters of the resolution model and the fractions of D_{tag} kaons over the total. In general we find good consistency between the parameters we derived from MC and the fit results.

For the D_{tag} modeling, we find that we get a better Likelihood by using the shapes derived from the generic Monte Carlo, instead of the pdf's derived from the exclusive sample, even though the *visual* agreement is roughly coincident. We therefore decide to use the shapes of the inclusive Monte Carlo in the nominal fit.

We plan to fix the parameters of the resolution of combinatorial backgrounds to the ones we find in the fits to the m_ν^2 sideband. To check the correctness of this procedure, we compare in the Monte Carlo the Δt shapes in the four charge combinations of combinatorial massband and sideband. The comparison is reported in figure 11.3; no evident structures appear in the ratio of massband and sideband distributions, so we can keep the parameters we fit on the sideband for the complete fit.

11.2 Fit to massband + sideband

We move to fitting the whole range of m_ν^2. Keeping fixed the parameters of the resolutions, and allowing to float $|q/p| - 1$, the reconstruction and tagging asymmetries, the dilutions, the D_{tag} fractions and the main parameters of the resolution in the peaking $B^0\overline{B}^0$ component, we find the results shown in figures 11.4 and 11.5.

We find no large discrepancies of detector related asymmetries and dilutions with respect to the predictions of the generic Monte Carlo. As for the parameters of the D_{tag} components, we

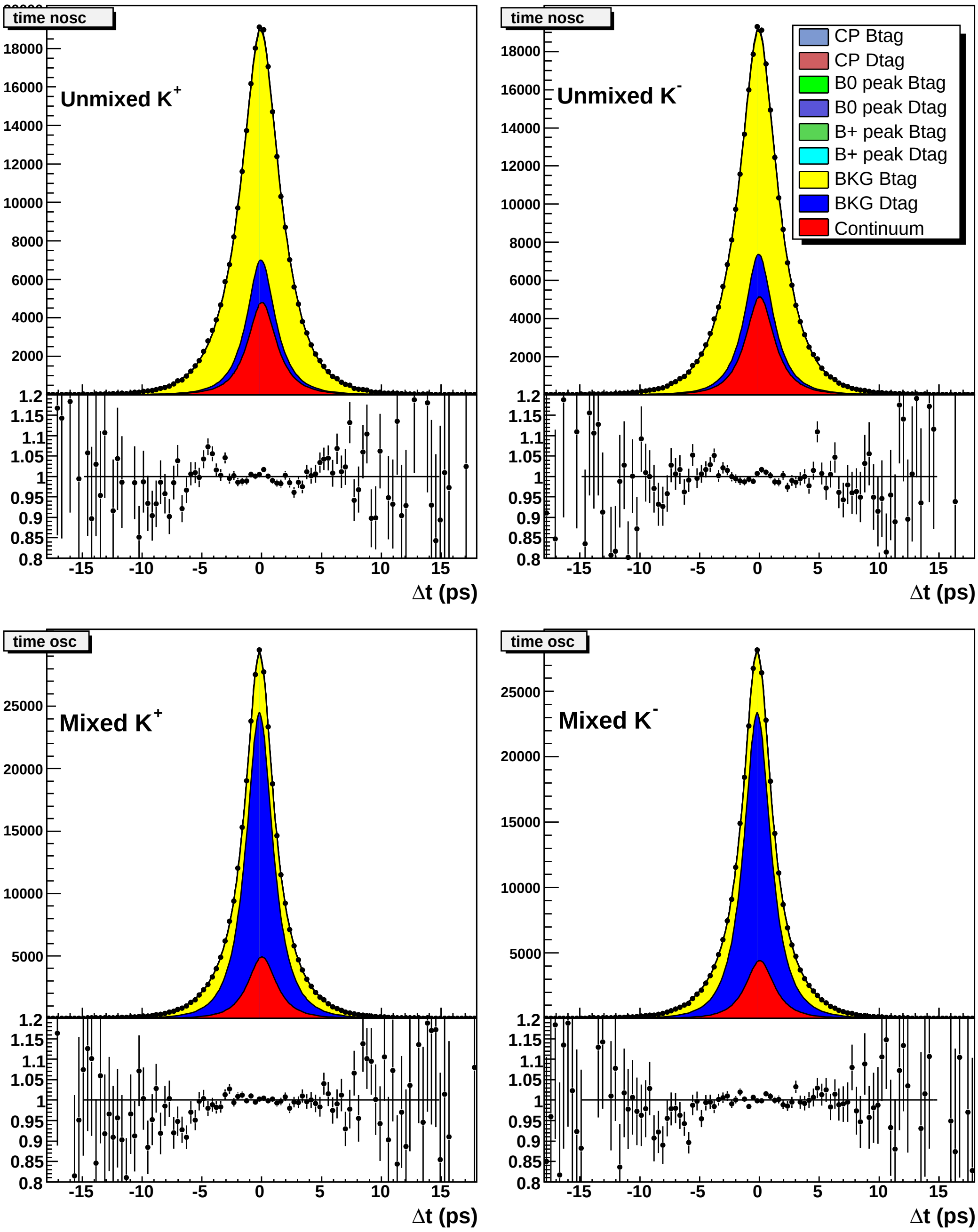

Figure 11.1: Fitted Δt distributions for m_ν^2 sideband on-peak data. The data used in this fit is a homogeneous sample corresponding to 33% of the available statistics.

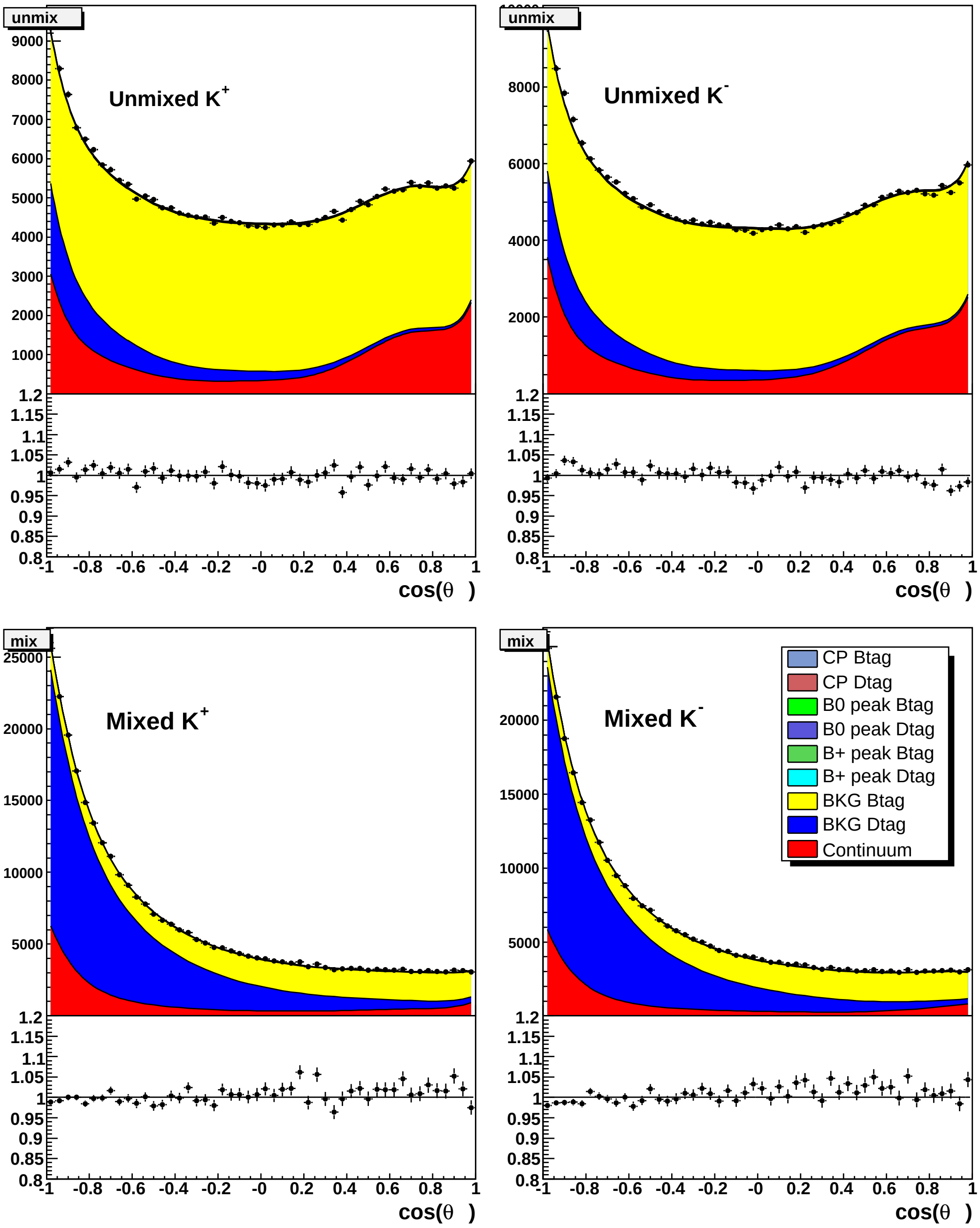

Figure 11.2: Fitted $\cos(\theta_{K\ell})$ distributions for m_ν^2 sideband on-peak data. The data used in this fit is a homogeneous sample corresponding to 33% of the available statistics.

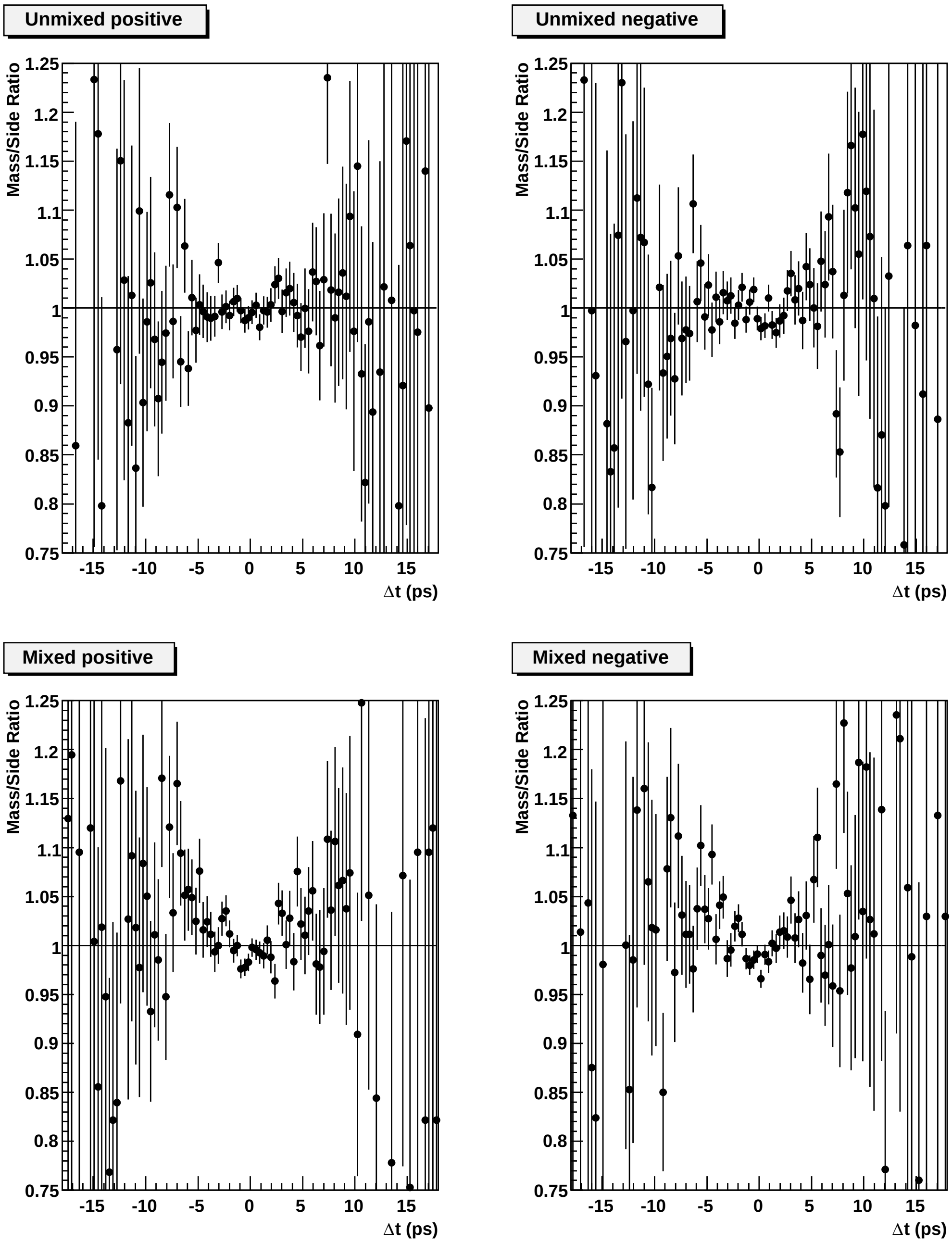

Figure 11.3: Ratio between the Δt distributions of combinatorial backgrounds in the m_ν^2 mass-band and in the sideband. The statistics used corresponds to 10% of the available statistics for the generic Monte Carlo.

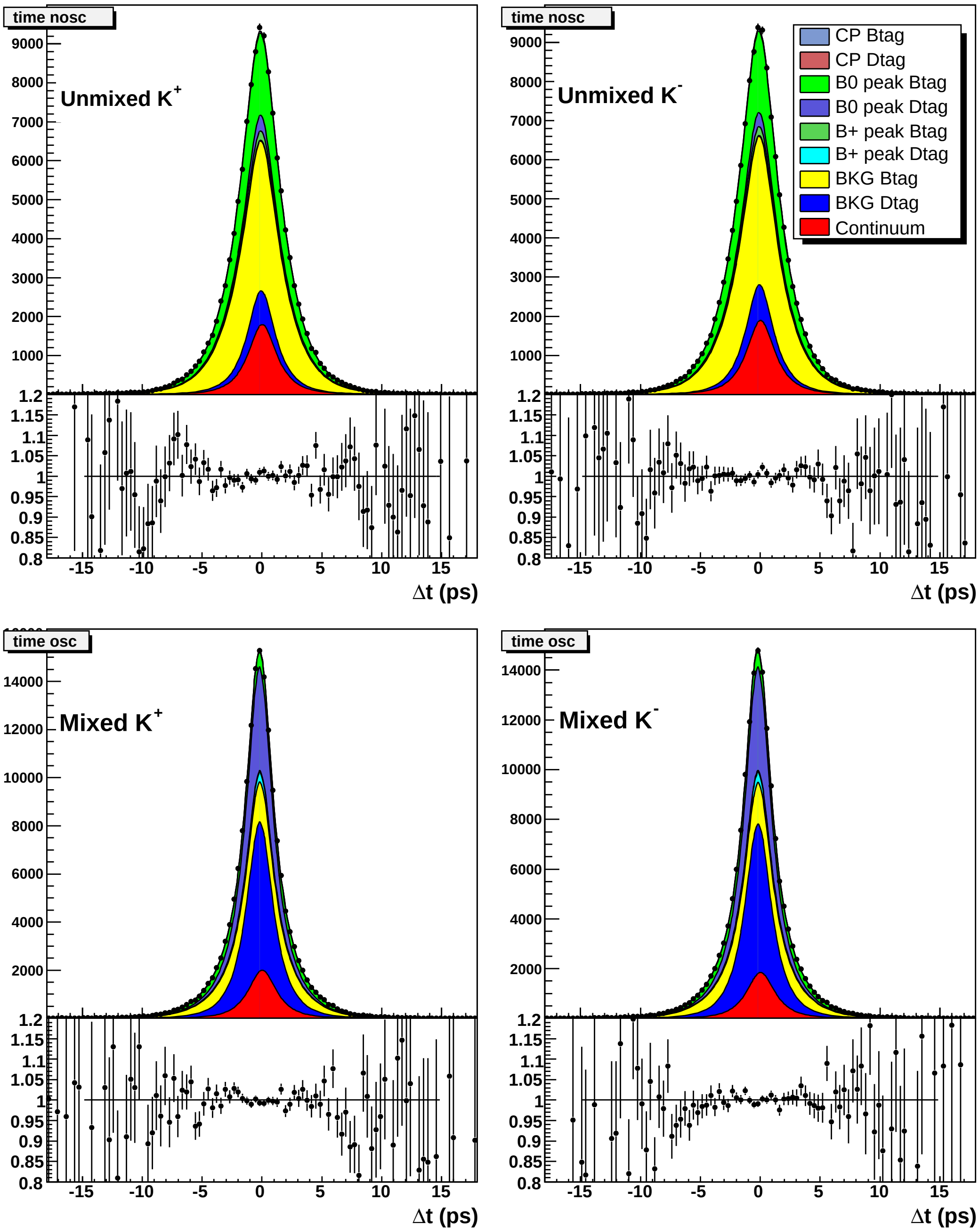

Figure 11.4: Fitted Δt distributions for m_ν^2 massband + sideband on-peak data. The data used in this fit is a homogeneous sample corresponding to 5% of the available statistics.

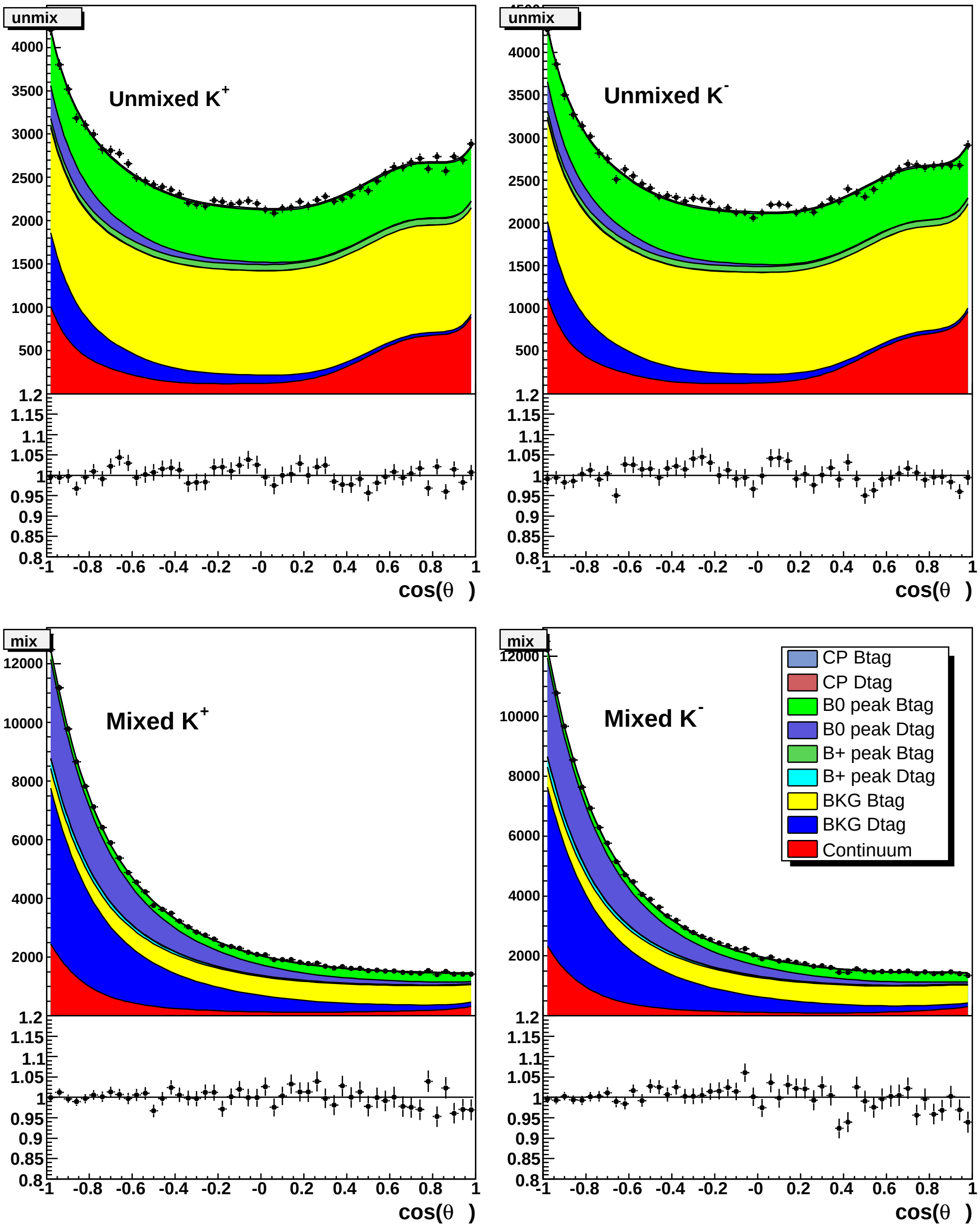

Figure 11.5: Fitted $\cos(\theta_{K\ell})$ distributions for m_ν^2 massband + sideband on-peak data. The data used in this fit is a homogeneous sample corresponding to 5% of the available statistics.

Table 11.1: Results of blinded $|q/p| - 1$ on the five series of fits performed on the on-peak data sample.

Fit series	(blinded) $\lvert q/p\rvert - 1$
series 15	0.0287 ± 0.0014
series 18	0.0280 ± 0.0025
series 20	0.0285 ± 0.0022
series 22	0.0275 ± 0.0025
series 25	0.0274 ± 0.0020

observe some instabilities in the value of $\Delta\omega$ (which corresponds to direct CP-violation of D mesons, as long as charge asymmetries are taken into account) for one or more components. This leads to finding a secondary minimum of the Likelihood, with $\Delta\omega$ for one or more components clearly inconsistent with zero. The reason of this instability is to be found in the similarity of the $\cos(\theta_{K\ell})$ distributions for each component, which gives no sufficient lever-arm to the fit to clearly distinguish them.

The problem is solved by repeating one of those fits starting from the previously found minimum (but setting all $\Delta\omega$ parameters to the initial value of zero); it usually converges to the proper minimum, so we allow all the ω, $\Delta\omega$ and the D_{tag} fractions to float, besides the ones of the charged peaking B_{tag} component, too small to be reliably fit (its parameters are fixed to the Monte Carlo predictions).

11.3 Fitting procedure

Given the number of parameters which we want to float in the nominal fit and the size of our data sample ($\sim$ 12 millions on-peak data events), we soon realized that it is not possible to run a single fit on the single-CPU machines available to us on the whole statistics.

We thus decide to perform a series of fits on the N homogeneous (with respect to the data-taking periods) subsamples into which the whole dataset is split. This way we can float all the physical parameters and most of the parameters describing the resolution of the peaking $B^0\overline{B}^0$ component. The final result is given by the arithmetic average of the N results and the associated error is given by $RMS/\sqrt{N-1}$, where RMS is the *root mean square* of the N results.

One advantage of this approach is that in this way we overcome the problem of correcting the error of a single fit for the effect introduced by events with two or more B_{tag} kaons (which represent $\sim$ 20% of the total), which tends to reduce - naively by $\sim$ 10% - the fit error on $|q/p|-1$. The drawback is that we need to account for an additional source of systematic uncertainty: the choice of the number of subsamples. As we will see in section 12.11 this systematic error is perfectly acceptable.

We perform five series of fits, each with the same parameters being floated, on 15, 18, 20, 22 and 25 subsamples respectively. In table 11.1 we present the (blinded) results obtained in each series along with the error computed with the method above explained. Also, in figure 11.3 we show the distributions of the results of each series with a gaussian with mean value and width set to the mean value and RMS of each distribution overlaid.

The results of the five different series are stable and within a 1 permille spread. We quote as the central value of our measurement the average of the averages of the five series and as statistical error we conservatively take the maximum statistical error we obtain from a single series. The blinded result we get is therefore:

$$\text{(blinded)} \quad |q/p| - 1 = 0.0280 \pm 0.025 \text{ (stat.)} \tag{11.1}$$

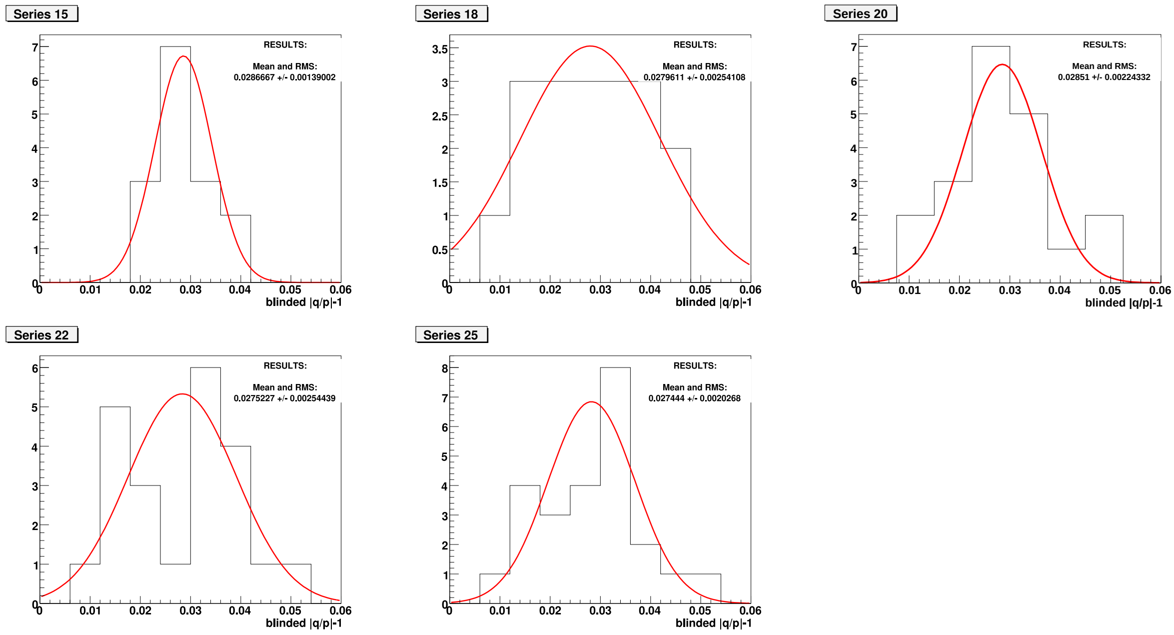

Figure 11.6: Distributions of the five series of nominal fits on the on-peak data. Overlaid to each distribution is a gaussian whose mean and width are set respectively to the arithmetic average and RMS of each distribution.

11.4 Unblinding τ_{B^0} and Δm

Before proceeding to the complete unblinding, we unblind τ_{B^0} and Δm of the peaking $B^0\overline{B}^0$ component. The results we get (from the series of fits on 15 subsamples of the whole dataset) are collected in table 11.2. The quoted errors are statistical only and are computed in the same way we estimate the error on $|q/p| - 1$.

Table 11.2: Unblinded results for τ_{B^0} and Δm (series 15) and comparison with the world averages. The error presented for the fit results is statistical only.

	Fit results (series 15)	World averages [4]
τ_{B^0}	1.490 ± 0.004	1.530 ± 0.009
Δm	0.5699 ± 0.0022	0.507 ± 0.005

We observe a very large discrepancy between the fit results and the world averages. The source of this discrepancy is to be found in a significant interplay between these two parameters (particularly Δm) and the parameters of the resolution. Repeating the nominal fit fixing τ_{B^0} and Δm we get the results displayed in figure 11.7 and 11.8.

It can be seen that the *visual* agreement is analogous of the one we can see on the nominal fits, thus the variations on τ_{B^0} and Δm are re-absorbed by the variations on the parameters of the resolution.

The impact of the incorrect measurement of τ_{B^0} and Δm on our measurement of $|q/p| - 1$ is treated in section 12.12.

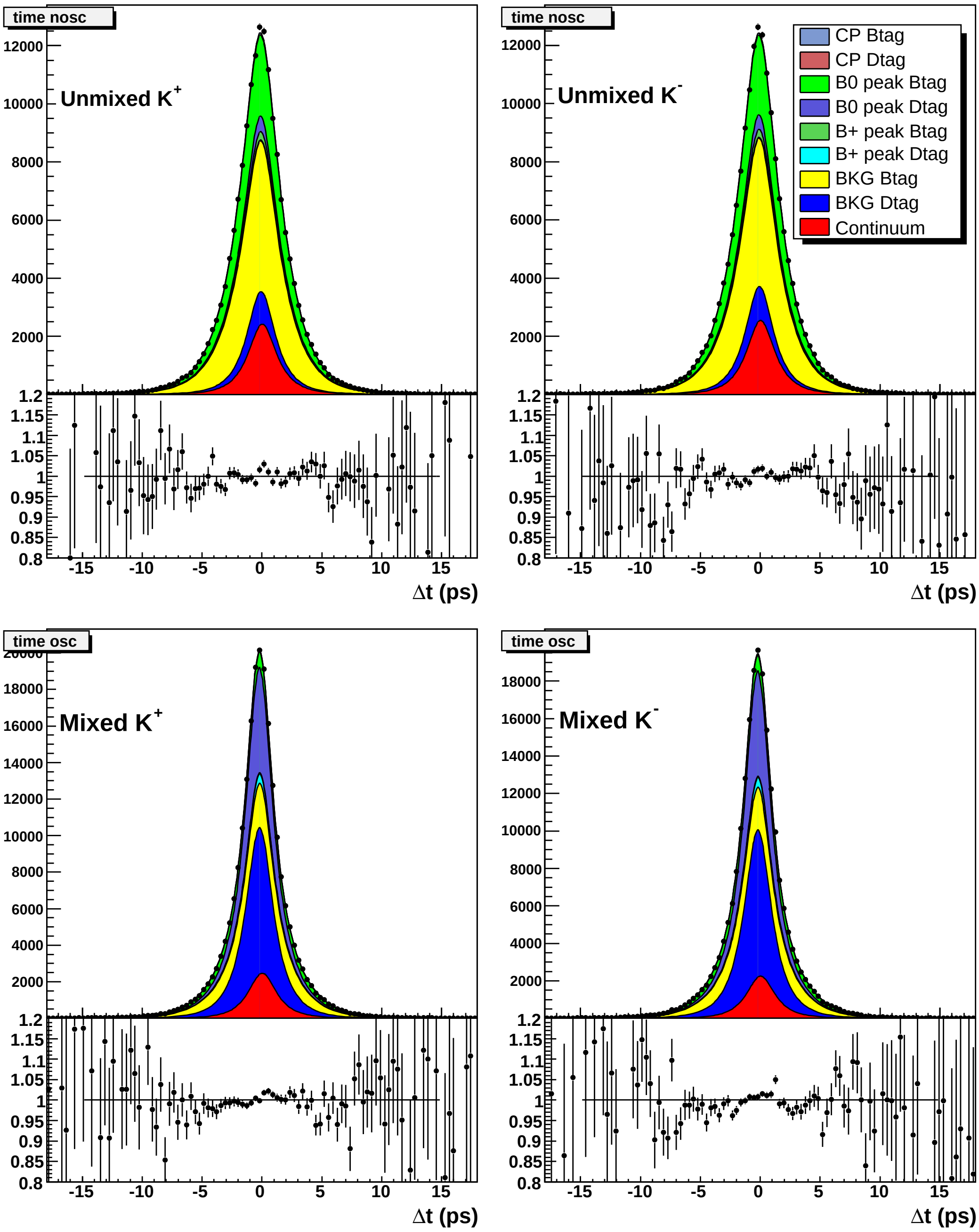

Figure 11.7: Fitted Δt distributions for m_{ν}^2 massband + sideband on-peak data. The data used in this fit is a homogeneous sample corresponding to 6.7% of the available statistics.

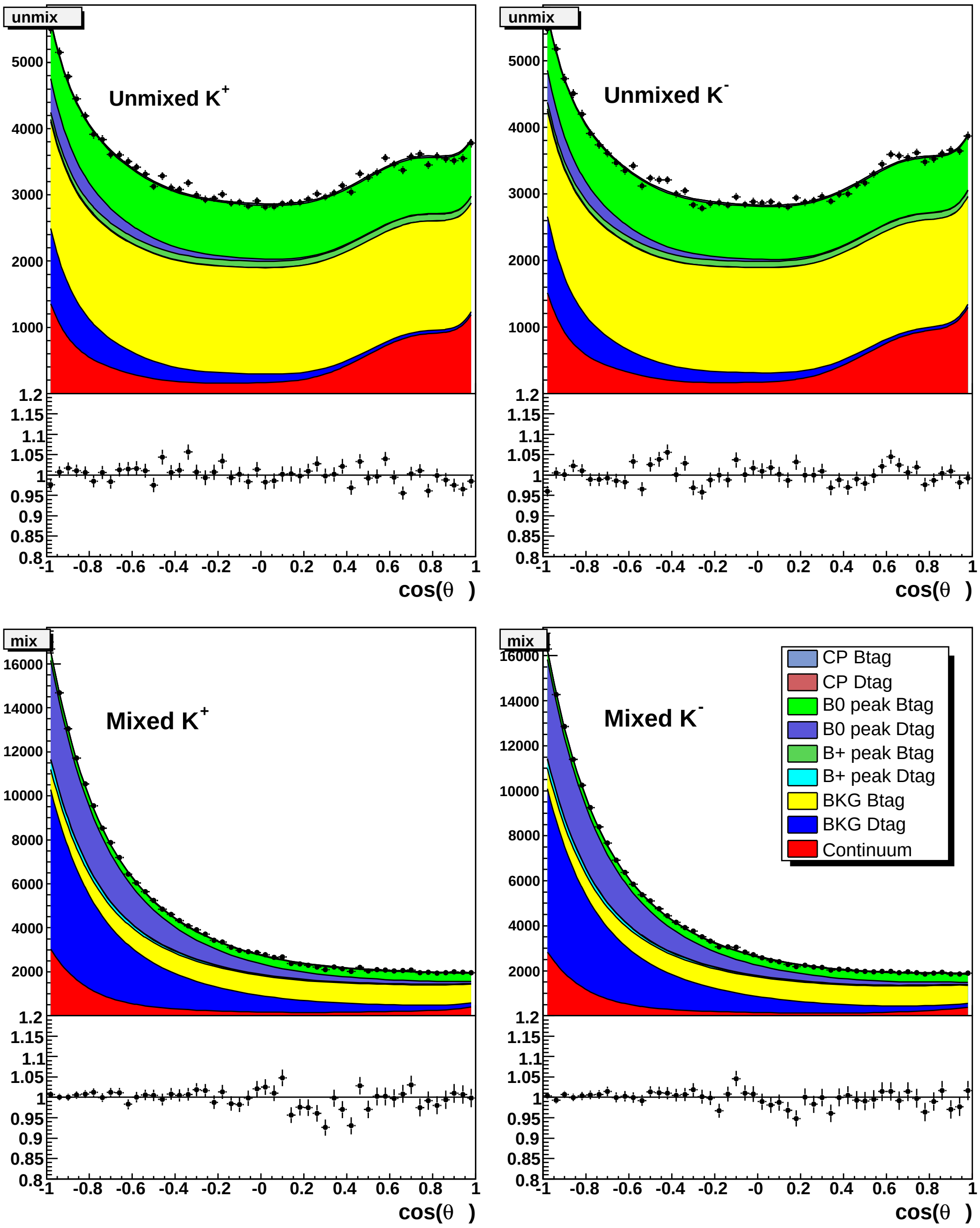

Figure 11.8: Fitted $\cos(\theta_{K\ell})$ distributions for m_ν^2 massband + sideband on-peak data. The data used in this fit is a homogeneous sample corresponding to 6.7% of the available statistics.

11.5 Fitted parameters on the nominal fit

We report in tables 11.3-11.5 the fit results for the parameters which have been floated in the nominal fit. The averages presented have been computed on the results of the series on 15 subsamples and the errors are again computed as $RMS/\sqrt{14}$.

Table 11.3: Fit results for the parameters of the peaking $B^0\overline{B}^0$ component (besides the detector related asymmetries, common for each sample) floated in the nominal fit. Here the averages of the series on 15 subsamples are shown.

Parameter	Fit result
A_{tag}	0.0111 ± 0.0030
$A_{rec}(e)$	0.0007 ± 0.0023
$A_{rec}(\mu)$	0.0069 ± 0.0017
D_0	0.440 ± 0.006
D_1	0.250 ± 0.008
$\Delta\omega_0$	-0.014 ± 0.004
$\Delta\omega_1$	0.016 ± 0.005
f_n	0.911 ± 0.007
$s_{n,0}$	0.832 ± 0.012
$s_{n,1}$	0.271 ± 0.011
$s_{w,0}$	2.07 ± 0.13
$s_{w,1}$	0.71 ± 0.05
o_n	0.057 ± 0.007
o_w	0.23 ± 0.04
τ_{G1}	0.0024 ± 0.0011
$\tau_{G2,0}$	0.83 ± 0.08
$\tau_{G2,1}$	-0.04 ± 0.07
$f_{G2,0}$	0.610 ± 0.029
$f_{G2,1}$	-0.254 ± 0.027
$\omega_{D_{tag}}$	0.0857 ± 0.0006
$\Delta\omega_{D_{tag}}$	0.0008 ± 0.0011
D_{tag} fraction (Unmixed Positive)	0.0982 ± 0.0009
D_{tag} fraction (Unmixed Negative)	0.0988 ± 0.0008
D_{tag} fraction (Mixed Positive)	0.7120 ± 0.0008
D_{tag} fraction (Mixed Negative)	0.7116 ± 0.0007

Table 11.4: Fit results for the parameters of the combinatorial $B^0\overline{B}^0$ component floated in the nominal fit. Here the averages of the series on 15 subsamples are shown.

Parameter	Fit result
D_0	0.269 ± 0.011
D_1	0.399 ± 0.007
$\Delta\omega$	-0.0011 ± 0.0006
$\omega_{D_{tag}}$	0.1344 ± 0.0011
$\Delta\omega_{D_{tag}}$	0.0032 ± 0.0031
D_{tag} fraction (Unmixed Positive)	0.1527 ± 0.0018
D_{tag} fraction (Unmixed Negative)	0.1551 ± 0.0024
D_{tag} fraction (Mixed Positive)	0.6112 ± 0.0023
D_{tag} fraction (Mixed Negative)	0.6117 ± 0.0022

Table 11.5: Fit results for the parameters of the combinatorial B^+B^- component floated in the nominal fit. Here the averages of the series on 15 subsamples are shown.

Parameter	Fit result
$\omega_{B_{tag}}$	0.3086 ± 0.0010
$\Delta\omega_{B_{tag}}$	0.0044 ± 0.0019
$\omega_{D_{tag}}$	0.1287 ± 0.0011
$\Delta\omega_{D_{tag}}$	-0.0044 ± 0.0026
D_{tag} fraction (Unmixed Positive)	0.1010 ± 0.0016
D_{tag} fraction (Unmixed Negative)	0.0975 ± 0.0016
D_{tag} fraction (Mixed Positive)	0.6280 ± 0.0028
D_{tag} fraction (Mixed Negative)	0.6229 ± 0.0026

Chapter 12

Systematic uncertainties

In this chapter we will discuss each source of systematic uncertainty on our measurement and give an estimate of it.

12.1 SVT alignment

The uncertainty in the alignment of the SVT has been checked following the standard recipe suggested by the tracking group and using four different configuration files corresponding to a relistic SVT misalignment. For each configuration, the generic $B\overline{B}$ Monte Carlo for Run2 has been reproduced, with the same selection code and settings used for the nominal production of data and Monte Carlo.

We run our standard fit over the nominal sample and the four samples produced with shifted SVT alignment and compare the results on the fitted value of $|q/p| - 1$, which are graphically presented in figure 12.1.

The largest deviation in the fitted value of $|q/p| - 1$ we observe between a pair of these samples is 0.0008 and we take it as the systematic error given by the alignment of the SVT.

12.2 Modeling of D_{tag} kaons pdf's

We compare the results on $|q/p| - 1$ obtained by using the D_{tag} shapes derived from the inclusive Monte Carlo (nominal fit) and from the on-peak data on the exclusive sample.

We take as systematic uncertainty associated to D_{tag} modeling the largest difference we found in fits run over data samples corresponding to 5% of the Run1-5 statistics, which is 0.0008.

12.3 Sample composition

We discuss here the effects of a potential incorrect determination of the sample composition described in section 5.5. The strongest assumption we do here is to get from the Monte Carlo the ratio between neutral and charged $B\overline{B}$ combinatorial events.

This ratio (slightly varying among the different charge combinations and lepton species) is predicted to be roughly 40:60. We evaluate the impact of a wrong fraction by performing a scan on the reweighted Monte Carlo samples (using only combinatorial events to enhance the effect) with the fraction fixed to 50:50 and 30:70.

Results on the main fitted parameters are shown in figure 12.2. No significant trend is seen by varying the generated value of $|q/p| - 1$; the only visible effect is a slight variation in the average value of reconstruction asymmetries.

As systematic uncertainty associated to the sample composition, we take the average of the moduli of the differences between the fit results in the modified configurations and the nominal

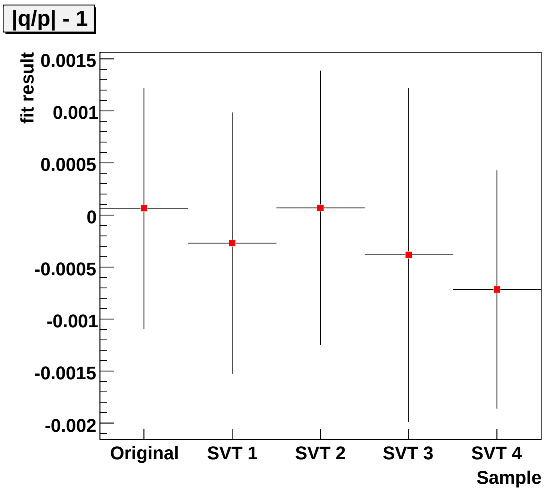

Figure 12.1: Fitted results on $|q/p|-1$ using the generic Run2 Monte Carlo with the nominal (first bin) and shifted (other four bins) SVT alignment.

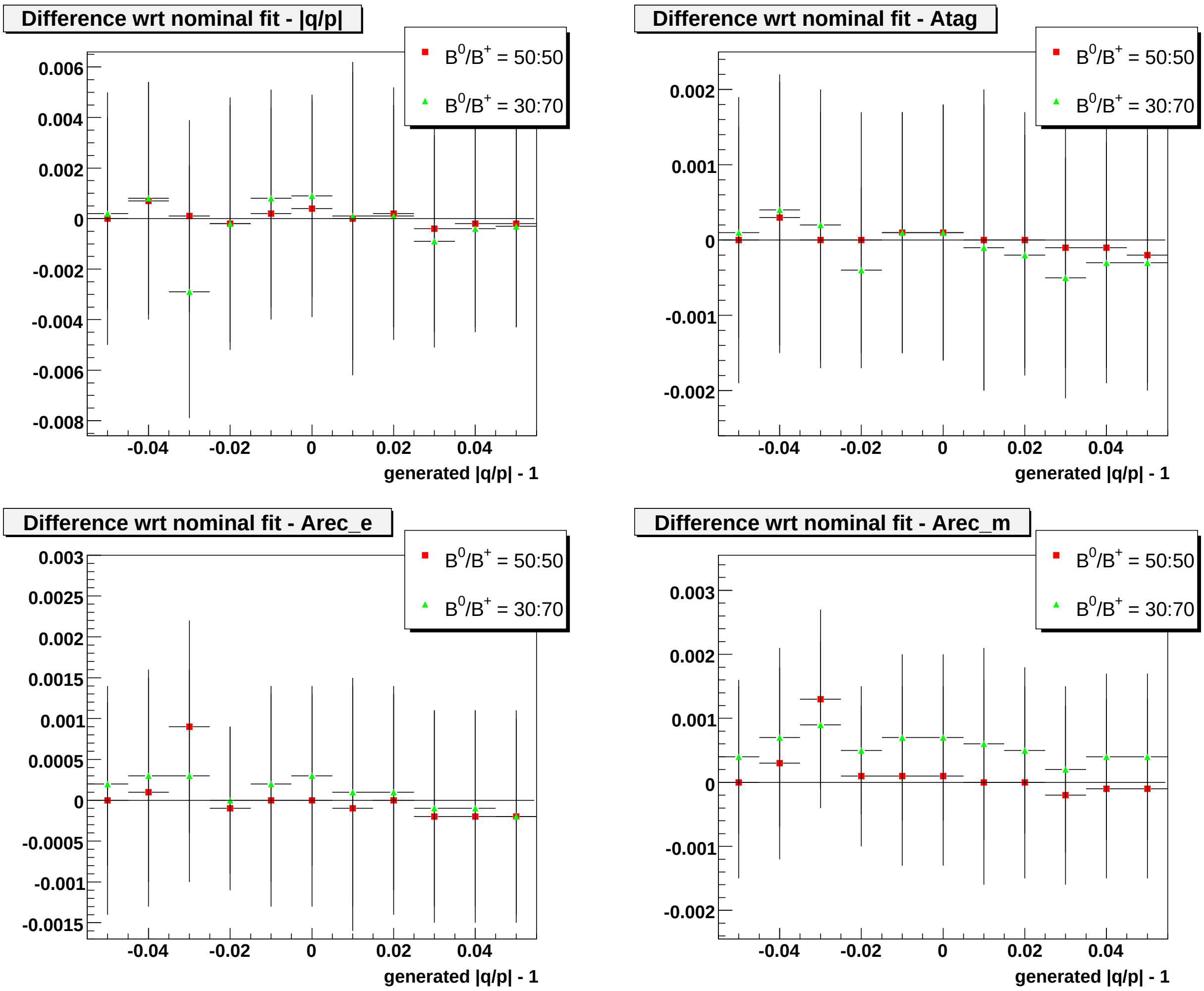

Figure 12.2: Differences with respect to nominal fit in fitted parameters fixing the ratio of $B^0\overline{B}^0$ over B^+B^- combinatorial to 50:50 (red squares) and 30:70 (green triangles). Results shown are $|q/p|-1$ (top left plot), A_{tag} (top right), $A_{rec}(e)$ (bottom left) and $A_{rec}(\mu)$ (bottom right).

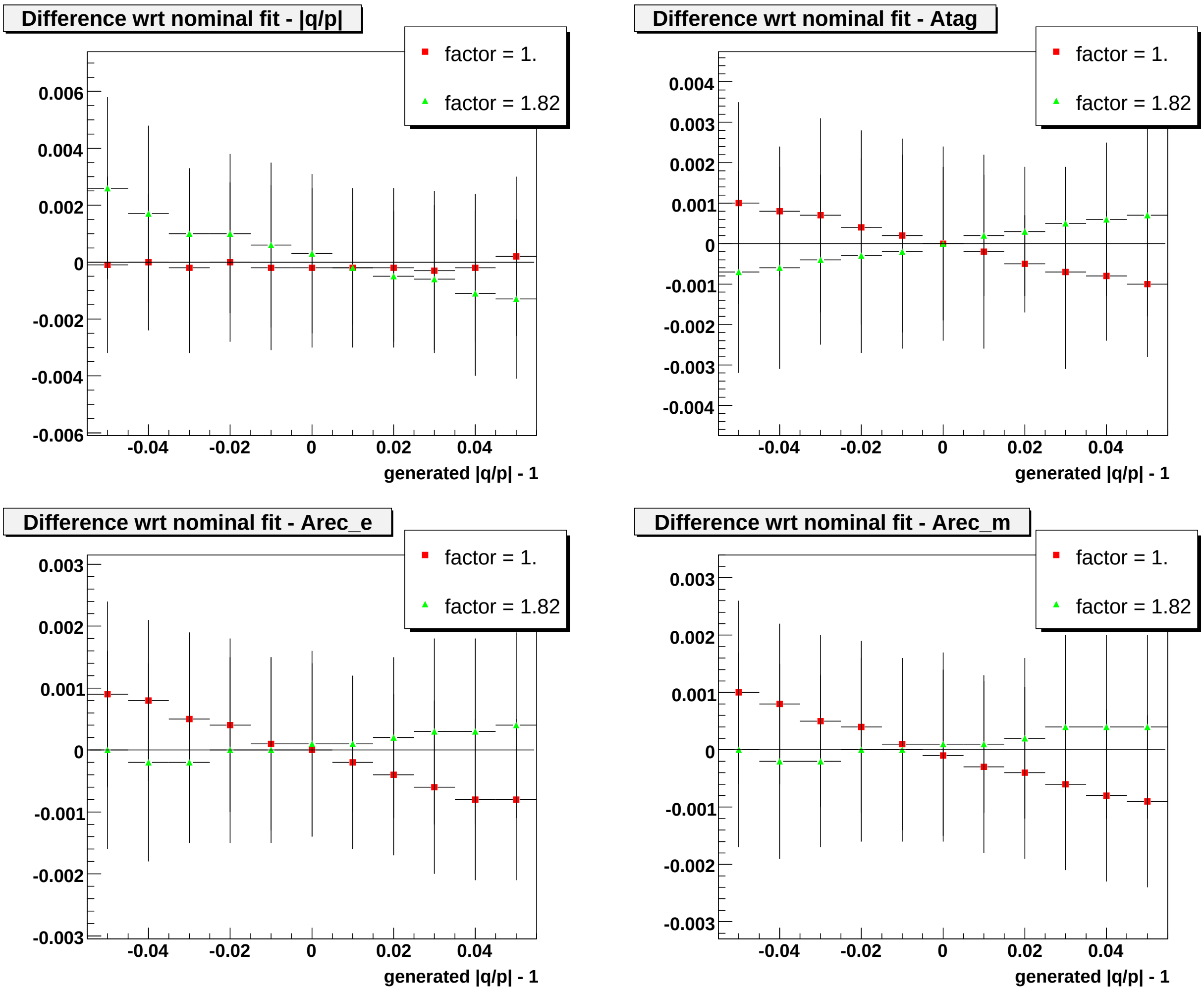

Figure 12.3: Differences with respect to nominal fit in fitted parameters using a correction factor equal to 1. (red squares) and 1.82 (green triangles) to the dependence on D_{tag} fractions for $B^0\overline{B}^0$ combinatorial. Results shown are $|q/p|-1$ (top left plot), A_{tag} (top right), $A_{rec}(e)$ (bottom left) and $A_{rec}(\mu)$ (bottom right).

ones. This is equal to 0.0005.

12.4 Correction factor for $B^0\overline{B}^0$ combinatorial

As we saw in section 9.4 the dependence on the generated value of $|q/p|-1$ of the asymmetries of D_{tag} kaons has to be corrected by a factor 1.41 (the value we get from our generic MC) in $B^0\overline{B}^0$ combinatorial with respect to peaking events.

We estimate the impact on the fitted $|q/p|$ by changing the correction factor to 1. and 1.82 and comparing the results we get in a scan over the $(B^0\overline{B}^0)$ reweighted Monte Carlo samples. Results are reported in figure 12.3.

It can be seen that the use of a wrong correction factor affects mostly the tagging and reconstruction asymmetries, which assume a dependence on the generated value of $|q/p|-1$. The effect on the fitted value of $|q/p|-1$ is very small when we use the same dependence of $B^0\overline{B}^0$ peaking events (factor = 1.), while it is more appreciable for a correction factor twice as large as the nominal one.

As systematic uncertainty we take a multiplicative factor corresponding to the absolute value

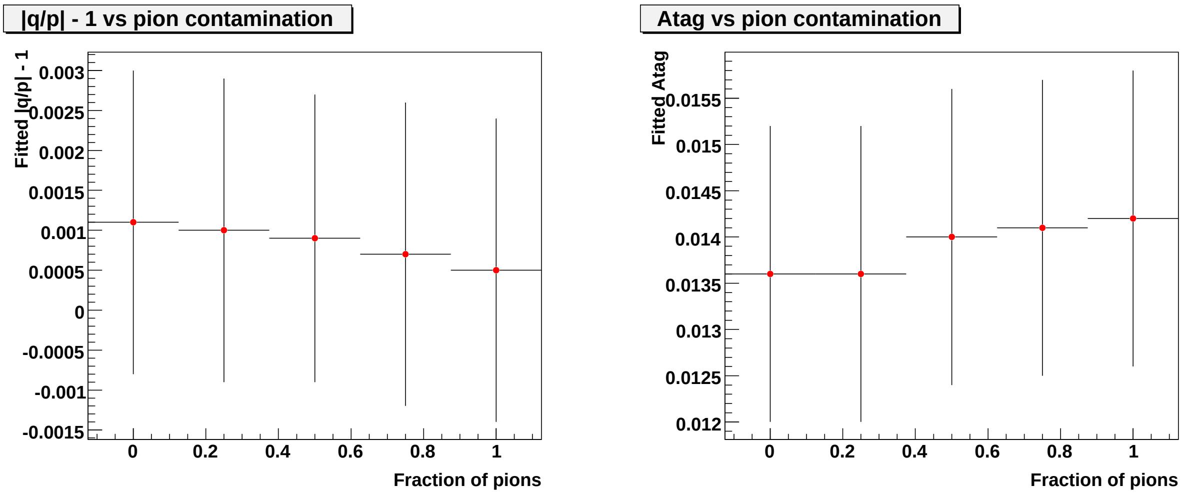

Figure 12.4: Fitted results on $|q/p| - 1$ (left plot) and A_{tag} (right) versus the fraction of pions passing the selection: 0 corresponds to no pions selected and 1 corresponds to the standard fraction of pions accepted by our algorithm.

of the slope of the linear function which fits the set of results obtained with the correction factor fixed to 1.82, which is 0.034.

12.5 Pion contamination in kaon sample

To estimate the effect of the presence of pions in our kaon sample, we vary on the Monte Carlo the fraction of pions entering our selection. We consider five $B^0\overline{B}^0$ MC samples with, respectively, 0%, 25%, 50%, 75% and 100% the amount of pions accepted by our selection cuts and run the standard fit over these.

It can be seen (figure 12.5) that, with a statistics corresponding to Run2 generic MC, there is a very slight trend in the fitted values of $|q/p| - 1$ and A_{tag} as a function of the fraction of pions entering the selection.

The difference in the fitted $|q/p| - 1$ of the nominal fit with respect to the no-pions case, which we take as our systematic uncertainty, is 0.0006.

12.6 Fixed parameters of the resolution

We vary by $\pm 1\sigma$ (the uncertainty is obtained from the fit in the m_ν^2 sideband) the parameters of the resolution (for both the $B\overline{B}$ combinatorial background and the continuum) which are kept fixed in the nominal fit. We take the conservative approach of floating $|q/p| - 1$ only, so every effect is completely absorbed by it. Statistical correlations among the parameters are kept into account.

The resulting systematic error is 0.0001.

12.7 Presence of decays to CP-eigenstates

We vary the effective parameters C_{eff} and S_{eff} found in 7.10 and their relative fractions with respect to the other $B^0\overline{B}^0$ decays in order to cover for their uncertainty. We consider the situations summarized in table 12.1.

Table 12.1: Summary on the parameters used in the tests of the systematics associated to fitting the CP-eigenstates components fixing their parameters to the values found on the generic Monte Carlo. We report the values used for C_{eff}, S_{eff} and the relative fractions of CP-eigenstates with respect to the other $B^0\overline{B}^0$ components (100% corresponds to the nominal fit).

Fit	C_{eff}	S_{eff}	fractions
nominal	-0.0144	-0.0780	100%
CP1	-0.0077	-0.0390	100%
CP2	-0.0288	-0.1560	100%
CP3	-0.0144	-0.0780	50%
CP4	-0.0144	-0.0780	200%
CP5	-0.0144	-0.0780	0%

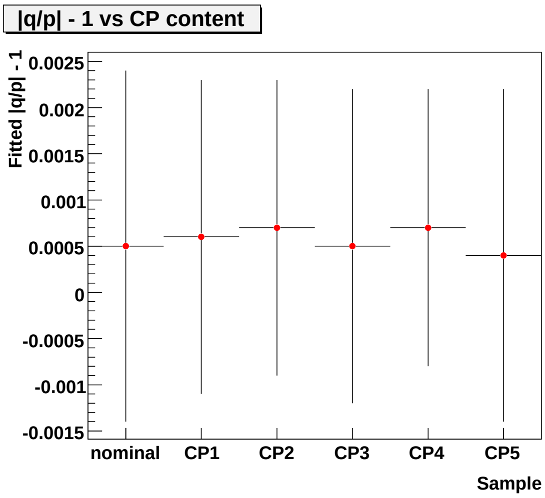

Figure 12.5: Fitted results on $|q/p| - 1$ for the fits with parameters of the CP-eigenstates component fixed to the configurations listed in table 12.1.

The results on the fitted values of $|q/p| - 1$ for the six configurations (the nominal and the five non-standard) are displayed in figure 12.5; the largest deviation we observe between two different configurations is 0.0003. We take this as the associated systematic uncertainty.

12.8 Measurement of the D_{tag} fractions

We compare the result obtained on the Monte Carlo by fixing the fractions of the D_{tag} component to the correct value given by the MC truth and the one given by floating all D_{tag} fractions, besides the ones relative to the peaking B^+B^- component.

The difference between the two fits, which we take as our systematic uncertainty is 0.0006.

12.9 Fraction of continuum

We vary the fraction of continuum background with respect to the amount given by the procedure described in section 5.5 by ±2% (this variation covers conservatively our uncertainty on this fraction) and repeat the nominal fit in several data subsamples carrying 5% of the available statistics.

The largest deviation we observe in the fitted value of $|q/p| - 1$ is 0.0003 and we take that as our systematic uncertainty.

12.10 Fake leptons

We estimate the effect of the mis-identification of non-lepton particles as the B_{rec} lepton by performing a fit on generic $B\overline{B}$ Monte Carlo with those particles removed.

Only slight variations on the reconstruction asymmetries are seen and we observe negligible deviations on the fitted value of $|q/p| - 1$: 0.0001.

12.11 Number of subsamples

We assume as systematic uncertainty on the choice of the number of subsamples into which the whole dataset is split half of the difference seen in the five series of nominal fits described in section 11.3.

The systematic uncertainty we quote on $|q/p| - 1$ is therefore 0.0007.

12.12 Variation of τ_{B^0} and Δm

As we saw in section 11.4, the values of τ_{B^0} and Δm for which the minimum of the nominal fit is found are significantly different from the world average.

To evaluate the impact of the incorrect measurement of these two parameters on the measurement of $|q/p| - 1$, we repeat a series of fits on data (15 samples) and on $B\overline{B}$ Monte Carlo + continuum (45 samples) with τ_{B^0} and Δm fixed to the PDG values. The difference on the average of the fit results is 0.0002 for the data and 0.0004 for the Monte Carlo.

To estimate the presence of a potential multiplicative bias caused by the incorrect estimate of the fraction of mixed events over the total, we run a scan on a sample of Toy Monte Carlo (generated with $|q/p| - 1 = 0.05$), fixing the value of Δm over a range 40% of its value wide. The only parameters which are allowed to float are τ_{B^0} and Δm. The results of the scan are reported in figure 12.12. The fitted $|q/p| - 1$ varies by $\sim 10\%$ of its value over the whole range scanned: since our fitted value of Δm differs by $\sim 12\%$ from the world average, we apply (conservatively, since the resolution parameters are not allowed to float) a multiplicative systematic uncertainty of 3%.

The quite conservative systematic uncertainty we quote is therefore $0.0005 \oplus (|q/p| - 1) \cdot 0.03$.

12.13 Fit bias

We estimate the potential bias introduced in the fitting procedure by performing two series of fits on the whole $B\overline{B}$ generic + continuum Monte Carlo statistics. The dataset is subdivided into 45 and 60 independent and homogeneous subsamples (having roughly the same size of the data samples used in the nominal fit) and we fit them floating the same parameters which are kept free in the nominal fit to the data. The results of the two series are displayed in table 12.2 and figure 12.13.

The fitted value of $|q/p| - 1$ on the generic + toy continuum Monte Carlo is below the expected value by $\sim 3\sigma$. As discussed in section 9.5, the source of this bias is not to be found in the events preselection stage of the analysis.

We correct the central value found on the nominal fit to the data by the average of the two results (0.004) and assign as systematic uncertainty half of this shift with its statistical uncertainty added in quadrature.

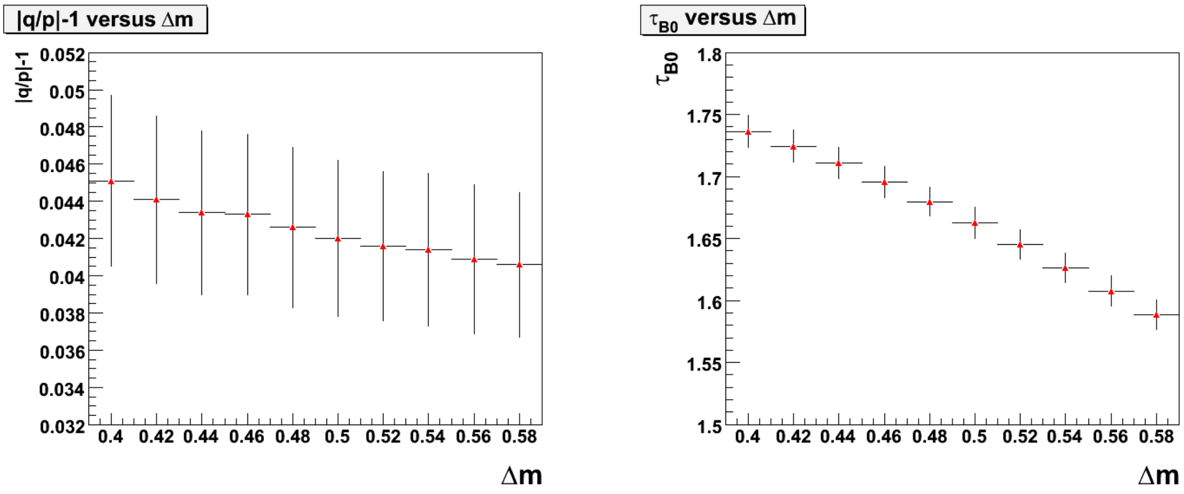

Figure 12.6: Results of the scan over Δm: the fitted values of $|q/p|-1$ (left plot) and τ_{B0} (right) are shown. Note: the random numbers used in the blinding procedure have been added to τ_{B^0} and Δm, so the values shown differ from the actual ones.

Table 12.2: Fitted $|q/p|-1$ on the two series of nominal fits to generic $B\overline{B}$ Monte Carlo + toy continuum.

	Fitted $\lvert q/p\rvert - 1$
series 45	-0.0035 ± 0.0011
series 60	-0.0046 ± 0.0013

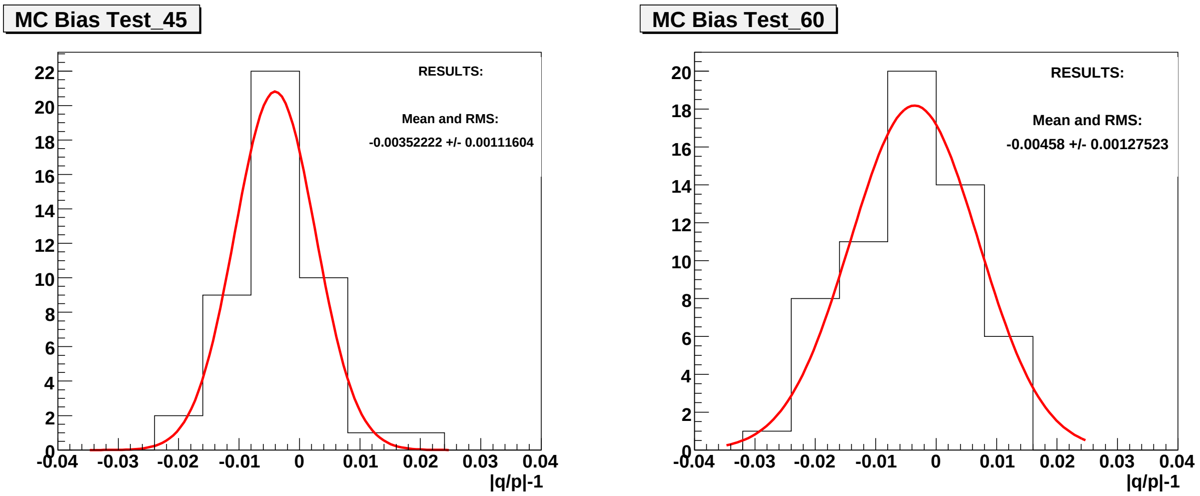

Figure 12.7: Distributions of single fit results for the series on 45 subsamples (left plot) and 60 subsamples (right). Overlaid to each distribution is a gaussian whose mean and width is set respectively to the arithmetic average and RMS of each distribution.

The resulting systematic uncertainty associated to the fit bias is the dominant one and is equal to 0.0023.

All the contributions entering the systematic error are summarized in table 12.3.

Table 12.3: Summary of systematic uncertainties on the measurement of $|q/p|$.

Source	Systematic uncertainty
SVT alignment	0.0008
D_{tag} modeling	0.0008
Sample composition	0.0005
Combinatorial correction factor	$(\lvert q/p\rvert - 1) \cdot 0.034$
Pion contamination	0.0006
Fixed parameters of the resolution	0.0001
CP-eigenstates	0.0003
Measurement of D_{tag} fractions	0.0006
Fraction of continuum	0.0003
Fake leptons	0.0001
Number of samples	0.0007
Variation of τ_{B^0} and Δm	$0.0005 \oplus (\lvert q/p\rvert - 1) \cdot 0.03$
Total without fit bias	$0.0018 \oplus (\lvert q/p\rvert - 1) \cdot 0.045$
Fit bias	0.0023
Total	$0.0029 \oplus (\lvert q/p\rvert - 1) \cdot 0.045$

Chapter 13

Conclusions

After making sure that the fit procedure has been *frozen* and the result is stable within the systematic errors we have computed, the Review Committee internal of the BABAR Collaboration authorized the unblinding on $|q/p|-1$.

The result, corrected for the bias we observe in the Monte Carlo, is:

$$|q/p|-1 = 0.0096 \pm 0.0025\ (\text{stat.}) \pm 0.0029\ (\text{syst.}) \tag{13.1}$$

This result is 2.5 standard deviations away from the CP-conserving case and is in very good agreement with the other BABAR result [45] obtained on the recoil of partially reconstructed $\overline{B}^0 \to D^{*+}\ell^-\bar{\nu}_\ell$, which uses the lepton tag. Also very good compatibility is found with Belle's result [42], while the compatibility of the BABAR measurement with dileptons [43] is at the $2.1\,\sigma$ level.

The main limit of this result is the large systematic uncertainty associated to the bias we observe in our Monte Carlo. With the full understanding of this source of systematic and running a single fit over the whole statistics taking advantage of dedicated computing resources, this analysis can aim at becoming the leading result in the measurement of CP-violation in $B^0\overline{B}^0$ Mixing.

List of Figures

List of Tables

Bibliography

[1] F. J. Hasert *et al., Nucl. Phys.* **B73**, 1 (1974).

[2] G. Arnison *et al., Phys. Lett.* **B122**, 103 (1983).

[3] G. Arnison *et al., Phys. Lett.* **B126**, 398 (1983).

[4] W. M. Yao *et al., J. Phys.* **G33**, 1 (2006).

[5] F. Mandl and G. Shaw, *Quantum Field Theory* (Revised Edition), Wiley and Sons (Great Britain, 1993).

[6] O. W. Greenberg, *et al., Phys. Rev. Lett.* **89**, 231602 (2002).

[7] C. S. Wu *et al., Phys. Rev.* **105**, 1413 (1957).

[8] J. D. Richman *et al., Rev. Mod. Phys.* **67**, 893 (2000).

[9] L. Wolfenstein *Phys. Rev. Lett.* **51**, 1945 (1983).

[10] C. Jarlskog *Phys. Rev. Lett.* **55**, 1039 (1985).

[11] M. Bona *et al., JHEP* **0610** 081 (2006).

[12] J. H. Christenson *et al., Phys. Rev. Lett.* **13**, 138 (1964).

[13] A. D. Sacharov, *ZhETF Pis. Red.* **5** 32 (1967); *JETP Lett.* **5**, 24 (1967).

[14] N. Cabibbo, *Phys. Rev. Lett.* **10**, 531 (1963).

[15] M. Kobayashi and T. Maskawa, *Prog. Th. Phys.* **49**, 652 (1973).

[16] B. Aubert *et al., Phys. Rev. Lett.* **93**, 131801 (2004).

[17] B. Aubert *et al., Phys. Rev. Lett.* **87**, 091801 (2001).

[18] K. Abe *et al., Phys. Rev. Lett.* **87**, 091802 (2001).

[19] J. Chay *et al., Phys. Lett.* **B247**, 399 (1999).

[20] A. J. Buras *et al., Nucl. Phys.* **B347**, 491 (1990).

[21] M. Ciuchini *et al., JHEP* **0308** 031 (2003).

[22] D. Becirevic *et al., JHEP* **0204** 025 (2002).

[23] U. Nierste *Nucl. Phys. Proc. Suppl.* **170**, 135 (2007).

[24] D. Cocolicchio *et al., Phys. Lett.* **B291**, 155 (1992).

[25] M. Bona *et al.* hep-ex/0709.0451 (2007).

[26] A. I. Sanda *et al., Phys. Rev.* **D56**, 6866-6874 (1997).

[27] M. Blanke *et al., JHEP* **0612**, 003 (2006).

[28] L. Randall *et al., Nucl. Phys.* **B540**, 37 (1999).

[29] V.M. Abazov *et al., Phys. Rev. Lett.* **98**, 121801 (2007).

[30] B. Aubert *et al., Phys. Rev.* **D70**, 012007 (2004).

[31] B. Aubert *et al., Phys. Rev. Lett.* **94**, 161803 (2004).

[32] O. Long *et al., Phys. Rev.* **D68**, 034010 (2003).

[33] R. Barate *et al., Phys. Lett.* **B492**, 275 (2000); P. Abreu *et al., Z. Phys.* **C68**, 13 (1995); R. Akers *et al., Z. Phys.* **C67**, 365 (1995).

[34] D. Busculic *et al., Z. Phys.* **C75**, 397 (1997); P. Abreu *et al., Phys. Lett.* **B338**, 409 (1994); G. Alexander *et al., Z. Phys.* **C72**, 377 (1996).

[35] H. Albrecht *et al., Phys. Lett.* **B324**, 249 (1994); J. E. Bartelt *et al., Phys. Rev. Lett.* **71**, 1680 (1993).

[36] P. Abreu *et al., Phys. Lett.* **B510**, 55 (2001); G. Abbiendi *et al., Phys. Lett.* **B482**, 15 (2000).

[37] P. Abreu *et al., Z. Phys.* **C76**, 579 (1997); G. Abbiendi *et al., Phys. Lett.* **B493**, 266 (2000).

[38] B. Aubert *et al., Phys. Rev. Lett.* **89**, 011802 (2002).

[39] B. Aubert *et al., Phys. Rev.* **D73**, 012004 (2006).

[40] B. Aubert *et al., Phys. Rev. Lett.* **95**, 042001 (2005).

[41] B. Aubert *et al.* hep-ex/0704.2080 (2007).

[42] E. Nakano *et al., Phys. Rev.* **D73**, 112002 (2006).

[43] B. Aubert *et al., Phys. Rev. Lett.* **96**, 251802 (2006).

[44] V.M. Abazov *et al., Phys. Rev.* **D74**, 092001 (2006).

[45] B. Aubert *et al.* hep-ex/0607091 (2006).

[46] P. F. Harrison *et al.*, The *BABAR* physics book: Physics at an Asymmetric B factory, SLAC-R-0504 (1998).

[47] P. Oddone *Annals N.Y. Acad. Sci.* **578**, 237 (1989).

[48] PEP-II - An Asymmetric *B* Factory, Conceptual Design Report, SLAC-418, LBL-5379 (1993).

[49] U. Wienands *et al.*, Invited talk at Albuquerque 2007, Particle Accelerator, 37.

[50] T. Mattison *et al.*, Background Measurements during PEP-II Commissioning, *Proceedings of the IEEE Particle Accelerator Conference (PAC99)*, New York, N.Y., USA (1999).

[51] B. Aubert *et al. Nucl. Instrum. Meth.* **A479**, 1 (2002).

[52] B. Aubert *et al., Phys. Rev. Lett.* **98**, 211802 (2007).

[53] M. Staric *et al., Phys. Rev. Lett.* **98**, 211803 (2007).

[54] D. H. Wrigth *et al.* hep-ph/0305240 (2003).

[55] T. Sjöstrand *Comput. Phys. Commun.* **82**, 74 (1994).

[56] E. Barberio *et al. Comput. Phys. Commun.* **79**, 291 (1994).

[57] V. Re *et al. Nucl. Instrum. Meth.* **A409**, 354 (1998).

[58] P. Coyle *et al. Nucl. Instrum. Meth.* **A343**, 292 (1994).

[59] R. Santonico *et al. Nucl. Instrum. Meth.* **A187**, 377 (1981).

[60] G. Battistoni *et al. Nucl. Instrum. Meth.* **A164**, 57 (1979).

[61] I. Narsky *StatPatternRecognition: A C++ Package for Statistical Analysis of High Energy Physics Data*, physics/0507143, 2005.

[62] I. Narsky *Optimization of Signal Significance by Bagging Decision Trees*, physics/0507157, 2005.

Acknowledgements

My eternal gratitude goes to Martino Margoni, who tirelessly assisted me during all the phases of this tough analysis, working well beyond his duties during holidays and weekends, I will never forget this. My warmest thanks also to Franco Simonetto for giving me the opportunity to apply this original analysis method to the measurement of CP-violation in $B^0\overline{B}^0$ mixing.

I would like also to thank the other members of the *BABAR* Padova group: Mario Posocco, Roberto Stroili, Peter Solagna, who assisted me in my six months taking care of the processing farms, Nicola Gagliardi and Marcello Rotondo, whose inspired experimental attitude led to the brilliant success of the *BABAR* Italia social after-dinner in Padova. Last but certainly not least I wish to thank the big heart of Mauro Morandin for addressing me to the University of Colorado and thanks also to Jim Smith and Bill Ford for trusting me and giving me the opportunity of working in their group.

Many thanks to the (former) undergraduate students who worked alongside me during my stay at the University of Padova: Lucio Biondaro, Carlotta Favaro, Stefano Cordeddu, Alessandro Sfondrini and Stefania Cerutti. A special thank to Claudio Borile and Cristiano Fontana: this thesis really took advantage of their work on the production of Toy and Reweighted Monte Carlo samples.

I cannot avoid to mention my colleagues of room 170, now working outside Padova: Antonio Bergnoli, Fabrizio *professor* Furano and most of all Elisa Stevanato (best known as *Clarissa*) for constituting an unreachable source of inspiration for her colleagues. Many thanks also to the habitual visitors of room 170, in particular to Moreno Marzolla, fellow of the indoor and the outdoor CAAAAFEEEEE' ritual, and to the *delegation*, bravely led by Luca Stevanato, supported by the worthy Cristiano Fontana and girlfriend. Best wishes to Giuliano Castelli, left alone in room 170, and also good luck to him if he will be involved in the even more challenging analysis of CP-violation in mixing with the single-tag technique.

I am also grateful to the other young Italian *BaBarians* with which I shared short and long periods at SLAC: Virglinia Azzolini, Elisabetta Baracchini, Marco Bomben, Marcella Bona, Annalisa Cecchi, Alberto Cervelli (co-author of the famous Cervelli-Gaz algorithm), Riccardo Cenci, Antonio and Tina Ceseracciu, Gigi Cibinetto, Roberto Covarelli, Emanuele Di Marco (*Baffetto*), Alessia D'Orazio, Enrico Feltresi, Paolo Franchini, Alfio Lazzaro, Vincenzo Lombardo, Giovanni Marchiori, Nicola Neri, Mario Pelliccioni, Maurizio Pierini (another great source of inspiration for me), Antonio Petrella, Elisabetta Prencipe, Matteo Rama, Francesco Renga, Roberto *sir* Sacco, Emmanuele Salvati (*Sarvà*), Valentina Santoro, Viola Sordini, Silvano Tosi, Marco Vignati and finally the *Derrick Twins* (and many apologies if I forgot somebody). A very special thank to Loredana Lopez and Elisa Manoni (the *IFR girls*) and Mirco Andreotti for sharing with me the task of taking care of the IFR. Thanks also to Henry Band, Bob Kowalewski, Masahiro Morii, Katherine George, Kevin Flood, Sasha Telnov and Chih-hsiang Cheng for useful discussions about my work.

I'm also indebted to the across-the-Ocean printers of this thesis: Matteo Agostini, Nicola Gagliardi and Giacomo Siviero.

My education would have not been possible without the full (material and psychological) support of my family: my mother Rina, my father Stefano (who always blindly trusted my achievements, never ever assuming a polemical attitude) and my sister Elena.

Then my thoughts go to the people of my town of Zermen for the nice and friendly environment in which I grew up. In particular many thanks to my cousin Alberto, Roberto, Marsia and her brother Alezzio, Peter and his cousin Heidi (unequalled teacher of *bon ton*), Federica, *Maestro* Luca *Signor* Curto, *don* Robèrt, Ginger, Marci, Erik Curto and Matia Ceccato, Eros, Rodney, *the Marshall* and all the many others I could not mention here.

Thanks also to the friends of the Associazione Astronomica Feltrina *Rheticus*, with whom I moved my first steps as an experimentalist (but mostly as an admirer of the sky), and thanks to Sara, for the funny experimental activity we have been involved into.

I would like to remember also my numerous flat-mates I had during my stay in Padova: Peter, Predrag, Roberto, Barbara, Antonio (*dottor Minchia*), his mother and his colleagues of the *Little Italy* community, Raffaella, Alessandro, Eduard, XXX, YYY, Damiano, Fabian and Mohammed.

Finally my due tribute to the glorious Associazione P.A.P.A., in particular to the most important members: Presidente, P.R., COCPMSC (*Oh my God, my husband!*), Banditore Vice Segretario Tesoriere, Vessillifera (first lab-mate at University) and her husband, Studente Modello (and his brother *Dr.* Studente Fratello, who still has to finish his homework), Capoclasse Elementare, Stinco Giocoliere, Terrorista, Scriba, Inquisitore, CVIP, Glicine, Bidonella, Eretico, Sessuologa, Arrembante (and friends) and Tegone.

For sure I forgot to mention somebody I am grateful to: my apologies. Anyway, *Evviva il Signor Segretario Tesoriere*!